九州大学学術情報リポジトリ
Kyushu University Institutional Repository

DEVELOPMENT AND APPLICATION OF A NEW NUMERICAL SIMULATION METHOD FOR DEBRIS FLOW WITH LARGE BOULDERS BY COUPLING 3D DDA

余, 鵬程

https://hdl.handle.net/2324/4110494

出版情報：Kyushu University, 2020, 博士（工学）, 課程博士
バージョン：
権利関係：

DEVELOPMENT AND APPLICATION OF A NEW NUMERICAL SIMULATION METHOD FOR DEBRIS FLOW WITH LARGE BOULDERS BY COUPLING 3D DDA

Pengcheng Yu

DEVELOPMENT AND APPLICATION OF A NEW NUMERICAL SIMULATION METHOD FOR DEBRIS FLOW WITH LARGE BOULDERS BY COUPLING 3D DDA

A Thesis Submitted
In Partial Fulfillment of the Requirements
For the Degree of
Doctor of Engineering

By

Pengcheng Yu

九州大学

to the

DEPARTMENT OF CIVIL AND STRUCTURAL ENGINEERING
GRADUATE SCHOOL OF ENGINEERING
KYUSHU UNIVERSITY
Fukuoka, Japan

July, 2020

DEPARTMENT OF CIVIL AND STRUCTURAL ENGINEERING
GRADUATE SCHOOL OF ENGINEERING
KYUSHU UNIVERSITY
Fukuoka, Japan

CERTIFICATE

The undersigned hereby certify that they have read and recommended to the Graduate School of Engineering for the acceptance of this thesis entitled, ‘‘***Development and application of a new numerical simulation method for debris flow with large boulders by coupling 3D DDA***” by **Pengcheng Yu** in partial fulfillment of the requirements for the degree of **Doctor of Engineering**.

Dated: July, 2020

Thesis Supervisor:

_____

Prof. Guangqi CHEN, Dr. Sci.

Examining Committee:

_____

Prof. Yasuhiro MITANI, Dr. Eng.

_____

Prof. Shinichiro YANO, Dr. Eng.

ABSTRACT

Debris flow is a geo-hazard frequently occurred in mountainous regions. Due to the sudden occurrence, high-speed motion and large volume of sediment, debris flow can cause serious disaster and is one of the major threats to residents and structures in susceptible areas. For example, the 1999 Venezuela debris flow killed about 15,000 lives and destroyed or damaged more than 88,000 buildings. Various kinds of countermeasures, such as check dams and concrete canals, have been developed for disaster mitigation. In order to design proper countermeasure structures, it is important and necessary to estimate the kinematic and mechanic behaviors of a potential debris flow as well as impact forces on structures in risk.

In recent decades, many studies on debris flows have been conducted by using numerical methods, analytical methods, empirical approaches based on in-situ investigations and laboratory experiments. With advancement of computer technique, numerical methods become more and more attracting in researchers in this field. Among them, conventional debris flow simulation (DFS) with a depth-integrated model based on Navier-Stokes equations has been widely used because it can be easily applied to simulate evolution of debris flow with bed-sediment erosion as well as estimate kinematic behaviors such as flowing velocity, depth and volume of debris flow and inundated area with high efficiency. However, since DFS is based on two-phase fluid of water and solid, called pure debris flow here, using the so-called volume concentration for different ratio of solid to water, there are seldom debris flows of two-phase fluid in nature. In fact, large boulders and driftwoods are often involved in debris flows, called boulder debris flow here, according to a large number of past events. It is obvious that the behaviors and impact force of boulder debris flow cannot be correctly estimated by DFS with two-phase fluid model. How to simulate boulder debris flows still remains unsolved problem.

This study aims at developing a new numeric technique for simulating boulder debris flows by coupling Discontinuous Deformation Analysis (DDA) with

conventional DFS. DDA is a powerful numerical method for modelling dynamic behaviors of a rock mass system involving discontinuities, and it has been well used for rock-fall analysis and landslide simulation. Thus, the dynamic behavior and impact force of the transported boulders in debris flow can be estimated by three-dimensional DDA while the kinematic and mechanic behaviors of two-phase fluid are estimated by conventional DFS. To this end, the existing 3D DDA is firstly improved by incorporating a damped contact model to simulate inelastic collisions. And then, a coupled method of improved DDA and DFS (3D DDA-DFS) is developed for simulating boulder debris flows. Subsequently, the impact force of large boulders on check dam are investigated and discussed through a series of conceptual examples. Finally, a case study is carried out using the developed 3D DDA-DFS method to discuss the kinematic and mechanic behaviors of a boulder debris flow based on a real catchment.

The contents of the thesis are organized as follows:

Chapter 1 introduces the background, the scope and objectives of the research. Previous studies on debris flow and the transported large boulders are reviewed. The existing methods are briefly discussed.

Chapter 2 reviews the state-of-the-arts of 3D DDA and DFS. The basic theories and equations are introduced together with their advantages and applications. The above-mentioned unsolved problems are also clarified.

Chapter 3 improves 3D DDA by incorporating a damped contact model for inelastic collision. Original DDA is based on perfectly elastic collision, but energy dissipation occurs almost in any real collisions in nature. If energy loss is not addressed, the collisions between large boulders, slope surface and structure could be inaccurate. In order to make DDA applicable to real collisions, a damped contact model based on linear spring-dashpot assumption is incorporated into 3D DDA. How to determine the control parameter viscous damping coefficient of dashpots is discussed and clarified using a predefined coefficient of restitution (COR). Inelastic collisions with unconstrained and fixed targets are carefully investigated. Rebound of a freefall block assembly is analyzed for demonstrating viscous damping effect.

The results show that the damping effect is significant and should be properly addressed.

Chapter 4 develops a fluid-solid coupling method called 3D DDA-DFS by coupling 3D DDA with DFS for simulating boulder debris flows. First, a framework for flow-solid interaction is proposed. Then, an interactive module is incorporated for evaluating the interactive forces between DFS flow and DDA solid blocks through the synchronization of the 3D DDA module and DFS module since time steps in both methods are quite different. Thirdly, the flow force on solid blocks, including static pressure, buoyancy and drag force, are incorporated for arbitrarily shaped polyhedral blocks on complex 3D terrain. In addition, the drag effect between adjacent blocks is addressed so that the calculated drag force is more realistic. Fourthly, since direct implementing of force from DDA blocks on DFS flow is not easy, which involves large deformed boundary condition in the flow governing equation, an equivalent solution is proposed by taking the action of blocks on flow as time-varying elevation of terrain node. Finally, the coupling scheme as well as the calculations of the interaction forces are validated by a number of examples.

Chapter 5 clarifies the behaviors of large boulders and driftwoods in debris flow. At first, a series of simulations are carried out on debris flows with boulders in a channel model with a downstream check dam. The impact forces and deformations that the dam suffers from are analyzed under different kinds of debris flows. The results show that (1) A boulder debris flow can destroy the check dam that cannot be destroyed by the corresponding pure debris flow, and the impact force of the boulder debris flow can be about 15 times larger in an example than that of the pure debris flow; (2) The impact forces and deformations are related to the size, distribution and shape of the boulders very much. The dam can be deformed slightly or largely and even destroyed totally under different boulders. Larger size, higher initial altitude, subcircular shape of the boulders are capable of causing more damages to the dam. And then, the behaviors of driftwoods in debris flow are also investigated. The movement looks reasonable, and the impact force is larger than that of pure debris flow but smaller than that of the boulder with the

same volume. The driftwoods can either be stopped by the dam or pass over the dam when overflowing occurs. The example shows that the driftwoods in debris flow can also be simulated by developed 3D DDA-DFS method.

Chapter 6 performs a case study by using the 3D DDA-DFS method to simulate potential debris flow with large boulders based on a real catchment located in Amami Oshima, Japan, where the 2010 Yohutagawa debris-flow event occurred. The same source area of the debris flow is used, and a number of boulders are distributed in the valley path. When debris flow passes by, the boulders are driven and move along with debris flow. The simulation results show that the transported boulders can break the dam, and more area will be affected by the alluvial fan although the dam was not destroyed under the real debris flows due to no large boulders involved. The dam safety is further analyzed by a number of dam properties and the results suggest that the strength of the dam should be much higher if boulders are involved in a potential debris rather than a pure debris flow. Therefore, the developed 3D DDA-DFS method is applicable to simulation of debris flow with large boulders. The 3D DDA-DFS can be used to check whether the check dam is safe under boulder debris flow, and the critical strength of check dam can also be determined by 3D DDA-DFS simulation.

Chapter 7 summarizes the conclusions and recommends the problems to be solved in future studies.

ACKNOWLEDGMENTS

It has been three years since I became a doctoral candidate in the department of civil and structural engineering, Kyushu University. I was grateful to have this study experience. I got a lot of help from many people both in research and daily life. Everything that I have achieved would not be possible without them, including this thesis.

I want to say special thanks to my supervisor, Prof. Dr. Guangqi Chen. He helped me to apply for this doctoral program position as well as my scholarship. His board professional knowledge and insightful research opinions have greatly inspired me. I benefit a lot from his patient guidance, wise ideals and rich research resources. Not only being a qualified researcher, he also shows me how to become a better person. In addition, the scientific research environment of Prof. Chen's team is favorable. I am so grateful to become a member of his team. It is him that makes me who I am today.

I also wish to express my thanks to my supervisor in my master studies, Prof. Dr. John X. Zhao. He is the one who led me into research field and shown me what it means to be a researcher. I also want to thank Prof. Dr. Yingbin Zhang. He taught me about DDA, which is the foundation of my current research. They kept giving me valuable suggestions and helping me as they can so that I can stand a better chance facing challenges.

I want to express my sincere gratitude to my thesis committee members, Prof. Dr. Guangqi Chen, Prof. Dr. Yasuhiro MITANI and Prof. Dr. Shinichiro YANO for their valuable time and comments on this thesis.

I wish to thank my friends and colleagues here in the laboratory, Mr. Longxiao Guo, Mr. Cungen Wang, Dr. Dejian Li, Ms. Xiao Cheng, Mr. Shilin Gong, Mr. Mingyao Xia, Ms. Hongyan Yu, Mr. Chengwen Cai, Ms. Hui Niu, Ms. Sijia Li, Mr. Qasim, Mr. Changze Li, Ms. Jiaying Li, Ms. Thuy, Mr. Jeep, Mr. Yan Liu. Thank you for the great discussions and precious memories.

A special thanks to the graduated doctors in this team, particularly, Dr. Lu Zheng, Dr. Hong Zhang, Dr. Zheng Han, Dr. Wei Wang, Dr. Yi He, Dr. Long Zhang and Dr. Guojun Liu. Your help is sincerely appreciated.

I am indebted to my parents for being aboard and far from home in these years. You never stopped encouraging me to pursue my dream. My achievements are also yours. I am also indebted to my girlfriend, Ms. Xinyan Peng. You kept me accompany since university. I do not need to emphasize your excellence. I am so grateful to have you beside me. After three years, we are about to start our new pages. Let us do it together.

I wish to thank the Department of Civil and Structural Engineering, Kyushu University. I also wish to thank the education section of the Consulate-general of the people's republic of China in Fukuoka. Your support is my strongest backing, especially in this special time.

Thanks for the financial support from the China Scholarship Council (CSC), which makes my research possible.

.

TABLE OF CONTENTS

ABSTRACT ..... **i**
ACKNOWLEDGMENTS ..... **v**
Table of Contents ..... **vii**
List of Figures ..... **x**
List of Tables ..... **xvii**
List of Notations or Acronym ..... **xviii**
CHAPTER 1 ..... **1**
1. Introduction **1**
1.1. Background 1
1.1.1. Some debris flow cases 2
1.1.2. Large boulders transported by debris flow 5
1.1.3. Triggering factors of debris flow 6
1.2. Research approaches 8
1.2.1. Approaches for debris flow 8
1.2.2. Approaches for the transported boulders 10
1.3. Scopes and objectives 14
1.3.1. Existing problems 14
1.3.2. Objectives of the thesis 15
1.4. Framework of the thesis 15
References 18
CHAPTER 2 ..... **29**
2. State-of-the-art of 3D DDA and debris flow simulation **29**
2.1. Introduction 29
2.2. 3D DDA: State-of-the-art 30
2.2.1. General dynamic equations 30
2.2.2. Simplex integration 33
2.2.3. Assembly of non-contact matrices 38
2.2.4. Assembly of contact matrices 42

2.2.5. Open-close iteration (OCI) 52
2.3. Debris flow simulation: State-of-the-art 52
2.3.1. Derivation of the governing equations 52
2.3.2. Rheology parameters and entrainment model 58
2.3.3. FDM scheme to solve the governing equations 60
2.4. Conclusions 61
Reference 62
CHAPTER 3 69
3. Improvements of 3D DDA by incorporating a damped contact model for inelastic collision 69
3.1. Introduction 69
3.2. Damped contact model in 3D DDA 70
3.3. Validation of the damped contact model 75
3.4. Determination of viscous damping coefficient: block collision with an unconstrained target 76
3.5. Determination of viscous damping coefficient: block collision with a fixed target 84
3.6. Application to blocks assembly freefall and rebound 86
3.7. Conclusions 88
Reference 91
CHAPTER 4 94
4. Development of a fluid-solid coupling method 3D DDA-DFS for simulating boulder debris flows 94
4.1. Introduction 94
4.2. Framework for flow-solid interaction used in 3D DDA-DFS 96
4.3. Calculation of block buoyancy 99
4.3.1. Calculation of block buoyancy 99
4.3.2. Fluid prism detection 102
4.3.3. Bottom face determination for the fluid prism (overlapped polygon search algorithm) 104
4.4. Calculation of fluid drag force and static pressure 109

4.5. Drag effect between adjacent blocks 111
4.6. An equivalent solution to address block actions on flow 118
4.7. Validation examples 119
4.8. Conclusions 126
Reference 128
CHAPTER 5 134
5. Clarification of the behaviors of large boulders and driftwoods in debris flow 134
5.1. Introduction 134
5.2. Model settings, parameters and construction..... 135
5.3. Configuration cases: dam stability under varying flow volume..... 140
5.4. The effect of boulders on the check dam..... 145
5.5. The effect of boulder size 149
5.6. The effect of boulder distribution..... 157
5.7. The effect of boulder shape 162
5.8. Simulation of driftwoods in debris flow..... 166
5.9. Conclusions 168
Reference 170
CHAPTER 6 172
6. Case study: using the 3D DDA-DFS method based on a real terrain territory model located in Amami Oshima, Japan to estimate check dam safety 172
6.1. Introduction 172
6.2. Model settings and parameters 173
6.3. Dam stability under pure debris flow and boulder debris flow 176
6.4. Estimation of safe dam parameters under boulder debris flow 179
6.5. Conclusions 184
Reference 186
CHAPTER 7 187
7. Conclusions and future studies 187
7.1. Highlights and major conclusions 187
7.2. Future studies..... 190

LIST OF FIGURES

Figure 1.1 Thick debris flow deposits in a channel of Quebrada San Julian near Caraballeda. The size of the boulders can be greater than a human (Larsen, M. C. et al., 2006) 3
Figure 1.2 Debris flow fan of Sanyanyu debris flow (Wang, G. L., 2013) 4
Figure 1.3 Photos taken for a debris flow breaking a dam at Kamikamihori, Mt. Yake, Japan, on 3 Aug. 1976 (Okuda, S. et al., 1977; Takahashi, T., 1981) 5
Figure 1.4 Observed large boulders in the area of the 1999 Venezuela debris flow event. ((Larsen, M. C. et al., 2006; Pérez, F. L., 2001; Wieczorek, G., 2001)) 6
Figure 1.5 Damaged concrete bridge beam by point impact loads of boulders (modified from Hunger, O. et al. (1984)) 11
Figure 1.6 Framework of the thesis 17
Figure 2.1 A 3D simplex (Shi, G., 1989) 33
Figure 2.2 Contact types in 3D DDA (modified after Peng, X. et al. (2020a)) 43
Figure 2.3 Schematic diagram of a contact (Yu, P. et al., 2020) 45
Figure 2.4 Illustrations of the geometric relations to locate P_1 47
Figure 2.5 Schematic diagram of debris flow 57
Figure 3.1 Schematic diagram of the damped contact model, in which contact springs and dampers are applied 71
Figure 3.2 Flowchart of 3D DDA (Red dash square denotes the modified subroutines) 74
Figure 3.3 Schematic diagram of a damped SDOF system (unit: m) 76
Figure 3.4 Comparison of simulated displacements in normal and shear vibrations and the theoretical solution 77
Figure 3.5 Motions of block 1 (m_1) and block 2 (m_2) (a) before (b) during and (c) after collision 78

Figure 3.6 3D DDA model of a block colliding with an unconstrained target block (unit: m) 81
Figure 3.7 (a) Results of post-collisional velocities from 3D DDA simulation and analytical solution and (b) relative error (m_1: m_2=1:1) 82
Figure 3.8 Collision time duration obtained from 3D DDA simulation and analytical solution and the relative error (m_1: m_2=1:1) 83
Figure 3.9 Results of post-collisional velocities from 3D DDA simulation and analytical solution and (b) relative error (m_1: m_2 = 1:3) 83
Figure 3.10 Collision time duration obtained from 3D DDA simulation and analytical solution and the relative error (m_1: m_2 = 1:3) 84
Figure 3.11 3D DDA model of a block colliding with a fixed target block (unit: m) 85
Figure 3.12 Results of post-collisional velocities and relative error 85
Figure 3.13 Collision time duration and the relative error 86
Figure 3.14 Schematic diagram of the blocks freefall and rebound model (unit: m) 87
Figure 3.15 Blocks freefall and rebound modelled by 3D DDA (a) case 1: c = 0 and (b) case 2: c = 30000 N/(m/s) (unit: m) 88
Figure 3.16 Results of post-collisional velocities and relative error when the mass of the fixed block is increased by 1000 times 90
Figure 3.17 Collision time duration and the relative error when the mass of the fixed block is increased by 1000 times 90
Figure 4.1 Schematic illustration of the boulders in debris flow 95
Figure 4.2 Modules of 3D DDA-DFS 97
Figure 4.3 Detailed structure of 3D DDA-DFS 98
Figure 4.4 Illustrative diagram for submerged volume Vs 100
Figure 4.5 Diagram of $\boldsymbol{V_f}$ under the condition of the block facet (a) over the fluid surface, (b) partially submerged by fluid, and (c) totally submerged by fluid 101
Figure 4.6 Methodology used in fluid prism detection: (a) project two polygons onto a common projection plane and identify the overlapped

polygon (b) trace back the overlapped polygon to its original position to identify the top facet(s) of the fluid prism. 103
Figure 4.7 Extend point storage by adding new intersections. The red number denotes the newly detected intersections that have not been recorded. The "*" and "-" symbols in the table mean the node is not shown in the figure and does not exist, respectively. 106
Figure 4.8 Illustration for "in" and "out" intersections 107
Figure 4.9 Two possible situations for edges coincide (a) same order, edge 2-3 regarded inside and (b) opposite order, edge 2-3 regarded as outside 107
Figure 4.10 Flow chart for the algorithm used to form overlapped polygons 108
Figure 4.11 The location of drag force F_d. C is the center of the velocity polygon 111
Figure 4.12 Two blocks in a flow field 112
Figure 4.13 Streamline patterns with velocity fields at (a) one cylinder, (b) L/D = 0.5, single mode, (c) L/D = 2, reattached mode and (d) L/D = 4, binary mode at Re = 535 (Yen, S. C. et al., 2008) 114
Figure 4.14 drag force calculation for block pair of different size 118
Figure 4.15 Elevation of terrain node to consider the disturbance of block to flow field 119
Figure 4.16 A block floating in flow to validate buoyancy calculation 120
Figure 4.17 Calculated d by 3D DDA-DFS and theoretical solution given by equation (4.23) 120
Figure 4.18 (a) A schematic figure and (b) calculation model in the 3D DDA-DFS of the block acceleration example (Unit: m, s) 121
Figure 4.19 Block acceleration model calculated by the extended 3D DDA with fluid dynamics 122
Figure 4.20 Block velocity calculated by the extended 3D DDA and analytical solution 123

Figure 4.21 (a) A schematic figure and (b) calculation model in the E-DDA of the block rotation deceleration example (Unit: m, s) 123
Figure 4.22 Diagram of the floated rotating block decelerated by fluid 125
Figure 4.23 Block angular velocity calculated by the extended 3D DDA and analytical solution 125
Figure 4.24 Example used to illustrate multi-block interaction 126
Figure 4.25 Simulated results for (a) considering blocks interaction in flow and (b) no interaction 127
Figure 5.1 Description of the adopted model (unit: m) 136
Figure 5.2 The dimension of the initial debris flow mass area (unit: m) 138
Figure 5.3 Block velocities in model generation 139
Figure 5.4 Block displacements in model generation 139
Figure 5.5 Flow depth of the simulation result with initial flow mass height 1 m 141
Figure 5.6 Flow depth of the simulation result with initial flow mass height 2 m 142
Figure 5.7 Flow depth of the simulation result with initial flow mass height 3 m 143
Figure 5.8 Average displacement of the dam in case 1 to 3 144
Figure 5.9 Total impact force on the dam in case 1 to 3 144
Figure 5.10 Force analysis diagram of dam stability 145
Figure 5.11 The cases used to illustrate the effect when boulders exist (a) the contrast cases without boulders, the initial flow mass height is 1 m (case 4) and 2 m (case 5) (b) the tested cases with boulders and initial flow mass height 1 m (case 6) and 2 m (case 7) (unit: m) 146
Figure 5.12 Flow depth and dam safety at t = 20 s for (a) initial height 1 m and no boulder (b) initial height 1 m with boulders (c) initial height 2 m and no boulder (b) initial height 2 m with boulders 147
Figure 5.13 Average displacement of the dam in case 4 to 7 148
Figure 5.14 Total impact force on the dam in case 4 to 7 148

Figure 5.15 (a) impact stress and (b) boulders distribution at first major impact (about 10.8 s) 150
Figure 5.16 (a) impact stress and (b) boulders distribution at second major impact (about 13.1 s) 150
Figure 5.17 (a) impact stress and (b) boulders distribution at the end of the simulation (20 s) 151
Figure 5.18 Flow depth and dam safety at *t* = 20 s with boulders of 1 m diameter 151
Figure 5.19 Flow depth and dam safety at *t* = 20 s with boulders of 2 m diameter 152
Figure 5.20 Schematic diagram for case 8, 9 and 10 with boulders of different sizes 153
Figure 5.21 Simulated flow depth and dam safety in case 8 154
Figure 5.22 Simulated flow depth and dam safety in case 9 154
Figure 5.23 Simulated flow depth and dam safety in case 10 155
Figure 5.24 Average velocities of the boulders in case 8 to 10 155
Figure 5.25 Average displacement of the dam in case 8 to 10 156
Figure 5.26 Total impact force on the dam in case 8 to 10 156
Figure 5.27 Schematic diagram for case 11 – 14 with boulders of different positions (unit: m) 157
Figure 5.28 Simulated flow depth and dam safety in case 11 158
Figure 5.29 Simulated flow depth and dam safety in case 12 159
Figure 5.30 Simulated flow depth and dam safety in case 13 159
Figure 5.31 Simulated flow depth and dam safety in case 14 160
Figure 5.32 Average velocities of the boulders in case 11 to 14 161
Figure 5.33 Average displacement of dam in case 11 to 14 161
Figure 5.34 Total impact force on dam in case 11 to 14 161
Figure 5.35 Schematic diagram for (a) case 15, dodecahedral boulders (b) case 16, cubic boulders and (c) case 17, tetrahedral boulders (unit: m) 162
Figure 5.36 Simulated flow depth and dam safety of case 15 163
Figure 5.37 Simulated flow depth and dam safety of case 16 163

Figure 5.38 Simulated flow depth and dam safety of case 17 164
Figure 5.39 Average velocities of the boulders in case 15 to 17 164
Figure 5.40 Average displacement of the dam in case 15 to 17 165
Figure 5.41 Total impact force on the dam in case 15 to 17..... 165
Figure 5.42 Schematic diagram for driftwoods simulation..... 166
Figure 5.43 Simulated flow depth and dam safety of case 18 167
Figure 5.44 Simulated flow depth and dam safety of case 19 167
Figure 5.45 Simulated flow depth and dam safety of case 20 168
Figure 5.46 The maximum total impact force on dam..... 168
Figure 6.1 Air photo of the morphology of 2010 Yohutagawa debris flow (based on the investigation of KKC, image © Google Maps, 2020 Maxar Technologies)..... 173
Figure 6.2 Studied model based on topology and debris flow of Yohutagawa, 2010..... 174
Figure 6.3 The check dam and the dimensions..... 174
Figure 6.4 Flow depth and dam in the initial state of the model with pure debris flow 176
Figure 6.5 Flow depth and dam at *t* = 120 s of simulation with pure debris flow 177
Figure 6.6 Initial flow depth and dam of the model with boulder debris flow 178
Figure 6.7 Flow depth and dam at *t* = 82 s of simulation with boulder debris flow 178
Figure 6.8 Flow depth and dam at *t* = 120 s of simulation with boulder debris flow 179
Figure 6.9 Flow depth and dam at *t* = 120 s of case 1 with cohesion 50 MPa (dam is safe)..... 180
Figure 6.10 Flow depth and dam at *t* = 120 s of case 1 with cohesion 40 MPa (dam is safe)..... 181
Figure 6.11 Flow depth and dam at *t* = 120 s of case 1 with cohesion 30 MPa (dam is unsafe)..... 181

Figure 6.12 Flow depth and dam at *t* = 120 s of case 2 with cohesion 30 MPa (dam is safe) 182
Figure 6.13 Flow depth and dam at *t* = 120 s of case 2 with cohesion 20 MPa (dam is unsafe) 183
Figure 6.14 Flow depth and dam at *t* = 120 s of case 3 with cohesion 10 MPa (dam is safe) 183
Figure 6.15 Flow depth and dam at *t* = 120 s of case 3 with cohesion 1 MPa (dam is safe) 184

LIST OF TABLES

Table 1.1 Classification of flow type landslides (Hungr, O. et al., 2001)..... 2
Table 1.2 Morphologic properties of Sanyanyu and Luojiayu catchments (Hu, K. et al., 2012)..... 4
Table 3.1 Calculated viscous damping ratios and coefficients used in 3D DDA model..... 81
Table 4.1 Critical spacing ratio with various Re (Chatterjee, D. et al., 2012) 115
Table 4.2 Coefficient c_d for upstream (US) and downstream (DS) cylinders (Chatterjee, D. et al., 2012)..... 115
Table 4.3 Relationship between critical spacing ratio and Re 116
Table 4.4 Values of r_1 and r_2 for different flow mode and Re..... 117
Table 6.1 Debris flow parameters used in analyses 175
Table 6.2 Solid phase parameters used in analyses..... 175
Table 6.3 Model control parameters used in analyses 175
Table 6.4 Virtual joint parameters of the dam in case 1-3..... 180
Table 6.5 Safety of the dam in case 1-3..... 184

LIST OF NOTATIONS OR ACRONYM

Notation or **Acronym**	**Description**
FDM	Finite difference method
SPH	Smoothed particle hydrodynamics
DFS	Debris flow simulation
F	Impact force
v	Velocity
k	Stiffness
E	Young's modulus
I	Section moment of inertia
L, l	Length
G	Weight
k_d	Factor
J	Inertia moment
G'	Weight subtracting the buoyancy
α	Impact angle
g	Gravitational acceleration
DWT	Deadweight ton
t	Time
DEM	Discrete element method
DDA	Discontinuous deformation analysis
3D DDA	Three-dimensional DDA
DFS	Debris flow simulation
$\boldsymbol{M}$	Coefficient matrices of mass

Notation or Acronym	**Description**
$\boldsymbol{C}$	Coefficient matrices of damping
$\boldsymbol{K}$	Coefficient matrices of stiffness
$\boldsymbol{F}$	Load matrix
$\boldsymbol{D}$	Displacement matrix
$\dot{\boldsymbol{D}}$	Velocity matrices
$\ddot{\boldsymbol{D}}$	Acceleration matrices
2D DDA	Two-dimensional DDA
u_0, v_0 and w_0	Rigid body translations in *x*-, *y*- and *z*- directions
r_x, r_y and r_z	Rotations around *x*-, *y*- and *z*- directions
ε_x, ε_y and ε_z	Normal strains in *x*-, *y*- and *z*- directions
γ_{yz}, γ_{zx}, and γ_{xy}	Shear stains in *x*-, *y*- and *z*- directions
n	Step number
t_0	Rotations around *z*- directions
Δt	Step time duration
OCI	Open-close iteration
Π	Potential energy
Ω	Domain of integration
$\vec{f}$	Force vector
$\vec{s}$	Displacement vector
i, j	Indexes
(x_i, y_i, z_i)	Coordinates of point i
J	Jacobi determinant
S	Simplex integral
$\boldsymbol{T}$	Displacement transformation matrix
d_{ji}	*J*-th displacement component of block *i*

Notation or Acronym	Description
$\boldsymbol{U}$	Rigid block translations
ρ	Density
$\boldsymbol{\sigma}$	Stress vector
$\boldsymbol{\varepsilon}$	Strain vector
E	Young's modulus
v	Poisson's ratio
V-F	Vertex-facet contact
E-E	Crossing edge-edge contact
V-V	Vertex-vertex contact
V-E	Vertex-edge contact
E-F	Edge-facet contact
F-F	Facet-facet contact
k_n, $k_s(k_\tau)$	Normal and shear contact spring stiffness
$\boldsymbol{n}$, $\boldsymbol{\tau}$	Normal and parallel vector to the entrance point
λ_{b1}, λ_{b2}	Auxiliary parameters
d_n	Overlapping distance
V	Volume
A_0	Double of the area
$\boldsymbol{v}_1$, $\boldsymbol{v}_2$	Auxiliary vectors
L_{rs}	Algebraic complement
$\boldsymbol{H}$, $\boldsymbol{G}$	Coefficient matrices
τ_c	Cohesion
φ	Friction angle
σ_c	Tensile stress
A	Area

Notation or Acronym	Description
v	Velocity vector
p	Pressure
T	Stress vector
g	Body acceleration
ρ_f	Density of debris flow mass
μ	Dynamic viscosity
ρ_p, ρ_w	Particle density in sediment and density of water
C	Sediment concentration
$\bar{l}$, $\bar{h}$	Characteristic flow dimension in x/y and z direction
H	Elevation of the debris flow
Z_b	Bed elevation
h	Flow thickness
F_s, F_b	Force on flow surface and base
ξ_b	Geometric correction factor
LHS	Left-hand side
M, N	x- and y- wise components of unit width discharge
α_1, α_2	Coefficients that adjust the discrepancy against the real one
$\bar{u}$, $\bar{v}$	Depth-averaged velocities in x and y direction
RHS	Right-hand side
β	Ratio of the vertical and horizontal normal force
T_{bx}, T_{by}	Bottom flow resistance in x and y direction
υ	Kinetic viscosity
β_a, β_p	Active and passive earth pressure coefficients
φ_f ,φ_b	Friction angle of the flow and bed
θ_x, θ_y	Slope inclinations along x and y direction

Notation or Acronym	Description
s_1`	Fatting parameter
θ	Local slope inclination
λ_1, λ_2	Pore pressure ratio at the bottom/top of layer 1/2
φ_{bulk}	Bulk basal friction angel
COR (e_i)	Coefficient of restitution
c_n, c_τ	Normal and shear viscous damping coefficient
v_{rn}, $v_{r\tau}$	Normal and shear relative velocity
ϕ	Friction angle
SDOF	Single-degree-of-freedom
ω	Angular frequency
p_0	Amplitude of the driving force
m	Mass
ξ	Damping ratio
ξ_n, ξ_v	Numerical and viscous damping ratio
ω_D	Damped angular frequency
c	Damping coefficient
a_u, a_d	Number of the upward and downward facets
$V_{f,i}$	Volume of the fluid polyhedron below the *i*-th facet
c_d	Drag coefficient
L/D	Space ratio
r_1, r_2	Coefficient for upstream and downstream blocks
Re	Reynolds number
u_∞	Local flow velocity
d	Length

CHAPTER 1

INTRODUCTION

1.1. BACKGROUND

Debris flow is a common geological phenomenon, in which a mixture of water, mud, and stones rushes downhill. Iverson, R. M. (1997) defined debris flow as "masses of poorly sorted sediment, agitated and saturated with water" surges down under gravity. A similar definition was given by Vandine, D. F. et al. (2002) as "a type of mass movement" that involves rapid movement of water-saturated material down a steep and confined channel. Takahashi, T. (2014) described the phenomenon as a flow of sediment and water mixture driven by gravity and attains large mobility. They also stressed that the mixture can be regarded as a flow of continuous fluid.

According to Varnes, D. J. (1978), debris flow refers to the fast travelling sediment (more than 1.5 m per day) containing less than 80% sand and finer granular material. In contrast to the term "earth" or "mud", "debris" is the loose and unsorted material with low plasticity (Hungr, O. et al., 2001). A more detailed classification for flow type landslide is given in Table 1.1 (Hungr, O. et al., 2001). In conclusion, debris flow refers to the rapid flow of saturated non-plastic debris (Hungr, O., 2005).

Although debris flow was noticed at least a hundred years ago, the scientific investigation of the mechanisms began in the 1960s (Takahashi, T., 2014). Rapp, A. (1960) claimed that 46% of the total displaced masses in Karkevagge from 1952

to 1960 were moved by debris flow. Debris flow is capable of creating huge structure damages and property loss. Dowling, C. A. et al. (2013) summarized the global debris flow from 1950 to 2011 together with the fatalities. Their research suggested that there is clearly an increasing tread in fatal debris flow count every ten years: in the 1950-1960 period, there were 10 fatal debris flows; in 1990-2000, it climbed to 55. As claimed by the authors (Dowling, C. A. et al., 2013), debris flows are becoming "disasters of social vulnerability".

Table 1.1 Classification of flow type landslides (Hungr, O. et al., 2001)

Type	Material	Water content	Velocity
Non-liquefied sand flow	Silt, sand, gravel, debris	Dry, moist, saturated	Various
Sand flow slide	Silt, sand, debris, weak rock	Saturated at rupture surface	Extremely rapid
Clay flow slid	Sensitive clay	Not below liquid limit	Extremely rapid
Peat flow	Peat	Saturated	Slow to very rapid
Earth flow	Clay or earth	Near plastic limit	Less than rapid
Debris flow	Debris	Saturated	Extremely rapid
Mud flow	Mud	Not below liquid limit	Greater than very rapid
Debris flood	Debris	Free water	Extremely rapid
Debris avalanche	Debris	Partly or fully saturated	Extremely rapid
Rock avalanche	Fragmented rock	Various, mainly dry	Extremely rapid

1.1.1. SOME DEBRIS FLOW CASES

In 1996, Typhoon Herb hit Taiwan island (Jan, C. D. et al., 2005). From 3 July to 1 August 1996, it brought a huge amount of rain, and the maximum 10-minute, 12-hour, 24-hour and 48-hour rainfall were 25 mm, 113 mm, 1158 mm, and 1987

mm, respectively. (Chiang, S., 1996; Chieng, P., 1998; Lin, S., 1998). The heavy rainfall triggered 52 debris flow in total (20 debris flow in other literature (Lin, M. L. et al., 2000)), and 90% of them located on the Chenyoulan stream watershed. The whole fatality was 73, and 463 people were injured in the event (Lin, M. L. et al., 2000).

The debris flows of Dec. 1999 in Venezuela were also induced by extreme rainfall (Larsen, M. C. et al., 2006; Wieczorek, G., 2001). Before the event, the northern coast of Venezuela lived about 300000 residents. But this district was covered by debris alluvial fans in the event. The death toll is catastrophic, about 15000 in total (Lopez, J. et al., 2003), although the exact number is hard to get. One of the mechanisms is the collapse of the prehistoric debris flows deposits. The average yielded sediment per area was about 1×10^5 m^3/km^2, and the mass per area was 1.7×10^5 t/km^2 (Larsen, M. C. et al., 2006). Many large boulders were observed in in-situ investigations (Figure 1.1).

Figure 1.1 Thick debris flow deposits in a channel of Quebrada San Julian near Caraballeda. The size of the boulders can be greater than a human (Larsen, M. C. et al., 2006)

From Aug. 7 to Aug. 8, 2010, huge rainfall hit Zhouqu County, northwestern China's Gansu Province (Dijkstra, T. et al., 2012; Tang, C. et al., 2011; Wang, G. L., 2013). Six villages, Chunchang, Luojiayu, Yueyuan, Wachang, Beimen, and Sanyanyu, were destroyed by the triggered debris flows, causing more than 1700 fatalities. There were 33 destroyed buildings and 22 partially damaged ones (Hu, K. et al., 2012; Yu, B. et al., 2010). Two major debris flows were triggered together, the Luojiayu debris flow and the Sanyanyu debris flow (Figure 1.2). The larger one, Sanyanyu debris flow, had a fan of 2 km in length and 0.41 km^2 of deposition zone (Wang, G. L., 2013). The morphology for those two debris flows is presented in Table 1.2 (Hu, K. et al., 2012). Based on the investigation of the debris fan and the formed landslide dams, the total runoff of the Sanyanyu debris flow and Luojiayu debris flow was approximately 1.8×10^6 m^3 (Cui, P. et al., 2013).

Table 1.2 Morphologic properties of Sanyanyu and Luojiayu catchments (Hu, K. et al., 2012)

	Catchment area (km^2)	Average gradient (%)	Mainstream length (km)	Elevation summit (m)	Elevation outlet (m)	Relative relief (m)
Sanyanyu	25.75	24.1	10.4	3828	1340	2488
Luojiayu	16.14	25.8	9.5	3780	1320	2460

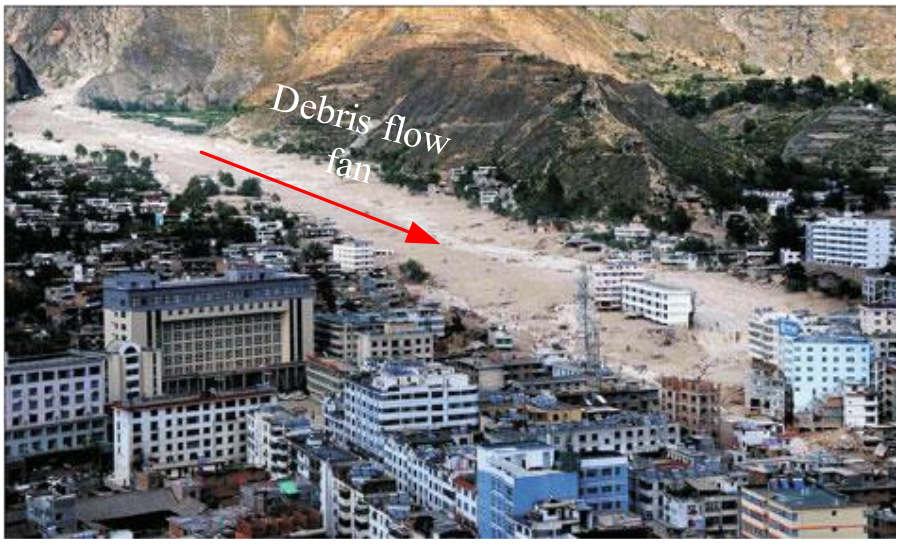

Figure 1.2 Debris flow fan of Sanyanyu debris flow (Wang, G. L., 2013)

1.1.2. LARGE BOULDERS TRANSPORTED BY DEBRIS FLOW

One of the significant characteristics is that debris flow is capable of carrying large boulders. Such phenomenon is very common among debris flow events. They were extensively documented by many researches (Arattano, M., 2000; Berti, M. et al., 1999; Davies, T. R. H., 1990; Kanji, M. A. et al., 2007; Kim, Y. et al., 2013). On 3 Aug. 1976, a dam at Kamikamihori, Mt. Yake, Japan was destroyed by debris flow. The process was recorded by photos, shown in Figure 1.3 (Okuda, S. et al., 1977; Takahashi, T., 1981). The large boulder brought by the debris flow is clear to see, whose velocity is about 3.7 m/s.

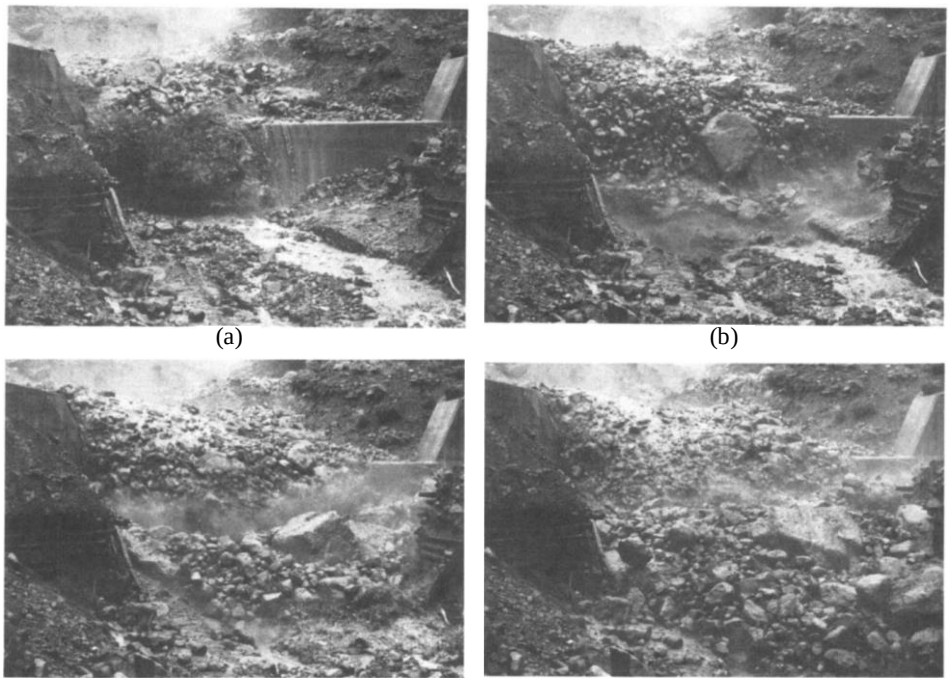

(a) (b) (c) (d)

Figure 1.3 Photos taken for a debris flow breaking a dam at Kamikamihori, Mt. Yake, Japan, on 3 Aug. 1976 (Okuda, S. et al., 1977; Takahashi, T., 1981)

There were a lot of transported boulders observed in the area of 1999 Venezuela debris flow, as presented in Figure 1.4. The photos are from literatures Larsen, M. C. et al. (2006), Wieczorek, G. (2001), and Pérez, F. L. (2001). The large boulder in Figure 1.4(a) was found deposited in the center of the channel of Quebrada Camuri Chiquito, whose size is 11.3 × 5.0 × 3.5 m. The investigation indicates that the source of those boulders was at least several kilometers away

Larsen, M. C. et al. (2006). Figure 1.4(b) shows a large boulder on the second floor of an extensively damaged building. The dimensions of the large boulders in Figure 1.4(c) and Figure 1.4(d) are 6.0 × 4.6 × 1.6 m and about 3 m tall, respectively (Larsen, M. C. et al., 2006; Pérez, F. L., 2001; Wieczorek, G., 2001).

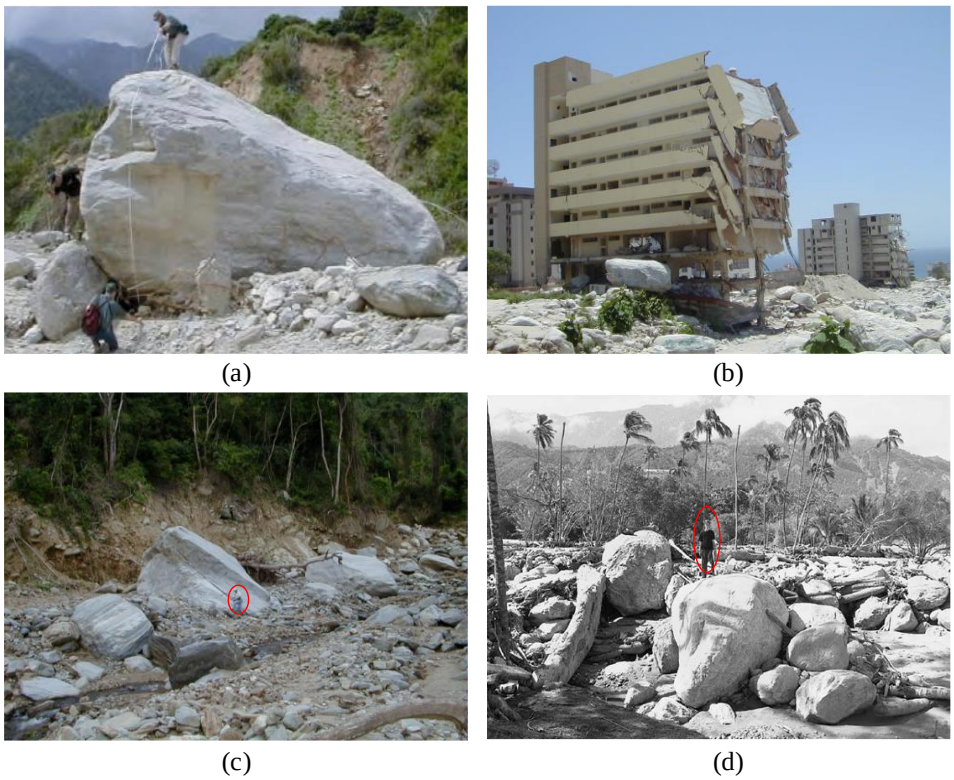

(a) (b)

(c) (d)

Figure 1.4 Observed large boulders in the area of the 1999 Venezuela debris flow event. ((Larsen, M. C. et al., 2006; Pérez, F. L., 2001; Wieczorek, G., 2001))

1.1.3. TRIGGERING FACTORS OF DEBRIS FLOW

Debris flows can be triggered by a series of factors (Wieczorek, G. F. et al., 2005), for example, intense rainfall (Caine, N., 1980; Chen, C. et al., 2005; Tang, C. et al., 2009) and rapid snowmelt (Church, M. et al., 1987; Decaulne, A. et al., 2005). Landslides can also trigger debris flows because the displaced landslide masses may develop to debris flow under certain conditions (Fleming, R. W. et al., 1989; Iverson, R. M. et al., 1997). Other than the causes mentioned above, earthquakes, volcanic eruptions, and destructions of lake can also induce landslides.

Rainfall may be the most common triggering factor (Wieczorek, G. F. et al., 2005). According to the researches of Dowling, C. A. et al. (2013), 143 events out

of 213 fatal debris flow cases from their database were triggered or caused by rainfall. The relationship between intense rainfall and shallow landslides which transformed into debris flows sere first observed by Campbell, R. H. (1975). In his theory, the rapid rainfall provides sufficient water that infiltrates into the soil and creates temporary aquifers. The positive pore pressures compromise the structural stability. A critical rainfall threshold was proposed based on rainfall intensity and duration (Starkel, L., 1979). This concept was further studied by many scholars (Caine, N., 2017; Chen, C. et al., 2005; Chen, N. et al., 2009; Guzzetti, F. et al., 2007; Van Asch, T. W. J. et al., 2013).

As analyzed by Dowling, C. A. et al. (2013), the landslide mobilized debris flows are the second most dominant. The undrained loading process may generate high pore pressure and makes it easier for sediments to be dug up (Hutchinson, J. et al., 1971; Sassa, K., 2000; Sassa, K. et al., 2005). The rapid snowmelts also trigger debris flows because the water infiltration can be significant (Horton, R. E., 1938). As another triggering factor, snowmelt is important especially in areas that have a low and changeable temperature (Decaulne, A. et al., 2005). The corresponding critical condition was also proposed by Chleborad, A. F. (1997) for the central Rocky Mountains, USA, which is a 6-day moving average of maximum daily temperature and 14.4°C. However, the rapid snowmelt caused debris flow has relatively low fatality (Dowling, C. A. et al., 2013).

The other triggering factors, such as earthquakes and breakage of landslide dam, is not as common as the factors mentioned above. Nevertheless, they also need to pay attention to because those uncommon triggerings like earthquakes tend to cost higher fatalities. (Dowling, C. A. et al., 2013; Santi, P. M. et al., 2010). On 17 Feb. 2006, a severe landslide and debris flow event was triggered by an earthquake in St. Bernard, Southern Leyte, Philippines. Two mild earthquakes (the stronger one has a magnitude of 2.6) were experienced. After the second earthquake at 10:30 a.m., the event occurred. The estimated maximum velocity is 120-130 m/s. More than 1110 people were killed and 3.2 km^2 area was covered. The approximate debris volume is 2×10^7 m^3. (Catane, S. G. et al., 2006; Catane, S. G. et al., 2008; Evans, S. G. et al., 2007; Orense, R. et al., 2006). Evidence also shows that the area after

earthquake is more vulnerable to debris flow triggering factors (Lin, C. et al., 2004; Tang, C. et al., 2012).

1.2. RESEARCH APPROACHES

1.2.1. APPROACHES FOR DEBRIS FLOW

The study of debris flow has been conducted for dozens of years. Those methodologies can be classified into three groups: empirical method, analytical method and numerical method. They will be briefed in this section.

Empirical methods usually based on in-situ investigations or laboratory experiments. They explored the desired key attributions of debris flow by studying the relationships between them and easily measured factors (Benda, L., 1990; Breien, H. et al., 2008; Fannin, R. J. et al., 2001; May, C. L., 2002; Rickenmann, D., 1999; Scott, K. M. et al., 2005). For example, Hunger, O. et al. (1984) conducted a quantitative analysis of debris flow for remedial measures in a two-year study along the Squamish Highway, north of Vancouver. Important properties of the debris flow were discussed with the approaches to obtain them, such as volume, frequency, runout distance, and impact force. The empirical knowledge is also obtained by conducting experiments. Sediment entrainment is a complex and key characteristic of debris flow. By designing proper experiments under controlled conditions, the nature of the entrainment process begins to reveal (Bouchut, F. et al., 2008; Mangeney, A. et al., 2010; Rickenmann, D. et al., 2003; Takahashi, T. et al., 1992). Other experiments are performed about initiation (Chen, N. S. et al., 2010; Gregoretti, C., 2010; Reid, M. E. et al., 1997), deposition (Liu, X., 1996; Major, J. J., 2000) and runout (De Haas, T. et al., 2015; Iverson, R. M., 2015; Remaître, A. et al., 2005).

Analytical method is to estimate the interesting properties in a semi-analytical way. Usually, they are mathematical deductions based on several assumptions. It has been used to obtain the erosion volume by the length and width of the erosion path (Luna, B. Q. et al., 2012; Medina, V. et al., 2010; Wang, G. et al., 2003). Hungr, O. (2000) analyzed debris flow runout by using the theory of uniformly progressive

flow and incorporating zoned longitudinal variation in rheology. Analytical method is also a good choice for designing of hazard mitigation structure. (Brighenti, R. et al., 2013) adopted a simplified analysis to estimate the impact force based on a simplified structural model.

The investigation and research regarding a specific practical debris flow case are also important. However, the empirical method can only approximately provide some typical characteristics to the case instead of a comprehensive understanding. It is also usually too complex for analytical model. With the rapid development of modern computer technology and simulation methods, numerical simulation for debris flow has been extensively applied as an important approach. By incorporating selected governing equations and boundary conditions, the initiation, runout, erosion and deposition can be evolved by computer efficiently. In the research community of debris flow, there are two major categories, the method based on the cellular automata (CA) model (Scheidl, C. et al., 2010; Toffoli, T., 1984), and based on Navier-Stokes equation (Brufau, P. et al., 2010; Hungr, O. et al., 2005).

Comparing to the method depending on Navier-Stokes equation, CA model is simpler because the equation solving process is avoided (D'ambrosio, D. et al., 2003; White, R. et al., 2000). It is mostly be used to predict the inundated area in a debris flow event. However, the mechanism of erosion cannot be well considered. On the other hand, although more complicated in partial differential equation solving, the method based on Navier-Stokes equation is more adaptable. To implement the equation solver, usually shallow water assumption is adopted by transforming Navier-Stokes equation into a depth-integrated form (Savage, S. B. et al., 1989; Vreugdenhil, C. B., 2013). The depth-integrated models have three advantages comparing to three-dimensional models (Iverson, R. M. et al., 2015): First, they generate model output with a level of detail comparable to that of field measurements and large-scale experiments; second, They embed the effects of the evolving positions of the upper and basal flow boundaries directly into the governing conservation equations, eliminating the need to separately resolve domain boundaries; third, They reduce the degrees of freedom in the conservation

equations themselves. A scheme of finite difference method (FDM) is applied to solve it (Iverson, R. M. et al., 2015; Savage, S. B. et al., 1989; Wang, C. et al., 2008). Some researchers also use Smoothed Particle Hydrodynamics (SPH) to solve the equation (Federico, I. et al., 2012).

However, since debris flow simulation (DFS) is based on a two-phase fluid of water and solid, called pure debris flow here, using the so-called volume concentration for different ratio of solid to water, there are seldom debris flows of two-phase fluid in nature. In fact, large boulders and driftwoods are often involved in debris flows, called boulder debris flow here, according to a large number of past events. It is obvious that the behaviors and impact force of boulder debris flow cannot be correctly estimated with a two-phase fluid model. How to simulate boulder debris flows remains an unsolved problem.

1.2.2. APPROACHES FOR THE TRANSPORTED BOULDERS

The travelling boulders in debris flow can be catastrophic. Hunger, O. et al. (1984) addressed that the point loads due to the boulders in debris flow may be more important in designing, which is related to the maximum boulder size and structures stiffness (Figure 1.5). The impact forces in actual debris flow events maybe one of the most important factors in boulder transporting. Although measuring impact force in a real debris flow is difficult, some valuable data were still documented. For example, A debris flow occurred in Jiangjia Ravine, China on Aug. 25, 2004. Just several days before the occurrence, a system of measuring equipment was set up at the middle reach of the Jiangjia drainage (Hu, K. et al., 2011). During the debris flow event, the impact force data was recorded. These data suggested that the impact forces generated by coarse grains are much larger than the fluid pressure (Hu, K. et al., 2011). Based on the measured impact forces, some empirical and semi-analytical theories were proposed to approximately estimate the impact force. Hunger, O. et al. (1984) suggested the following formula for impact force calculation of boulders:

$$F = \sqrt{mv^2k} \tag{1.1}$$

where F is the impact force, m is the boulder mass and v is the impact velocity; k is a stiffness factor of the structure, and for simple cases, it can be calculated by elastic theory. For example, for a simple beam, $k = 48EI/L^3$, with EI the bending stiffness and L the beam length. Semi-analytical solution proposed by (Zhang, S. et al., 1985) and (Zhang, S., 1993) for boulder impacts using a collisional theory in engineering mechanics:

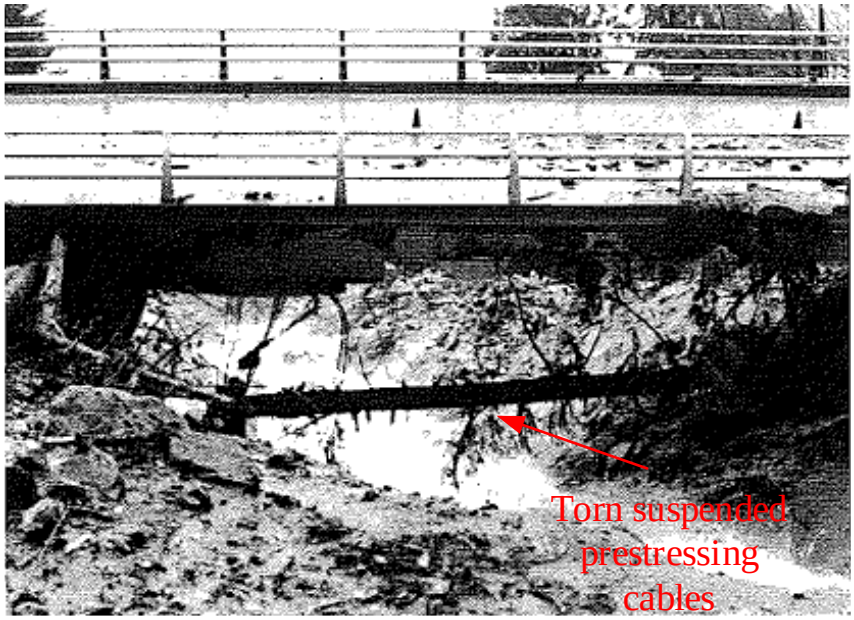

Figure 1.5 Damaged concrete bridge beam by point impact loads of boulders (modified from Hunger, O. et al. (1984))

$$F = k_d G \tag{1.2}$$

where G is the weight of the boulder, k_d is a factor. They further provided the expressions of F for cantilever beam and a simply supported beam:

$$F_{cantilever} = \sqrt{\frac{3EJG'v^2\cos^2\alpha}{gL^3}} \tag{1.3}$$

$$F_{simple} = \sqrt{\frac{48EJG'v^2\cos^2\alpha}{gL^3}} \tag{1.4}$$

where J is the inertia moment, G' is the weight of the boulder subtracting the buoyancy in flow, α is the impact angle, g is the gravitational acceleration. The impact force calculation has also recommended by standards and design codes

(Haehnel, R. B. et al., 2004). AASHTO (1998) suggested the following formula for vessel impact force on the piers based on a one-degree-of-freedom model:

$$F = 8.15v\sqrt{DWT} \tag{1.5}$$

where DWT is short for deadweight ton, which is a term that used in vessels. Suggestions of FEMA (1995) is derived by the impulse-momentum approach:

$$F = \frac{Gv}{gt} \tag{1.6}$$

where t is the impact duration. However, the estimation of t is required before the force calculation. Another limitation is that the F given in equation (1.6) is averaged instead of the maximum. To obtain the maximum force, a type of force history is assumed. For example, if the functional dependence of force on time is sinusoidal, the maximum force is given by $\pi F/2$. NAASRA (1990) suggested a work-energy form of impact force for woody debris on bridge piers, which is

$$F = \frac{Gv^2}{gl} \tag{1.7}$$

where l is the stopping distance of the debris. The value of l is given regarding different pier materials for a minimum mass.

A thorough understanding of the impact force imposed by those boulders is very important to hazard mitigation. The experiment method provides valuable data and facts to further researches. Jiang, Y. et al. (2012) studied the impact force of dry granular flow on a retaining wall. They verified the empirical impact force formula against experiments. Zeng, C. et al. (2014) conducted experiments to study the failure of the columns in debris flow. They claimed that when the boulders are larger than 0.5 m in diameter, the impact force of those boulders plays a major role in column failures instead of flow velocity. Experimental analysis of the impact force of viscous debris flow was also performed by Cui, P. et al. (2015). Inspiring results were obtained about the mechanism, but they also figured out that the impact loads of big boulders were difficult to address.

Comparing to the methods listed above, the numerical simulation has not been widely adopted for the mixture of debris flow and large boulders because of its complex nature. Although the numerical simulation approach for debris flow is well-developed, taking the travelling large boulders into consideration is still challenging because it is a coupled two-phase system involving fluid phase and discontinuous, large deformed solid phase. Some researchers already attempted to propose applicable methods to address the complex phenomenon by coupling methods. Some discontinuous method, such as Discrete Element Method (DEM) (Cundall, P. A. et al., 1979; Ting, J. M. et al., 1992), has been incorporating into debris flow (Asmar, B. N. et al., 2003). The original purpose of the coupling method in debris flow research is to simulate the motion of the solid particles as well as flow evolution as a multi-phase debris flow simulator (Leonardi, A. et al., 2013). Other coupling methods have also been proposed (Felix, D. et al., 2018; Kong, Y. et al., 2018). These coupling formed methods have the potential to solve the large boulder transporting problem in debris flow. A two-phase model, including a continuum depth-integrated fluid phase and a non-continuum large particle DEM phase, was proposed to simulate the transported large boulders amid debris flow (Martinez, C. et al., 2011; Martinez, C. et al., 2010; Martinez, C. E. et al., 2011). Those researches provided useful insights to the simulation of the phenomenon involving transported large boulders.

However, the simulation of debris flow with large boulders, called boulder debris flow, is still challenging. The empirical or semi-empirical formulae are mostly adopted to describe the impact force caused by travelling large boulders. Although the research for numerical simulation approaches has been initiated, the consideration of boulders and the interaction between the two phases are simple. For example, the shape of boulders is sphere or quasi-spherical, the interaction force is simple, the drag force between adjacent blocks is not considered, and the boulder reaction to flow is not addressed. The related details will be discussed in the following section. Those factors are essential to reveal the true nature of the transported large boulders in debris flow.

1.3. SCOPES AND OBJECTIVES

1.3.1. EXISTING PROBLEMS

As introduced in previous sections, the large boulders transported by debris flow are capable of huge damages to structures. Methods were already proposed to simulate the phenomenon (Martinez, C. et al., 2011; Martinez, C. et al., 2010; Martinez, C. E. et al., 2011). Their works are inspiring, and the results are very useful to design the protective structures. But there is still room for improvement. First, the boulder shape is limited. Although DEM allows polyhedron particles, the DEM element used in their researches is spherical. This could partly because the transported large boulders in non-spherical shape may lead to complex geometrical and mechanical problems. Nevertheless, the large boulders involved can be of any shape, referring to Figure 1.1 and Figure 1.4. The shape of boulders clearly affects the dynamic behavior of the transported boulders. Second, the flow force on boulders in the previous study is simple. The boulders are assumed to be completely submerged by flow. Third, the boulder drag forces are also not affected by the existence of other nearby boulders in flow. Fourth, the existence of DEM elements does not interrupt the flow field. This would limit the application of the method in situations where the debris flow is blocked by obstacles such as a check dam. It also faces difficulties in the estimation of dam safety under the condition of debris flow and transported large boulders, which is very important in hazard mitigation analysis.

The major limitations listed above require further investigation. The simulation involves the following aspects: (1) the motion of debris flow; (2) the motion of large boulders and dam blocks if the dam is damaged (3) interactions between solid boulders, dam blocks and debris flow. Apparently, a single two-phase flow method is not enough for the entire simulation. Discontinuous deformation analysis (DDA) (Shi, G. et al., 1985; Shi, G. H. et al., 1989) is a rapidly developed method in recent years. Details about this method will be given in Section 2. The theory of DDA is built on blocky systems in which the blocks are of arbitrary polygon shape. Implicit scheme is adopted in DDA, which makes the result

unconditionally convergent. Three-dimensional DDA (3D DDA) will be used to simulate the solid phase, for example, the dam and travelling boulders, and the debris flow will be calculated using the widely accepted depth-integrated shallow water equation. In fact, large boulders and driftwoods are often involved in debris flows, called boulder debris flow here, according to a large number of past events. It is obvious that the behaviors and impact force of boulder debris flow cannot be correctly estimated by debris flow simulation (DFS) with yhe two-phase fluid model. How to simulate boulder debris flows remains an unsolved problem.

1.3.2. OBJECTIVES OF THE THESIS

The main objective of this study is to develop a new numeric technique for simulating boulder debris flows by coupling 3D DDA with conventional DFS, and then it is used to analyze the impact force of large boulders on check dam. It is worth mention that the large boulder referred to in this thesis means the boulder with diameters greater than 3 m as discussed in chapter 5. For this purpose, a series of developments should be fulfilled, in detail:

(1) Development of a coupled 3D DDA-DFS method for simulating boulder debris flow;

(2) Clarification of the behaviors of large boulders and driftwoods in debris flow;

(3) Case study about dam safety based on a real catchment of Yohutagawa.

1.4. FRAMEWORK OF THE THESIS

The thesis consists of the following chapters.

Chapter 1 introduces the background, the scope and objectives of the research. Previous studies on debris flow and the transported large boulders are reviewed. The existing methods are briefly discussed.

Chapter 2 reviews the state-of-the-art of 3D DDA and DFS. The basic theories and equations are introduced together with their advantages and applications. The above-mentioned unsolved problems are also clarified.

Chapter 3 improves 3D DDA by incorporating a damped contact model for inelastic collisions. In order to make DDA applicable to real collisions, a damped contact model based on linear spring-dashpot assumption is incorporated into 3D DDA. Then the determination of the control parameter of dashpots and viscous damping coefficient is discussed and clarified using a predefined coefficient of restitution (COR). Inelastic collisions with unconstrained and fixed targets are carefully investigated. After that, the rebound of a freefall block assembly is analyzed for demonstrating a viscous damping effect.

Chapter 4 develops a fluid-solid coupling method called 3D DDA-DFS by coupling 3D DDA with DFS for simulating boulder debris flows. First, a framework for flow-solid interaction is proposed. Then, an interactive module is incorporated for evaluating the interactive forces between DFS flow and DDA solid blocks through the synchronization of the 3D DDA module and DFS module since time steps in both methods are quite different. Thirdly, the flow force on solid blocks, including static pressure, buoyancy and drag force, are incorporated for arbitrarily shaped polyhedral blocks on complex 3D terrain. In addition, the drag effect between adjacent blocks is addressed so that the calculated drag force is more realistic. Fourthly, an equivalent solution is proposed by taking the action of blocks on flow as a time-varying elevation of terrain node. Finally, the coupling scheme as well as the calculations of the interaction forces are validated by a number of examples.

Chapter 5 clarifies the behaviors of large boulders and driftwoods in debris flow. At first, a series of simulations are carried out on debris flows with boulders in a channel model with a downstream check dam. The impact forces and deformations that the dam suffers from are analyzed under different kinds of debris flows. And then, the behaviors of driftwoods in debris flow are also investigated.

Chapter 6 performs a case study by using the 3D DDA-DFS method to simulate potential debris flow with large boulders based on a real catchment located in Amami Oshima, Japan, where the 2010 Yohutagawa debris-flow event occurred. The same source area of the debris flow is used, and some boulders are distributed in the valley path. The dam safety is further analyzed by several dam properties and

the results suggest that the strength of the dam should be much higher if boulders are involved in a potential debris flow rather than a pure debris flow.

Chapter 7 summarizes the conclusions and recommends the problems to be solved in future studies.

The thesis framework is shown in Figure 1.6.

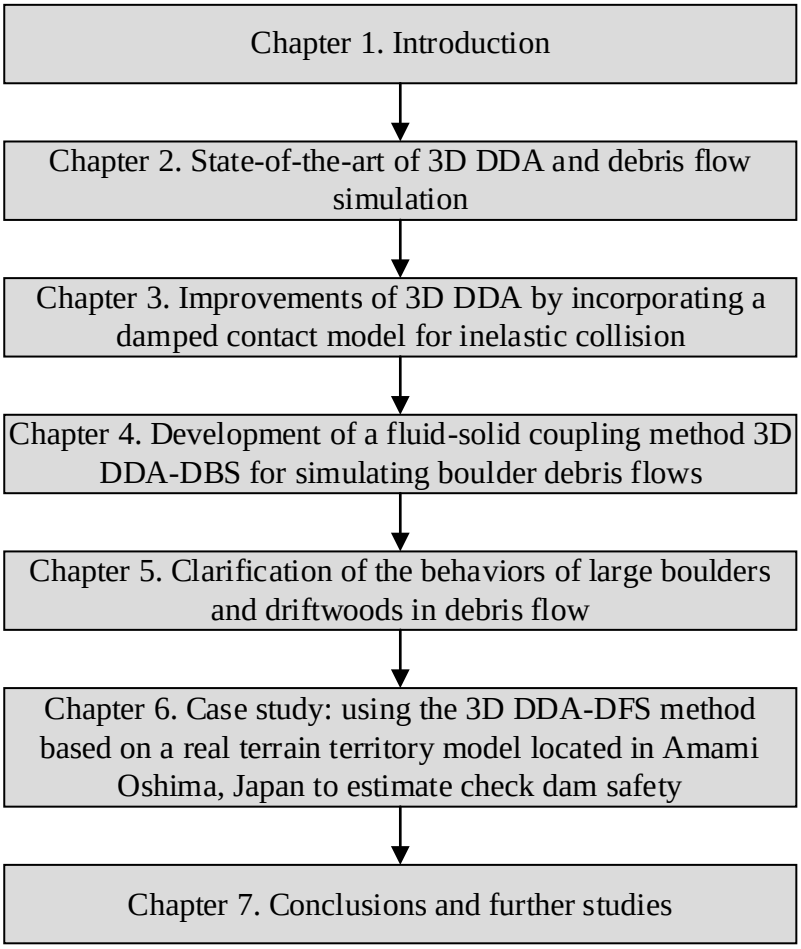

Figure 1.6 Framework of the thesis

REFERENCES

Aashto. (1998). LRFD bridge design specifications, 2nd edition. American Association of State Highways and Transportation Officials.

Arattano, M. (2000). On debris flow front evolution along a rorrent. Physics and Chemistry of the Earth, Part B: Hydrology, Oceans and Atmosphere, 25(9), 733-740.

Asmar, B. N., Langston, P. A., & Ergenzinger, P. (2003). The potential of the Discrete Element Method to simulate debris flow. Paper presented at the Debris-Flow Hazards Mitigation: Mechanics, Prediction and Assessment.

Benda, L. (1990). The influence of debris flows on channels and valley floors in the Oregon Coast Range, USA. Earth Surface Processes and Landforms, 15(5), 457-466.

Berti, M., Genevois, R., Simoni, A., & Tecca, P. R. (1999). Field observations of a debris flow event in the Dolomites. Geomorphology, 29(3-4), 265-274.

Bouchut, F., Fernández-Nieto, E. D., Mangeney, A., & Lagrée, P. Y. (2008). On new erosion models of Savage–Hutter type for avalanches. Acta Mechanica, 199(1-4), 181-208.

Breien, H., De Blasio, F. V., Elverhøi, A., & Høeg, K. (2008). Erosion and morphology of a debris flow caused by a glacial lake outburst flood, Western Norway. Landslides, 5(3), 271-280.

Brighenti, R., Segalini, A., & Ferrero, A. M. (2013). Debris flow hazard mitigation: a simplified analytical model for the design of flexible barriers. Computers and Geotechnics, 54, 1-15.

Brufau, P., Garcia-Navarro, P., Ghilardi, P., Natale, L., & Savi, F. (2010). 1D Mathematical modelling of debris flow. Journal of Hydraulic Research, 38(6), 435-446.

Caine, N. (1980). The rainfall intensity-duration control of shallow landslides and debris flows. Geografiska Annaler: Series A, Physical Geography, 62(1-2), 23-27.

Caine, N. (2017). The rainfall intensity - duration control of shallow landslides and debris flows. Geografiska Annaler: Series A, Physical Geography, 62(1-2), 23-27.

Campbell, R. H. (1975). Soil slips, debris flows, and rainstorms in the Santa Monica Mountains and vicinity, southern California (Vol. 851): US Government Printing Office.

Catane, S. G., Cabria, H. B., Tomarong, C. P., Saturay, R. M., Zarco, M. a. H., & Pioquinto, W. C. (2006). Catastrophic rockslide-debris avalanche at St. Bernard, Southern Leyte, Philippines. Landslides, 4(1), 85-90.

Catane, S. G., Cabria, H. B., Zarco, M. a. H., Saturay, R. M., & Mirasol-Robert, A. A. (2008). The 17 February 2006 Guinsaugon rock slide-debris avalanche, Southern Leyte, Philippines: deposit characteristics and failure mechanism. Bulletin of Engineering Geology and the Environment, 67(3).

Chen, C., Chen, T., Yu, F., Yu, W., & Tseng, C. (2005). Rainfall duration and debris-flow initiated studies for real-time monitoring. Environmental Geology, 47(5), 715-724.

Chen, N., Yang, C., Zhou, W., Hu, G., Li, H., & Hand, D. (2009). The critical rainfall characteristics for torrents and debris flows in the Wenchuan earthquake stricken area. Journal of Mountain Science, 6(4), 362-372.

Chen, N. S., Zhou, W., Yang, C. L., Hu, G. S., Gao, Y. C., & Han, D. (2010). The processes and mechanism of failure and debris flow initiation for gravel soil with different clay content. Geomorphology, 121(3-4), 222-230.

Chiang, S. (1996). Rainfall associated with Typhoon Herb in central Taiwan. Proceedings of Typhoon Herb and Engineering Environment, Taipei, Taiwan, 1-7.

Chieng, P. (1998). A record of sediment hazards caused by typhoon Herb and their restorations. Council of Agriculture, Taipei, Taiwan and the Chinese Water and Soil Conservation Association, Taipei, Taiwan [in Chinese].

Chleborad, A. F. (1997). Temperature, snowmelt, and the onset of spring season landslides in the central Rocky Mountains. U.S. Department of the Interior, U.S. Geological Survey.

Church, M., & Miles, M. J. (1987). Meteorological antecedents to debris flow in southwestern British Columbia; some case studies. Debris flows/avalanches: process, recognition. and miti-gation. Edited by J. E. Costa and G. E. Wieczorek. Geological Society of America. Reviews in Engineering Geology, 7, 63-79.

Cui, P., Zeng, C., & Lei, Y. (2015). Experimental analysis on the impact force of viscous debris flow. Earth Surface Processes and Landforms, 40(12), 1644-1655.

Cui, P., Zhou, G. G. D., Zhu, X. H., & Zhang, J. Q. (2013). Scale amplification of natural debris flows caused by cascading landslide dam failures. Geomorphology, 182, 173-189.

Cundall, P. A., & Strack, O. D. L. (1979). A discrete numerical model for granular assemblies. Geotechnique, 29(1), 47-65.

D'ambrosio, D., Di Gregorio, S., Iovine, G., Lupiano, V., Rongo, R., & Spataro, W. (2003). First simulations of the Sarno debris flows through Cellular Automata modelling. Geomorphology, 54(1-2), 91-117.

Davies, T. R. H. (1990). Debris-flow surges — experimental simulation. Journal of Hydrology (New Zealand), 29(1), 18-46.

De Haas, T., Braat, L., Leuven, J. R. F. W., Lokhorst, I. R., & Kleinhans, M. G. (2015). Effects of debris flow composition on runout, depositional mechanisms, and deposit morphology in laboratory experiments. Journal of Geophysical Research: Earth Surface, 120(9), 1949-1972.

Decaulne, A., Sæmundsson, Þ., & Petursson, O. (2005). Debris flow triggered by rapid snowmelt: a case study in the glei .arhjalli area, northwestern iceland. Geografiska Annaler: Series A, Physical Geography, 87(4), 487-500.

Dijkstra, T., Chandler, J., Wackrow, R., Meng, X., Ma, D., Gibson, A., Whitworth, M., Foster, C., Lee, K., & Hobbs, P. (2012). Geomorphic controls and debris flows-the 2010 Zhouqu disaster, China. Paper presented at the 11th International Symposium on Landslides and 2nd North American Symposium on Landslides.

Dowling, C. A., & Santi, P. M. (2013). Debris flows and their toll on human life: a global analysis of debris-flow fatalities from 1950 to 2011. Natural Hazards, 71(1), 203-227.

Evans, S. G., Guthrie, R. H., Roberts, N. J., & Bishop, N. F. (2007). The disastrous 17 February 2006 rockslide-debris avalanche on Leyte Island, Philippines: a catastrophic landslide in tropical mountain terrain. Natural Hazards and Earth System Science, 7(1), 89-101.

Fannin, R. J., & Wise, M. P. (2001). An empirical-statistical model for debris flow travel distance. Canadian Geotechnical Journal, 38(5), 982-994.

Federico, I., Marrone, S., Colagrossi, A., Aristodemo, F., & Antuono, M. (2012). Simulating 2D open-channel flows through an SPH model. European Journal of Mechanics - B/Fluids, 34, 35-46.

Felix, D., Li, X., & Zhao, J. (2018). A unified CFD-DEM approach for modeling of debris flow impacts on flexible barriers. International Journal for Numerical and Analytical Methods in Geomechanics, 42(14), 1643-1670.

Fema. (1995). Engineering principles and practices for retrofitting flood prone residential buildings.

Fleming, R. W., Ellen, S. D., & Algus, M. A. (1989). Transformation of dilative and contractive landslide debris into debris flows—an example from Marin County, California. Engineering Geology, 27(1-4), 201-223.

Gregoretti, C. (2010). The initiation of debris flow at high slopes: experimental results. Journal of Hydraulic Research, 38(2), 83-88.

Guzzetti, F., Peruccacci, S., Rossi, M., & Stark, C. P. (2007). The rainfall intensity–duration control of shallow landslides and debris flows: an update. Landslides, 5(1), 3-17.

Haehnel, R. B., & Daly, S. F. (2004). Maximum impact force of woody debris on floodplain structures. Journal of Hydraulic Engineering, 130(2), 112-120.

Horton, R. E. (1938). Phenomena of the contact zone between the ground surface and a layer of melting snow. Associacion Internationale d'Hydrologie Scientifique, 244, 545-561.

Hu, K., Cui, P., & Zhang, J. (2012). Characteristics of damage to buildings by debris flows on 7 August 2010 in Zhouqu, Western China. Natural Hazards and Earth System Sciences, 12(7), 2209-2217.

Hu, K., Wei, F., & Li, Y. (2011). Real-time measurement and preliminary analysis of debris-flow impact force at Jiangjia Ravine, China. Earth Surface Processes and Landforms, 36(9), 1268-1278.

Hunger, O., & Morgan, G. C. (1984). Quantitative analysis of debris torrent hazards for design of remedial measures. Canadian Geotechnical Journal, 21(4), 663-677.

Hungr, O. (2000). Analysis of debris flow surges using the theory of uniformly progressive flow. Earth Surface Processes and Landforms, 25(5), 483-495.

Hungr, O. (2005). Classification and terminology. In Debris-flow hazards and related phenomena (pp. 9-23): Springer.

Hungr, O., Evans, S., & Hutchinson, I. (2001). A review of the classification of landslides of the flow type. Environmental & Engineering Geoscience, 7(3), 221-238.

Hungr, O., Mcdougall, S., & Bovis, M. (2005). Entrainment of material by debris flows. In Debris-flow hazards and related phenomena (pp. 135-158): Springer.

Hutchinson, J., & Bhandari, R. (1971). Undrained loading, a fundamental mechanism of mudflows and other mass movements. Geotechnique, 21(4), 353-358.

Iverson, R. M. (1997). The physics of debris flows. Reviews of Geophysics, 35(3), 245-296.

Iverson, R. M. (2015). Scaling and design of landslide and debris-flow experiments. Geomorphology, 244, 9-20.

Iverson, R. M., & Ouyang, C. J. (2015). Entrainment of bed material by Earth-surface mass flows: Review and reformulation of depth-integrated theory. Reviews of Geophysics, 53(1), 27-58.

Iverson, R. M., Reid, M. E., & Lahusen, R. G. (1997). Debris-flow mobilization from landslides. Annual Review of Earth and Planetary Sciences, 25(1), 85-138.

Jan, C. D., & Chen, C. L. (2005). Debris flows caused by Typhoon Herb in Taiwan. In M. Jakob & O. Hungr (Eds.), Debris-flow hazards and related phenomena. Berlin Heidelberg: Praxis. Springer.

Jiang, Y., & Towhata, I. (2012). Experimental study of dry granular flow and impact behavior against a rigid retaining wall. Rock Mechanics and Rock Engineering, 46(4), 713-729.

Kanji, M. A., Cruz, P. T., & Massad, F. (2007). Debris flow affecting the Cubatão Oil Refinery, Brazil. Landslides, 5(1), 71-82.

Kim, Y., Nakagawa, H., Kawaike, K., & Zhang, H. (2013). Study on characteristic analysis of closed-type sabo dam with a flap due to dynamic force of debris flow. Disaster Prevention Research Institute Annuals. B, 56(B).

Kong, Y., Zhao, J. D., & Li, X. Y. (2018). Coupled CFD/DEM modeling of multiphase debris flow over a natural erodible terrain: the Yu Tung Road case. Paper presented at the Proceedings of the Second JTC1 Workshop on Triggering and Propagation of Rapid Flow-like Landslides, Hong Kong.

Larsen, M. C., Wieczorek, G. F., & Latrubesse, E. (2006). Geomorphic effects of large debris flows and flash floods, northern Venezuela, 1999. Zeitschrift für Geomorphologie Neue Folge, Supplementband, 145, 147-175.

Leonardi, A., Wittel, F. K., Mendoza, M., & Herrmann, H. J. (2013). Multiphase debris flow simulations with the discrete element method coupled with a lattice-Boltzmann fluid. Paper presented at the Proceedings of III International Conference on Particle-based Methods, PARTICLES.

Lin, C., Shieh, C., Yuan, B., Shieh, Y., Liu, S., & Lee, S. (2004). Impact of Chi-Chi earthquake on the occurrence of landslides and debris flows: example from the Chenyulan River watershed, Nantou, Taiwan. Engineering Geology, 71(1-2), 49-61.

Lin, M. L., & Jeng, F. S. (2000). Characteristics of hazards induced by extremely heavy rainfall in Central Taiwan — Typhoon Herb. Engineering Geology, 58(2), 191-207.

Lin, S. (1998). Report on typhoon Herb of 1996. Meteorological Bulletin, 42(1), 80-102.

Liu, X. (1996). Size of a debris flow deposition: model experiment approach. Environmental Geology, 28(2), 70-77.

Lopez, J., Perez, D., & Garcia, R. (2003). Hydrologic and geomorphologic evaluation of the 1999 debris-flow event in Venezuela. Paper presented at the Proc. Int. Conf. on Debris-Flow Hazards Mitigation: Mechanics, Prediction, and Assessment.

Luna, B. Q., Remaître, A., Van Asch, T. W. J., Malet, J. P., & Van Westen, C. J. (2012). Analysis of debris flow behavior with a one dimensional run-out model incorporating entrainment. Engineering Geology, 128, 63-75.

Major, J. J. (2000). Gravity-driven consolidation of granular slurries: implications for debris-flow deposition and deposit characteristics. Journal of Sedimentary Research, 70(1), 64-83.

Mangeney, A., Roche, O., Hungr, O., Mangold, N., Faccanoni, G., & Lucas, A. (2010). Erosion and mobility in granular collapse over sloping beds. Journal of Geophysical Research, 115(F3).

Martinez, C., Garcia-Martinez, R., & Miralles-Wilhelm, F. (2011). A two-phase debris flow model with boulder transport. International Journal of Safety and Security Engineering, 1(4), 389-402.

Martinez, C., Miralles-Wilhelm, F., & Garcia-Martinez, R. (2010). Debris flow modelling accounting for large boulder transport. Paper presented at the Monitoring, Simulation, Prevention and Remediation of Dense and Debris Flows III.

Martinez, C. E., Miralles-Wilhelm, F., & Garcia-Martinez, R. (2011). Quasi-three dimensional two-phase debris flow model accounting for boulder transport. Italian Journal of Engineering Geology and Environment-Book, 3, 457-466.

May, C. L. (2002). Debris flows through different forest age classes in the central Oregon Coast range. Journal of the American Water Resources Association, 38(4), 1097-1113.

Medina, V., & Bateman, A. (2010). Debris flow entrainment experiments at UPC, interpretation and challenges. Latest Trends on Engineering Mechanics, Structures, Engineering Geology, 38-44.

Naasra. (1990). Highway bridge design specification. National Association of Australian State Road Authorities.

Okuda, S., Suwa, H., Okunishi, K., Nakano, M., & Yokoyama, K. (1977). Synthetic observation on debris flow, Part 3, observation at Valley Kamikamihorizawa of Mt. Yakedake in 1976. Annuals, Disaster Prevention Research Institute, Kyoto Univ., 20(20B-1), 237-263, (In Japanese).

Orense, R., & Sapuay, S. (2006). Preliminary report on the 17 February 2006 Leyte, Philippines landslide. Soils and Foundations, 46(5), 685-693.

Pérez, F. L. (2001). Matrix granulometry of catastrophic debris flows (December 1999) in central coastal Venezuela. Catena, 45(3), 163-183.

Rapp, A. (1960). Recent development of mountain slopes in Kärkevagge and Surroundings, Northern Scandinavia. Geografiska Annaler, 42(2-3), 65-200.

Reid, M. E., Lahusen, R. G., & Iverson, R. M. (1997). Debris-flow initiation experiments using diverse hydrologic triggers. Debris-Flow Hazards Mitigation: Mechanics, Prediction and Assessment, 1-11.

Remaître, A., Malet, J.-P., Maquaire, O., Ancey, C., & Locat, J. (2005). Flow behaviour and runout modelling of a complex debris flow in a clay-shale basin. Earth Surface Processes and Landforms, 30(4), 479-488.

Rickenmann, D. (1999). Empirical relationships for debris flows. Natural Hazards, 19(1), 47-77.

Rickenmann, D., Weber, D., & Stepanov, B. (2003). Erosion by debris flows in field and laboratory experiments. Debris-flow hazards mitigation: mechanics, prediction, and assessment, 1, 883-894.

Santi, P. M., Hewitt, K., Vandine, D. F., & Barillas Cruz, E. (2010). Debris-flow impact, vulnerability, and response. Natural Hazards, 56(1), 371-402.

Sassa, K. (2000). Mechanism of flows in granular soils. Paper presented at the ISRM international symposium.

Sassa, K., & Gonghui, W. (2005). Mechanism of landslide-triggered debris flows: Liquefaction phenomena due to the undrained loading of torrent deposits. In Debris-flow hazards and related phenomena (pp. 81-104): Springer.

Savage, S. B., & Hutter, K. (1989). The motion of a finite mass of granular material down a rough incline. Journal of Fluid Mechanics, 199, 177-215.

Scheidl, C., & Rickenmann, D. (2010). Empirical prediction of debris-flow mobility and deposition on fans. Earth Surface Processes and Landforms, 35, 157-173.

Scott, K. M., Vallance, J. W., Kerle, N., Luis Macías, J., Strauch, W., & Devoli, G. (2005). Catastrophic precipitation-triggered lahar at Casita volcano, Nicaragua: occurrence, bulking and transformation. Earth Surface Processes and Landforms, 30(1), 59-79.

Shi, G., & Goodman, R. E. (1985). Two dimensional discontinuous deformation analysis. International Journal for Numerical and Analytical Methods in Geomechanics, 9(6), 541-556.

Shi, G. H., & Goodman, R. E. (1989). Generalization of two-dimensional discontinuous deformation analysis for forward modeling. International Journal for Numerical and Analytical Methods in Geomechanics, 13(4), 359-380.

Starkel, L. (1979). The role of extreme meteorological events in the shaping of mountain relief. Geographica Polonica, 41, 13-20.

Takahashi, T. (1981). Debris flow. Annual review of fluid mechanics, 13(1), 57-77.

Takahashi, T. (2014). Debris flow mechanics, prediction and countermeasures. London: CRC Press.

Takahashi, T., Nakagawa, H., Harada, T., & Yamashiki, Y. (1992). Routing debris flows with particle segregation. Journal of Hydraulic Engineering, 118(11), 1490-1507.

Tang, C., Rengers, N., Van Asch, T. W. J., Yang, Y. H., & Wang, G. F. (2011). Triggering conditions and depositional characteristics of a disastrous debris flow event in Zhouqu city, Gansu Province, northwestern China. Natural Hazards and Earth System Sciences, 11(11), 2903-2912.

Tang, C., Van Asch, T. W. J., Chang, M., Chen, G. Q., Zhao, X. H., & Huang, X. C. (2012). Catastrophic debris flows on 13 August 2010 in the Qingping area,

southwestern China: The combined effects of a strong earthquake and subsequent rainstorms. Geomorphology, 139-140, 559-576.

Tang, C., Zhu, J., Li, W. L., & Liang, J. T. (2009). Rainfall-triggered debris flows following the Wenchuan earthquake. Bulletin of Engineering Geology and the Environment, 68(2), 187-194.

Ting, J. M., & Corkum, B. T. (1992). Computational laboratory for discrete element geomechanics. Journal of Computing in Civil Engineering, 6(2), 129-146.

Toffoli, T. (1984). Cellular automata as an alternative to (rather than an approximation of) differential equations in modeling physics. Physica D: Nonlinear Phenomena, 10(1-2), 117-127.

Van Asch, T. W. J., Tang, C., Alkema, D., Zhu, J., & Zhou, W. (2013). An integrated model to assess critical rainfall thresholds for run-out distances of debris flows. Natural Hazards, 70(1), 299-311.

Vandine, D. F., & Bovis, M. (2002). History and goals of Canadian debris flow research, a review. Natural Hazards, 26(1), 67-80.

Varnes, D. J. (1978). Slope movement types and processes. Special report, 176, 11-33.

Vreugdenhil, C. B. (2013). Numerical methods for shallow-water flow (Vol. 13): Springer Science & Business Media.

Wang, C., Li, S., & Esaki, T. (2008). GIS-based two-dimensional numerical simulation of rainfall-induced debris flow. Natural Hazards Earth System Science, 8(1), 47-58.

Wang, G., Sassa, K., & Fukuoka, H. (2003). Downslope volume enlargement of a debris slide–debris flow in the 1999 Hiroshima, Japan, rainstorm. Engineering Geology, 69(3-4), 309-330.

Wang, G. L. (2013). Lessons learned from protective measures associated with the 2010 Zhouqu debris flow disaster in China. Natural Hazards, 69(3), 1835-1847.

White, R., & Engelen, G. (2000). High-resolution integrated modelling of the spatial dynamics of urban and regional systems. Computers, Environment and Urban Systems, 24(5), 383-400.

Wieczorek, G. (2001). Debris-flow and flooding hazards caused by the December 1999 storm in coastal Venezuela. US Geological Survey Open File Report, 1, 40.

Wieczorek, G. F., & Glade, T. (2005). Climatic factors influencing occurrence of debris flows. In Debris-flow hazards and related phenomena (pp. 325-362): Springer.

Yu, B., Yang, Y., Su, Y., Huang, W., & Wang, G. (2010). Research on the giant debris flow hazards in Zhouqu County, Gansu Province on August 7, 2010. Journal of Engineering Geology, 18(4), 437-444, (in Chinese).

Zeng, C., Cui, P., Su, Z., Lei, Y., & Chen, R. (2014). Failure modes of reinforced concrete columns of buildings under debris flow impact. Landslides, 12(3), 561-571.

Zhang, S. (1993). A comprehensive approach to the observation and prevention of debris flows in China. Natural Hazards, 7(1), 1-23.

Zhang, S., & Yuan, J. (1985). Impact force of debris flow and its detection. Memoirs of Lanzhou Institute of Glaciology and Cryopedology, Chinese Academy of Sciences. Beijing: Science Press, 269-274.

CHAPTER 2

STATE-OF-THE-ART OF 3D DDA AND DEBRIS FLOW SIMULATION

2.1. INTRODUCTION

Discontinuous Deformation Analysis (DDA) was first introduced by Shi (Shi, G. H. et al., 1989). Up to now, DDA has gained wide usage in practical simulations in geotechnical and geological engineering (Hatzor, Y. H. et al., 2004; Wang, W. et al., 2017; Wu, J. H. et al., 2011; Zhang, Y. et al., 2015). DDA studies blocky systems controlled by discontinuities, being able to capture the motions and stresses both in static and dynamic conditions. In two-dimensional (2D) space, a single block is depicted by their geometries and six mechanical variables, including rigid-body translations at the block center in two orthotropic directions, linear strains in two orthotropic directions, a rotation and a shear strain. When two blocks are in contact, stiff contact springs are added to prevent them from penetrating. DDA has been carefully verified in various conditions (Maclaughlin, M. M. et al., 2006) such as block sliding on an inclined plane (Hatzor, Y. H. et al., 2001; Tsesarsky, M. et al., 2005), stability (Zhang, Y. B. et al., 2015) and wedge-shaped block (Yeung, M. R. et al., 2003). Improvements are proposed to extend the application (Peng, X. et al., 2019c) or to acquire higher accuracy (Wu, J. H., 2015; Yu, P. et al., 2019a). Contact treatment is essential in DDA, and attentions are attracted to improve the contact searching algorithm (Jafari, A. et al., 2007; Shi, G., 2015; Wang, X. et al., 2019; Zhang, H. et al., 2015; Zheng, F. et al., 2018) and mechanism (Peng, X. et al., 2019b; Zhang, Y. et al., 2014). The calculational amount of DDA is usually

quite large due to complex contact condition, and therefore parallelization of DDA in 2D (Fu, X. D. et al., 2016; Peng, X. et al., 2020b) and 3D (Cheng, X. et al., 2015; Peng, X. et al., 2019a) space were proposed. The further investigation of DDA allows it to be used in varies practical cases (Chen, G. Q. et al., 2013; Chen, K.-T. et al., 2018; Peng, X. et al., 2018; Wang, W. et al., 2016; Wang, W. et al., 2019; Wu, J.-H. et al., 2017; Wu, J. H. et al., 2011; Wu, J. H. et al., 2004; Yu, P. et al., 2019b). 3D DDA shares similar theory with the 2D version, however it is more suitable for the practical application because most of the cases are three dimensional. Since only 3D DDA is used in this research, the introduction in this section will focus on 3D DDA.

Although more complicated in partial differential equation solving, the method based on Navier-Stokes equation is more adaptable. To implement the equation solver, usually shallow water assumption is adopted by transforming Navier-Stokes equation into a depth-integrated form (Savage, S. B. et al., 1989; Vreugdenhil, C. B., 2013). The depth-integrated models have three advantages comparing to three-dimensional models (Iverson, R. M. et al., 2015): First, they generate model output with a level of detail comparable to that of field measurements and large-scale experiments; second, They embed the effects of the evolving positions of the upper and basal flow boundaries directly into the governing conservation equations, eliminating the need to separately resolve domain boundaries; third, They reduce the degrees of freedom in the conservation equations themselves. A scheme of finite difference method (FDM) is applied to solve it (Iverson, R. M. et al., 2015; Savage, S. B. et al., 1989; Wang, C. et al., 2008). Some researchers also use Smoothed Particle Hydrodynamics (SPH) to solve the equation (Federico, I. et al., 2012).

2.2. 3D DDA: State-of-the-art

2.2.1. General dynamic equations

In general, a dynamic system can be described by a matrix-formed equation

$$\boldsymbol{M}\ddot{\boldsymbol{D}} + \boldsymbol{C}\dot{\boldsymbol{D}} + \boldsymbol{K}\boldsymbol{D} = \boldsymbol{F} \tag{2.1}$$

where $\boldsymbol{M}$, $\boldsymbol{C}$ and $\boldsymbol{K}$ are coefficient matrices standing for mass, damping and stiffness. The term $\boldsymbol{F}$ is load matrix. $\boldsymbol{D}$ is the displacement matrix, which is the unknown in DDA method. $\dot{\boldsymbol{D}}$ and $\ddot{\boldsymbol{D}}$ denote the velocity and acceleration matrices. Equation (2.1) is fundamental for both 2D and 3D DDA. However, only 3D DDA is illustrated here since the research mainly focuses on three-dimensional space. In 3D DDA, the displacement matrix $\boldsymbol{D}$ is comprised of six displacement components and their corresponding first-order derivative, i.e. strains:

$$\boldsymbol{D} = [u_0 \;\; v_0 \;\; w_0 \;\; r_x \;\; r_y \;\; r_z \;\; \varepsilon_x \;\; \varepsilon_y \;\; \varepsilon_z \;\; \gamma_{yz} \;\; \gamma_{zx} \;\; \gamma_{xy}]^{\mathrm{T}} \tag{2.2}$$

where u_0, v_0 and w_0 are rigid body translations in x-, y- and z- directions, respectively; r_x, r_y and r_z are rotations around x-, y- and z- directions, respectively; ε_x, ε_y and ε_z are the three normal strains in x-, y- and z- directions, respectively; γ_{yz}, γ_{zx}, and γ_{xy} are the three shear strains, respectively. The displacement-based equation is somehow similar to the Finite Element Method (FEM), in which the nodal displacement variables are used as unknowns. In DDA method, equation (2.1) is transformed into a step-by-step scheme through a time discretization in step n, time t_0:

$$\boldsymbol{M}\ddot{\boldsymbol{D}}_{n+1} + \boldsymbol{C}\dot{\boldsymbol{D}}_{n+1} + \boldsymbol{K}\boldsymbol{D}_{n+1} = \boldsymbol{F}_{n+1} \tag{2.3}$$

where the subscript denotes the values in time step $n + 1$. Equation (2.3) suggests that the governing equations in step n are established based on the temporally unknown system state of $t_0 + \Delta t$ (step time duration), which has to be assumed in prior and then checked. DDA introduces an "open-close iteration (OCI)" process to validate the convergency. In addition, accumulated deformations before step n is left along since equation (2.3) is incremental (the influences of initial strains and stresses are still addressed), therefore initial conditions of step n are

$$\boldsymbol{D}(0) = \boldsymbol{0}, \dot{\boldsymbol{D}}(0) = \dot{\boldsymbol{D}}_0 \tag{2.4}$$

A premise of DDA is the constant acceleration within one step, therefore an equation of second-order accuracy is formed

$$\boldsymbol{D}_{n+1} = \boldsymbol{D}_n + \dot{\boldsymbol{D}}_n \Delta t + \frac{1}{2}\ddot{\boldsymbol{D}}_n \Delta t^2 \tag{2.5}$$

and:

$$\ddot{\boldsymbol{D}}_{n+1} = \ddot{\boldsymbol{D}}_n \tag{2.6}$$

Combining equation (2.4) – (2.6) the accelerations at the end of step *n* is calculated by

$$\ddot{\boldsymbol{D}}_{n+1} = \frac{2}{\Delta t^2}\boldsymbol{D}_{n+1} - \frac{2}{\Delta t}\dot{\boldsymbol{D}}_n \tag{2.7}$$

Velocity is also calculated based on constant acceleration using equation (2.7):

$$\dot{\boldsymbol{D}}_{n+1} = \dot{\boldsymbol{D}}_n + \Delta t \ddot{\boldsymbol{D}}_{n+1} = \frac{2}{\Delta t}\boldsymbol{D}_{n+1} - \dot{\boldsymbol{D}}_n \tag{2.8}$$

Substituting equation (2.7) and (2.8) into equation (2.3), a function of $\ddot{\boldsymbol{D}}_{n+1}$ is obtained:

$$\left(\frac{2}{\Delta t^2}\boldsymbol{M} + \frac{2}{\Delta t}\boldsymbol{C} + \boldsymbol{K}\right)\cdot \boldsymbol{D}_{n+1} = \boldsymbol{F}_{n+1} + (\frac{2}{\Delta t}\boldsymbol{M} + \boldsymbol{C})\cdot \dot{\boldsymbol{D}}_{n+1} \tag{2.9}$$

or in a concise form

$$\hat{\boldsymbol{K}}\boldsymbol{D}_{n+1} = \hat{\boldsymbol{F}}_{n+1} \tag{2.10}$$

The following sections will introduce how to generate the associated matrices in 3D DDA. The principle of minimum potential energy is adopted to generate the associated matrices. In a DDA system, the potential energy can be related to one or two blocks. Let Π be the potential energy, and

$$\Pi = \int_{\Omega} \vec{f} \cdot \vec{s} dx \tag{2.11}$$

where Ω denotes the domain of integration, $\vec{f}$ and $\vec{s}$ are the force vector that contributes to the potential energy and the corresponding displacement vector. Then the matrices are generated by

$$\frac{\partial^2 \Pi}{\partial \boldsymbol{D}_i^{\,2}} \rightarrow \boldsymbol{K}_{ii} \tag{2.12}$$

$$\frac{\partial^2 \Pi}{\partial \boldsymbol{D}_j^{\,2}} \rightarrow \boldsymbol{K}_{jj} \tag{2.13}$$

$$\frac{\partial^2 \Pi}{\partial \boldsymbol{D}_i \partial \boldsymbol{D}_j} \rightarrow \boldsymbol{K}_{ij} \tag{2.14}$$

$$\frac{\partial^2 \Pi}{\partial \boldsymbol{D}_j \partial \boldsymbol{D}_i} \rightarrow \boldsymbol{K}_{ji} \tag{2.15}$$

$$-\frac{\partial \Pi(0)}{\partial \boldsymbol{D}_i} \rightarrow \boldsymbol{F}_i \tag{2.16}$$

$$-\frac{\partial \Pi(0)}{\partial \boldsymbol{D}_j} \rightarrow \boldsymbol{F}_j \tag{2.17}$$

where the subscripts i and j denote the indexes of the two involved blocks; subscripts ii, jj, ij and ji indicate the position of the submatrices. It is obvious that $\boldsymbol{K}_{ij} = \boldsymbol{K}_{ji}$, which implies that matrix $\boldsymbol{K}$ is symmetric.

2.2.2. SIMPLEX INTEGRATION

Before deriving equations, it is beneficial to illustrate the integration method that is adopted in blocky systems – simplex integration. Only 3D simplex integration is introduced here.

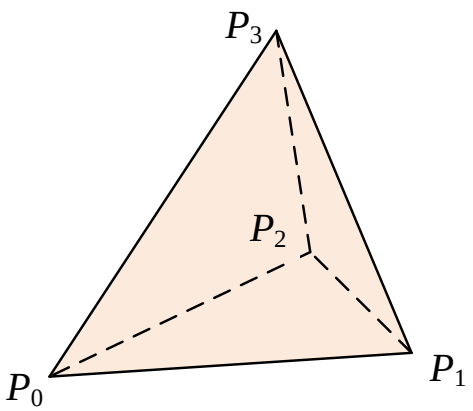

Figure 2.1 A 3D simplex (Shi, G., 1989)

A 3D simplex is a generalized notion of a tetrahedron. Figure 2.1 shows a 3D simplex $P_0P_1P_2P_3$. The coordinates of the vertices are P_0 (x_0, y_0, z_0), P_1 (x_1, y_1, z_1), P_2 (x_2, y_2, z_2), P_3 (x_3, y_3, z_3). 3D simplex integration is defined by

$$\int_{P_0P_1P_2P_3} f(x,y,z)D(x,y,z) = \sin(J)\iiint_{P_0P_1P_2P_3} f(x,y,z)dxdydz \tag{2.18}$$

where $f(x, y, z)$ is a polynomial of x, y and z; J is Jacobi determinant, which is expressed by

$$J = \begin{vmatrix} x_1 - x_0 & x_2 - x_0 & x_3 - x_0 \\ y_1 - y_0 & y_2 - y_0 & y_3 - y_0 \\ z_1 - z_0 & z_2 - z_0 & z_3 - z_0 \end{vmatrix} = \begin{vmatrix} 1 & x_0 & y_0 & z_0 \\ 1 & x_1 & y_1 & z_1 \\ 1 & x_2 & y_2 & z_2 \\ 1 & x_3 & y_3 & z_3 \end{vmatrix} \tag{2.19}$$

The essence of the simplex integral is to calculate the following integral

$$\iiint_{P_0P_1P_2P_3} x^{a_1} y^{a_2} z^{a_3} dxdydz \tag{2.20}$$

Because a general polyhedron can be divided into several simplexes, the integration of a polygon of n facets, in which the facet j is noted by $P_0^j P_1^j \cdots P_{m_j-1}^j$, can also be decomposed by several integrations. Denoting the integration as

$$S_{x^{m_1} y^{m_2} z^{m_3}} = \sum_{j=1}^{n} \sum_{k=1}^{m_j-2} \iiint_{OP_0^j P_k^j P_{k+1}^j} x^{a_1} y^{a_2} z^{a_3} dxdydz \tag{2.21}$$

where O (0, 0, 0) is the coordinate origin. In 3D DDA, a_1, a_2 and a_3 are integers, and the situations of $a_1 \leq 1$, $a_2 \leq 1$, $a_3 \leq 1$ and $a_1 + a_2 + a_3 \leq 2$ are used. Shi, G. (1989) has solved the integral in (2.21) with the following results:

$$S_0 = \sum_{j=1}^{n} \sum_{k=1}^{m_j-2} \iiint_{OP_0^j P_k^j P_{k+1}^j} 1dxdydz = \frac{1}{6} \sum_{j=1}^{n} \sum_{k=1}^{m_j-2} \begin{vmatrix} x_0^j & y_0^j & z_0^j \\ x_k^j & y_k^j & z_k^j \\ x_{k+1}^j & y_{k+1}^j & z_{k+1}^j \end{vmatrix} \tag{2.22}$$

$$S_x = \sum_{j=1}^{n} \sum_{k=1}^{m_j-2} \iiint_{OP_0^j P_k^j P_{k+1}^j} x dxdydz$$

$$= \frac{1}{24} \sum_{j=1}^{n} \sum_{k=1}^{m_j-2} \begin{vmatrix} x_0^j & y_0^j & z_0^j \\ x_k^j & y_k^j & z_k^j \\ x_{k+1}^j & y_{k+1}^j & z_{k+1}^j \end{vmatrix} (x_0^j + x_k^j + x_{k+1}^j) \tag{2.23}$$

$$S_y = \sum_{j=1}^{n} \sum_{k=1}^{m_j-2} \iiint_{OP_0^j P_k^j P_{k+1}^j} y dxdydz$$

$$= \frac{1}{24} \sum_{j=1}^{n} \sum_{k=1}^{m_j-2} \begin{vmatrix} x_0^j & y_0^j & z_0^j \\ x_k^j & y_k^j & z_k^j \\ x_{k+1}^j & y_{k+1}^j & z_{k+1}^j \end{vmatrix} (y_0^j + y_k^j + y_{k+1}^j) \tag{2.24}$$

$$S_z = \sum_{j=1}^{n} \sum_{k=1}^{m_j-2} \iiint_{OP_0^j P_k^j P_{k+1}^j} z dxdydz$$

$$= \frac{1}{24} \sum_{j=1}^{n} \sum_{k=1}^{m_j-2} \begin{vmatrix} x_0^j & y_0^j & z_0^j \\ x_k^j & y_k^j & z_k^j \\ x_{k+1}^j & y_{k+1}^j & z_{k+1}^j \end{vmatrix} (z_0^j + z_k^j + z_{k+1}^j) \tag{2.25}$$

$$S_{xx} = \sum_{j=1}^{n} \sum_{k=1}^{m_j-2} \iiint_{OP_0^j P_k^j P_{k+1}^j} x^2 dxdydz$$

$$= \frac{1}{60} \sum_{j=1}^{n} \sum_{k=1}^{m_j-2} \begin{vmatrix} x_0^j & y_0^j & z_0^j \\ x_k^j & y_k^j & z_k^j \\ x_{k+1}^j & y_{k+1}^j & z_{k+1}^j \end{vmatrix} (x_0^j x_0^j + x_0^j x_k^j + x_0^j x_{k+1}^j + x_k^j x_k^j + x_k^j x_{k+1}^j + x_{k+1}^j x_{k+1}^j)$$

(2.26)

$$S_{yy} = \sum_{j=1}^{n} \sum_{k=1}^{m_j-2} \iiint_{OP_0^j P_k^j P_{k+1}^j} y^2 dxdydz$$

$$= \frac{1}{60} \sum_{j=1}^{n} \sum_{k=1}^{m_j-2} \begin{vmatrix} x_0^j & y_0^j & z_0^j \\ x_k^j & y_k^j & z_k^j \\ x_{k+1}^j & y_{k+1}^j & z_{k+1}^j \end{vmatrix} (y_0^j y_0^j + y_0^j y_k^j + y_0^j y_{k+1}^j + y_k^j y_k^j + y_k^j y_{k+1}^j + y_{k+1}^j y_{k+1}^j)$$

(2.27)

$$S_{zz}=\sum_{j=1}^{n}\sum_{k=1}^{m_j-2}\iiint_{OP_0^jP_k^jP_{k+1}^j} z^2dxdydz$$

$$=\frac{1}{60}\sum_{j=1}^{n}\sum_{k=1}^{m_j-2}\begin{vmatrix} x_0^j & y_0^j & z_0^j \\ x_k^j & y_k^j & z_k^j \\ x_{k+1}^j & y_{k+1}^j & z_{k+1}^j \end{vmatrix}(z_0^jz_0^j+z_0^jz_k^j+z_0^jz_{k+1}^j+z_k^jz_k^j+z_k^jz_{k+1}^j+z_{k+1}^jz_{k+1}^j) \tag{2.28}$$

$$S_{xy}=\sum_{j=1}^{n}\sum_{k=1}^{m_j-2}\iiint_{OP_0^jP_k^jP_{k+1}^j} xydxdydz$$

$$=\frac{1}{120}\sum_{j=1}^{n}\sum_{k=1}^{m_j-2}\begin{vmatrix} x_0^j & y_0^j & z_0^j \\ x_k^j & y_k^j & z_k^j \\ x_{k+1}^j & y_{k+1}^j & z_{k+1}^j \end{vmatrix}(2x_0^jy_0^j+x_0^jy_k^j+x_0^jy_{k+1}^j+x_k^jy_0^j \tag{2.29}$$

$$+2x_k^jy_k^j+x_k^jy_{k+1}^j+x_{k+1}^jy_0^j+x_{k+1}^jy_k^j+2x_{k+1}^jy_{k+1}^j)$$

$$S_{yz}=\sum_{j=1}^{n}\sum_{k=1}^{m_j-2}\iiint_{OP_0^jP_k^jP_{k+1}^j} yzdxdydz$$

$$=\frac{1}{120}\sum_{j=1}^{n}\sum_{k=1}^{m_j-2}\begin{vmatrix} x_0^j & y_0^j & z_0^j \\ x_k^j & y_k^j & z_k^j \\ x_{k+1}^j & y_{k+1}^j & z_{k+1}^j \end{vmatrix}(2y_0^jz_0^j+y_0^jz_k^j+y_0^jz_{k+1}^j+y_k^jz_0^j \tag{2.30}$$

$$+2y_k^jz_k^j+y_k^jz_{k+1}^j+y_{k+1}^jz_0^j+y_{k+1}^jz_k^j+2y_{k+1}^jz_{k+1}^j)$$

$$S_{zx}=\sum_{j=1}^{n}\sum_{k=1}^{m_j-2}\iiint_{OP_0^jP_k^jP_{k+1}^j} zxdxdydz$$

$$=\frac{1}{120}\sum_{j=1}^{n}\sum_{k=1}^{m_j-2}\begin{vmatrix} x_0^j & y_0^j & z_0^j \\ x_k^j & y_k^j & z_k^j \\ x_{k+1}^j & y_{k+1}^j & z_{k+1}^j \end{vmatrix}(2z_0^jx_0^j+z_0^jx_k^j+z_0^jx_{k+1}^j+z_k^jx_0^j \tag{2.31}$$

$$+2z_k^jx_k^j+z_k^jx_{k+1}^j+z_{k+1}^jx_0^j+z_{k+1}^jx_k^j+2z_{k+1}^jx_{k+1}^j)$$

Specifically, S_0 is the volume of the block i. Referring to formulae (2.22) – (2.31), the integrations related to 3D DDA can be resolved. For example, the following integration will be used in Section 2.2.3.1:

$$\iiint \boldsymbol{T}_i^{\mathrm{T}}\cdot\boldsymbol{T}_i\mathrm{d}x\mathrm{d}y\mathrm{d}z \tag{2.32}$$

where $\boldsymbol{T}_i$ is the displacement transformation matrix, which is calculated by the point coordinate (x, y, z):

$$\boldsymbol{T}_i = \begin{bmatrix} 1 & 0 & 0 & 0 & \tilde{z} & -\tilde{y} & \tilde{x} & 0 & 0 & 0 & \tilde{z}/2 & \tilde{y}/2 \\ 0 & 1 & 0 & -\tilde{z} & 0 & \tilde{x} & 0 & \tilde{y} & 0 & \tilde{z}/2 & 0 & \tilde{x}/2 \\ 0 & 0 & 1 & \tilde{y} & -\tilde{x} & 0 & 0 & 0 & \tilde{z} & \tilde{y}/2 & \tilde{x}/2 & 0 \end{bmatrix} \tag{2.33}$$

Substituting equation (2.33) into formula (2.32) results in

$$\iiint \boldsymbol{T}_i^{\mathrm{T}} \cdot \boldsymbol{T}_i \mathrm{d}x\mathrm{d}y\mathrm{d}z = \begin{bmatrix} \mathbf{A} & \mathbf{B} \\ \mathbf{B}^{\mathrm{T}} & \mathbf{C} \end{bmatrix} \tag{2.34}$$

with 6×6 submatrices:

$$\mathbf{A} = \begin{bmatrix} S & & & & & \\ 0 & S & & & Sym & \\ 0 & 0 & S & & & \\ & & & S_2 + S_3 & & \\ & \mathbf{0} & & -S_4 & S_1 + S_3 & \\ & & & -S_5 & -S_6 & S_1 + S_2 \end{bmatrix} \tag{2.35}$$

$$\mathbf{B} = \begin{bmatrix} & & & \mathbf{0} & & \\ 0 & -S_6 & S_6 & \frac{S_2 - S_3}{2} & \frac{S_4}{2} & -\frac{S_5}{2} \\ S_5 & 0 & -S_5 & -\frac{S_4}{2} & \frac{S_3 - S_1}{2} & \frac{S_6}{2} \\ -S_4 & S_4 & 0 & \frac{S_5}{2} & -\frac{S_6}{2} & \frac{S_1 - S_2}{2} \end{bmatrix} \tag{2.36}$$

$$\mathbf{C} = \begin{bmatrix} S_1 & & & & & \\ 0 & S_2 & & & Sym & \\ 0 & 0 & S_3 & & & \\ 0 & \frac{S_6}{2} & \frac{S_6}{2} & \frac{S_2 + S_3}{2} & & \\ \frac{S_5}{2} & 0 & \frac{S_5}{2} & \frac{S_4}{4} & \frac{S_1 + S_3}{4} & \\ \frac{S_4}{2} & \frac{S_4}{2} & 0 & \frac{S_5}{4} & \frac{S_6}{4} & \frac{S_1 + S_2}{4} \end{bmatrix} \tag{2.37}$$

where the symbols S_1 to S_6 are defined as

$$\begin{cases} S_1 = S_{xx} - x_0 S_x \\ S_2 = S_{yy} - y_0 S_y \\ S_3 = S_{zz} - z_0 S_z \\ S_4 = S_{xy} - x_0 S_y \\ S_5 = S_{zx} - z_0 S_x \\ S_6 = S_{yz} - y_0 S_z \end{cases} \tag{2.38}$$

2.2.3. ASSEMBLY OF NON-CONTACT MATRICES

Matrices of contact terms are unique in DDA method, which is worth a detailed illustration. This content will be given in Section 2.2.4. Here the non-contact matrices include inertia force, body force, point loading, point displacement constrain, initial stress, and elastic stress. The method to obtain the matrices are similar: obtain the potential energy first, then take derivatives with respect to each variable. To unify the symbols, displacement vector in block *i* is rewritten as

$$\boldsymbol{D}_i = [d_{1i} \;\; d_{2i} \;\; d_{3i} \;\; d_{4i} \;\; d_{5i} \;\; d_{6i} \;\; d_{7i} \;\; d_{8i} \;\; d_{9i} \;\; d_{10i} \;\; d_{11i} \;\; d_{12i}]^{\mathrm{T}} \tag{2.39}$$

where d_{ji} is the *j*-th displacement component of block *i*. Moreover, rigid block translations $\boldsymbol{U}_i = [u_i, v_i, w_i]^{\mathrm{T}}$ of a point in block *i* can be calculated by

$$\boldsymbol{U}_i = \boldsymbol{T}_i \boldsymbol{D}_i \tag{2.40}$$

where u_i, v_i, w_i are the translation components in of an arbitrary point within block *i*, and the displacement transformation matrix $\boldsymbol{T}_i$ is expressed by:

$$\boldsymbol{T}_i = \begin{bmatrix} 1 & 0 & 0 & 0 & \tilde{z} & -\tilde{y} & \tilde{x} & 0 & 0 & 0 & \tilde{z}/2 & \tilde{y}/2 \\ 0 & 1 & 0 & -\tilde{z} & 0 & \tilde{x} & 0 & \tilde{y} & 0 & \tilde{z}/2 & 0 & \tilde{x}/2 \\ 0 & 0 & 1 & \tilde{y} & -\tilde{x} & 0 & 0 & 0 & \tilde{z} & -\tilde{y}/2 & -\tilde{x}/2 & 0 \end{bmatrix} \tag{2.41}$$

where $\tilde{x} = x - x_0$, $\tilde{y} = y - y_0$ and $\tilde{z} = z - z_0$ are local coordinates, and (x_0, y_0, z_0) is the coordinate of a reference point in block *i*. In 3D DDA, the center of a block is chosen to be the reference point because, in this way, the expressions can be simplified. Detailed derivations will be given in the following sections.

2.2.3.1. INERTIA FORCE

Inertial force is a time-varying body force. It is expressed by

$$\vec{f}_n = [f_x \quad f_y \quad f_z]^{\mathrm{T}} = -\rho \frac{\partial^2 \boldsymbol{U}}{\partial t^2} = -\rho \boldsymbol{T}_i \cdot \frac{\partial^2 \boldsymbol{D}_i}{\partial t^2} \tag{2.42}$$

where f_x, f_y and f_z are the components of inertial force in x-, y- and z- directions; ρ is the block density, t is time. The integration of body force should be over the whole block. Therefore, the corresponding potential energy Π_a is calculated by

$$\begin{aligned} \Pi_a &= -\iiint \boldsymbol{U} \cdot \vec{f}_n \mathrm{d}x\mathrm{d}y\mathrm{d}z = \iiint [\boldsymbol{D}_i^{\mathrm{T}} \cdot \boldsymbol{T}_i^{\mathrm{T}}] \cdot [\rho \boldsymbol{T}_i \cdot \frac{\partial^2 \boldsymbol{D}_i}{\partial t^2}] \mathrm{d}x\mathrm{d}y\mathrm{d}z \\ &= \rho \boldsymbol{D}_i^{\mathrm{T}} \cdot \iiint \boldsymbol{T}_i^{\mathrm{T}} \cdot \boldsymbol{T}_i \mathrm{d}x\mathrm{d}y\mathrm{d}z \cdot \frac{\partial^2 \boldsymbol{D}_i}{\partial t^2} \end{aligned} \tag{2.43}$$

By introducing equation (2.7), it is further extended as

$$\Pi_a = \rho \boldsymbol{D}_i^{\mathrm{T}} \cdot \iiint \boldsymbol{T}_i^{\mathrm{T}} \cdot \boldsymbol{T}_i \mathrm{d}x\mathrm{d}y\mathrm{d}z \cdot \left(\frac{2}{\Delta t^2} \boldsymbol{D}_i - \frac{2}{\Delta t} \boldsymbol{V}_i \right) \tag{2.44}$$

Here $\boldsymbol{V}_i$ is used instead of $\dot{\boldsymbol{D}}_i$ because the velocities from the previous step are used, instead of the unknown velocities in the current step. Only $\boldsymbol{D}_i$ is unknown in equation (2.44). Taking derivatives for $\boldsymbol{D}_i$ yielding the components that should be added to stiffness and force matrices:

$$\frac{2\rho}{\Delta t^2} \iiint \boldsymbol{T}_i^{\mathrm{T}} \cdot \boldsymbol{T}_i \mathrm{d}x\mathrm{d}y\mathrm{d}z \rightarrow \boldsymbol{K}_{ii} \tag{2.45}$$

$$\frac{2\rho}{\Delta t} \iiint \boldsymbol{T}_i^{\mathrm{T}} \cdot \boldsymbol{T}_i \mathrm{d}x\mathrm{d}y\mathrm{d}z \cdot \boldsymbol{V}_i \rightarrow \boldsymbol{F}_i \tag{2.46}$$

The integrations in the above two equations are already addressed in Section 2.2.2.

2.2.3.2. BODY FORCE

The potential energy of body force Π_V is similar to the inertia force:

$$\begin{aligned} \Pi_V &= -\iiint \mathbf{U} \cdot \vec{f}_V \mathrm{d}x\mathrm{d}y\mathrm{d}z \\ &= -S_{i,0} \boldsymbol{D}_i^{\mathrm{T}} [f_x \quad f_y \quad f_z \quad 0 \quad 0 \quad 0 \quad 0 \quad 0 \quad 0 \quad 0 \quad 0 \quad 0]^{\mathrm{T}} \end{aligned} \tag{2.47}$$

where f_x, f_y and f_z are the three components x-, y- and z- directions of body force; $S_{i,1}$ denotes the integration S_1 of block i in equation (2.22). Since no second-order term of $\boldsymbol{D}_i^{\mathrm{T}}$ exists, the body force does not contribute to the global stiffness matrix. Only force term is added:

$$S_{i,1}[f_x \quad f_y \quad f_z \quad 0 \quad 0 \quad 0 \quad 0 \quad 0 \quad 0 \quad 0 \quad 0 \quad 0]^{\mathrm{T}} \rightarrow \boldsymbol{F}_i \tag{2.48}$$

2.2.3.3. POINT LOADING

Assume a point load $\vec{f}_n = [f_x \quad f_y \quad f_z]^{\mathrm{T}}$ is exerted on point P (x, y, z) within block i, the potential energy Π_p is

$$\Pi_p = -[u \quad v \quad w]\cdot[f_x \quad f_y \quad f_z]^{\mathrm{T}} = -\boldsymbol{D}_i^{\mathrm{T}}\cdot\boldsymbol{T}_i^{\mathrm{T}}\cdot[F_x \quad F_y \quad F_z]^{\mathrm{T}} \tag{2.49}$$

where f_x, f_y and f_z are the three components x-, y- and z- directions of point loading. Since no second-order term of $\boldsymbol{D}_i^{\mathrm{T}}$ exists, the body force does not contribute to the global stiffness matrix. Only force term is added:

$$\boldsymbol{T}_i^{\mathrm{T}}[f_x \quad f_y \quad f_z]^{\mathrm{T}} \rightarrow \boldsymbol{F}_i \tag{2.50}$$

2.2.3.4. POINT DISPLACEMENT CONSTRAIN

In 3D DDA, the point displacement constrain is set by implementing a very stiff spring. The effect of the constrain spring is to change the displacement (u, v, w) of point P (x, y, z) within block i, to (u', v', w'). When $u' = v' = w' = 0$, the constrain is performs as a fixed point. The potential energy Π_c is expressed by

$$\begin{aligned}\Pi_m &= \frac{p}{2}[(u-u')^2+(v-v')^2+(w-w')^2] \\ &= \frac{p}{2}\boldsymbol{D}_i^{\mathrm{T}}\boldsymbol{T}_i^{\mathrm{T}}\boldsymbol{T}_i\boldsymbol{D}_i - p\boldsymbol{D}_i^{\mathrm{T}}\boldsymbol{T}_i^{\mathrm{T}}[u' \quad v' \quad w']^{\mathrm{T}} + p[u' \quad v' \quad w']\cdot[u' \quad v' \quad w']^{\mathrm{T}}\end{aligned} \tag{2.51}$$

Take derivatives for $\boldsymbol{D}_i^{\mathrm{T}}$, the added terms to stiffness and force matrices are

$$p\boldsymbol{T}_i^{\mathrm{T}}\boldsymbol{T}_i \rightarrow \boldsymbol{K}_{ii} \tag{2.52}$$

$$p\boldsymbol{T}_i^{\mathrm{T}}\cdot[u_m \quad v_m \quad w_m]^{\mathrm{T}} \rightarrow \boldsymbol{F}_i \tag{2.53}$$

2.2.3.5. INITIAL STRESS

Initial stress is constant and predefined. Denote stress vector $\boldsymbol{\sigma}_0$ as

$$\boldsymbol{\sigma}_0 = [0 \quad 0 \quad 0 \quad 0 \quad 0 \quad 0 \quad \sigma_x^0 \quad \sigma_y^0 \quad \sigma_z^0 \quad \tau_{yz}^0 \quad \tau_{zx}^0 \quad \tau_{xy}^0]^{\mathrm{T}} \tag{2.54}$$

The potential energy Π_s contributed by initial stress is expressed by

$$\Pi_s = \iiint (\boldsymbol{\varepsilon}^{\mathrm{T}} \cdot \boldsymbol{\sigma}_s)\mathrm{d}x\mathrm{d}y\mathrm{d}z = S_{i,0}\boldsymbol{D}_i^{\mathrm{T}} \cdot \boldsymbol{\sigma}_0 \tag{2.55}$$

Taking derivatives of Π_s yields added matrices. Since no second-order term of $\boldsymbol{D}_i^{\mathrm{T}}$ exists, the body force does not contribute to the global stiffness matrix. Only force term is added:

$$-S_{i,0}\boldsymbol{\sigma}_0 \rightarrow \boldsymbol{F}_i \tag{2.56}$$

2.2.3.6. ELASTIC STRESS

Elastic stress exists within every block in each step. Regarding block *i*, the elastic stress is a time-dependent variable. Since constant stress is assumed within a block, it is no longer a function to coordinate. The potential energy Π_e of elastic stress is computed by

$$\Pi_e = \iiint \frac{1}{2}(\boldsymbol{\varepsilon}^{\mathrm{T}} \cdot \boldsymbol{\sigma})\mathrm{d}x\mathrm{d}y\mathrm{d}z \tag{2.57}$$

where $\boldsymbol{\varepsilon}$ and $\boldsymbol{\sigma}$ are the strain and stress vector:

$$\boldsymbol{\sigma} = [0 \quad 0 \quad 0 \quad 0 \quad 0 \quad 0 \quad \sigma_x \quad \sigma_y \quad \sigma_z \quad \tau_{yz} \quad \tau_{zx} \quad \tau_{xy}]^{\mathrm{T}} \tag{2.58}$$

$$\boldsymbol{\varepsilon} = [0 \quad 0 \quad 0 \quad 0 \quad 0 \quad 0 \quad \varepsilon_x \quad \varepsilon_y \quad \varepsilon_z \quad \gamma_{yz} \quad \gamma_{zx} \quad \gamma_{xy}]^{\mathrm{T}} \tag{2.59}$$

The blocks in 3D DDA are elastic, a physical equation is given below:

$$\boldsymbol{\sigma} = \boldsymbol{E} \cdot \boldsymbol{\varepsilon} \tag{2.60}$$

where $\boldsymbol{E}$ is expressed by

$$\boldsymbol{E} = \frac{E}{(1+\nu)(1-2\nu)} \cdot \begin{bmatrix} 0 & 0 & 0 & 0 & 0 & 0 & 0 & 0 & 0 & 0 & 0 & 0 \\ 0 & 0 & 0 & 0 & 0 & 0 & 0 & 0 & 0 & 0 & 0 & 0 \\ 0 & 0 & 0 & 0 & 0 & 0 & 0 & 0 & 0 & 0 & 0 & 0 \\ 0 & 0 & 0 & 0 & 0 & 0 & 0 & 0 & 0 & 0 & 0 & 0 \\ 0 & 0 & 0 & 0 & 0 & 0 & 0 & 0 & 0 & 0 & 0 & 0 \\ 0 & 0 & 0 & 0 & 0 & 0 & 0 & 0 & 0 & 0 & 0 & 0 \\ 0 & 0 & 0 & 0 & 0 & 0 & 1-\nu & \nu & \nu & 0 & 0 & 0 \\ 0 & 0 & 0 & 0 & 0 & 0 & \nu & 1-\nu & \nu & 0 & 0 & 0 \\ 0 & 0 & 0 & 0 & 0 & 0 & \nu & \nu & 1-\nu & 0 & 0 & 0 \\ 0 & 0 & 0 & 0 & 0 & 0 & 0 & 0 & 0 & \frac{1}{2}-\nu & 0 & 0 \\ 0 & 0 & 0 & 0 & 0 & 0 & 0 & 0 & 0 & 0 & \frac{1}{2}-\nu & 0 \\ 0 & 0 & 0 & 0 & 0 & 0 & 0 & 0 & 0 & 0 & 0 & \frac{1}{2}-\nu \end{bmatrix} \tag{2.61}$$

where E is Young's modulus, ν is Poisson's ratio. Equation (2.57) is expanded by introducing equation (2.61):

$$\Pi_e = \iiint \frac{1}{2}(\boldsymbol{D}_i^{\mathrm{T}} \cdot \boldsymbol{E}_i \cdot \boldsymbol{D}_i)\mathrm{d}x\mathrm{d}y\mathrm{d}z = \frac{S_{i,0}}{2}(\boldsymbol{D}_i^{\mathrm{T}} \cdot \boldsymbol{E}_i \cdot \boldsymbol{D}_i) \tag{2.62}$$

Taking derivatives of Π_e yields matrices that should be added to the global stiffness:

$$S_{i,0}\boldsymbol{E}_i \rightarrow \boldsymbol{K}_{ii} \tag{2.63}$$

2.2.4. ASSEMBLY OF CONTACT MATRICES

Contacts occur when blocks interact with each other. Such behavior makes a blocky system non-linear, which increases difficulties in equation solving. DDA incorporates a contact detection and enforcement theory, which is able to address the complex contact phenomenon. At the beginning of each step, DDA will find all possible contacts in the current step (including those contact pairs which are not in contact yet, however possible at the end of the step), referred to as contact detection. Subsequently, all the contacts are analyzed, and the entrance planes are assigned.

Based on the information, proper contact springs are added to each contact to prevent blocks from overlapping with each other. This system state will be checked in the following subroutines, called post judgement, in OCI. If checked to be convergent, the solver will move on, update the data to prepare for the next step; otherwise, the contact springs must be adjusted. Contact detection and post judgement used in 3D DDA will be introduced in the following sections.

2.2.4.1. CONTACT TYPES AND DETECTION

There are seven types of contacts in total in 3D DDA. Those contacts are: (a) vertex-facet (V-F); (b) crossing edge-edge (E-E); (c) vertex-vertex (V-V); (d) vertex-edge (V-E); (e) edge-facet (E-F); (f) parallel E-E; (g) facet-facet (F-F). They are presented in Figure 2.2. The first four types of them are fundamental contact types. The combination of them may construct the last three types. For example, a parallel E-E may consist of two V-E contacts, or one V-V and one V-F contacts; an F-F contact may consist of three V-F contacts.

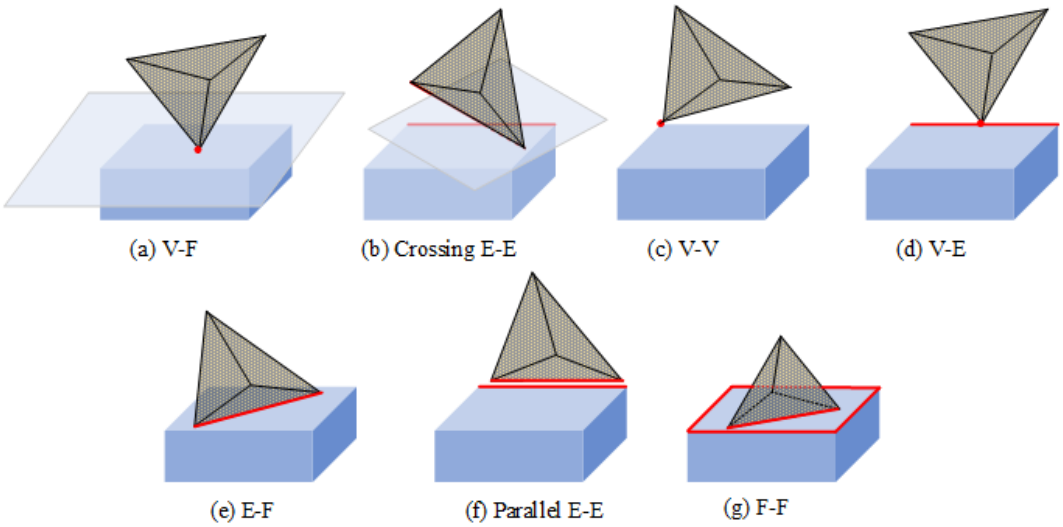

Figure 2.2 Contact types in 3D DDA (modified after Peng, X. et al. (2020a))

When searching for the contacts, an order is followed: regarding two target blocks, distances between every pair of their vertices are first checked. If the distance of two vertices falls into the range of the allowed contact distance, then these two vertices are in contact as V-V contact; subsequently, the distance of a vertex and the edges from another block is checked to find possible V-E contacts.

If the distance is no greater than the maximum allowed contact distance, and all the involved vertices, including the ends of the checked edge, are not forming V-V contacts, this V-E contact is valid and will be recorded. The following judgement for V-F and crossing E-E are similar, the distance is used as a criterion. Note that for a V-F contact, the projection of vertex to the facet plane should be within a specific area related to the facet range.

With all the contacts are detected, the entrance plane is identified afterwards. There are two entrance types in 3D DDA, i.e. V-F and crossing E-E, and the ways to determine contact point and entrance planes are different. As shown in Figure 2.2 (a) and (b), in a V-F entrance mode, the entrance plane is the facet plane; in a crossing E-E entrance mode, the entrance plane is determined by the two cross edges in contact together: it is parallel to both of the edges. The contact point is then calculated based on the entrance plane and the motion of the associated vertices. Formulae about contact point positions are given as follows.

Figure 2.3 shows a typical contact that is formed between a point P_a (also marked as P_1) and a facet (characterized by the first three vertices P_2, P_3 and P_4) (Yu, P. et al., 2020). The entrance point is P_a on block i and the facet belonging to block j is the entrance facet. The coincidence point located on the entrance face is marked as P_b. For P_k (k = 1, 2, 3, 4), the coordinate and displacement are (x_k, y_k, z_k) and (u_k, v_k, w_k), respectively. The apostrophe denotes the position after deformation, for example, P_a and P_b move to P_a' and P_b', respectively. Two contact springs, the normal contact spring with stiffness k_n and the shear contact spring with stiffness k_s, are added to the contact. The directions of local coordinate $\boldsymbol{n}$ and $\boldsymbol{\tau}$ are normal to the entrance plane and parallel to projection on the plane of the entrance point displacement, respectively.

The location of the entrance point is different in the two entrance modes. For a V-F type entrance, as shown in Figure 2.3, P_a on block i and P_b on a facet of block j are both required. It is easy to observe that $P_a = P_1$. The corresponding point P_b is located by two auxiliary parameters λ_{b1} and λ_{b2}, which is expressed by

$$\overrightarrow{P_1P_4} = \lambda_{b1}\overrightarrow{P_2P_4} + \lambda_{b2}\overrightarrow{P_3P_4} \tag{2.64}$$

On the other hand, for a crossing E-E contact, P_a and P_b are the closet point to another edge, and parameters used to locate P_a and P_b are λ_a and λ_b, which is expressed by

$$\overrightarrow{P_1P_a} = \lambda_a \overrightarrow{P_1P_2} \tag{2.65}$$

$$\overrightarrow{P_3P_b} = \lambda_b \overrightarrow{P_3P_4} \tag{2.66}$$

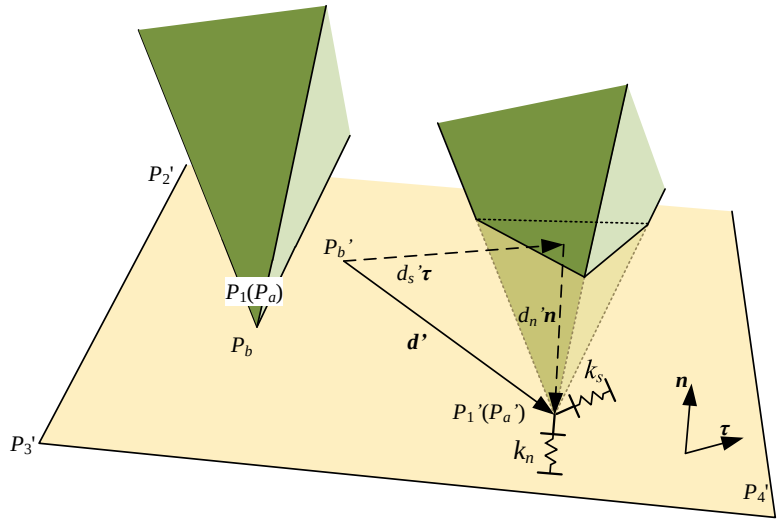

Figure 2.3 Schematic diagram of a contact (Yu, P. et al., 2020)

However, equation (2.64) – (2.66) is not accurate enough because the position of points varies in one step, from their position P at the beginning of the step, to P' at the end of the step. An algorithm should be adopted to determine where exactly point P_1 touches facet $P_2P_3P_4$, i.e. P_a. To find this point, an interpolation parameter γ ($0 \le \gamma \le 1$) is introduced to express the moving path of a point P_r:

$$P_r(\gamma) = [x_r(\gamma) \quad y_r(\gamma) \quad z_r(\gamma)]^{\mathrm{T}} = [x_r + \gamma u_r \quad y_r + \gamma v_r \quad z_r + \gamma w_r]^{\mathrm{T}} \tag{2.67}$$

Equation (2.67) suggests that the location of P_r on the moving path is determined by γ. When $\gamma = 0$, $P_r(\gamma) = P_r$; when $\gamma = 1$, $P_r(\gamma) = P_r$'. The overlapping distance $d_n(\gamma)$ between $P_1(\gamma)$ and the entrance plane is

$$d_n(\gamma) \approx \frac{V}{A_0} + \frac{\gamma}{A_0}\left(\begin{vmatrix} 1 & u_1 & y_1 & z_1 \\ 1 & u_2 & y_2 & z_2 \\ 1 & u_3 & y_3 & z_3 \\ 1 & u_4 & y_4 & z_4 \end{vmatrix} + \begin{vmatrix} 1 & x_1 & v_1 & z_1 \\ 1 & x_2 & v_2 & z_2 \\ 1 & x_3 & v_3 & z_3 \\ 1 & x_4 & v_4 & z_4 \end{vmatrix} + \begin{vmatrix} 1 & x_1 & y_1 & w_1 \\ 1 & x_2 & y_2 & w_2 \\ 1 & x_3 & y_3 & w_3 \\ 1 & x_4 & y_4 & w_4 \end{vmatrix} \right) \quad (2.68)$$

with V the volume of polyhedron $P_1P_2P_3P_4$ and A_0 the double of the area of $P_2P_3P_4$, which are calculated by

$$V = \begin{vmatrix} 1 & x_1 & y_1 & z_1 \\ 1 & x_2 & y_2 & z_2 \\ 1 & x_3 & y_3 & z_3 \\ 1 & x_4 & y_4 & z_4 \end{vmatrix} \quad (2.69)$$

$$A_0 = \sqrt{\begin{vmatrix} y_3 - y_2 & z_3 - z_2 \\ y_4 - y_2 & z_4 - z_2 \end{vmatrix}^2 + \begin{vmatrix} z_3 - z_2 & x_3 - x_2 \\ z_4 - z_2 & x_4 - x_2 \end{vmatrix}^2 + \begin{vmatrix} x_3 - x_2 & y_3 - y_2 \\ x_4 - x_2 & y_4 - y_2 \end{vmatrix}^2} \quad (2.70)$$

It is obvious that the entrance point should satisfy

$$d_n(\gamma_0) = 0 \quad (2.71)$$

Where $P_1(\gamma_0)$ is the entrance point. The value of γ_0 is calculated by a linear interpolation based on $d_n(0)$ and $d_n(1)$:

$$\gamma_0 = \frac{d_n(0)}{d_n(0) - d_n(1)} \quad (2.72)$$

According to the illustration above, equation (2.64) is modified as

$$\overrightarrow{P_1(\gamma_0)P_4(\gamma_0)} = \boldsymbol{v}_1 + \boldsymbol{v}_2 = \lambda_{b1}\overrightarrow{P_2(\gamma_0)P_4(\gamma_0)} + \lambda_{b2}\overrightarrow{P_3(\gamma_0)P_4(\gamma_0)} \quad (2.73)$$

where $\boldsymbol{v}_1$ and $\boldsymbol{v}_2$ are two auxiliary vectors. From the perspective of geometry, λ_{b1} and λ_{b2} are computed by

$$\lambda_{b1} = \frac{\boldsymbol{v}_1}{\overline{P_2(\gamma_0)P_4(\gamma_0)}} = \frac{h_3}{h_1} = \frac{(\overrightarrow{P_1(\gamma_0)P_3(\gamma_0)} \times \overrightarrow{P_1(\gamma_0)P_4(\gamma_0)}) \cdot \boldsymbol{n}}{(\overrightarrow{P_2(\gamma_0)P_3(\gamma_0)} \times \overrightarrow{P_2(\gamma_0)P_4(\gamma_0)}) \cdot \boldsymbol{n}} \quad (2.74)$$

$$\lambda_{b2} = \frac{\boldsymbol{v}_2}{\overline{P_3(\gamma_0)P_4(\gamma_0)}} = \frac{h_4}{h_2} = \frac{(\overrightarrow{P_1(\gamma_0)P_4(\gamma_0)} \times \overrightarrow{P_1(\gamma_0)P_2(\gamma_0)}) \cdot \boldsymbol{n}}{(\overrightarrow{P_3(\gamma_0)P_4(\gamma_0)} \times \overrightarrow{P_3(\gamma_0)P_2(\gamma_0)}) \cdot \boldsymbol{n}} \quad (2.75)$$

In summary, the location of P_a and P_b are given by

$$P_a = P_1' \tag{2.76}$$

$$P_b = \lambda_{b1} P_2' + \lambda_{b2} P_3' + \left(1 - \lambda_{b1} - \lambda_{b2}\right) P_4' \tag{2.77}$$

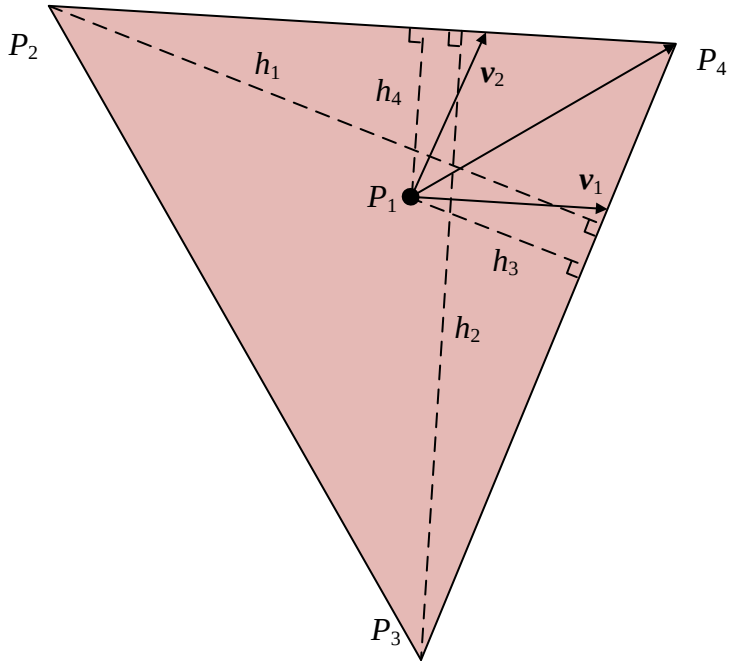

Figure 2.4 Illustrations of the geometric relations to locate P_1

On the other hand, for the crossing E-E entrance type, because γ_0 is already obtained, the coefficient λ_a and λ_b are computed by

$$\lambda_a = \frac{\overline{P_1(\gamma_0)P_a(\gamma_0)}}{\overline{P_1(\gamma_0)P_2(\gamma_0)}} \tag{2.78}$$

$$\lambda_b = \frac{\overline{P_3(\gamma_0)P_b(\gamma_0)}}{\overline{P_3(\gamma_0)P_4(\gamma_0)}} \tag{2.79}$$

Recalling equation (2.76) and (2.77), the location of P_a and P_b are given by

$$P_a = (1 - \lambda_a) P_1' + \lambda_a P_2' \tag{2.80}$$

$$P_b = (1 - \lambda_b) P_3' + \lambda_b P_4' \tag{2.81}$$

The locations of P_a and P_b will be used in Section 2.2.4.3.

2.2.4.2. CONTACT SUBMATRIX

Because the magnitude of the normal contact spring force is proportional to the entrance distance d_n'. It is calculated by

$$d_n' \approx \frac{V}{A_0} + \frac{1}{A_0}\left(\begin{vmatrix} 1 & u_1 & y_1 & z_1 \\ 1 & u_2 & y_2 & z_2 \\ 1 & u_3 & y_3 & z_3 \\ 1 & u_4 & y_4 & z_4 \end{vmatrix} + \begin{vmatrix} 1 & x_1 & v_1 & z_1 \\ 1 & x_2 & v_2 & z_2 \\ 1 & x_3 & v_3 & z_3 \\ 1 & x_4 & v_4 & z_4 \end{vmatrix} + \begin{vmatrix} 1 & x_1 & y_1 & w_1 \\ 1 & x_2 & y_2 & w_2 \\ 1 & x_3 & y_3 & w_3 \\ 1 & x_4 & y_4 & w_4 \end{vmatrix} \right) \tag{2.82}$$

To simplify the expressions, an algebraic complement L_{rs} of determinant V about element v_{rs}, is introduced:

$$L_{rs} = (-1)^{r+s} V_{rs} \tag{2.83}$$

Subsequently, equation (2.82) is re-written as

$$d_n' \approx d_n + \frac{1}{A_0}\begin{bmatrix} L_{12} & L_{13} & L_{14} \end{bmatrix}\begin{bmatrix} u_1 \\ v_1 \\ w_1 \end{bmatrix} + \frac{1}{A_0}\sum_{r=2}^{4}\left(\begin{bmatrix} L_{r2} & L_{r3} & L_{r4} \end{bmatrix}\begin{bmatrix} u_r \\ v_r \\ w_r \end{bmatrix} \right) \tag{2.84}$$

with

$$d_n = \left(\sum_{r=1}^{4} L_{r1} \right) / A_0 \tag{2.85}$$

Using $\boldsymbol{D}_i$ to replace the deformation vector by recalling equation (2.40), d_n' is obtained by

$$d_n' \approx d_n + \boldsymbol{H}\boldsymbol{D}_i + \boldsymbol{G}\boldsymbol{D}_j \tag{2.86}$$

where $\boldsymbol{H}$ and $\boldsymbol{G}$ are coefficient matrices, which are different in V-F and crossing E-E entrance model. In entrance V-F,

$$\boldsymbol{H} = \frac{1}{A_0}[L_{12} \quad L_{13} \quad L_{14}] \cdot \boldsymbol{T}_{i,p_1} \tag{2.87}$$

$$\boldsymbol{G} = \frac{1}{A_0}\sum_{r=2}^{4}[L_{r2} \quad L_{r3} \quad L_{r4}] \cdot \boldsymbol{T}_{j,p_r} \tag{2.88}$$

where $\boldsymbol{T}_{i,P_1}$ indicates the displacement transforming matrix of point P_1 on block i. The same meaning goes for $\boldsymbol{T}_{j,Pr}$. Meanwhile, in a crossing E-E entrance mode,

$$\boldsymbol{H} = \frac{1}{A_0}\sum_{r=1}^{2}[L_{r2} \quad L_{r3} \quad L_{r4}]\cdot \boldsymbol{T}_{i,p_r} \tag{2.89}$$

$$\boldsymbol{G} = \frac{1}{A_0}\sum_{r=3}^{4}[L_{r2} \quad L_{r3} \quad L_{r4}]\cdot \boldsymbol{T}_{j,pr} \tag{2.90}$$

where edge P_1P_2 belongs to block i and edge P_3P_4 belongs to block j. With the expressions of entrance distance, the potential energy Π_n is obtained by a model of a deformed spring:

$$\begin{aligned}\Pi_n &= \frac{k_n}{2}(d_n')^2 = \frac{k_n}{2}(d_n + \boldsymbol{H}\cdot\boldsymbol{D}_i + \boldsymbol{G}\cdot\boldsymbol{D}_j)^2 \\ &= \frac{k_n}{2}(d_n^2 + 2d_n\boldsymbol{H}\cdot\boldsymbol{D}_i + 2d_n\boldsymbol{G}\cdot\boldsymbol{D}_j + \boldsymbol{H}\cdot\boldsymbol{D}_i\cdot\boldsymbol{D}_i^{\mathrm{T}}\cdot\boldsymbol{H}^{\mathrm{T}} \\ &\quad + \boldsymbol{G}\cdot\boldsymbol{D}_j\cdot\boldsymbol{D}_j^{\mathrm{T}}\cdot\boldsymbol{G}^{\mathrm{T}} + 2\boldsymbol{H}\cdot\boldsymbol{D}_i\cdot\boldsymbol{D}_j^{\mathrm{T}}\cdot\boldsymbol{G}^{\mathrm{T}})\end{aligned} \tag{2.91}$$

Taking derivatives of Π_n yields matrices that should be added to the global stiffness and force matrices:

$$k_n\boldsymbol{H}^{\mathrm{T}}\cdot\boldsymbol{H} \rightarrow \boldsymbol{K}_{ii} \tag{2.92}$$

$$k_n\boldsymbol{G}^{\mathrm{T}}\cdot\boldsymbol{G} \rightarrow \boldsymbol{K}_{jj} \tag{2.93}$$

$$k_n\boldsymbol{H}^{\mathrm{T}}\cdot\boldsymbol{G} \rightarrow \boldsymbol{K}_{ij} \tag{2.94}$$

$$k_n\boldsymbol{G}^{\mathrm{T}}\cdot\boldsymbol{H} \rightarrow \boldsymbol{K}_{ji} \tag{2.95}$$

$$-k_n d_n\boldsymbol{H}^{\mathrm{T}} \rightarrow \boldsymbol{F}_i \tag{2.96}$$

$$-k_n d_n\boldsymbol{G}^{\mathrm{T}} \rightarrow \boldsymbol{F}_j \tag{2.97}$$

The shear contact spring force is also proportional to the shear contact displacement d_τ', therefore

$$d_\tau' = \sqrt{\left|\overrightarrow{P_b'P_a'}\right|^2 - \left(\overrightarrow{P_b'P_a'} \cdot \boldsymbol{n}\right)^2} = \sqrt{\begin{bmatrix} x_a + u_a - x_b - u_b \\ y_a + v_a - y_b - v_b \\ z_a + w_a - z_b - w_b \end{bmatrix}^{\mathrm{T}} \boldsymbol{N} \begin{bmatrix} x_a + u_a - x_b - u_b \\ y_a + v_a - y_b - v_b \\ z_a + w_a - z_b - w_b \end{bmatrix}} \quad (2.98)$$

with

$$\boldsymbol{N} = \boldsymbol{E} - \boldsymbol{n} \cdot \boldsymbol{n}^{\mathrm{T}} \quad (2.99)$$

where $\boldsymbol{n}$ indicates the external unit normal of the entrance facet. Similarly, the potential energy Π_τ is obtained:

$$\begin{aligned} \Pi_\tau &= \frac{k_\tau}{2}(d_\tau')^2 \\ &= \frac{k_\tau}{2}\left(\begin{bmatrix} x_a - x_b \\ y_a - y_b \\ z_a - z_b \end{bmatrix}^{\mathrm{T}} \boldsymbol{N} \begin{bmatrix} x_a - x_b \\ y_a - y_b \\ z_a - z_b \end{bmatrix} + \begin{bmatrix} u_a - u_b \\ v_a - v_b \\ w_a - w_b \end{bmatrix}^{\mathrm{T}} \boldsymbol{N} \begin{bmatrix} u_a - u_b \\ v_a - v_b \\ w_a - w_b \end{bmatrix}\right) \\ &\quad + k_\tau \begin{bmatrix} u_a - u_b \\ v_a - v_b \\ w_a - w_b \end{bmatrix}^{\mathrm{T}} \boldsymbol{N} \begin{bmatrix} x_a - x_b \\ y_a - y_b \\ z_a - z_b \end{bmatrix} \end{aligned} \quad (2.100)$$

Using $\boldsymbol{D}_i$ to replace the deformation vector by recalling equation (2.40), d_τ' is obtained by

$$\begin{aligned} \Pi_\tau &= k_\tau \left(\frac{1}{2}\begin{bmatrix} x_a - x_b \\ y_a - y_b \\ z_a - z_b \end{bmatrix}^{\mathrm{T}} \boldsymbol{N} + \boldsymbol{D}_i^{\mathrm{T}} \boldsymbol{T}_{i,p_a}^{\mathrm{T}} \boldsymbol{N} - \boldsymbol{D}_j^{\mathrm{T}} \boldsymbol{T}_{j,p_b}^{\mathrm{T}} \boldsymbol{N}\right) \begin{bmatrix} x_a - x_b \\ y_a - y_b \\ z_a - z_b \end{bmatrix} \\ &\quad + \frac{k_\tau}{2} \boldsymbol{D}_i^{\mathrm{T}} \boldsymbol{T}_{i,p_a}^{\mathrm{T}} \boldsymbol{N} \boldsymbol{T}_{i,p_a} \boldsymbol{D}_i + \frac{k_\tau}{2} \boldsymbol{D}_j^{\mathrm{T}} \boldsymbol{T}_{j,p_b}^{\mathrm{T}} \boldsymbol{N} \boldsymbol{T}_{j,p_b} \boldsymbol{D}_j \\ &\quad - \frac{k_\tau}{2} \boldsymbol{D}_i^{\mathrm{T}} \boldsymbol{T}_{i,p_a}^{\mathrm{T}} \boldsymbol{N} \boldsymbol{T}_{j,p_b} \boldsymbol{D}_j - \frac{k_\tau}{2} \boldsymbol{D}_j^{\mathrm{T}} \boldsymbol{T}_{j,p_b}^{\mathrm{T}} \boldsymbol{N} \boldsymbol{T}_{i,p_a} \boldsymbol{D}_i \end{aligned} \quad (2.101)$$

Taking derivatives of Π_τ yields matrices that should be added to the global stiffness and force matrices:

$$k_\tau \boldsymbol{T}_{i,p_a}^{\mathrm{T}} \boldsymbol{N} \boldsymbol{T}_{i,p_a} \rightarrow \boldsymbol{K}_{ii} \quad (2.102)$$

$$k_\tau \boldsymbol{T}_{j,p_b}^{\mathrm{T}} \boldsymbol{N} \boldsymbol{T}_{j,p_b} \rightarrow \boldsymbol{K}_{jj} \quad (2.103)$$

$$-k_\tau \boldsymbol{T}_{i,p_a}^{\mathrm{T}} \boldsymbol{N} \cdot \boldsymbol{T}_{j,p_b} \rightarrow \boldsymbol{K}_{ij} \tag{2.104}$$

$$-k_\tau \boldsymbol{T}_{j,p_b}^{\mathrm{T}} \boldsymbol{N} \boldsymbol{T}_{i,p_a} \rightarrow \boldsymbol{K}_{ji} \tag{2.105}$$

$$-k_\tau \boldsymbol{T}_{i,p_a}^{\mathrm{T}} \boldsymbol{N} \begin{bmatrix} x_a - x_b \\ y_a - y_b \\ z_a - z_b \end{bmatrix} \rightarrow \boldsymbol{F}_i \tag{2.106}$$

$$k_\tau \boldsymbol{T}_{j,p_b}^{\mathrm{T}} \boldsymbol{N} \begin{bmatrix} x_a - x_b \\ y_a - y_b \\ z_a - z_b \end{bmatrix} \rightarrow \boldsymbol{F}_j \tag{2.107}$$

2.2.4.3. FRICTION SUBMATRIX

When the contact state of a contact transfers to sliding, the shear contact spring is removed and replaced by friction. In 3D DDA, the Coulomb friction law is adopted to calculate friction. In such a situation, the shear force $\boldsymbol{F}_f$ imposed on the contact point P_a can be expressed by

$$\boldsymbol{F}_f = -|\boldsymbol{F}_n| \tan\phi \boldsymbol{s} = -k_n |d_n'| \tan\phi \boldsymbol{\tau} \tag{2.108}$$

where $\boldsymbol{F}_n$ is the normal contact force. The shear displacement in this step is expressed by

$$\boldsymbol{d}_f' = [u_a - u_b \quad v_a - v_b \quad w_a - w_b] \cdot \boldsymbol{\tau} \cdot \boldsymbol{\tau} \tag{2.109}$$

The potential energy Π_f is calculated by

$$\begin{aligned} \Pi_f &= \boldsymbol{F}_f \boldsymbol{d}_f' = |\boldsymbol{F}_f| [u_a - u_b \quad v_a - v_b \quad w_a - w_b] \boldsymbol{\tau} \\ &= |\boldsymbol{F}_f| [u_a \quad v_a \quad w_a] \boldsymbol{\tau} - |\boldsymbol{F}_f| [u_b \quad v_b \quad w_b] \boldsymbol{\tau} \end{aligned} \tag{2.110}$$

Using $\boldsymbol{D}_i$ to replace the deformation vector by recalling equation (2.40), Π_f becomes

$$\Pi_f = |\boldsymbol{F}_f| \boldsymbol{D}_i^{\mathrm{T}} \cdot \boldsymbol{T}_i^{\mathrm{T}}(x_a, y_a, z_a) \boldsymbol{\tau} - |\boldsymbol{F}_f| \boldsymbol{D}_j^{\mathrm{T}} \cdot \boldsymbol{T}_j^{\mathrm{T}}(x_b, y_b, z_b) \boldsymbol{\tau} \tag{2.111}$$

Taking derivatives of Π_f yields matrices that should be added to the global force matrix:

$$-\left|\boldsymbol{F}_f\right|\boldsymbol{T}_{i.p_a}^{\mathrm{T}}\boldsymbol{\tau} \rightarrow \boldsymbol{F}_i \tag{2.112}$$

$$\left|\boldsymbol{F}_f\right|\boldsymbol{T}_{j,p_b}^{\mathrm{T}}\boldsymbol{\tau} \rightarrow \boldsymbol{F}_j \tag{2.113}$$

2.2.5. OPEN-CLOSE ITERATION (OCI)

After solving the governing equations, an OCI is implemented to determine the valid system state. In the OCI, the final states of all contacts after solving the governing equations are tested and compared to those assumed before. The system state is considered valid only if all the calculated contact states are consistent with the initial ones. The OCI follows the criteria that the shear spring force cannot exceed the maximum friction, and the distance serves as evidence to determine open and close:

$$k_n d_n > 0 \quad \text{and} \quad k_\tau d_\tau \le k_n d_n \tan\varphi + \tau_c A \;\rightarrow\; \text{locked} \tag{2.114}$$

$$k_n d_n > 0 \quad \text{and} \quad k_\tau d_\tau > k_n d_n \tan\varphi + \tau_c A \;\rightarrow\; \text{sliding} \tag{2.115}$$

$$k_n d_n < -\sigma_c A \;\rightarrow\; \text{open} \tag{2.116}$$

where τ_c, φ, σ_c and A are cohesion, friction angle, tensile stress and contact area of the contact.

2.3. DEBRIS FLOW SIMULATION: STATE-OF-THE-ART

2.3.1. DERIVATION OF THE GOVERNING EQUATIONS

Although debris flow is a complex mixture that includes components of water, soil and stones, it is commonly treated as granular flow (Iverson, R. M. et al., 1997). A set of shallow-water equations are adopted to reduce the flow from a 3D type on a complex terrain to a simpler 2D situation because comparing to the horizontal expansions, the vertical depth is relatively small (Gray, J. M. N. T. et al., 1999; Iverson, R. M., 1997b; Savage, S. B. et al., 1989). However, the governing equations in shallow-water form are still derived from the original famous Navier-

Stokes equation, and then they are numerically solved by an FDM method (Han, Z. et al., 2015a). The depth-integrated equations used are based on previous researches (Iverson, R. M., 1997b; Savage, S. B. et al., 1989; Wu, J. et al., 2013b).

Navier-stokes equation is basically a momentum conservation, which can be given in a vector form:

$$\rho\frac{\partial \mathbf{v}}{\partial t}+\rho\mathbf{v}\cdot\nabla(\mathbf{v})=-\nabla p+\nabla\mathbf{T}+\rho\mathbf{g} \tag{2.117}$$

where ∇ is the divergence calculus; $\mathbf{v}$ is the velocity vector; t is time; p and ρ are the pressure and density of the flow; $\mathbf{T}$ is the stress vector; $\mathbf{g}$ is the body acceleration vector. A continuity equation also holds:

$$\nabla\mathbf{v}=0 \tag{2.118}$$

In a typical 3D space measured by an orthogonal rectangular coordinate system (x, y, z) with z-axis upright, the body acceleration vector $\mathbf{g}$ becomes (0, 0, g) with g the gravitational acceleration. If define $\mathbf{v}$ by the components u, v and w along the axes, equation (2.117) and (2.118) can be written as

$$\frac{\partial u}{\partial x}+\frac{\partial v}{\partial y}+\frac{\partial w}{\partial z}=0 \tag{2.119}$$

$$\rho_f\left(\frac{\partial u}{\partial t}+u\frac{\partial u}{\partial x}+v\frac{\partial u}{\partial y}+w\frac{\partial u}{\partial z}\right)=-\frac{\partial p}{\partial x}+\mu\left(\frac{\partial^2 u}{\partial x^2}+\frac{\partial^2 u}{\partial y^2}+\frac{\partial^2 u}{\partial z^2}\right) \tag{2.120}$$

$$\rho_f\left(\frac{\partial v}{\partial t}+u\frac{\partial v}{\partial x}+v\frac{\partial v}{\partial y}+w\frac{\partial v}{\partial z}\right)=-\frac{\partial p}{\partial y}+\mu\left(\frac{\partial^2 v}{\partial x^2}+\frac{\partial^2 v}{\partial y^2}+\frac{\partial^2 v}{\partial z^2}\right) \tag{2.121}$$

$$\rho_f\left(\frac{\partial w}{\partial t}+u\frac{\partial w}{\partial x}+v\frac{\partial w}{\partial y}+w\frac{\partial w}{\partial z}\right)=\rho_f g-\frac{\partial p}{\partial z}+\mu\left(\frac{\partial^2 w}{\partial x^2}+\frac{\partial^2 w}{\partial y^2}+\frac{\partial^2 w}{\partial z^2}\right) \tag{2.122}$$

where ρ_f and p are debris flow density and pressure; μ is the dynamic viscosity. Considering the fact that the scales of x and y are much larger than z (Gray, J. M. N. T. et al., 1999; Iverson, R. M., 1997b; Savage, S. B. et al., 1989). However, it is worth mention that in debris flow, the term “debris flow density” refers to the averaged density of the mixture containing fluid and small solid particles. It is calculated by

$$\rho_f = \rho_p C + (1-C)\rho_w \tag{2.123}$$

where ρ_p, ρ_w are the particle density in sediment and density of water, C is the sediment concentration. This parameter is used in two-phase flow to consider the solid phase. Apparently, only the small particles can be handled in this way. Define the characteristic flow dimension in x/y direction as $\bar{l}$ and $\bar{h}$ in z-direction, the result $\varepsilon = \bar{h}/\bar{l} \ll 1$. It further leads to the conclusions that $u \gg w$ and $v \gg w$. A normalized equation form was studied by Iverson, R. M. (1997a), which suggested that equation (2.122) can be simplified by

$$0 = \rho_f g - \frac{\partial p}{\partial z} \tag{2.124}$$

The information about the normalized version of equations together with the derivation of equation (2.122) is not detailed here, and the interested reader is suggested to refer to Iverson, R. M. (1997a). The pressure of the flow at position z is obtained by integrating equation (2.122) with respect to z, which yields

$$p = \rho_f g \left(H - z\right) \tag{2.125}$$

where H is the elevation of the debris flow surface. Let $z = Z_b$ and Z_b is the bed elevation (see Figure 2.5), then the pressure at the bottom of the flow p_b is

$$p_b = \rho_f g \left(H - Z_b\right) = \rho_f g h \tag{2.126}$$

where h is the flow thickness. Since equation (2.122) has been simplified due to the scale discrepancy, an integration along z-direction is conducted so that the 3D equations can be transferred into a 2D form. In addition, the kinematic boundary conditions at the surface and bottom are written as (Han, Z., 2015; Iverson, R. M. et al., 2015; Pudasaini, S. P. et al., 2003; Wang, C. et al., 2008)

$$\left(u\frac{\partial z}{\partial x} + v\frac{\partial z}{\partial y} - w \right)\Bigg|_{z=Z_b} = 0 \tag{2.127}$$

$$\left(\frac{\partial z}{\partial t} + u\frac{\partial z}{\partial x} + v\frac{\partial z}{\partial y} - w \right)\Bigg|_{z=H} = 0 \tag{2.128}$$

The erosion is considered as:

$$\frac{\partial H}{\partial t} = \frac{\partial h}{\partial t} - E \tag{2.129}$$

where E is the bed material entrainment rate, and $h = H - Z_b$ is the flow depth.

On the other hand, equation (2.119) – (2.121) are also integrated along z coordinate through the flow. Integration for the left-hand side (LHS) of equation (2.119) yields:

$$\begin{aligned}\int_{Z_b}^{H}\left(\frac{\partial u}{\partial x}+\frac{\partial v}{\partial y}+\frac{\partial w}{\partial z}\right)dz &= \int_{Z_b}^{H}\left(\frac{\partial u}{\partial x}+\frac{\partial v}{\partial y}\right)dz + w\Big|_{z=Z_b}^{z=H} \\ &= \frac{\partial}{\partial x}\int_{Z_b}^{H} u dz + \frac{\partial}{\partial y}\int_{Z_b}^{H} v dz + \left(u\frac{\partial z}{\partial x} + v\frac{\partial z}{\partial y} - w\right)\Bigg|_{z=Z_b}^{z=H}\end{aligned} \tag{2.130}$$

The accurate integration of velocities with respect to depth requires a full understanding of velocity distribution along z-direction. Although researches have illustrated some characteristics of flow velocity (Han, Z. et al., 2015b), an assumed mean flow velocity is often adopted in numerical simulations for debris flow. Define depth-averaged velocities of the flow by integrating corresponding variables from the flow bottom to the surface and being divided by the flow depth:

$$\bar{u} = \frac{1}{h}\int_{Z_b}^{H} u dz, \quad \bar{v} = \frac{1}{h}\int_{Z_b}^{H} v dz \tag{2.131}$$

Bring equation (2.127)-(2.129) and (2.131) to equation (2.130), it is simplified as

$$\frac{\partial h}{\partial t} + \frac{\partial M}{\partial x} + \frac{\partial N}{\partial y} = E \tag{2.132}$$

where $M = \bar{u}h$ and $N = \bar{v}h$ are x- and y- wise components of unit width discharge. This is the continuity equation of debris flow. Similarly, the left side of equation (2.120) and (2.121) are also integrated from flow bottom to the surface:

$$\int_{Z_b}^{H} \rho_f \left(\frac{\partial u}{\partial t} + u\frac{\partial u}{\partial x} + v\frac{\partial u}{\partial y} + w\frac{\partial u}{\partial z} \right) dz$$

$$= \rho_f \left(\frac{\partial}{\partial t}\int_{Z_b}^{H} u dz + \frac{\partial}{\partial x}\int_{Z_b}^{H} u^2 dz + \frac{\partial}{\partial y}\int_{Z_b}^{H} uv dz \right) - \rho_f \left(u\frac{\partial z}{\partial t} + u^2\frac{\partial z}{\partial x} + uv\frac{\partial z}{\partial y} - uw \right)\Bigg|_{z=Z_b}^{z=H} \tag{2.133}$$

Considering following integration formulae

$$\int_{Z_b}^{H} u^2 dz = \alpha_1 h\bar{u}^2 = \alpha_1 \bar{u}M, \quad \int_{Z_b}^{H} uv dz = \alpha_2 h\bar{u}\bar{v} = \alpha_2 \bar{v}M \tag{2.134}$$

where α_1 and α_2 are coefficients that adjust the discrepancy of uniform velocity profile against the real one. According to Savage, S. B. et al. (1989), for a blunt velocity profile, $\alpha_1 = \alpha_2 = 1$, meanwhile equals 1.2 for parabolic one. When a stone-type debris flow occurs on a slope with a rough surface, $\alpha_1 = \alpha_2 = 1.25$ (Takahashi, T. et al., 1992). Let $\alpha_1 = \alpha_2$, equation (2.133) becomes

$$\int_{Z_b}^{H} \rho_f \left(\frac{\partial u}{\partial t} + u\frac{\partial u}{\partial x} + v\frac{\partial u}{\partial y} + w\frac{\partial u}{\partial z} \right) dz = \rho_f \left[\frac{\partial M}{\partial t} + \alpha\frac{\partial(\bar{u}M)}{\partial x} + \alpha\frac{\partial(\bar{v}M)}{\partial y} \right] \tag{2.135}$$

Similar integrations are also taken for the right-hand side (RHS) of equation (2.120)

$$\int_{z=Z_b}^{z=H} (RHS)\, dz = -\int_{z=Z_b}^{z=H} \frac{\partial p}{\partial x} dz + \mu \int_{z=Z_b}^{z=H} \left(\frac{\partial^2 u}{\partial x^2} + \frac{\partial^2 u}{\partial y^2} + \frac{\partial^2 u}{\partial z^2} \right) dz \tag{2.136}$$

The first term is about pressure. Equation (2.125) gives the expression of p, therefore the following equation can be established:

$$\int_{z=Z_b}^{z=H} \frac{\partial p}{\partial x} dz = \rho_f g \int_{z=Z_b}^{z=H} \frac{\partial H}{\partial x} dz = \rho_f gh\frac{\partial H}{\partial x} \tag{2.137}$$

The terms involving second-order partial derivatives are also integrated as follow:

$$\int_{z=Z_b}^{z=H} \frac{\partial^2 u}{\partial x^2} dz = \beta \frac{\partial^2 h\bar{u}}{\partial x^2} \tag{2.138}$$

$$\int_{z=Z_b}^{z=H} \frac{\partial^2 u}{\partial y^2} dz = \beta \frac{\partial^2 h\bar{u}}{\partial y^2} \tag{2.139}$$

$$\int_{z=Z_b}^{z=H} \frac{\partial^2 u}{\partial z^2} dz = \left.\frac{\partial u}{\partial z}\right|_{z=Z_b}^{z=H} \tag{2.140}$$

where β is the ratio of the vertical and horizontal normal force within debris flow. The RHS of equation (2.140) represents the shear rate, which can be derived by stress boundary condition (Naef, D. et al., 2006):

$$\left.\frac{\partial u}{\partial z}\right|_{z=H} = 0, \quad \left.\frac{\partial u}{\partial z}\right|_{z=Z_b} = \frac{T_{bx}}{\mu} \tag{2.141}$$

where T_{bx} is the bottom flow resistance in x-direction. Substituting equation (2.137) – (2.141) into equation (2.136) gives

$$\int_{z=Z_b}^{z=H} (RHS)\, dz = -\rho_f gh \frac{\partial H}{\partial x} + \mu\beta \left(\frac{\partial^2 h\bar{u}}{\partial x^2} + \frac{\partial^2 h\bar{u}}{\partial y^2} \right) - T_{bx} \tag{2.142}$$

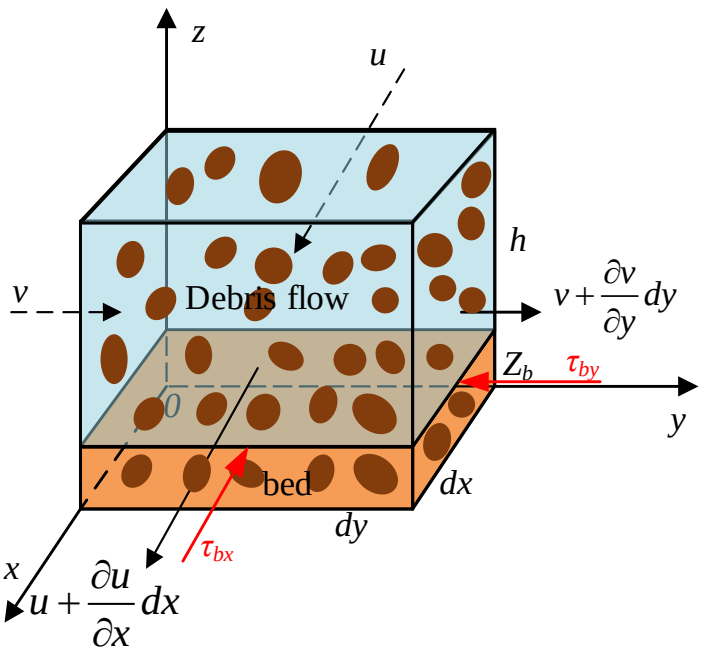

Figure 2.5 Schematic diagram of debris flow

Combing equation (2.135) and (2.142), the x- wise momentum equation is derived as

$$\frac{\partial M}{\partial t} + \alpha \frac{\partial (Mu)}{\partial x} + \alpha \frac{\partial (Mv)}{\partial y} = -\frac{\partial H}{\partial x} gh + \upsilon\beta \left(\frac{\partial^2 M}{\partial x^2} + \frac{\partial^2 M}{\partial y^2} \right) - \frac{T_{bx}}{\rho_f} \tag{2.143}$$

where $\upsilon = \mu/\rho_f$ is the kinetic viscosity. The y- wise momentum equation can be obtained following a similar pattern above, yielding

$$\frac{\partial N}{\partial t}+\alpha\frac{\partial(Nu)}{\partial x}+\alpha\frac{\partial(Nv)}{\partial y}=-\frac{\partial H}{\partial y}gh+\upsilon\beta\left(\frac{\partial^2 N}{\partial x^2}+\frac{\partial^2 N}{\partial y^2}\right)-\frac{T_{by}}{\rho_f} \tag{2.144}$$

where T_{by} is the bottom flow resistance in y-direction.

2.3.2. RHEOLOGY PARAMETERS AND ENTRAINMENT MODEL

The previous work of Han, Z. (2015) and Han, Z. et al. (2015a) are followed in this section. Involved variables and parameters should be first determined before the application. The earth pressure ratio β ranges from the active and passive earth pressure coefficients β_a and β_p, which are further related to the dynamic friction angle of the flow φ_f and bed φ_b. The expressions are (Begueria, S., 2009; Iverson, R. M. et al., 2001):

$$\begin{cases} \beta_a=\dfrac{1-\sin\varphi_f}{1+\sin\varphi_f},\quad \beta_p=\dfrac{1+\sin\varphi_f}{1-\sin\varphi_f}, & \varphi_f<\varphi_b \\ \beta_a,\beta_p=\dfrac{2\pm2\sqrt{1-\cos^2\varphi_f\left(1+\tan^2\varphi_b\right)}}{\cos^2\varphi_f}-1, & \varphi_f\geq\varphi_b \end{cases} \tag{2.145}$$

When erosion takes place, $\beta = \beta_a$; otherwise $\beta = \beta_b$. The resistance terms at the flow bottom are expressed by the Coulomb frictional law with viscosity (Han, Z. et al., 2015a; Wang, C. et al., 2008; Wu, J. et al., 2013a; Wu, J. et al., 2013b):

$$\begin{cases} T_x=\mu\rho_f\sqrt{gh}\cos\theta_x\tan\varphi_f \\ T_y=\mu\rho_f\sqrt{gh}\cos\theta_y\tan\varphi_f \end{cases} \tag{2.146}$$

where θ_x and θ_y are the slope inclinations along x and y-direction.

The erosion is analyzed in a three-layer model, including the flow, the erodible sediment and the bed, which was adopted by Iverson, R. M. (2012). Because of erosion and deposition, the exchange of the mass between flow and erodible sediment is possible, and during which the mass and momentum should conserve.

As given by previous literatures (Crosta, G. B. et al., 2009; Iverson, R. M., 2012), it further demands the following relationship:

$$E = \frac{\tau_{1bot} - \tau_{2top}}{\rho_f \left(v_{1bot} - v_{2top} \right)} \tag{2.147}$$

where τ denotes the shear stress; the subscripts 1 and 2 refer to the flow layer and erodible bed layer, and the subscripts *bot* and *top* indicate the location of the stress, i.e. at the bottom or top of the layer. This equation is capable of describing a so-called "jump" which is possible in shear stress and velocity. Nevertheless, the variables involved in equation (2.147) cannot be easily obtained. It is desired to use a more generally accepted quantity which is directly measured, for example, the average velocity $\overline{v}_1$, to replace v_{1bot} in the denominator. Johnson, C. G. et al. (2012) investigated the velocity profile in geophysical mass flows by experiments. Based on the flow velocity profile, the following relationship between v_1 and $\overline{v}_1$ exists:

$$\frac{v_1}{\overline{v}_1} = 1 - s_1 + 2s_1 \frac{z - (H - h)}{h} \tag{2.148}$$

where s_1 is a fatting parameter, and a good fitting to measured data from large-scale debris flow experiments is achieved for $s_1 = 0.5$ according to (Johnson, C. G. et al., 2012). Let $z = (H - h)$, it is then reduced to

$$v_{1bot} = \left(1 - s_1\right)\overline{v}_1 \tag{2.149}$$

On the other hand, the interface shear stresses are expressed by Mohr-Coulomb friction law:

$$\tau_{1bot} = \tan\varphi_f \left(\rho_f gh\cos\theta - p_{1bot} \right) + c \tag{2.150}$$

$$\tau_{2top} = \tan\varphi_b \left(\rho_f gh\cos\theta - p_{2top} \right) + c \tag{2.151}$$

where p_{1bot} and p_{2top} are interface pore pressure at the bottom/top of layer 1/2, θ is the local slope inclination, and c is the cohesion. Defining pore pressure ratio λ_1 and λ_2 as

$$\lambda_1 = p_{1bot} / \rho_f gh\cos\theta \tag{2.152}$$

$$\lambda_2 = p_{2top} / \rho_f gh\cos\theta \tag{2.153}$$

In addition, a bulk basal friction angel φ_{bulk} is adopted to reduce the involved variables (Hungr, O. et al., 2009):

$$\tan\varphi_{bulk} = (1-\lambda_1)\tan\varphi_f \tag{2.154}$$

Using φ_{bulk} to replace φ_f in equation (2.150) yields

$$\tau_{1bot} = \rho_f gh\cos\theta\tan\varphi_{bulk} + c \tag{2.155}$$

Substituting equation (2.149), (2.151) and (2.155) to equation (2.147), the erosion is eventually expressed by

$$E = \frac{gh\cos\theta\left[\tan\varphi_{bulk} - \tan\varphi_b(1-\lambda_2)\right]}{(1-s_1)\bar{v}_1} \tag{2.156}$$

2.3.3. FDM SCHEME TO SOLVE THE GOVERNING EQUATIONS

The presented FDM is a forward differential semi-Lagrangian method suggested by Wang, C. et al. (2008), Begueria, S. (2009) and Han, Z. (2015). A leapfrog time-differencing is adopted. For the linear terms, a forward difference scheme is applied, meanwhile a central difference scheme for nonlinear terms. The *x*- and *y* wise discharges *M* and *N* are defined at the edges of the mesh cells, and the flow depth is in the middle of the cell.

The discharge *M* is first evaluated by the variables in current step using the following discretized equation transformed from equation (2.143):

$$\frac{M_{i,j+1/2}^{n+2} - M_{i,j+1/2}^{n}}{2\Delta t} + \frac{\alpha}{\Delta x}\left[\left(\frac{M_{i+1,j+1/2}^{n} - M_{i,j+1/2}^{n}}{2h_{i+1/2,j+1/2}^{n+1}}\right)^2 - \left(\frac{M_{i,j+1/2}^{n} - M_{i-1,j+1/2}^{n}}{2h_{i-1/2,j-1/2}^{n+1}}\right)^2\right]$$
$$+\frac{\alpha}{\Delta y}\frac{\left(M_{i,j+1/2}^{n} + M_{i,j+3/2}^{n}\right)\left(N_{i+1/2,j+1}^{n} + N_{i-1/2,j+1}^{n}\right)}{h_{i-1/2,j+1/2}^{n+1} + h_{i+1/2,j+1/2}^{n+1} + h_{i+1/2,j+3/2}^{n+1} + h_{i-1/2,j+3/2}^{n+1}} -$$
$$\frac{\alpha}{\Delta y}\frac{\left(M_{i,j+1/2}^{n} + M_{i,j-1/2}^{n}\right)\left(N_{i+1/2,j}^{n} + N_{i-1/2,j}^{n}\right)}{h_{i-1/2,j-1/2}^{n+1} + h_{i+1/2,j-1/2}^{n+1} + h_{i+1/2,j+1/2}^{n+1} + h_{i-1/2,j+1/2}^{n+1}} =$$

$$-g\frac{\left(h_{i+1/2,j+1/2}^{n+1}+h_{i-1/2,j+1/2}^{n+1}\right)\left(H_{i+1/2,j+1/2}^{n+1}-H_{i-1/2,j+1/2}^{n+1}\right)}{2\Delta x}+$$
$$\frac{\upsilon\beta}{2}\left[\frac{M_{i-1/2,j+1/2}^{n}+M_{i,j+3/2}^{n}-2M_{i,j+1/2}^{n}}{\left(\Delta x\right)^{2}}+\frac{M_{i,j-1/2}^{n}+M_{i,j+3/2}^{n}-2M_{i,j+1/2}^{n}}{\left(\Delta y\right)^{2}}\right]- \quad (2.157)$$
$$g\cos\theta_x\tan\varphi\frac{h_{i+1/2,j+1/2}^{n+1}+h_{i-1/2,j+1/2}^{n+1}}{2}$$

where the superscripts involving n denote the quantity in step n, i.e. current step. Discharge N is also derived in a similar way from equation (2.144). With the new variables in step n + 2, the flow depth is also derived using

$$\frac{h_{i+1/2,j+1/2}^{n+3}-h_{i+1/2,j+1/2}^{n+1}}{2\Delta t}+\frac{M_{i+1,j+1/2}^{n+2}-M_{i,j+1/2}^{n+2}}{\Delta x}+\frac{N_{i+1/2,j+1}^{n+2}-N_{i+1/2,j}^{n+2}}{\Delta y}=E_n \quad (2.158)$$

which is discretized from equation (2.132). The updated flow motions are used to estimate the bed entrainment E by equation (2.156). The parameters will be further discussed in the following sections based on adopted examples. The computer code based on the theory given in Section 2.3 for debris flow simulation is named DFS.

2.4. CONCLUSIONS

In this chapter, a brief introduction has been presented for both 3D DDA and DFS together with their recent development and application.

As a discontinuous method, 3D DDA is suitable in analyzing cases involving large deformation, such as the large boulders and detached dam blocks. In addition, the block shape in 3D DDA can be arbitrary polyhedron, the influence of boulder shape thus can be studied by altering boulder polyhedron. However, in current 3D DDA, the energy dissipation during impacts cannot be addressed, which may lead to the over-estimation of post-collisional velocities of the blocks. Moreover, the flow action should be included. They will be illustrated in the following sections.

DFS used in this research is based on depth-integrated equations. The equations are then solved by FDM. How to address the block actions to flow is still problematic because the positions and gestures of blocks keep changing during a simulation. It will also be introduced in the following sections.

REFERENCE

Begueria, S. (2009). A GIS-based numerical model for simulating the kinematics of mud and debris flows over complex terrain. Natural Hazards and Earth System Sciences, 9(6), 1897–1909.

Chen, G. Q., Zheng, L., Zhang, Y. B., & Wu, J. (2013). Numerical simulation in rockfall analysis: a close comparison of 2-D and 3-D DDA. Rock Mechanics and Rock Engineering, 46(3), 527-541.

Chen, K.-T., & Wu, J.-H. (2018). Simulating the failure process of the Xinmo landslide using discontinuous deformation analysis. Engineering Geology, 239, 269-281.

Cheng, X., Xiao, J., Miao, Q., & Wang, Y. (2015). Design and implementation of a software architecture for 3D-DDA. Science China Technological Sciences, 58(9), 1604-1608.

Crosta, G. B., Imposimato, S., & Roddeman, D. (2009). Numerical modelling of entrainment/deposition in rock and debris-avalanches. Engineering Geology, 109(1-2), 135-145.

Federico, I., Marrone, S., Colagrossi, A., Aristodemo, F., & Antuono, M. (2012). Simulating 2D open-channel flows through an SPH model. European Journal of Mechanics - B/Fluids, 34, 35-46.

Fu, X. D., Sheng, Q., Zhang, Y. H., & Chen, J. (2016). Investigation of highly efficient algorithms for solving linear equations in the discontinuous deformation analysis method. International Journal for Numerical and Analytical Methods in Geomechanics, 40(4), 469-486.

Gray, J. M. N. T., Wieland, M., & Hutter, K. (1999). Gravity-driven free surface flow of granular avalanches over complex basal topography. Proceedings of the Royal Society of London. Series A: Mathematical, Physical and Engineering Sciences, 455(1985), 1841-1874.

Han, Z. (2015). Development of a comprehensive method for debris-flow analysis over complex topography considering nonuniform velocity distribution and bed-sediment erosion. (Ph.D.). Kyushu University.

Han, Z., Chen, G., Li, Y., Tang, C., Xu, L., He, Y., Huang, X., & Wang, W. (2015a). Numerical simulation of debris-flow behavior incorporating a dynamic method for estimating the entrainment. Engineering Geology, 190, 52-64.

Han, Z., Chen, G., Li, Y., Wang, W., & Zhang, H. (2015b). Exploring the velocity distribution of debris flows: An iteration algorithm based approach for complex cross-sections. Geomorphology, 241, 72-82.

Hatzor, Y. H., Arzi, A. A., Zaslavsky, Y., & Shapira, A. (2004). Dynamic stability analysis of jointed rock slopes using the DDA method: King Herod's Palace, Masada, Israel. International Journal of Rock Mechanics and Mining Sciences, 41(5), 813-832.

Hatzor, Y. H., & Feintuch, A. (2001). The validity of dynamic block displacement prediction using DDA. International Journal of Rock Mechanics and Mining Sciences, 38(4), 599-606.

Hungr, O., & Mcdougall, S. (2009). Two numerical models for landslide dynamic analysis. Computers & Geosciences, 35(5), 978-992.

Iverson, R. M. (1997a). Hydraulic modeling of unsteady debris-flow surges with solid-fluid interactions. Paper presented at the First International Conference on Debris-Flow Hazards Mitigation: Mechanics, Prediction, and Assessment: Hydraulics Division, New York.

Iverson, R. M. (1997b). The physics of debris flows. Reviews of Geophysics, 35(3), 245-296.

Iverson, R. M. (2012). Elementary theory of bed-sediment entrainment by debris flows and avalanches. Journal of Geophysical Research: Earth Surface, 117(F3).

Iverson, R. M., & Denlinger, R. P. (2001). Flow of variably fluidized granular masses across three-dimensional terrain: 1. Coulomb mixture theory. Journal of Geophysical Research: Solid Earth, 106(B1), 537-552.

Iverson, R. M., & Ouyang, C. J. (2015). Entrainment of bed material by Earth-surface mass flows: Review and reformulation of depth-integrated theory. Reviews of Geophysics, 53(1), 27-58.

Iverson, R. M., Reid, M. E., & Lahusen, R. G. (1997). Debris-flow mobilization from landslides. Annual Review of Earth and Planetary Sciences, 25(1), 85-138.

Jafari, A., & Keneti, A. J. M. T. (2007). Improvement of contact detection in'approaching faces' method for use in three-dimensional discontinuous deformation analysis. 116(2), 79-87.

Johnson, C. G., Kokelaar, B. P., Iverson, R. M., Logan, M., Lahusen, R. G., & Gray, J. M. N. T. (2012). Grain-size segregation and levee formation in geophysical mass flows. Journal of Geophysical Research: Earth Surface, 117(F1).

Maclaughlin, M. M., & Doolin, D. M. (2006). Review of validation of the discontinuous deformation analysis (DDA) method. International Journal for Numerical and Analytical Methods in Geomechanics, 30(4), 271-305.

Naef, D., Rickenmann, D., Rutschmanj, P., & Mcardell, B. W. (2006). Comparison of flow resistance relations for debris flows using a one-dimensional finite element simulation model. Natural Hazards and Earth System Science, 6(1), 155-165.

Peng, X., Chen, G., Yu, P., Zhang, Y., Guo, L., Wang, C., Cheng, X., & Niu, H. (2019a). Parallel computing of three-dimensional discontinuous deformation analysis based on OpenMP. Computers and Geotechnics, 106, 304-313.

Peng, X., Chen, G., Yu, P., Zhang, Y., & Wang, J. (2019b). Improvement of joint definition and determination in three-dimensional discontinuous deformation analysis. Computers and Geotechnics, 110, 148-160.

Peng, X., Chen, G., Yu, P., Zhang, Y., Zhang, H., & Guo, L. (2020a). A full-stage parallel architecture of three-dimensional discontinuous deformation analysis using OpenMP. Computers and Geotechnics, 118.

Peng, X., Yu, P., Chen, G., Xia, M., & Zhang, Y. (2019c). Development of a Coupled DDA–SPH Method and its Application to Dynamic Simulation of Landslides Involving Solid–Fluid Interaction. Rock Mechanics and Rock Engineering, 53(1), 113-131.

Peng, X., Yu, P., Chen, G., Xia, M., & Zhang, Y. (2020b). CPU-accelerated explicit discontinuous deformation analysis and its application to landslide analysis. Applied Mathematical Modelling, 77, 216-234.

Peng, X., Yu, P., Zhang, Y., & Chen, G. (2018). Applying modified discontinuous deformation analysis to assess the dynamic response of sites containing discontinuities. Engineering Geology, 246, 349-360.

Pudasaini, S. P., & Hutter, K. (2003). Rapid shear flows of dry granular masses down curved and twisted channels. Journal of Fluid Mechanics, 495, 193-208.

Savage, S. B., & Hutter, K. (1989). The motion of a finite mass of granular material down a rough incline. Journal of Fluid Mechanics, 199, 177-215.

Shi, G. (1989). Discontinuous deformation analysis a new numerical model for the static and dynamics of block systems. (Ph.D.). UC Berkeley, USA.

Shi, G. (2015). Contact theory. Science China Technological Sciences, 58(9), 1450-1496.

Shi, G. H., & Goodman, R. E. (1989). Generalization of two-dimensional discontinuous deformation analysis for forward modeling. International Journal for Numerical and Analytical Methods in Geomechanics, 13(4), 359-380.

Takahashi, T., Nakagawa, H., Harada, T., & Yamashiki, Y. (1992). Routing debris flows with particle segregation. Journal of Hydraulic Engineering, 118(11), 1490-1507.

Tsesarsky, M., Hatzor, Y. H., & Sitar, N. (2005). Dynamic displacement of a block on an inclined plane: Analytical, experimental and DDA results. Rock Mechanics and Rock Engineering, 38(2), 153-167.

Vreugdenhil, C. B. (2013). Numerical methods for shallow-water flow (Vol. 13): Springer Science & Business Media.

Wang, C., Li, S., & Esaki, T. (2008). GIS-based two-dimensional numerical simulation of rainfall-induced debris flow. Natural Hazards Earth System Science, 8(1), 47-58.

Wang, W., Chen, G. Q., Zhang, H., Zhou, S. H., Liu, S. G., Wu, Y. Q., & Fan, F. S. (2016). Analysis of landslide-generated impulsive waves using a coupled

DDA-SPH method. Engineering Analysis with Boundary Elements, 64, 267-277.

Wang, W., Chen, G. Q., Zhang, Y. B., Zheng, L., & Zhang, H. (2017). Dynamic simulation of landslide dam behavior considering kinematic characteristics using a coupled DDA-SPH method. Engineering Analysis with Boundary Elements, 80, 172-183.

Wang, W., Yin, K., Chen, G., Chai, B., Han, Z., & Zhou, J. (2019). Practical application of the coupled DDA-SPH method in dynamic modeling for the formation of landslide dam. Landslides, 16(5), 1021-1032.

Wang, X., Wu, W., Zhu, H., Lin, J.-S., & Zhang, H. (2019). Contact detection between polygonal blocks based on a novel multi-cover system for discontinuous deformation analysis. Computers and Geotechnics, 111, 56-65.

Wu, J.-H., Do, T. N., Chen, C.-H., & Wang, G. (2017). New geometric restriction for the displacement–constraint points in discontinuous deformation analysis. International Journal of Geomechanics, 17(5).

Wu, J., Chen, G.-Q., Zheng, L., & Zhang, Y.-B. (2013a). GIS-based numerical modelling of debris flow motion across three-dimensional terrain. Journal of Mountain Science, 10(4), 522-531.

Wu, J., Chen, G., Zheng, L., & Zhang, Y. (2013b). GIS-based numerical simulation of Amamioshima debris flow in Japan. Frontiers of Structural and Civil Engineering, 7(2), 206-214.

Wu, J. H. (2015). The elastic distortion problem with large rotation in discontinuous deformation analysis. Computers and Geotechnics, 69(Supplement C), 352-364.

Wu, J. H., & Chen, C. H. (2011). Application of DDA to simulate characteristics of the Tsaoling landslide. Computers and Geotechnics, 38(5), 741-750.

Wu, J. H., Ohnishi, Y., & Nishiyama, S. (2004). Simulation of the mechanical behavior of inclined jointed rock masses during tunnel construction using Discontinuous Deformation Analysis (DDA). International Journal of Rock Mechanics and Mining Sciences, 41(5), 731-743.

Yeung, M. R., Jiang, Q. H., & Sun, N. (2003). Validation of block theory and three-dimensional discontinuous deformation analysis as wedge stability analysis methods. International Journal of Rock Mechanics and Mining Sciences, 40(2), 265-275.

Yu, P., Chen, G., Peng, X., Zhang, Y., & Zhang, H. (2020). Exploring inelastic collisions using modified three-dimensional discontinuous deformation analysis incorporating a damped contact model. Computers and Geotechnics, 121.

Yu, P., Zhang, Y., Peng, X., Chen, G., & Zhao, J. X. (2019a). Distributed-Spring Edge-to-Edge Contact Model for Two-Dimensional Discontinuous Deformation Analysis. Rock Mechanics and Rock Engineering, 53(1), 365-382.

Yu, P., Zhang, Y., Peng, X., Wang, J., Chen, G., & Zhao, J. X. (2019b). Evaluation of impact force of rock landslides acting on structures using discontinuous deformation analysis. Computers and Geotechnics, 114.

Zhang, H., Chen, G., Zheng, L., Han, Z., Zhang, Y., Wu, Y., & Liu, S. (2015). Detection of contacts between three-dimensional polyhedral blocks for discontinuous deformation analysis. International Journal of Rock Mechanics and Mining Sciences, 78, 57-73.

Zhang, Y., Xu, Q., Chen, G., Zhao, J., & Zheng, L. (2014). Extension of discontinuous deformation analysis and application in cohesive-frictional slope analysis. International Journal of Rock Mechanics and Mining Sciences, 70, 533-545.

Zhang, Y., Zhang, J., Chen, G., Zheng, L., & Li, Y. (2015). Effects of vertical seismic force on initiation of the Daguangbao landslide induced by the 2008 Wenchuan earthquake. Soil Dynamics and Earthquake Engineering, 73, 91-102.

Zhang, Y. B., Wang, J. M., Xu, Q., Chen, G. Q., Zhao, J. X., Zheng, L., Han, Z., & Yu, P. C. (2015). DDA validation of the mobility of earthquake-induced landslides. Engineering Geology, 194, 38-51.

Zheng, F., Jiao, Y. Y., & Sitar, N. (2018). Generalized contact model for polyhedra in three - dimensional discontinuous deformation analysis. International Journal for Numerical Analytical Methods in Geomechanics, 42(13), 1471-1492.

CHAPTER 3

IMPROVEMENTS OF 3D DDA BY INCORPORATING A DAMPED CONTACT MODEL FOR INELASTIC COLLISION [1]

3.1. INTRODUCTION

Energy dissipation is an important issue that must be solved when estimating collisions. Most collisions, in reality, are partially inelastic because there is always kinetic energy loss (transferred into plastic deformation, heat, and so on). In this research, the trajectory of boulders is highly affected by the collision behavior since multiple collisions may occur between boulders and terrain. The dynamic equation in conventional 3D DDA typically excludes damping terms for simplicity. The possibly existing damping effect is reflected by a so-called dynamic ratio (Fu, X. D. et al., 2015). It describes global energy dissipation by reducing the inherited velocities of blocks from the previous step. Such treatment is simple and effective for some damping situations such as air resistance but apparently is not suitable for the transient and local energy loss in collisions. On the other hand, DDA adopts a Newmark integration scheme with $\beta = 0.5$ and $\gamma = 1$ (Wang, C. et al., 1996), which

[1] Chapter 3 is based on the following journal papers:

Yu P, Chen G, Peng X, Guo L, Zhang Y (2019) Extension and application of Discontinuous Deformation Analysis with a damped contact spring model International Journal of Rock Mechanics and Mining Sciences 123 doi:10.1016/j.ijrmms.2019.104123

Yu P, Chen G, Peng X, Zhang Y, Zhang H (2020) Exploring inelastic collisions using modified three-dimensional discontinuous deformation analysis incorporating a damped contact model Computers and Geotechnics 121 doi:10.1016/j.compgeo.2020.103456

introduces an additional algorithmic or numerical damping (Doolin, D. M. et al., 2004). Under the condition of low damping, the numerical damping relates to the circular frequency and step size (Fu, X. D. et al., 2015), which is not appropriate to address the energy loss during collisions as well.

A damped contact model is a good solution to dissipate additional collisional energy. Although the viscous damping in contact has been established in DDA (Mortazavi, A. et al., 2001; Sasaki, T. et al., 2005; Yu, P. et al., 2019), detailed investigation of collision phenomenons is still desired. A predictable rebounding simulation will certainly benefit the parameter selections, which in turn increases the simulation precision. The control parameter of the damper, viscous damping coefficient, is derived from a given coefficient of restitution (COR). COR is a fundamental parameter to measure the collisions. It has been proven that a simple relationship between COR and viscous damping coefficient can be established if a linear spring-dashpot model is employed in contacts (Campbell, C. S., 2002; Schwager, T. et al., 2007). Therefore, 3D DDA is promising to accurately model the collision phenomenon by a calculated viscous damping coefficient with predefined COR, thus showing more realistic simulation results.

3.2. DAMPED CONTACT MODEL IN 3D DDA

The diagram in Figure 2.3 is borrowed here to illustrate the implementation of the damped contact model, in which the normal and shear contact force imposed on the contact point P_a is exerted by a spring and a viscous dashpot which is proportional to the relative velocity, as shown in Figure 2.5. In the normal entrance plane direction, the contact force $\boldsymbol{F}_n$ is given by

$$\boldsymbol{F}_n = -\left(k_n d_n^{'} + c_n v_{rn}\right)\boldsymbol{n} \tag{3.1}$$

where k_n and c_n are the normal spring stiffness and the normal viscous damping coefficient, respectively; $\boldsymbol{n}$ indicates the external unit normal of the entrance face and can be expressed as (n_x, n_y, n_z); v_{rn} is the normal relative velocity of P_a with respect to the contact point P_b and can be calculated by taking the dot product of $\boldsymbol{n}$ and the relative velocity ($\boldsymbol{v}_a$ - $\boldsymbol{v}_b$) (with $\boldsymbol{v}_a$ and $\boldsymbol{v}_b$ being the velocity vectors of P_a and

P_b at the start of the current time step, respectively). Based on the derivations given in equation (2.82) – (2.91) in Section 2.2.4.2, the contribution Π_n to the global potential energy is

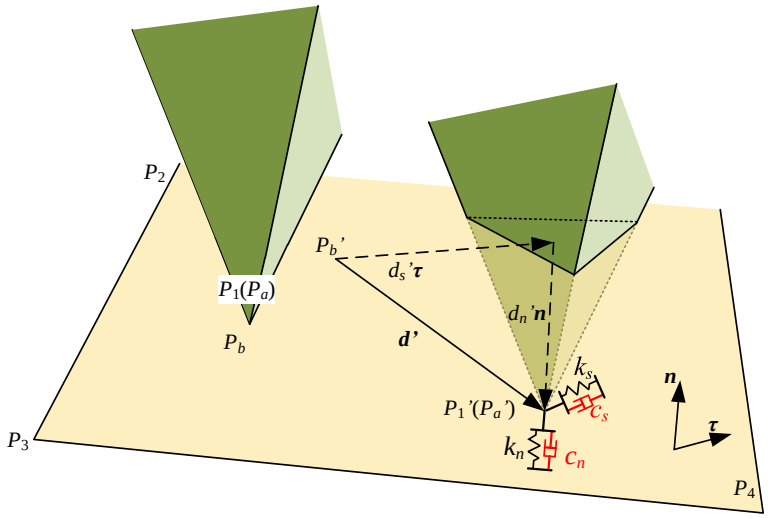

Figure 3.1 Schematic diagram of the damped contact model, in which contact springs and dampers are applied

$$\Pi_n = \frac{k_n}{2}(d_n')^2 + c_n v_{rn} \begin{bmatrix} u_a - u_b \\ v_a - v_b \\ w_a - w_b \end{bmatrix}^{\mathrm{T}} \boldsymbol{n}$$
$$= \frac{k_n}{2}(d_n + \boldsymbol{H}\boldsymbol{D}_i + \boldsymbol{G}\boldsymbol{D}_j)^2 + c_n v_{rn}\left(\boldsymbol{D}_i^{\mathrm{T}}\boldsymbol{T}_{i,p_a}^{\mathrm{T}} - \boldsymbol{D}_j^{\mathrm{T}}\boldsymbol{T}_{j,p_b}^{\mathrm{T}}\right)\boldsymbol{n} \tag{3.2}$$

with

$$\boldsymbol{H} = \frac{1}{A_0}\sum_{r=1}^{2}[L_{r2} \quad L_{r3} \quad L_{r4}]\boldsymbol{T}_{i,p_r} \tag{3.3}$$

$$\boldsymbol{G} = \frac{1}{A_0}\sum_{r=3}^{4}[L_{r2} \quad L_{r3} \quad L_{r4}]\boldsymbol{T}_{j,pr} \tag{3.4}$$

Taking derivatives of Π_n yields matrices that should be added to the global stiffness and force matrices:

$$k_n \boldsymbol{H}^{\mathrm{T}}\boldsymbol{H} \rightarrow \boldsymbol{K}_{ii} \tag{3.5}$$

$$k_n \boldsymbol{G}^{\mathrm{T}}\boldsymbol{G} \rightarrow \boldsymbol{K}_{jj} \tag{3.6}$$

$$k_n \boldsymbol{H}^{\mathrm{T}} \boldsymbol{G} \rightarrow \boldsymbol{K}_{ij} \tag{3.7}$$

$$k_n \boldsymbol{G}^{\mathrm{T}} \boldsymbol{H} \rightarrow \boldsymbol{K}_{ji} \tag{3.8}$$

$$-k_n d_n \boldsymbol{H}^{\mathrm{T}} - c_n v_{rn} \boldsymbol{T}_{i.p_a}^{\mathrm{T}} \boldsymbol{n} \rightarrow \boldsymbol{F}_i \tag{3.9}$$

$$-k_n d_n \boldsymbol{G}^{\mathrm{T}} + c_n v_{rn} \boldsymbol{T}_{j,p_b}^{\mathrm{T}} \boldsymbol{n} \rightarrow \boldsymbol{F}_j \tag{3.10}$$

For the shear direction, the shear force $\boldsymbol{F}_\tau$ imposed on the contact point P_a can be expressed as

$$\boldsymbol{F}_s = -\left(k_\tau d_\tau' + c_\tau v_{r\tau}\right)\boldsymbol{\tau} \tag{3.11}$$

where k_τ and c_τ are the shear spring stiffness and the shear viscous damping coefficient, respectively; $\boldsymbol{\tau}$ indicates the unit vector along the projection vector of the relative velocity ($\boldsymbol{v}_a$ - $\boldsymbol{v}_b$) with respect to the entrance face and can be written as (τ_x, τ_y, τ_z); $v_{r\tau}$ is the shear component of ($\boldsymbol{v}_a$ - $\boldsymbol{v}_b$), defined as the dot product of ($\boldsymbol{v}_a$ - $\boldsymbol{v}_b$) and $\boldsymbol{\tau}$. Based on the derivations given in equation (2.98) – (2.101) in Section 2.2.4.2, the contribution Π_τ to the global potential energy is

$$\begin{aligned}
\Pi_\tau &= \frac{k_\tau}{2}(d_\tau')^2 + c_\tau v_{r\tau} \begin{bmatrix} u_a - u_b \\ v_a - v_b \\ w_a - w_b \end{bmatrix}^{\mathrm{T}} \boldsymbol{\tau} \\
&= \frac{k_\tau}{2}\left(\begin{bmatrix} x_a - x_b \\ y_a - y_b \\ z_a - z_b \end{bmatrix}^{\mathrm{T}} \boldsymbol{N} \begin{bmatrix} x_a - x_b \\ y_a - y_b \\ z_a - z_b \end{bmatrix} + \begin{bmatrix} u_a - u_b \\ v_a - v_b \\ w_a - w_b \end{bmatrix}^{\mathrm{T}} \boldsymbol{N} \begin{bmatrix} u_a - u_b \\ v_a - v_b \\ w_a - w_b \end{bmatrix} \right) \\
&\quad + k_\tau \begin{bmatrix} u_a - u_b \\ v_a - v_b \\ w_a - w_b \end{bmatrix}^{\mathrm{T}} \boldsymbol{N} \begin{bmatrix} x_a - x_b \\ y_a - y_b \\ z_a - z_b \end{bmatrix} + c_\tau v_{r\tau} \begin{bmatrix} u_a - u_b \\ v_a - v_b \\ w_a - w_b \end{bmatrix}^{\mathrm{T}} \boldsymbol{\tau}
\end{aligned} \tag{3.12}$$

It is further expanded as

$$
\begin{aligned}
\Pi_\tau = & \frac{k_\tau}{2}\boldsymbol{D}_i^{\mathrm{T}}\boldsymbol{T}_{i,p_a}^{\mathrm{T}}\boldsymbol{N}\boldsymbol{T}_{i,p_a}\boldsymbol{D}_i + \frac{k_\tau}{2}\boldsymbol{D}_j^{\mathrm{T}}\boldsymbol{T}_{j,p_b}^{\mathrm{T}}\boldsymbol{N}\boldsymbol{T}_{j,p_b}\boldsymbol{D}_j \\
& -\frac{k_\tau}{2}\boldsymbol{D}_i^{\mathrm{T}}\boldsymbol{T}_{i,p_a}^{\mathrm{T}}\boldsymbol{N}\boldsymbol{T}_{j,p_b}\boldsymbol{D}_j - \frac{k_\tau}{2}\boldsymbol{D}_j^{\mathrm{T}}\boldsymbol{T}_{j,p_b}^{\mathrm{T}}\boldsymbol{N}\boldsymbol{T}_{i,p_a}\boldsymbol{D}_i \\
& +c_\tau v_{r\tau}\left(\boldsymbol{D}_i^{\mathrm{T}}\boldsymbol{T}_{i,p_a}^{\mathrm{T}} - \boldsymbol{D}_j^{\mathrm{T}}\boldsymbol{T}_{j,p_b}^{\mathrm{T}}\right)\boldsymbol{\tau}
\end{aligned} \tag{3.13}
$$

Taking derivatives of Π_τ yields matrices that should be added to the global stiffness and force matrices:

$$k_\tau \boldsymbol{T}_{i,p_a}^{\mathrm{T}}\boldsymbol{N}\boldsymbol{T}_{i,p_a} \rightarrow \boldsymbol{K}_{ii} \tag{3.14}$$

$$k_\tau \boldsymbol{T}_{j,p_b}^{\mathrm{T}}\boldsymbol{N}\boldsymbol{T}_{j,p_b} \rightarrow \boldsymbol{K}_{jj} \tag{3.15}$$

$$-k_\tau \boldsymbol{T}_{i,p_a}^{\mathrm{T}}\boldsymbol{N}\boldsymbol{T}_{j,p_b} \rightarrow \boldsymbol{K}_{ij} \tag{3.16}$$

$$-k_\tau \boldsymbol{T}_{j,p_b}^{\mathrm{T}}\boldsymbol{N}\boldsymbol{T}_{i,p_a} \rightarrow \boldsymbol{K}_{ji} \tag{3.17}$$

$$-k_\tau \boldsymbol{T}_{i,p_a}^{\mathrm{T}}\boldsymbol{N}\begin{bmatrix} x_a - x_b \\ y_a - y_b \\ z_a - z_b \end{bmatrix} - c_\tau v_{r\tau}\boldsymbol{T}_{i,p_a}^{\mathrm{T}}\boldsymbol{\tau} \rightarrow \boldsymbol{F}_i \tag{3.18}$$

$$k_\tau \boldsymbol{T}_{j,p_b}^{\mathrm{T}}\boldsymbol{N}\begin{bmatrix} x_a - x_b \\ y_a - y_b \\ z_a - z_b \end{bmatrix} + c_\tau v_{r\tau}\boldsymbol{T}_{j,p_b}^{\mathrm{T}}\boldsymbol{\tau} \rightarrow \boldsymbol{F}_j \tag{3.19}$$

The implementation of normal and shear dampers will also affect the frictions as well as the open-close criteria. When the state of a contact changes from locked to sliding, the shear contact spring is removed and replaced by a frictional force using the Coulomb friction law. In such a situation, the shear force $\boldsymbol{F}_s$ imposed on the contact point P_a can be expressed as

$$\boldsymbol{F}_\tau = -\left|\boldsymbol{F}_n\right|\tan\phi\boldsymbol{s} - c_\tau v_{r\tau}\boldsymbol{\tau} \tag{3.20}$$

where ϕ is the friction angle, $\boldsymbol{s}$ is the unit vector of relative shear displacement of P_a with respect to P_b calculated in the previous iteration step or time step. The potential energy of the shear forces between the contact point pair can be computed by

$$\Pi_\tau = |\boldsymbol{F}_n| \tan\phi \begin{bmatrix} u_a - u_b \\ v_a - v_b \\ w_a - w_b \end{bmatrix}^{\mathrm{T}} \boldsymbol{s} + c_\tau v_{r\tau} \begin{bmatrix} u_a - u_b \\ v_a - v_b \\ w_a - w_b \end{bmatrix}^{\mathrm{T}} \boldsymbol{\tau} \tag{3.21}$$

It is further expanded as

$$\Pi_\tau = |\boldsymbol{F}_n| \tan\phi \left(\boldsymbol{D}_i^{\mathrm{T}} \boldsymbol{T}_{i,p_a}^{\mathrm{T}} - \boldsymbol{D}_j^{\mathrm{T}} \boldsymbol{T}_{j,p_b}^{\mathrm{T}} \right) \boldsymbol{s} + c_\tau v_{r\tau} \left(\boldsymbol{D}_i^{\mathrm{T}} \boldsymbol{T}_{i,p_a}^{\mathrm{T}} - \boldsymbol{D}_j^{\mathrm{T}} \boldsymbol{T}_{j,p_b}^{\mathrm{T}} \right) \boldsymbol{\tau} \tag{3.22}$$

Taking derivatives of Π_f yields matrices that should be added to the global stiffness and force matrices:

$$-|\boldsymbol{F}_n| \tan\phi \boldsymbol{T}_{i,p_a}^{\mathrm{T}} \boldsymbol{s} - c_\tau v_{r\tau} \boldsymbol{T}_{i,p_a}^{\mathrm{T}} \boldsymbol{\tau} \rightarrow \boldsymbol{F}_i \tag{3.23}$$

$$|\boldsymbol{F}_n| \tan\phi \boldsymbol{T}_{j,p_b}^{\mathrm{T}} \boldsymbol{s} + c_\tau v_{r\tau} \boldsymbol{T}_{j,p_b}^{\mathrm{T}} \boldsymbol{\tau} \rightarrow \boldsymbol{F}_j \tag{3.24}$$

The flowchart of 3D DDA in Figure 3.2 shows the subroutines that are modified to incorporate the damped contact model (circled by red dash square).

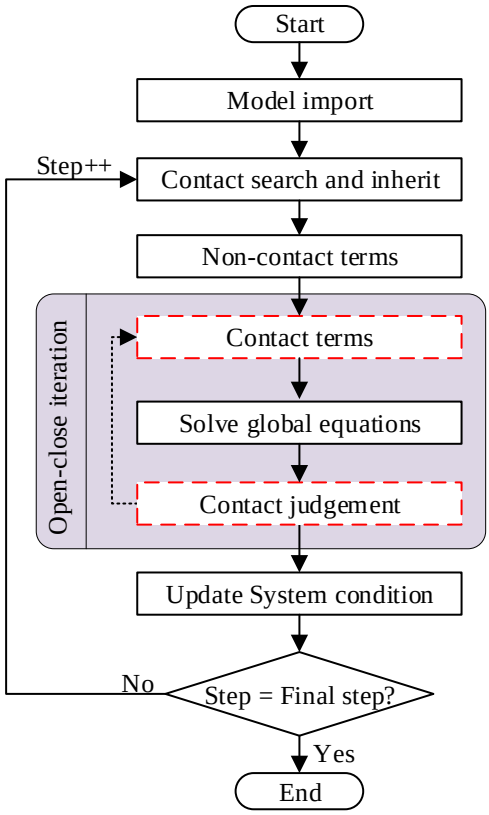

Figure 3.2 Flowchart of 3D DDA (Red dash square denotes the modified subroutines)

3.3. VALIDATION OF THE DAMPED CONTACT MODEL

The 2D validation has been elaborately studied in the previous work of the authors (Yu, P. et al., 2019). For brevity, only the damped Single-Degree-Of-Freedom (SDOF) system, as illustrated in Figure 3.3, is modelled by 3D DDA to validate the implementation of the damped contact model. The base block is fixed, and above which there is a vibrating block. The joint between the two blocks is sufficiently strong to hold them together. Since the two blocks are connected by the contact springs and dashpots, the system behaves as a damped SDOF system.

When the time-varying driving force takes the sinusoidal form as $F = p_0 \sin\omega_0 t$ (let ω_0 equals ω for simplicity), the dynamic response of the vibrating block is theoretically obtained as (Fu, X. et al., 2015; Yu, P. et al., 2019)

$$x(t) = \frac{p_0}{k}\frac{1}{2\xi}\left[e^{-\xi\omega t}\left(\cos(\omega_D\,\mathrm{t}) + \frac{\xi}{\sqrt{1-\xi^2}}\sin(\omega_D\,\mathrm{t})\right) - \cos(\omega_0 t)\right] \tag{3.25}$$

where $x(t)$ is the time-varying dynamic displacement, p_0 is the amplitude of the driving force, k is the stiffness of the SDOF system, m is the block mass, ξ is the total damping ratio, ω and ω_D are the undamped and damped angular frequencies, respectively ($\omega = \sqrt{k/m}$, $\omega_D = \omega\sqrt{1-\xi^2}$). In the modified 3D DDA incorporating the damped contact model, both numerical damping and viscous damping contribute to the energy dissipation. Denote ξ_n as numerical damping ratio and ξ_v as viscous damping ratio. The total damping ratio ξ can be expressed as

$$\xi = \xi_n + \xi_v \tag{3.26}$$

Previous literatures have discussed the approach to calculate ξ_n in low damping situation (Doolin, D. M. et al., 2004; Fu, X. D. et al., 2015), which reads

$$\xi_n = \frac{\ln(1+\frac{\Omega^2}{2})}{2\Omega} \tag{3.27}$$

where $\Omega = \omega\Delta t$ with Δt being the step size. In addition, the viscous damping ratio is calculated as

$$\xi_v = \frac{c}{2m\omega} \tag{3.28}$$

where c is the damping coefficient. When c, k and m are determined, one can compute the total damping ratio ξ and further obtain the dynamic response of the vibrating block.

On the other hand, the SDOF system is modelled by the modified 3D DDA. In order to illustrate the performances of the damped contact model in shear and normal contact directions, two driving forces F_1 and F_2 with the same magnitude $p_0\sin\omega_0 t$ (=1000sin20t N) but in shear and normal directions, are loaded separately, as shown in Case 1 and Case 2. The physical properties are: $k_n = k_\tau = 400$ kPa, c = 1980 N/(m/s) (100 kPa and 495 N/(m/s) in the modified 3D DDA due to being evenly divided by four contacts) and m = 1000 kg. The step size is 0.0001 s. Thus, ω = 20 rad/s, ω_D = 19.975 rad/s, and damping ratio ξ = 0.05. The simulation results in normal and shear directions are presented in Figure 3.4, together with the theoretical solution. Both the normal and shear displacement responses simulated by the modified 3D DDA demonstrate satisfactory agreement with the theoretical solution, which validates the successful implementation of the damped contact model.

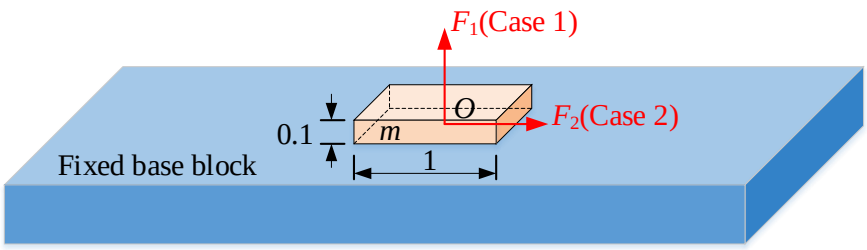

Figure 3.3 Schematic diagram of a damped SDOF system (unit: m)

3.4. Determination of viscous damping coefficient: block collision with an unconstrained target

When a normal collision occurs between two blocks, the energy dissipation can be measured by normal COR, defined as

$$e_i = \frac{v_{t,2} - v_{t,1}}{v_{0,1} - v_{0,2}} \tag{3.29}$$

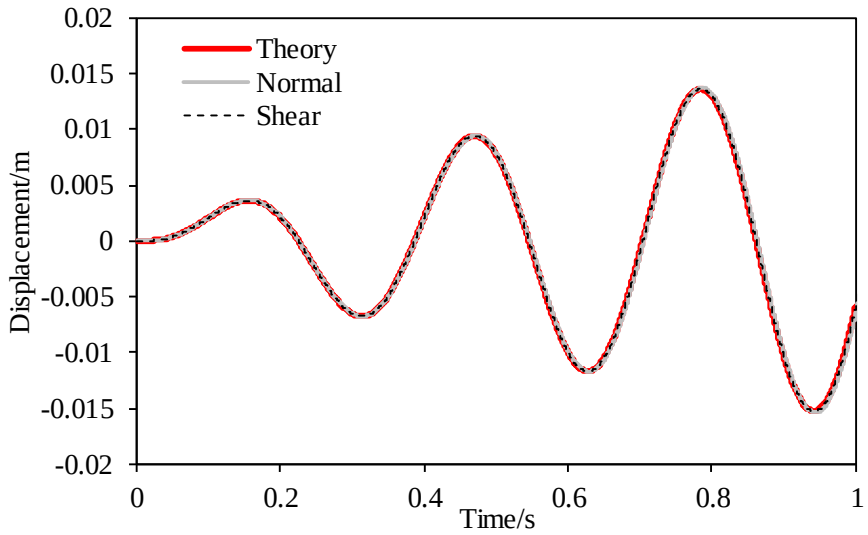

Figure 3.4 Comparison of simulated displacements in normal and shear vibrations and the theoretical solution

where e_i represents normal COR; v is the normal velocity; the subscripts 1 and 2 denote the two blocks in collision; and the subscripts 0 and t denote the velocities before and after collision, as shown in Figure 3.5. In this case, the velocity directions are perpendicular to the contact interface. Because of the energy dissipation, COR generally ranges from 0 (perfectly inelastic collision) to 1 (perfectly elastic collision). For brevity, the face-to-face collision studied here is a one-dimensional collision, with the moving directions of the two blocks parallel to the line connecting their gravity centers.

When the linear dashpot-spring contact model is adopted, COR can be derived directly from the relevant parameters, which makes other external factors such as impact velocity irrelevant to COR (Schafer, J. et al., 1996). Therefore, a simple deduction can be given to determine a proper damping coefficient for a given COR (Schafer, J. et al., 1996; Schwager, T. et al., 2007). It is assumed that the dissipated energy is consumed by the dashpots in contacts. The impact process can be described by a dynamic equation as

$$x_1 - x_2 = \frac{v_{0,1} - v_{0,2}}{\omega_D} \sin \omega_D t \cdot e^{-\xi \omega t}, \quad t \in [0, \frac{\pi}{\omega_D}] \tag{3.30}$$

with

$$\omega = \sqrt{\frac{k(m_1 + m_2)}{m_1 m_2}}, \xi = \frac{c}{2}\sqrt{\frac{m_1 + m_2}{k m_1 m_2}} \tag{3.31}$$

where x is the displacement, m_1 and m_2 are the masses of block 1 and 2, respectively. The motions of blocks during a collision are available by calculating the impact process with initial condition $x = 0$ and initial velocity v_0. By taking derivative of equation (3.30), the relative velocity $v_1 - v_2$ ($0 \leqslant t \leqslant \pi/\omega_D$) can be derived as

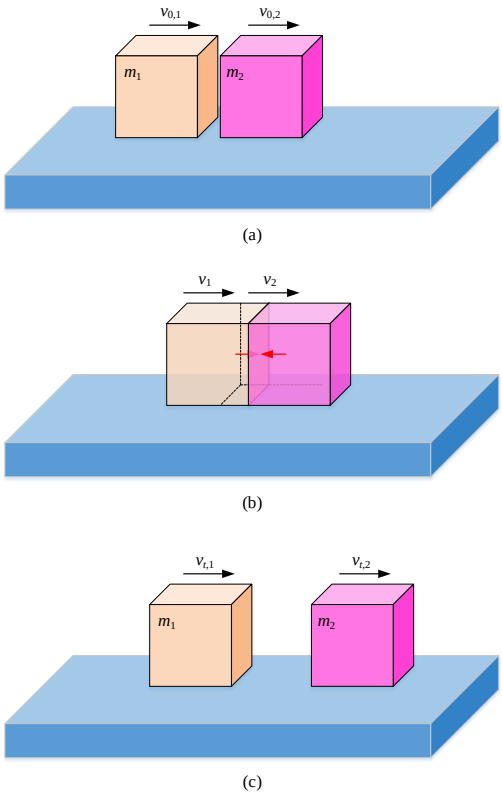

Figure 3.5 Motions of block 1 (m_1) and block 2 (m_2) (a) before (b) during and (c) after collision

$$v_1 - v_2 = (v_{0,1} - v_{0,2})e^{-\xi\omega t}(\cos\omega_D t - \xi\frac{\omega}{\omega_D}\sin\omega_D t) \tag{3.32}$$

Let $t = \pi/\omega_D$, the post-collisional relative velocity $v_{t,1} - v_{t,2}$ is then calculated by

$$v_{t,1} - v_{t,2} = -(v_{0,1} - v_{0,2})e^{-\xi\pi\omega/\omega_D} \tag{3.33}$$

Rearranging equation (3.33) and introducing equation (3.29), the relationship between COR and ξ is derived as

$$e_i = e^{-\pi\xi/\sqrt{1-\xi^2}} \tag{3.34}$$

or

$$\xi = -\frac{\ln e_i}{\sqrt{\ln^2 e_i + \pi^2}} \tag{3.35}$$

This result is consistent with previous studies in collisional damping between spherical particles (Campbell, C. S., 2002; Caserta, A. J. et al., 2016; Schwager, T. et al., 2007). Because the damping in DDA comes from two sources: numerical damping and the introduced viscous damping, the numerical damping contribution should be removed from the total one to obtain the viscous damping coefficient:

$$c = 2(\xi - \xi_n)\sqrt{\frac{m_1 m_2}{m_1 + m_2}k} = 2(-\frac{\ln e_i}{\sqrt{\ln^2 e_i + \pi^2}} - \frac{\ln(1+\Omega^2/2)}{2\Omega})\sqrt{\frac{m_1 m_2}{m_1 + m_2}k} \tag{3.36}$$

Theoretically, the post-collisional velocities can be solved using the momentum conservation equation

$$m_1 v_{0,1} + m_2 v_{0,2} = m_1 v_{t,1} + m_2 v_{t,2} \tag{3.37}$$

Substituting equation (3.29) into equation (3.37), one can have

$$\begin{cases} v_{t,1} = \dfrac{(m_1 - e_i m_2)v_{0,1} + (1+e_i)m_2 v_{0,2}}{m_1 + m_2} \\ v_{t,2} = \dfrac{(1+e_i)m_1 v_{0,1} + (m_2 - e_i m_1)v_{0,2}}{m_1 + m_2} \end{cases} \tag{3.38}$$

Especially, when $m_1 = m_2 = m$, equations (3.36) and (3.38) reduce to

$$c = (-\frac{\ln e_i}{\sqrt{\ln^2 e_i + \pi^2}} - \frac{\ln(1+\Omega^2/2)}{2\Omega})\sqrt{2mk} \tag{3.39}$$

$$\begin{cases} v_{t,1} = \dfrac{(1-e_i)v_{0,1} + (1+e_i)v_{0,2}}{2} \\ v_{t,2} = \dfrac{(1+e_i)v_{0,1} + (1-e_i)v_{0,2}}{2} \end{cases} \tag{3.40}$$

Note that in the above derivations, ξ, Ω, ω_D and ω are parameters in a transient dynamic system which is formed during a collision.

The collision case is also investigated using the modified 3D DDA. The constructed 3D DDA model is shown in Figure 3.6, which consists of a moving block with mass m_1 and a stationary target block with mass m_2 (m_1: m_2=1:1). The blocks are both cubic with edge length 1 m. The initial velocity of block 1 is 1 m/s. The relevant physical properties are: density 1000 kg/m^3, Young's modulus 100 GPa and Poisson's ratio 0.2. The control parameters are: step size 0.0001 s, maximum displacement ratio 0.05 and contact spring stiffness 0.1 MPa. The high Young's modulus can keep the block rigid during collisions. The selected contact spring stiffness is much lower than Young's modulus because low contact spring stiffness can keep a small numerical damping ratio. If the numerical damping is not small enough, the discussion under low damping condition cannot be involved. Equation (3.39) is adopted to determine the corresponding viscous damping coefficient in the simulation. For focusing on the study of collision behavior, external actions such as gravity are not considered. To show the performance of the adopted damped contact model, different values of COR representing various inelastic collisions, ranging from 0.1 to 0.9, are selected. Note that the COR cannot be 1 because of the existence of numerical damping (Ohnishi, Y. et al., 2006). The corresponding viscous damping coefficients are thus derived from equation (3.39), listed in Table 3.1.

The simulated velocities under different values of COR are illustrated in Figure 3.7(a), together with the analytical solutions. The relative errors are presented in Figure 3.7 (b). The relative error is defined by

$$r = \left| \frac{Value_s - Value_a}{Value_a} \right| \tag{3.41}$$

where $Value_s$ and $Value_a$ respectively denote the simulated and analytical results.

Figure 3.7 suggests that the post-collisional velocities of both blocks evolve linearly with the increase of COR, and they converge to the analytical solutions, with the maximum relative error less than 0.3%. The relative error for Block 1 increases with the increasing COR but the opposite situation occurs for Block 2. By analyzing the absolute error, it is found that the difference between relative errors

of the two blocks mainly results from the post-collisional velocity magnitude ($v_{t,1}$ drops and $v_{t,2}$ increases as COR increases), which serves as a denominator in equation (3.41).

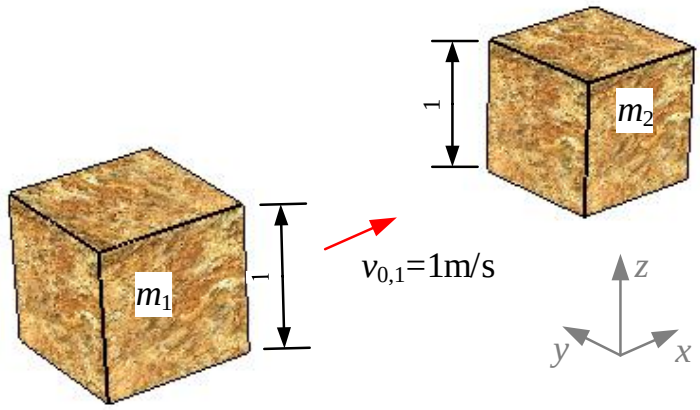

Figure 3.6 3D DDA model of a block colliding with an unconstrained target block (unit: m)

Table 3.1 Calculated viscous damping ratios and coefficients used in 3D DDA model

COR	Block mass ratio 1:1		Block mass ratio 1:3	
	ξ_v	c_{DDA} (= c/4, N/(m/s))	ξ_v	c_{DDA} (= c/4, N/(m/s))
0.1	0.590448	4175.097	0.590578	5114.553
0.2	0.455243	3219.052	0.455372	3943.641
0.3	0.35715	2525.432	0.35728	3094.134
0.4	0.279291	1974.885	0.279421	2419.854
0.5	0.214747	1518.488	0.214876	1860.884
0.6	0.159786	1129.857	0.159916	1384.911
0.7	0.112101	792.6762	0.112231	971.9498
0.8	0.070143	495.9873	0.070273	608.5816
0.9	0.032811	232.0112	0.032941	285.2783

Moreover, the collision time durations obtained by both the analytical solution and 3D DDA simulation are also provided in Figure 3.8. The collision time duration t_{col} is analytically given by

$$t_{col} = \frac{\pi}{\omega_D} = \sqrt{\frac{m(\ln^2 e_i + \pi^2)}{2k}} \tag{3.42}$$

The simulated collision time durations match well with the analytical results, and higher COR leads to shorter duration. The relative error is smaller than 0.1 %.

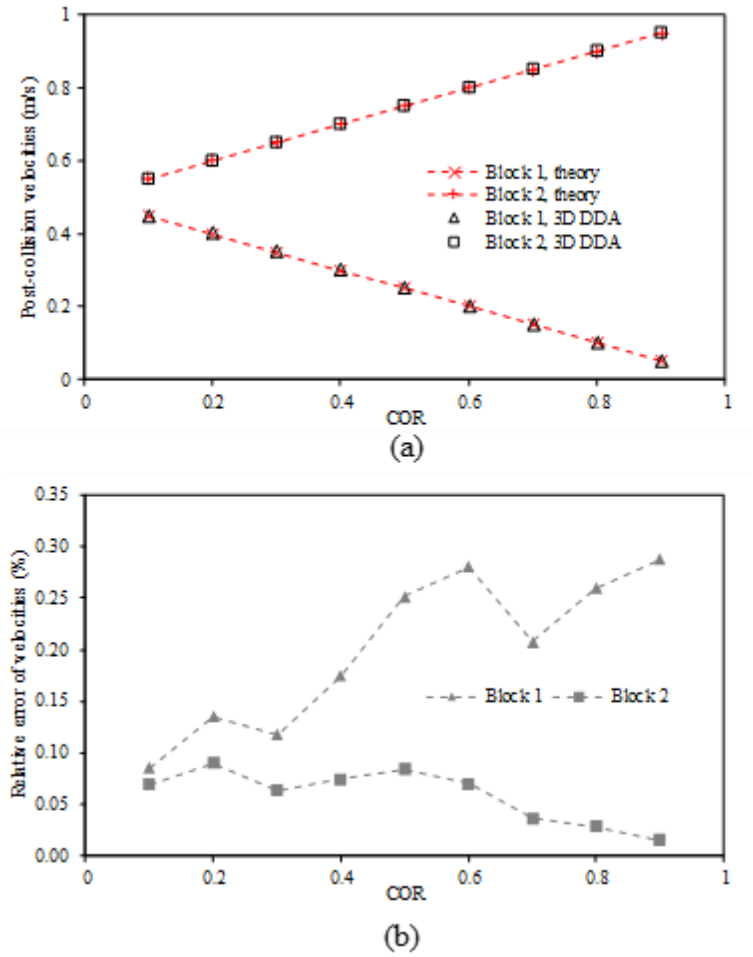

Figure 3.7 (a) Results of post-collisional velocities from 3D DDA simulation and analytical solution and (b) relative error (m_1: m_2=1:1)

To further test the robustness of the adopted damped contact model under different collision conditions, another model with a block mass ratio 1:3 is also explored by changing the density of Block 2 to 3000 kg/m^3. The viscous damping coefficients are also listed in Table 3.1. The results are given in Figure 3.9 and Figure 3.10. The changing of the block mass ratio does not compromise the simulation accuracy. However, the relative error illustrated in Figure 3.9 (b) seems to be higher compared to Figure 3.7 (b). It is due to the small velocity (0.025 m/s)

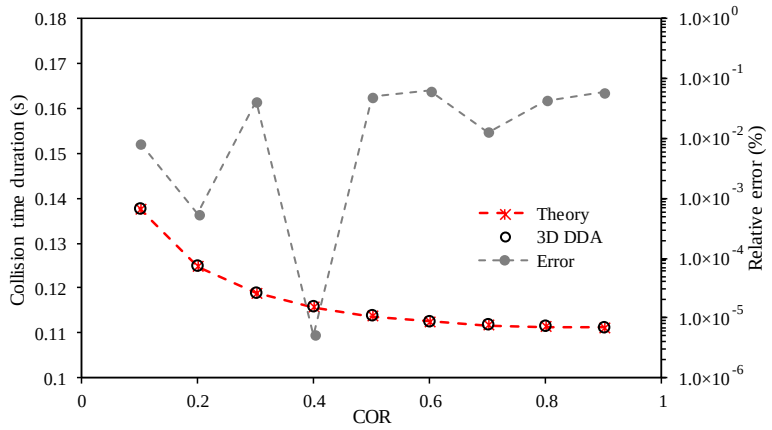

Figure 3.8 Collision time duration obtained from 3D DDA simulation and analytical solution and the relative error (m_1: m_2=1:1)

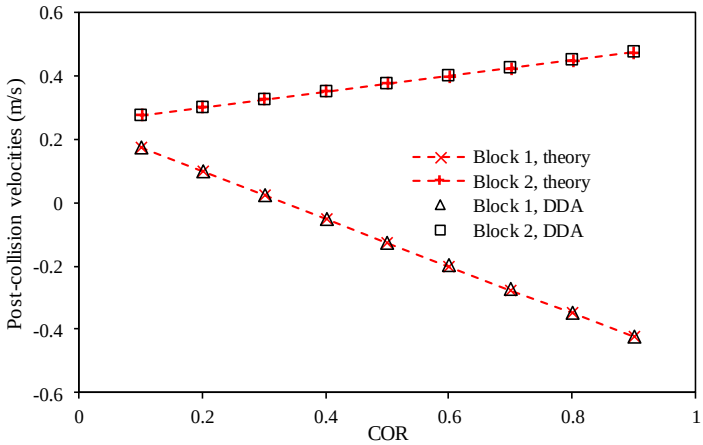

(a)

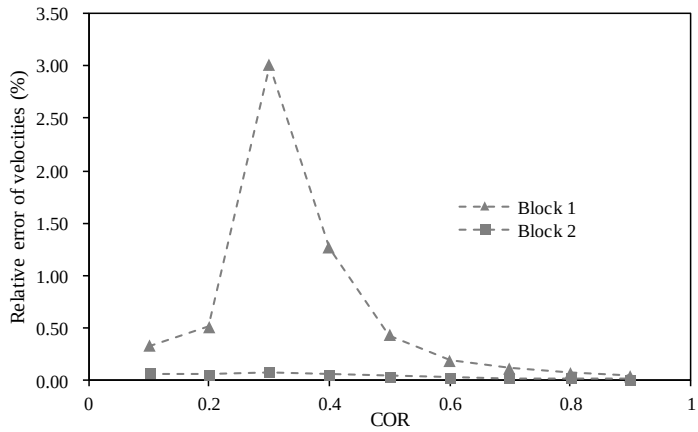

(b)

Figure 3.9 Results of post-collisional velocities from 3D DDA simulation and analytical solution and (b) relative error (m_1: m_2 = 1:3)

of Block 1 at COR of 0.3. Although it still decreases with the growth of COR, the collision time seems to be extended when the mass of Block 2 increases.

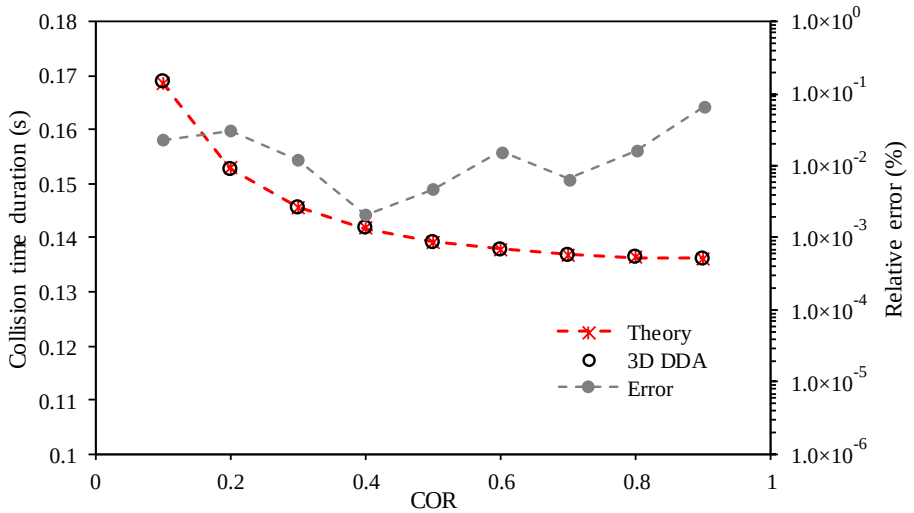

Figure 3.10 Collision time duration obtained from 3D DDA simulation and analytical solution and the relative error (m_1: m_2 = 1:3)

3.5. Determination of viscous damping coefficient: block collision with a fixed target

In view of mathematics, collision with a fixed block is the ultimate state of the collision with an unconstrained block that has a significantly large mass. When $v_{0,2} = 0$ and $m_2 \to \infty$, it can be derived from equation (3.37) that $v_{t,2} \to 0$. Thus, the definition of COR is simplified as

$$e_i = -\frac{v_{t,1}}{v_{0,1}} \tag{3.43}$$

Similarly, the viscous damping coefficient can be obtained as (let $m_1 = m$)

$$c = 2\left(-\frac{\ln e_i}{\sqrt{\ln^2 e_i + \pi^2}} - \frac{\ln(1+\Omega^2/2)}{2\Omega}\right)\sqrt{mk} \tag{3.44}$$

For a specific COR, the post-collisional velocity is analytically calculated from equation (3.43). A 3D DDA model is constructed as shown in Figure 3.11. The small cubic block 1 moves towards the fixed target block 2 and then rebounds. The physical properties and control parameters used in previous examples are adopted.

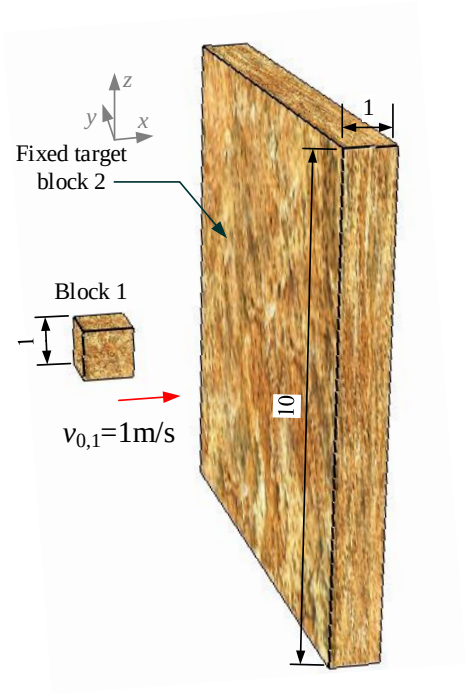

Figure 3.11 3D DDA model of a block colliding with a fixed target block (unit: m)

The post-collisional velocities are calculated and illustrated in Figure 3.12. The predicted velocities are in coincidence with the analytical results. The maximum relative error occurs at the COR that makes the rebounding velocity minimum. The collision time duration is presented in Figure 3.13, showing good agreement between the simulated results and the analytical one. Although the simulated collision time durations are slightly longer than the theoretical results, the relative error drops as COR grows.

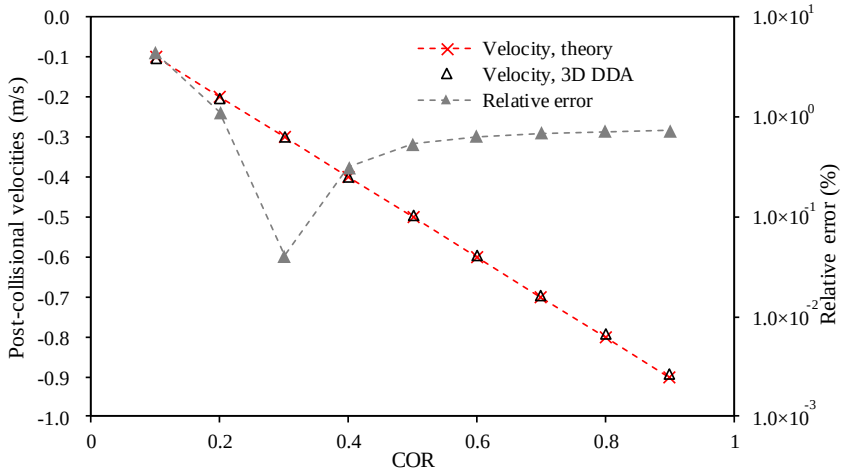

Figure 3.12 Results of post-collisional velocities and relative error

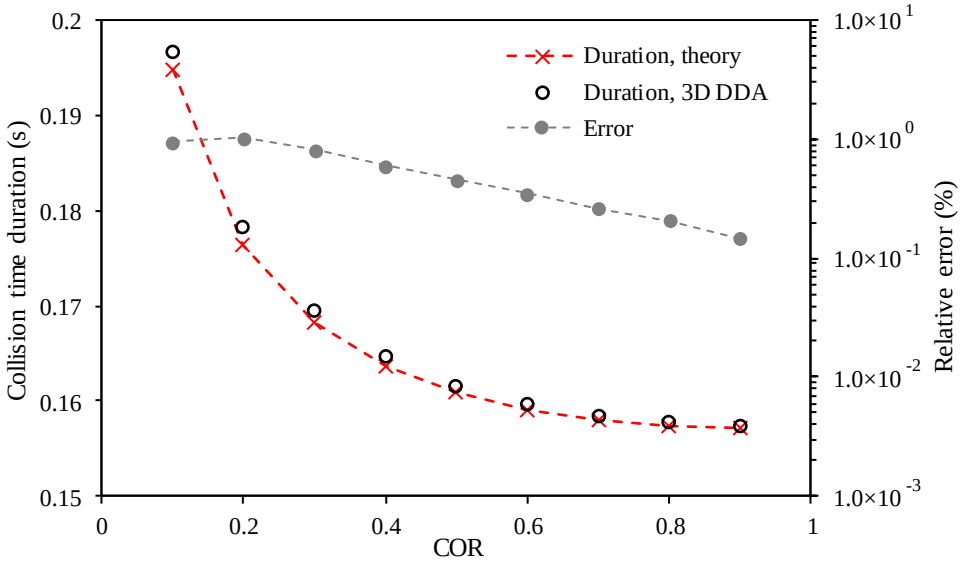

Figure 3.13 Collision time duration and the relative error

3.6. APPLICATION TO BLOCKS ASSEMBLY FREEFALL AND REBOUND

The discussions in sections 3.4 and 3.5 focus on the investigation of detailed behavior for a single block collision. To extend the application of the implemented damped contact model to a more complicated dynamic system that involves multiple block collisions, another example is explored as shown in Figure 3.4. The falling object, with dimensions 2.5 m × 2.5 m × 2.5 m, consists of 125 small blocks (0.5 m × 0.5 m × 0.5 m). These blocks are initially suspended 2.5 m above the fixed base block. When the simulation starts, the blocks will fall driven by gravity and rebound after collision with the base block. The physical properties used in the simulation are: gravitational acceleration 9.8 m/s^2, density 2500 kg/m^3, Young's modulus 100 GPa and Poisson's ratio 0.2. All the joints involved in the model are: frictional angle 45°, cohesion 10 MPa and tensile 0. The control parameters adopted are: maximum step size 0.0005 s, maximum displacement ratio 0.01 and contact spring stiffness 10 GPa. A large Young's modulus is selected in this example for eliminating the influence of block deformation involved in rigid blocks. The selection of contact spring stiffness is based on the range suggested by Shi, G. (1989) and Wu, J. (2003).

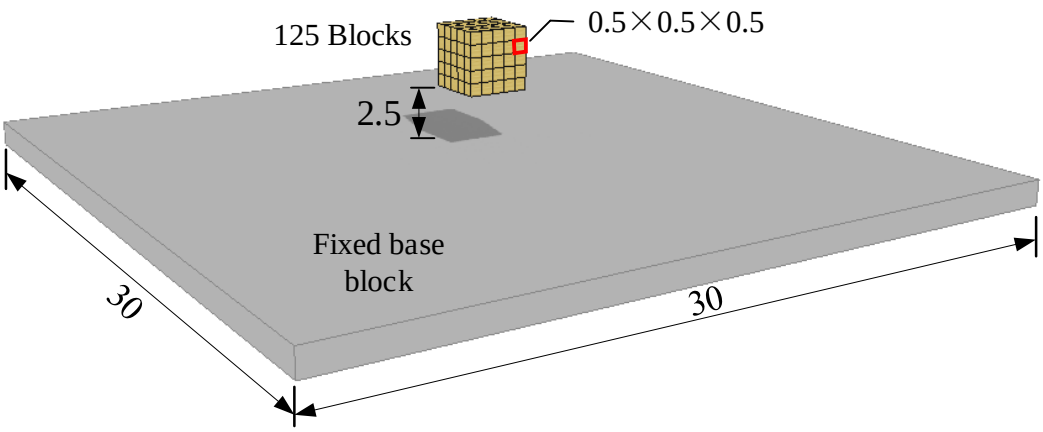

Figure 3.14 Schematic diagram of the blocks freefall and rebound model (unit: m)

The problem is simulated under the condition of nearly elastic (case 1: c = 0) and inelastic (case 2: c = 30000 N/(m/s)), and the simulation snapshots are presented in Figure 3.15. The freefall blocks show identical motions in two cases at the beginning due to the absence of collision and first touch the base block at t = 0.714 s. After 0.714 s, the blocks in two cases behave differently. The blocks then rebound and reach the highest at about t = 1.5 s. The blocks rebound much lower in the inelastic case 2 (4.54 m versus 6.41 m as marked in Figure 3.15). In other words, the upper three levels of blocks jump up in the midair and rebound evidently higher if viscous damping is not involved. In addition, the blocks in the inelastic case 2 exhibit smaller horizontal displacements. The horizontal motion arises from the non-zero Poisson's ratio, which allows the growth of the horizontal strains due to the vertical impact, thereby causing penetrations in horizontal direction. Although these horizontal strains are small and transient, horizontal motions can still be recognizable because (1) the contact spring force is highly sensitive to penetration, and (2) there is no constrain on blocks in horizontal direction. Simulations have also been conducted under the condition of zero Poisson's ratio and the horizontal expansion gets restrained. When t approaches about 2.0 s and 2.5 s, the blocks fall back to the base. This example demonstrates the effect of viscous damping in multiple block collisions, showing that it should be properly addressed to ensure more accurate descriptions of dynamic behaviors such as rockfall predictions.

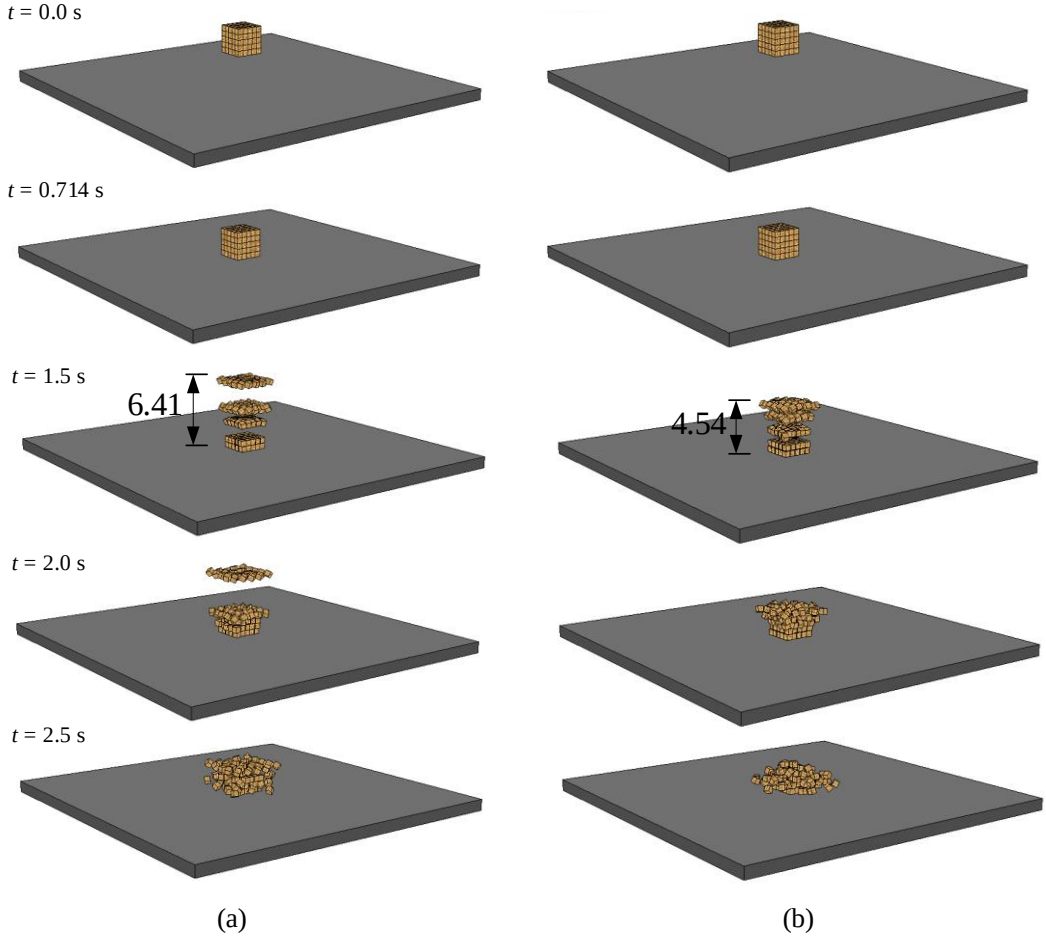

Figure 3.15 Blocks freefall and rebound modelled by 3D DDA (a) case 1: $c = 0$ and (b) case 2: c = 30000 N/(m/s) (unit: m)

3.7. CONCLUSIONS

In this paper, a damped contact model is incorporated into 3D DDA, and the modified 3D DDA is applied to estimate the partially inelastic collisions. A damped SDOF system is studied to validate the implemented damped contact model both in normal and shear directions. Subsequently, the modified 3D DDA is applied to block collision simulations. A relationship between COR and c is established in partially inelastic collisions so that the viscous damping can accurately absorb the dissipated kinetic energy, providing plausible and consistent simulation results. In the examples of block collision with unconstrained and fixed targets, the post-collisional velocities and collision time duration yielded from 3D DDA simulations show perfect agreement with those calculated theoretically.

High accuracy is observed in the single block collision examples. However, the error in the case of a collision with a fixed target (Figure 3.12 and Figure 3.13) seems to be higher compared to the collision with an unconstrained target. It possibly results from the fixed points defined to lock the target block because they are not absolutely "fixed". In 3D DDA, fixed points are reinforced by stiff springs, which means the fixed block can also slightly move during collisions. Such small motion is usually negligible, but it is still reflected in the error analysis. Detailed discussion on fixed points is not presented in this paper, and the interested reader can refer to literatures (Doolin, D. M., 2005; Wu, J.-H. et al., 2017; Yeung, M.-C. R., 1991). One may speculate that the error will be reduced once the motion of the fixed block reduces. It is tested by an example in which the mass of the fixed block is greatly increased (1000 times) so that the velocity of the fixed target block is much smaller. The results are given in Figure 3.16 and Figure 3.17. Both the errors of post-collisional velocity and collision time duration are significantly reduced by one to two orders of magnitude compared to Figure 3.12 and Figure 3.13.

A multiple blocks freefall and collision example is also successfully modelled by the modified 3D DDA. The results imply that viscous damping has an important influence on dynamic behaviors of the collision process, thus enabling the necessity of being properly addressed to approach reality. However, it is not easy to explicitly determine a global damping coefficient for a complicated system. An alternative approach is to evaluate an average COR for the target blocks. The two-block model provided in Section 3.4 is then utilized to calculate a damping coefficient because the dynamic characteristics for the entire model is complex. If the numerical damping ratio is hard to obtain, a small step size is recommended to reduce the numerical damping ratio. If permitted, the COR should be evaluated by experiments. The tested blocks should be of the similar material, size and shape with those involved in simulations (Durda, D. D. et al., 2011; Hastie, D. B., 2013; Leconte, M. et al., 2006; Lifshitz, J. M. et al., 1964). Alternatively, a scaling can be adopted for evaluating COR of large blocks (Asteriou, P. et al., 2013; Asteriou, P. et al., 2015). For preliminary simulations, it is also acceptable to evaluate the COR empirically by the shape and degree of elasticity of the block. The relevant researches for

modelling the dynamic response of complex systems can be conducted in the future work.

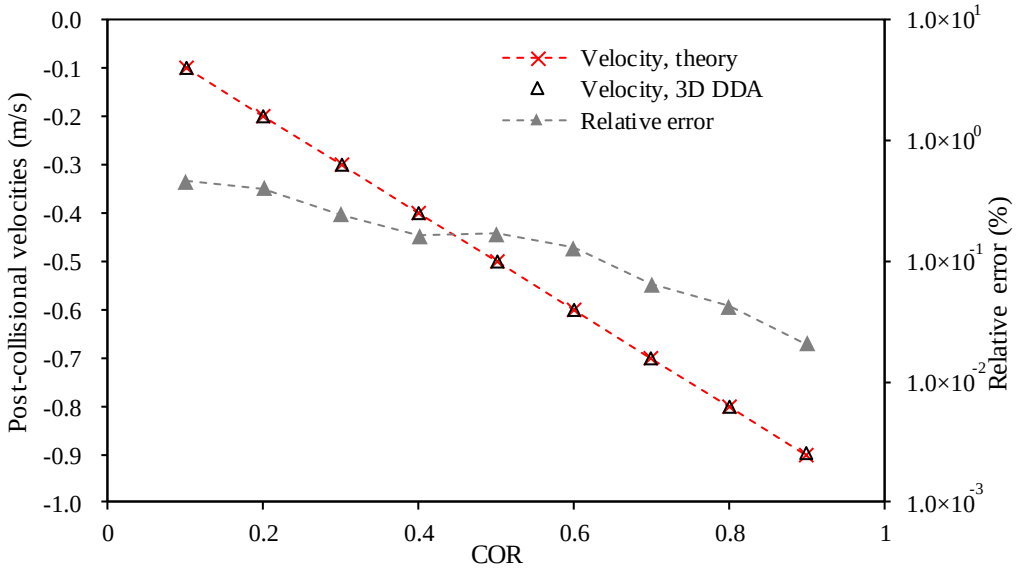

Figure 3.16 Results of post-collisional velocities and relative error when the mass of the fixed block is increased by 1000 times

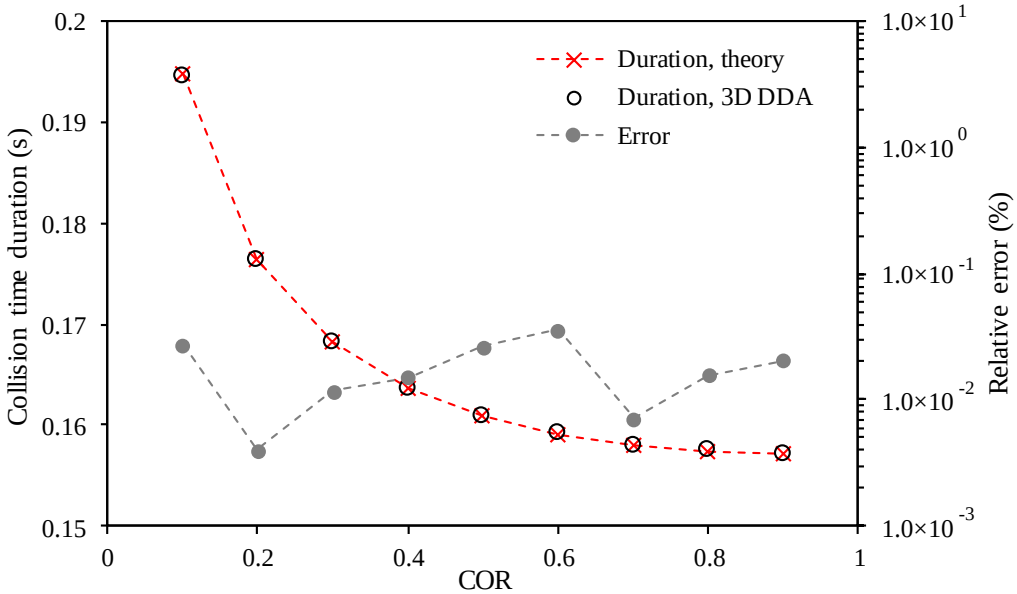

Figure 3.17 Collision time duration and the relative error when the mass of the fixed block is increased by 1000 times

REFERENCE

Asteriou, P., Saroglou, H., & Tsiambaos, G. (2013). Rockfall: Scaling factors for the Coefficient of Restitution. Rock Mechanics for Resources, Energy and Environment, 195-200.

Asteriou, P., & Tsiambaos, G. (2015). Empirical model for predicting rockfall trajectory direction. Rock Mechanics and Rock Engineering, 49(3), 927-941.

Campbell, C. S. (2002). Granular shear flows at the elastic limit. Journal of Fluid Mechanics, 465, 261-291.

Caserta, A. J., Navarro, H. A., & Cabezas-Gómez, L. (2016). Damping coefficient and contact duration relations for continuous nonlinear spring-dashpot contact model in DEM. Powder Technology, 302, 462-479.

Doolin, D. M. (2005). Unified displacement boundary constraint formulation for discontinuous deformation analysis (DDA). International Journal for Numerical and Analytical Methods in Geomechanics, 29(12), 1199-1207.

Doolin, D. M., & Sitar, N. (2004). Time integration in discontinuous deformation analysis. Journal of Engineering Mechanics, 130(3), 249-258.

Durda, D. D., Movshovitz, N., Richardson, D. C., Asphaug, E., Morgan, A., Rawlings, A. R., & Vest, C. (2011). Experimental determination of the coefficient of restitution for meter-scale granite spheres. Icarus, 211(1), 849-855.

Fu, X., Sheng, Q., & Zhang, Y. (2015). Damping problem in discontinuous deformation analysis method. Rock and Soil Mechanics, 36(7), 2057-2062. (In Chinese).

Fu, X. D., Sheng, Q., Zhang, Y. H., & Chen, J. (2015). Application of the discontinuous deformation analysis method to stress wave propagation through a one-dimensional rock mass. International Journal of Rock Mechanics and Mining Sciences, 80, 155-170.

Hastie, D. B. (2013). Experimental measurement of the coefficient of restitution of irregular shaped particles impacting on horizontal surfaces. Chemical Engineering Science, 101, 828-836.

Leconte, M., Garrabos, Y., Palencia, F., Lecoutre, C., Evesque, P., & Beysens, D. (2006). Inelastic ball-plane impact: An accurate way to measure the normal restitution coefficient. Applied Physics Letters, 89(24).

Lifshitz, J. M., & Kolsky, H. (1964). Some experiments on anelastic rebound. Journal of the Mechanics and Physics of Solids, 12(1), 35-43.

Mortazavi, A., & Katsabanis, P. D. (2001). Modelling burden size and strata dip effects on the surface blasting process. International Journal of Rock Mechanics and Mining Sciences, 38(4), 481-498.

Ohnishi, Y., Nishiyama, S., & Sasaki, T. (2006). Development and application of discontinuous deformation analysis. Rock Mechanics in Underground Construction, 59-70.

Sasaki, T., Hagiwara, I., Sasaki, K., Horikawa, S., Ohnishi, Y., Nishiyama, S., & Yoshinaka, R. (2005). Earthquake response analysis of a rock-fall by discontinuous deformation analysis. Paper presented at the ICADD-7, Honolulu, Hawaii.

Schafer, J., Dippel, S., & Wolf, D. E. (1996). Force schemes in simulations of granular materials. Journal De Physique I, 6(1), 5-20.

Schwager, T., & Pöschel, T. (2007). Coefficient of restitution and linear–dashpot model revisited. Granular Matter, 9(6), 465-469.

Shi, G. (1989). Discontinuous deformation analysis a new numerical model for the static and dynamics of block systems. (Ph.D.). UC Berkeley, USA.

Wang, C., Chuang, C., & Sheng, J. (1996). Time integration theories for the DDA method with finite element meshes. Paper presented at the Proceedings of 1st Int. Forum on Discontinuous Deformation Analysis (DDA) and Simulations of Discontinuous Media.

Wu, J.-H., Do, T. N., Chen, C.-H., & Wang, G. (2017). New geometric restriction for the displacement–constraint points in discontinuous deformation analysis. International Journal of Geomechanics, 17(5).

Wu, J. (2003). Numerical analysis of discontinuous rock masses using discontinuous deformation analysis. (Ph.D.). Kyoto University.

Yeung, M.-C. R. (1991). Application of Shi's discontinuous deformation analysis to the study of rock behavior. (Ph.D.). University of California, Berkeley.

Yu, P., Chen, G., Peng, X., Guo, L., & Zhang, Y. (2019). Extension and application of Discontinuous Deformation Analysis with a damped contact spring model. International Journal of Rock Mechanics and Mining Sciences, 123.

CHAPTER 4

DEVELOPMENT OF A FLUID-SOLID COUPLING METHOD 3D DDA-DFS FOR SIMULATING BOULDER DEBRIS FLOWS

4.1. INTRODUCTION

Given the complex nature of the coupled problem involving solid and fluid (shown in Figure 4.1), numerical simulation is regarded as a powerful tool to capture the developing process and interaction mechanism. Several approaches have been employed to simulate the fluid phase in a coupled system, such as Finite Element Method (FEM) (Kaidi, S. et al., 2012) and Smoothed Particle Hydrodynamics (SPH) (Mikola, R. et al., 2013; Wang, W. et al., 2016; Wang, W. et al., 2017).

In research area of debris flow, a theoretical fluid method is generally adopted in which the flow is considered as depth-integrated, thus transforming a 3D flow to 2D. Such flow form is commonly used in numerical simulation for debris flow (Gao, L. et al., 2017; Han, Z. et al., 2015; Han, Z. et al., 2014; Shen, W. et al., 2018). In this approach, the fluid model is defined upon a meshed terrain. The terrain can be hypothetical, or a real observation extracted from Digital Elevation Model database. In each terrain grid cell, the physical condition of fluid is determined by density, velocities and flow depth. This solution is based on a two-phase flow model which regarding the solid phase as a volume concentration, as mentioned in the previous sections. However, in many practical debris flow cases, there are many

large boulders and driftwoods. Those objects have the potential to pose huge damage to the protective structures such as check dams. Apparently, pure debris flow cannot consider the large objects. Therefore, it is important to introduce the solid phase into current debris flow simulation.

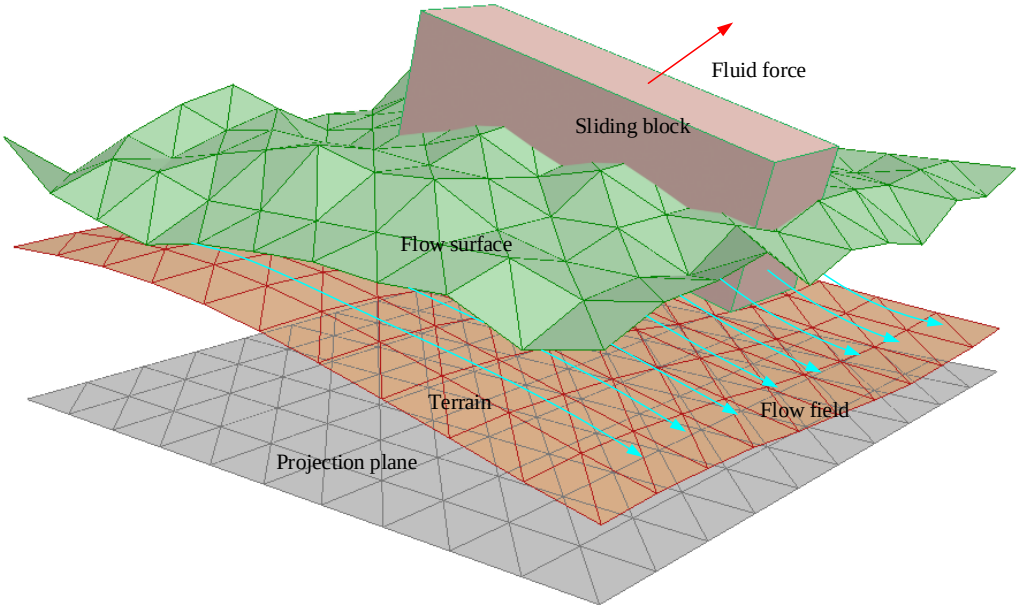

Figure 4.1 Schematic illustration of the boulders in debris flow

Discontinuous deformation analysis (DDA) (Shi, G., 1989) is a powerful method for analyzing the movement of discrete systems with large element displacement, it is adopted to calculate the solid phase motions under flow actions. DDA studies discrete or blocky systems containing discontinuities, such as a slope with joints (Zhang, Y. et al., 2014), a masonry building (Li, Z. J. et al., 2018), or rockfalls (Chen, G. Q. et al., 2013). The wide applications cover landslide (Ma, G. C. et al., 2010; Wu, J. H. et al., 2011; Zhang, Y. et al., 2013; Zhang, Y. et al., 2015; Zhang, Y. B. et al., 2015), rockfall (Ma, G. C. et al., 2008; Wu, J.-H. et al., 2005; Zheng, L. et al., 2011) and other areas (Guo, L. et al., 2019; Wu, J. H. et al., 2004). Extensions and modification are also integrated into DDA to overcome the limitations (Doolin, D. M., 2005; Fu, X. D. et al., 2015; Peng, X. et al., 2019b; Peng, X. et al., 2018; Yu, P. et al., 2019; Zhang, Y. B. et al., 2015) or improve the accuracy (Bao, H. R. et al., 2012; Ma, S. Q. et al., 2017; Wang, L.-Z. et al., 2013).

Computational efficiency is also an important aspect of extensive applications of DDA. Researchers tried to improve calculation speed by refining contact search algorithm (Hopkins, M. A., 2014; Wang, X. et al., 2019) or implementing parallel technology (Jiao, Y.-Y. et al., 2019; Peng, X. et al., 2019a). However, current three-dimensional DDA (3D DDA) only deals with solid blocks, and the fluid phase cannot be considered yet.

Based on the introductions of solid and fluid phase, a debris flow simulation method incorporating 3D DDA (3D DDA-DFS) is proposed in this paper. The interaction between solid and fluid is passed by interactive forces, which include buoyancy, drag force and static pressure. An algorithm is proposed to calculate buoyancy for blocks of arbitrary shape in the condition of uneven fluid surfaces. The drag forces on blocks are derived by a simplified formulation related to the local velocity of the blocks and then implemented facet by facet. The static pressure is also applied if the block is not entirely surrounded by flow. In addition, the drag effect between adjacent blocks is addressed so that the calculated drag force is more realistic. An equivalent solution is also proposed by taking the action of blocks on flow as time-varying elevation of terrain node since the direct evaluation of forces on debris flow by blocks is difficult. Finally, the coupling scheme as well as the calculations of the interaction forces are validated by a number of examples.

4.2. Framework for flow-solid interaction used in 3D DDA-DFS

An appropriate interactive framework is fundamental for the coupled 3D DDA-DFS method. It should be able to simultaneously solve the problems of: (1) large solid displacement; (2) debris flow evolution on complex terrain and (3) the real time interactions between solid and flow. Therefore, a 3D-DDA program incorporating a proper interactive module is a good solution. The brief framework is given in Figure 4.2. In this scheme, the interactive actions are performed by forces on solid blocks, and the representative variations in terrain. The fluid field can be defined in accordance with in-situ investigation or calculated together with the solid model by solving Navier-Stokes Equations. Since the fluid actions on solid blocks should be considered, they are first calculated and then added to the corresponding

blocks as point loads. Buoyancy is acted on the center of buoyancy, meanwhile, the drag force is an equivalent resultant of the pressure at the center of each submerged facet. According to equation (2.50), the fluid forces acted on block *i* are then added to the force terms in the global governing equilibrium equations as

$$\boldsymbol{T}_i^{\mathrm{T}}[f_x \quad f_y \quad f_z]^{\mathrm{T}} \rightarrow \boldsymbol{F}_i \tag{4.1}$$

Obviously, the calculations of fluid actions on blocks are critical in the coupling scheme. The buoyancy and drag force are considered here. On the other hand, the block resistance to flow is also addressed. However, the adopted scheme shows difficulties in directly adding the block resisting force to flow. Therefore, an indirective way is employed in which the block resistance is considered by terrain node elevation. They will be introduced in the following contents. The detailed 3D DDA-DFS structure is presented in Figure 4.3 in a flow chart.

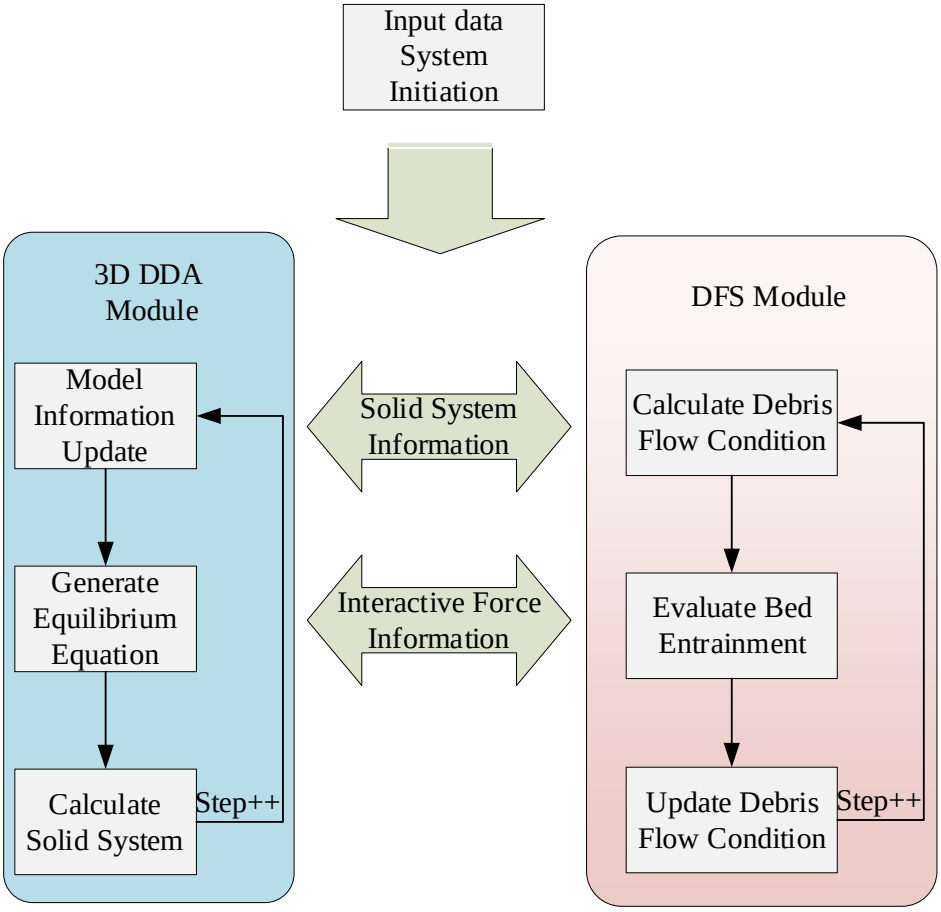

Figure 4.2 Modules of 3D DDA-DFS

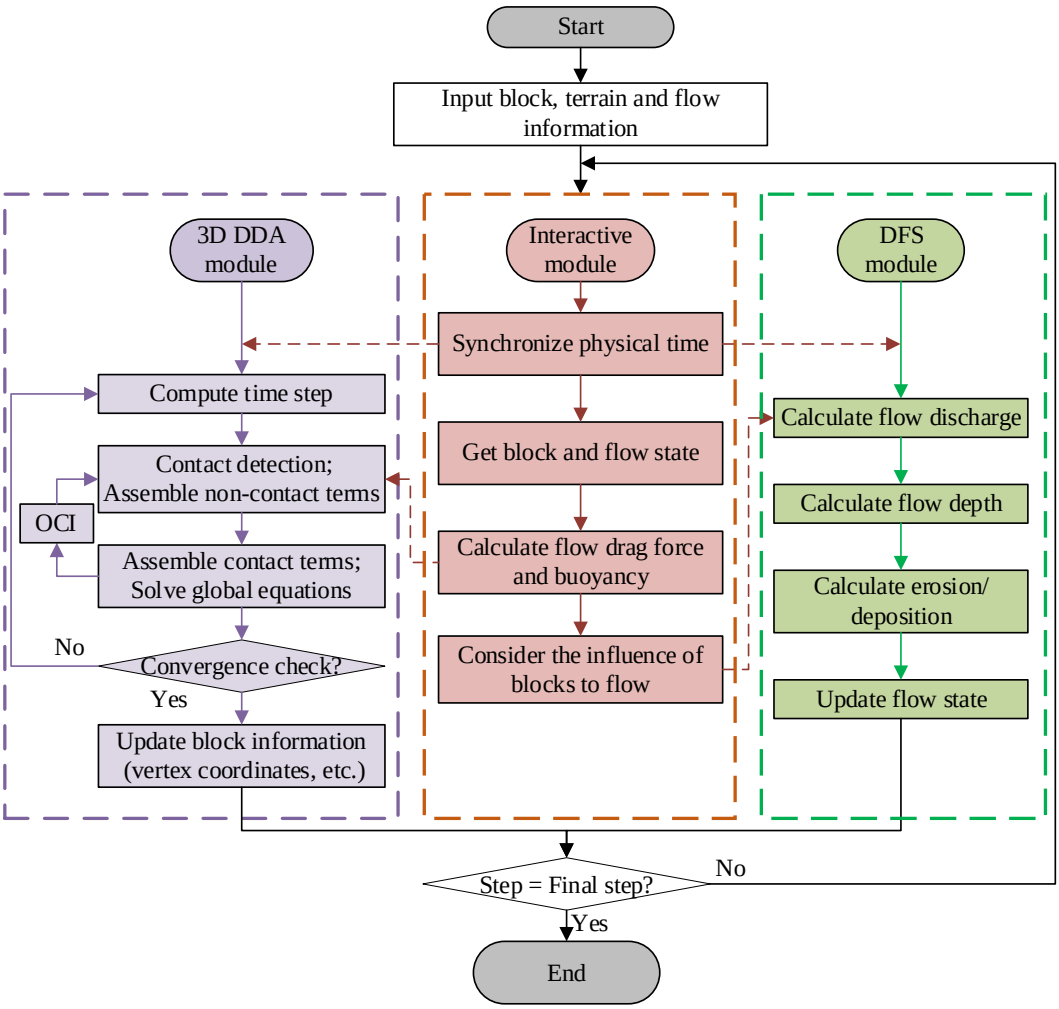

Figure 4.3 Detailed structure of 3D DDA-DFS

As described above, the 3D DDA-DFS program consists of three modules, 3D DDA module (marked by light purple), DFS module (marked by green) and interactive module (marked by pink). When the program initiates, data import and environment setup are executed in prior. In each step, the interactive module is performed first. The subroutine “Synchronize physical time” schedules which module is executed in the current step. The reason for the existence of this subroutine is that the step durations of 3D DDA module and DFS module are independent, which may lead to desynchronized physical time for the same system. For example, if the 3D DDA module has a step time duration of 0.01 s, while in DFS module it is 0.001 s, then 3D DDA module will be performed every ten times executions of DFS module, and vice versa. Subsequently, the modules are

performed separately as demanded. The interactive module uses the flow and block data to determine the flow force on the blocks in 3D DDA module. In the block system, the block positions are first checked for contacts, then the non-contact terms are assembled. The fluid actions are addressed in this part, in which a set of point loads are added. Although the flow forces are not point loads in nature, however, they are equivalent to point loads with the same effects to make it simple. After that, the following subroutines are executed, including adding and subtracting contact term, equation solving and post contact judgement. Meanwhile, when DFS module initiates, the block data is referred to estimate the blockage to the flow. The flow is calculated by the introduced equations in the previous sections.

4.3. CALCULATION OF BLOCK BUOYANCY

The buoyancy of a block in the fluid is proportionate to the volume of displaced fluid that must be first calculated. In this section, an algorithm is introduced, which has the advantages of being implemented easily and having the potential to calculate the volume submerged by uneven fluid surface for rapid flow. Moreover, this algorithm remains effective regardless of polyhedron shape, including the concave ones.

4.3.1. CALCULATION OF BLOCK BUOYANCY

A polyhedron block in 3D DDA is composed of several adjacent facets. Denote a z-wise unit vector as $\boldsymbol{n}_z$ = (0, 0, 1). For any block facet with an outer normal $\boldsymbol{n}$, it can be either “upward facet” or “downward facet” and defined by

$$\begin{aligned} &\boldsymbol{n}\cdot\boldsymbol{n}_z > 0 \rightarrow \text{"}upward\ \ facet\text{"} \\ &\boldsymbol{n}\cdot\boldsymbol{n}_z < 0 \rightarrow \text{"}downward\ \ facet\text{"} \end{aligned} \tag{4.2}$$

It should be noted that if $\boldsymbol{n}_z\cdot\boldsymbol{n}$ = 0, the facet is ignored automatically in the volume calculation process because it is vertical and the contribution to the displaced volume is nearly 0. Instead of computing it directly, which can be troublesome when the block shape is arbitrary or the fluid surface is uneven, the displaced volume Vs is calculated by the following formulation (see Figure 4.4):

$$V_s = \sum_{i=0}^{a_u} V_{f,i} - \sum_{i=0}^{a_d} V_{f,i} \tag{4.3}$$

where a_u and a_d are the numbers of the upward and downward facets, respectively. $V_{f,i}$ is the volume of the fluid polyhedron below the i-th facet and it is a truncated prism (hereinafter, fluid prism for short).

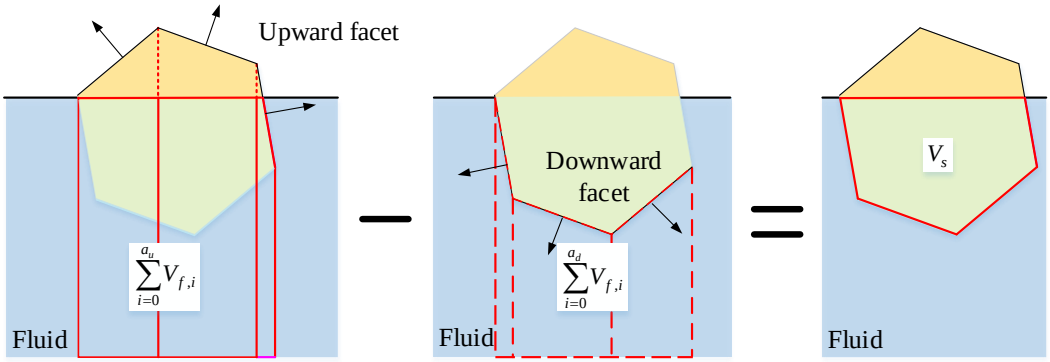

Figure 4.4 Illustrative diagram for submerged volume *Vs*

Equation (4.3) suggests that the volume of the displaced fluid *Vs* of a block is calculated through the fluid prisms $V_{f,i}$. Referring to Figure 4.5, let polygon *ABCDE* denote the *i*-th block facet. In addition, a horizontal projection plane Ω_0 is defined as a reference plane, served as the base of the fluid prism below the facet. The lines connecting the original vertices and their projections go through the fluid surface plane Ω', and the intersections are denoted by capital letters with a prime. As presented in Figure 4.5, the relative location of the block facet and the fluid can be categorized into three types:

(i) the whole facet is above the fluid surface (Figure 4.5 (a)),

(ii) it is partially submerged (Figure 4.5 (b)),

(iii) it is completely submerged (Figure 4.5 (c)).

The definition of $V_{f,i}$ varies for these three types. The fluid prisms for the above three types are respectively defined in the following:

(i) $A'B'C'D'E'$-$A_0B_0C_0D_0E_0$,

(ii) $B'C'M'N'$-$B_0C_0M_0N_0$ and $A'N'M'D'E'$-$A_0N_0M_0D_0E_0$,

(iii) $ABCDE$-$A_0B_0C_0D_0E_0$.

The fluid prisms are shown in red bold lines in Figure 4.5. Due to the different geometric composition of the fluid prism, the relative spatial location of the block facet and the fluid surface needs to be identified. Moreover, additional treatment should be adopted to determine the submerged partial facet in type (ii).

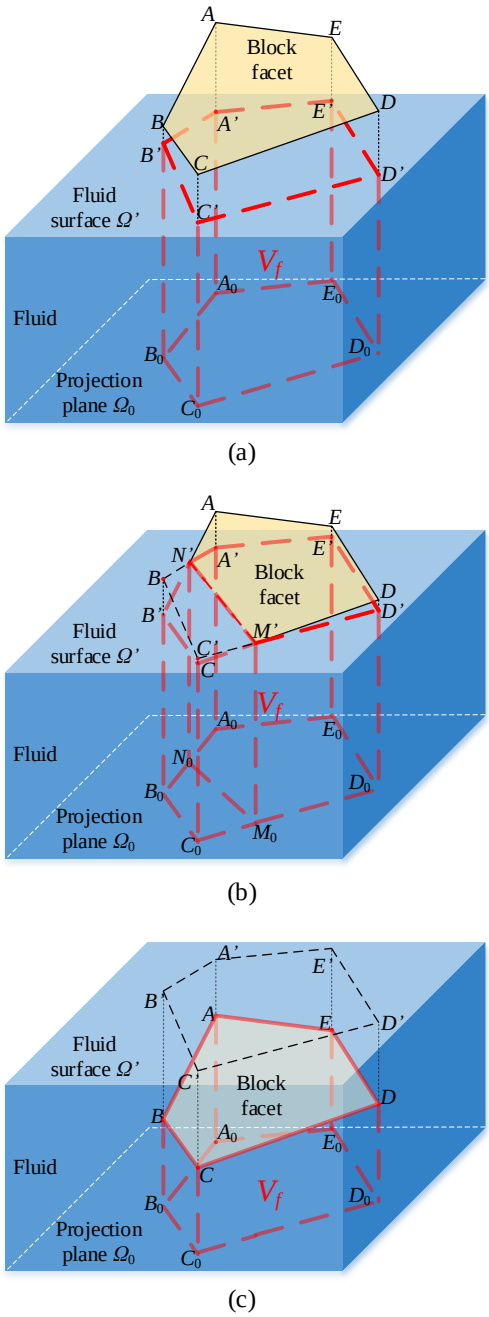

Figure 4.5 Diagram of V_f under the condition of the block facet (a) over the fluid surface, (b) partially submerged by fluid, and (c) totally submerged by fluid

4.3.2. FLUID PRISM DETECTION

Because of the dynamic flowing and natural base elevation, the surface of the fluid may not always be flat. Sometimes it is like a surface assembled by many small plane fractions. When the flow surface variation in the vertical direction cannot be neglected, the fluid prism also has to be disintegrated into small ones with respect to the flow surface mesh pattern. For every facet of a block, before detecting its fluid prism under a fluid surface fraction, two preconditions are set to rule out the situations of zero fluid prism volume. First, the dot product $\boldsymbol{n}_z \cdot \boldsymbol{n}$ should be larger than a certain value (e.g. 1×10^{-6}), and if

$$\boldsymbol{n} \cdot \boldsymbol{n}_z \leq 1\times10^{-6} \tag{4.4}$$

The facet is automatically ignored because in this case, the facet is nearly perpendicular to the reference plane and contributes little to the fluid prism volume. By applying such a screening process, probable calculation singularities like division by zero are also avoided. Second, in the case of a limited fluid coverage, the projections of the facet and a fluid surface fraction should be at least partially overlapped, i.e.

$$\Omega_{f'} \cap \Omega_{s'} \neq \varnothing \tag{4.5}$$

where Ω denotes a polygon, and the subscript *f*' and *s*' denote the projection of flow surface and solid facet. Therefore, the valid fluid prism is limited within the overlapped area instead of the whole projection area.

To satisfy the first precondition, the judgement through the dot product is sufficient. Regarding the second precondition, the fundamental problem is how to yield the possible overlapped polygon according to the given two polygons. A possible solution is to project the two spatial polygons onto a horizontal reference plane and figure out the overlapped part (if not exist, the second precondition cannot be satisfied so that no fluid prism exists), and then trace back to the original surfaces. The existence of terrain mesh ensures the regular projection of the flow surface fraction. Detection of the overlapped part between two polygons in the same horizontal plane reduces the problem dimensions from three to two, and the

projecting operation is quite simple that one just needs to set the vertical coordinate of the associated vertices to 0. A non-skew prism's volume is determined by its top and bottom faces. As a result, the outline of the methodology used in fluid prism detection is shown in Figure 4.6.

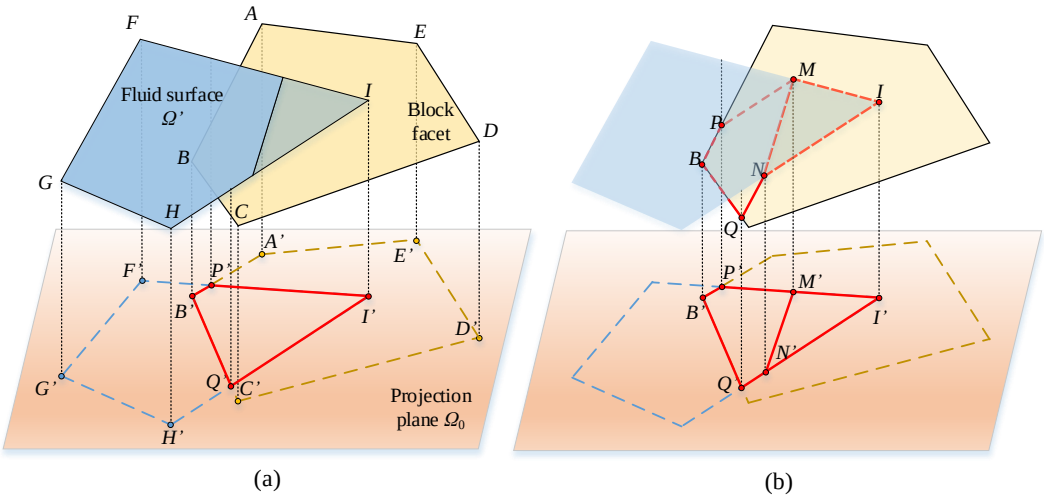

Figure 4.6 Methodology used in fluid prism detection: (a) project two polygons onto a common projection plane and identify the overlapped polygon (b) trace back the overlapped polygon to its original position to identify the top facet(s) of the fluid prism.

(1) Identify the possible overlapped polygon *P'B'Q'I'* between the two projection polygons *A'B'C'D'E'* and *F'G'H'I'* (Figure 4.6 (a)):

$$\Omega_{P'B'Q'I'} = \Omega_{A'B'C'D'E'} \cap \Omega_{F'G'H'I'} \tag{4.6}$$

The overlapped polygon *P'B'Q'I'* serves as the bottom of the fluid prism. Note that *P'* and *Q'* are intersections of the projected borders.

(2) Determine the top faces of the fluid prism by projecting the overlapped projection polygon *P'B'Q'I'* back onto the original planes including fluid surface fraction and block facet (Figure 4.6 (b)). Based on the definition, the actual top surface of the fluid prism should make the fluid prism smallest in all the probable prisms that compassed by fluid surface and block facet.

The determination of the top and bottom faces of the fluid prism makes it possible to obtain the volume through simplex integration described in Section 2.2.2.

Since the top faces can be located by projecting back the bottom faces, identifying the bottom faces is critical, which will be discussed in detail in the following section.

4.3.3. Bottom face determination for the fluid prism (overlapped polygon search algorithm)

Finding the overlapped polygons for the projections of the block facet and fluid surface fraction is equivalent to a clipping polygon problem in computer graphics domain, which aims to find out the parts of a polygon (object polygon) within another predefined polygon (clip polygon). In 1974, a polygon-clipping algorithm was proposed by Sutherland and Hodgman (so-called Sutherland–Hodgman algorithm) (Sutherland, I. E. et al., 1974). Conventional Sutherland–Hodgman algorithm extends every clip polygon edge to the boundary line which divides the two-dimensional space into two sides – the visible side and invisible side. Only the object polygon part located on the visible side counts as visible. This process is looped for all the clip polygon edges, and the final fraction remaining visible is the clipped polygon. Sutherland–Hodgman algorithm is simple and easy to code. However, it may yield problematic results if the concave polygons are involved since a concave polygon may cross the visible/invisible boundary line. Since in 3D DDA the block shape is general, a Weiler–Atherton clipping algorithm may be more suitable (Weiler, K. et al., 1977) due to the capability for concave polygons. It is already referred to in existing literature when considering material cohesion in face-to-face contact in 3D DDA (Zhang, H. et al., 2016), which involves overlapped polygon area calculation. To thoroughly go through the process, a detailed explanation is presented. Some preconditions are assumed to be fulfilled before discussion: 1. Both candidate polygons, convex or concave, are composed of vertices listed counterclockwise; 2. Both candidate polygons cannot be self-intersecting; 3. With regard to the computational error, if the distance between two points is smaller than a very small value (e.g. 1×10^{-6}), then these two points are indistinguishable and recognized as one.

Step 1: Data structure

Several alternatives are available in data storage such as the linked list and arrays. For simplicity, the most fundamental element (i.e., "class") in C++ is used. A point information class *point_inf*[] is defined to store every point, including the vertices of the subject and the clip polygons as well as the potential intersection points of edges. All the points of polygons are ordered and numbered counterclockwise. The information of point with index *i* is stored in *point_inf*[*i*], which includes: 1. bool variable *isP1*, if true, point *i* belongs to polygon 1; 2. bool variable *isP2*, if true, point *i* belongs to polygon 2; 3. integers *prev_index1* and *prev_index2*, store the point index before point *i* in polygon 1 and polygon 2, respectively; 4. integers *next_index1* and *next_index2*, store the next point index in polygon 1 and polygon 2. One may observe that if point *i* is the intersection of two edges, then *isP1* = *isP2* = true.

Step 2: Extend point series by inserting intersection points

The edges of the two projection polygons are investigated pairwise through a loop to check for the possible intersections. The intersection checking subroutine is fundamental and will be executed frequently, which must be both effective and accurate. The following algorithm is implemented to obtain intersections (Shi, G., 1989): for edge *AB* and edge *CD* with given coordinates $A(x_A, y_A)$, $B(x_B, y_B)$, $C(x_C, y_C)$ and $D(x_D, y_D)$, the intersection is obtained by solving t_1 and t_2 in

$$\begin{pmatrix} x_B - x_A & x_C - x_D \\ y_B - y_A & y_C - y_D \end{pmatrix} \begin{pmatrix} t_1 \\ t_2 \end{pmatrix} = \begin{pmatrix} x_C - x_A \\ y_C - y_A \end{pmatrix}, \; t_1, t_2 \in [0,1] \tag{4.7}$$

If the following conditions hold:

$$\begin{vmatrix} x_B - x_A & x_C - x_D \\ y_B - y_A & y_C - y_D \end{vmatrix} = 0 \;\; or \;\; t_1 \notin [0,1] \;\; or \;\; t_2 \notin [0,1] \tag{4.8}$$

then no intersection exists between edge *AB* and *CD*. Otherwise, the intersection is $(x_A+(x_B-x_A)t_1,\ y_A+(y_B-y_A)t_1)$. A new intersection should be stored in *point_inf*[]. When all intersections are detected, they should be inserted into the polygon node lists. As shown in Figure 4.7, edge 1-2 of polygon 1 crosses polygon 2 four times and yield four intersections points 10-13. They are ordered by their respective distance to point 1 from close to far (13-11-12-10). Such order information is

written to the array for the corresponding polygon as *prev_index and next_index*. Note that the newly detected intersections may change the existing records, for example, *point_inf*[1].*next_index1* changes from 2 to 13.

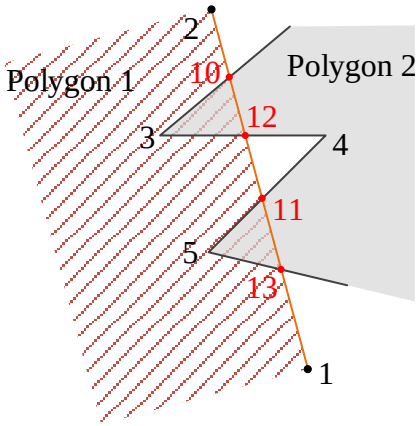

Point index	*prev_ index1*	*next_ index1*	*prev_ index2*	*next_ index2*
1	*	13	-	-
2	10	*	-	-
3	-	-	10	12
4	-	-	12	11
5	-	-	11	13
...	...	...	...	...
10	12	2	*	3
11	13	12	4	5
12	11	10	3	4
13	1	11	5	*

Figure 4.7 Extend point storage by adding new intersections. The red number denotes the newly detected intersections that have not been recorded. The "*" and "-" symbols in the table mean the node is not shown in the figure and does not exist, respectively.

Step 3. Check the in/out status of all the intersecting points

An in/out state is checked for every intersection. The point class *point_inf*[] already contains all the vertices and intersects, including their orders. Following the data in *next_index1* and *next_index2*, two lists of points composing polygon 1 and 2 are formed. Referring to Figure 4.8 and using polygon 2 as the clipper, for example, the parts of polygon 1 inside polygon 2 is defined as the overlapped polygon. The intersections are potential separations of a clipped polygon from the rest part of the polygon. An intersection is defined as "in" state if the polygon 1 enters polygon 2 through it following the node list and "out" state for the opposite. It is decided by the positions of its previous and next edges by definition. As for an intersection *P*, the criterion is expressed as

$$\begin{aligned} &If\ \ (E_p \notin \Omega_2 \setminus \partial\Omega_2 \text{ and } E_n \in \Omega_2 \setminus \partial\Omega_2),\quad P\ is\ "in"\ state; \\ &If\ \ (E_p \in \Omega_2 \setminus \partial\Omega_2 \text{ and } E_n \notin \Omega_2 \setminus \partial\Omega_2),\quad P\ is\ "out"\ state; \end{aligned} \tag{4.9}$$

where E_p and E_n represent the previous and next edge of *P*, respectively; $\Omega_2 \setminus \partial\Omega_2$ denotes the region within polygon 2 without boundary. However, it is still possible

that the edge coincides with an edge from polygon 2 (Figure 4.9). In this case, another criterion is applied:

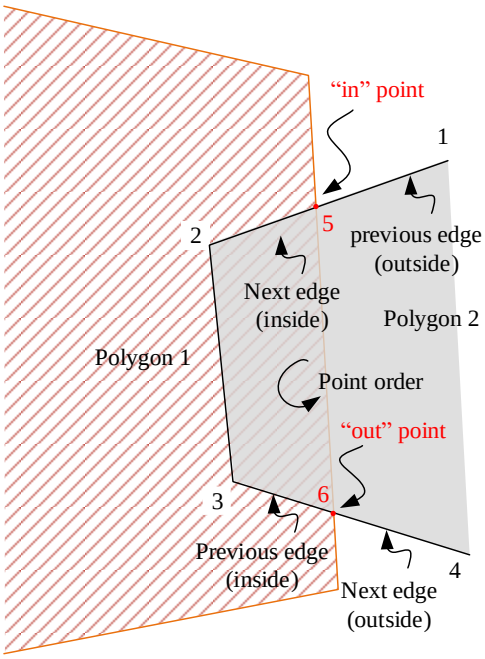

Figure 4.8 Illustration for "in" and "out" intersections

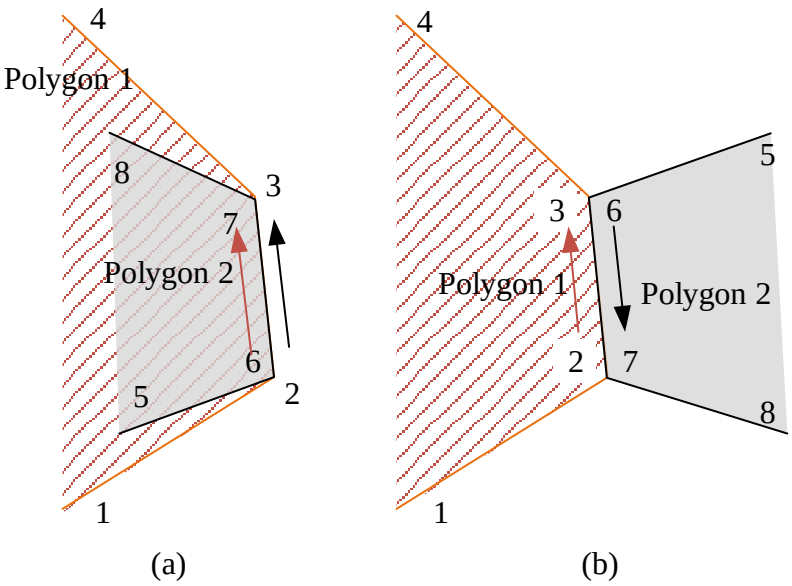

Figure 4.9 Two possible situations for edges coincide (a) same order, edge 2-3 regarded inside and (b) opposite order, edge 2-3 regarded as outside

$$
\begin{aligned}
&When\ E_1 \in \partial\Omega_2 \text{ and } \vec{E}_1 = k\vec{E}_2 : \\
&\qquad If\ \ k > 0,\ \ def\ \ E_1 \in \Omega_2; \\
&\qquad If\ \ k < 0,\ \ def\ \ E_1 \notin \Omega_2;
\end{aligned}
\tag{4.10}
$$

where E_1 and E_1 are edges of polygon 1 and 2. The sign of coefficient k implies the relative direction of the paralleled edges. With the complementary of equation (4.10), the position of E_1 is definite (inside or outside polygon 2). As a result, all the possible edge positions are identified and categorized, which gives a clear judgement for the in/out state of intersections.

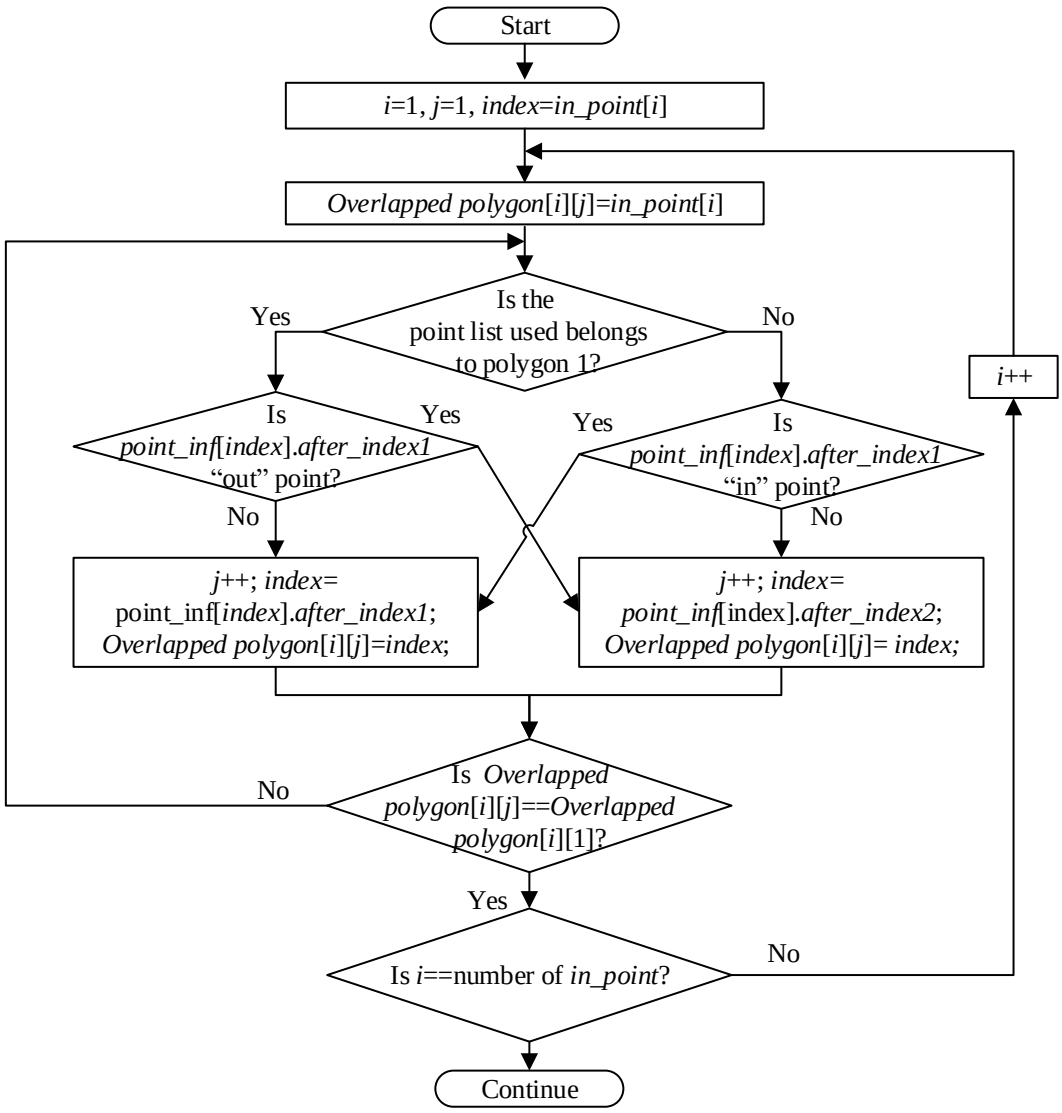

Figure 4.10 Flow chart for the algorithm used to form overlapped polygons

Step 4. Form the clipped polygons

Pick one "in" state intersection, mark it as the first node of an overlapped polygon. Then the following node is the one recorded in *next_index1*. This process will keep looping unless it comes across an "out" point. If so, the next node of the overlapped polygon will be the one in *next_index2*. Similarly, for an "in" point, the point search should be back to polygon 1 by using *next_index1*. In addition, if the next point is the same one with the first point, then the overlapped polygon is closed, and then one should begin to search another one until all the "in" state points are searched. A flow chart of the algorithm is illustrated in Figure 4.10.

The overlapped polygons serve as the bottom faces of the fluid prisms. With the bottom already known, the top faces are easily obtained by tracing back the bottom faces to the original position. A prism is then constructed by the bottom and top faces. After that, recalling the simplex integration formulation in Section 2.2.2 solves the volume directly.

4.4. CALCULATION OF FLUID DRAG FORCE AND STATIC PRESSURE

When the velocities of fluid and a solid block are different, a dynamic fluid drag appears. A generalized expression of the drag force F_d can be described as (Hoerner, S. F., 1965)

$$F_d = c_d \frac{\rho_f v^2 A}{2} \tag{4.11}$$

where v is the relative velocity, and A is the drag area, i.e. the projected frontal area of the block. Equation (4.11) suggests that the drag force is proportional to the dynamic pressure ($0.5\rho_f v^2$). c_d is a coefficient. Many researchers have dedicated their effort in determining the relationship between drag force and other factors (Bearman, P. W. et al., 1982; Bishop, R. E. D. et al., 1964; Lo, S.-C. et al., 2005; Troesch, A. W. et al., 1991). Referring to previous literatures (Hoerner, S. F., 1965; Jsce, 1971) about flow over square cylinders, the magnitude of c_d can be approximately regarded as fixed in a certain Reynolds number range. In addition, the Federal Highway Administration of United State (FHWA) suggests c_d equals 2

on condition that the piers are square (Zevenbergen, L. et al., 2012). Given that the blocks in DDA are usually square, the formulation for drag force F is then rewritten as

$$F_d = \rho_f v^2 A \tag{4.12}$$

Equation (4.12) is also recommended by Hunger et al. (Hunger, O. et al., 1984), but they suggested a coefficient 1.5 to address "the forming of a stagnant wedge in front of the toe of the barrier". It is unquestionable for fixed barriers, but the blocks in this study, which compose the boulders and dams, are mostly flexible. The stagnant wedge is not easily formed against the toe of the blocks. Therefore, it is reasonable to disregard the suggested coefficient. This formulation is performed facet by facet. By defining F_d as perpendicular to the facet, v is changed to the normal components to the facet. When applying equation (4.12), there is another rule defining the existence of drag force: for a given relative velocity vector $\boldsymbol{v} = (v_x, v_y, v_z)$ and a block facet with an outer normal $\boldsymbol{n} = (n_x, n_y, n_z)$, the fluid drag force exists only when

$$\boldsymbol{v} \cdot \boldsymbol{n} < 0 \tag{4.13}$$

It means that the drag force is assumed to be acted on the facet with outer normal against fluid velocity. Equation (4.12) suggests that the drag force calculation can be transferred into the calculation of the valid drag area of block facets. The valid drag area should be submerged by fluid, and this requirement can also be transferred to a polygon clipping problem. As a result, an algorithm similar to the one used in section 4.3.3 is performed to identify the drag area. Note that a facet may span several terrain mesh cells which are different in velocity. To make it simple, the fluid velocity is averaged in the spanned cells as $\bar{v}_f$:

$$\bar{v}_f = \int v_f \, dA \approx (\sum_n v_{fi} A_i) / n \tag{4.14}$$

where n is the number of terrain mesh cells involved, v_{fi} and A_i (i=1-n) are the velocity and area of the cells. However, the perpendicular relative velocity on vertices still may be different. To applying equation (4.12), the integration of such

velocity is calculated first by simplex integration, then averaged to the whole facet. The averaged normal components of the relative velocity is the v used in equation (4.12). The position of F_d locates on the projection point on the facet projected by the center of the relative velocity polyhedron (see Figure 4.11).

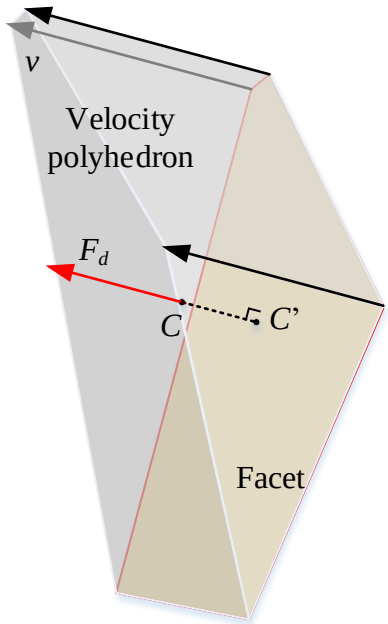

Figure 4.11 The location of drag force F_d. C is the center of the velocity polygon

The static pressure of a facet is relatively simple. It should be addressed only when the block is not surrounded by flow. The submerged part of the facet has been determined during drag force calculation. When static pressure should be considered, the resultant force of the static pressure can be calculated by multiplying the area of the submerged facet by the pressure on the center of the submerged partial facet. The direction of the resultant force is perpendicular and pointing to the facet.

4.5. Drag effect between adjacent blocks

The discussions above show how to calculate the drag force in a predefined flow field. However, the existence of solid blocks affects the flow field in reality. The accurate depiction of the disturbed flow field is both difficult and unnecessary. But it has to be addressed because the disturbance can be significant. For example, two blocks, an upstream one and a downstream one, are in a flow field, and the top

view is shown in Figure 4.12. The dimensions of them are L, and there is a distance D between them. When they are far enough, i.e. $L/D \rightarrow 0$, they can be treated as two individual blocks. If the flow field is uniform, then they share the same flow drag force F, which is calculated by equation (4.12). However, when d and l are in the same order of magnitude, the two blocks begin to affect each other. In particular, the distance D is small and $L/D \rightarrow \infty$, the drag force on the downstream block, i.e. block 2, is significantly reduced. A coefficient r is employed to describe the interaction between blocks:

$$F_{1,r} = r_1 F, \ F_{2,r} = r_2 F, \tag{4.15}$$

where r_1 and r_2 are the coefficients for upstream and downstream blocks. The reason for this phenomenon is that the vortices are generated around the blocks.

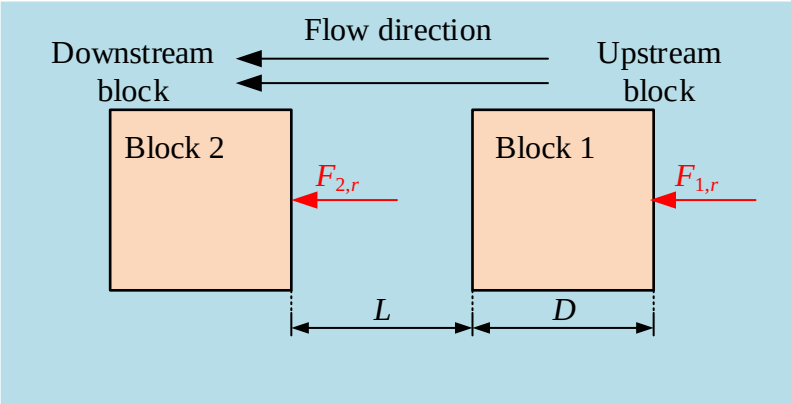

Figure 4.12 Two blocks in a flow field

The flow around solid blocks can be very complex, especially for the blocks in arbitrary polyhedral shapes. A simpler version of the problem is the interaction of tandem cylinders in flow, which has been studied by research communities by means of experiments (Bhattacharyya, S. et al., 2008; Sakamoto, H. et al., 1987) or numerical simulation (Rajani, B. N. et al., 2009; Zhao, X. et al., 2016). A set of typical experiments from Yen, S. C. et al. (2008) are used to introduce the varying flow state with the blocks. Several streamline patterns from their research are demonstrated in Figure 4.13. Figure 4.13(a) is a comparison for the rest of the figures, in which only one cylinder is placed. The flow is separated by the cylinder and two vortices are formed behind the square cylinder. The center of a vortex is

referred to as a node. After the saddle point, the streamlines join together, however the flow field does not recover to the original pattern, at least within the presented range. Figure 4.13(b)-(d) show the flow patterns as L/D increases from 0.5 to 4. When L/D = 0.5, the two cylinders are quite close, and two small vortices are observed near the gap. The velocity in the gap is not significant, and the two cylinders can be treated as one, therefore the flow pattern is called the single model. It is apparent that in this case, the drag force on the downstream cylinder is smaller to the single block situation since the flow velocity around it is small. In Figure 4.13(c), the distance between the two cylinders is enough for the separated flow stream to reattach. Four vortices, two minor ones and two major ones, are formed around the downstream cylinder. The drag force on the downstream cylinder also starts to grow. As the gaping continues increasing, the pattern in Figure 4.13(d) shows four fully developed vortices behind two cylinders. Although not completely recovered, the drag force on the downstream cylinder increases and approaches the level of single cylinder situation. Due to such reason, the flow pattern is named as the vertex sheet of the binary mode. The varying of the drag force on the upstream regarding the distance is not obvious, but it is clear that the changing of distance is also a factor to the force. It is also reported that the Reynolds number (Re) of square also affects the drag force (Yen, S. C. et al., 2008). Re is an elemental constant in fluid mechanics, which is defined by

$$\mathrm{Re} = u_{\infty} D / \upsilon \tag{4.16}$$

where u_{∞} is the local flow velocity, υ is the kinetic viscosity.

By the discussion above, one may conclude that Re and distance between two blocks show a significant influence on the drag forces. In addition, the influence is non-linear. It is unnecessary to address such influence in very high accuracy in the mixture of debris flow and boulder. Therefore, an approximate estimation of the blocks interaction in flow is adopted with the following assumptions:

(a) For each block in debris flow, a boundary box is used to make the block square. The squares edges and facets are parallel or perpendicular to the flow velocity without any askew.

(b) The study about tandem square cylinders are used to estimate the flow.

(c) The parameter R and spacing ratio *L*/*D* are employed as variables.

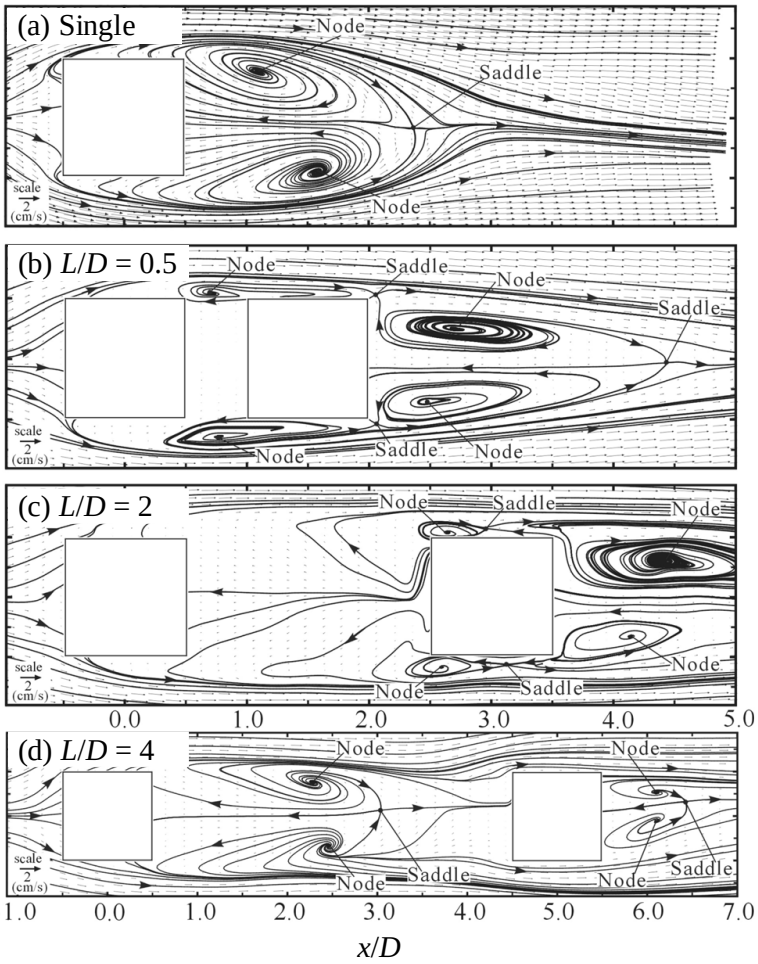

Figure 4.13 Streamline patterns with velocity fields at (a) one cylinder, (b) *L*/*D* = 0.5, single mode, (c) *L*/*D* = 2, reattached mode and (d) *L*/*D* = 4, binary mode at Re = 535 (Yen, S. C. et al., 2008)

With the above assumptions, a solution to determine the ratio r_1 and r_1 is given as follows. First, calculate the Re for a given block in flow. The local flow velocity, kinetic viscosity and block geometry can determine Re. The local Re is used to find the corresponding critical spacing ratio. This parameter is important because the drag force exhibits drastically different when the spacing ratio is smaller or larger than it. Those two conditions are referred to as mode 1 and mode 2. Second, the actual spacing ratio is computed to decide which flow state it is, and the combination of flow state and Re are used to determine r_1 and r_2. The studies about

tandem cylinders in flow are referred. Note that those researches are mainly focused on the drag force coefficient c_d (in equation (4.11)), which is different from the coefficient r_1 and r_2. To provide comprehensive illustrations to the related background, the c_d is still used in the introduction. However, they will eventually be transformed into r_1 and r_2 used in equation (4.15).

Table 4.1 Critical spacing ratio with various Re (Chatterjee, D. et al., 2012)

Re	$(L/D)_c$
50	5–7
75	5–7
100	4–5
125	3–4
150	3–4

Table 4.2 Coefficient c_d for upstream (US) and downstream (DS) cylinders (Chatterjee, D. et al., 2012)

	c_d									
	Re = 50		Re = 75		Re = 10		Re = 125		Re = 150	
L/D	US	DS	US	DS	US	DS	US	DS	US	DS
1	1.7227	0.0688	1.5566	-0.067	1.5001	0.1553	1.4964	-0.227	1.5182	-0.291
2	1.7014	0.1441	1.5396	-0.017	1.4713	-0.127	1.4572	-0.238	1.4732	-0.324
3	1.6875	0.225	1.5335	0.0656	1.4543	-0.048	1.4318	-0.209	1.4507	-0.283
4	1.6809	0.3051	1.5178	0.9745	1.4304	-0.03	1.4607	0.3396	1.5449	1.1375
5	1.7263	0.3545	1.611	1.0593	1.5329	1.1931	1.5345	1.0896	1.5743	1.2571
7	1.7544	1.1187	1.6366	1.0862	1.5929	0.9283	1.598	0.9278	1.6357	1.103
10	1.7624	1.3186	1.6442	1.2342	1.6088	0.9518	1.6144	0.9253	1.6445	0.9346

Studies have been performed under different flow conditions and cylinder arrangements to explore the drag coefficient. It has been noticed that a critical spacing ratio exists which separates the coefficient curve. Chatterjee, D. et al. (2012) studied the condition of Re = 50-150. In their study, the critical spacing ratio ranges from 3-7 for various Re numbers, as listed in Table 4.1. The c_d in equation (4.11) is also measured, given in Table 4.2. From these two tables, a rough relationship can be given between Re and c_d. The data is similar to the researches from other

literatures (Singha, S. et al., 2010), in which a brief formula is provided. It seems that the drag coefficient of the upstream cylinder does not change significantly, however, the downstream one is greatly affected.

When Re ranges from hundreds to thousands, the critical spacing ratio and the corresponding drag force coefficient c_d were also studied. A relationship between the critical spacing ratio and Re has been proposed for $400 \leq \mathrm{Re} \leq 1200$ (Tatsutani, K. et al., 1993):

$$(L/D)_c = 168\,\mathrm{Re}^{-\frac{2}{3}} \tag{4.17}$$

Equation (4.17) also agrees with the numerical results obtained by Sohankar, A. (2012). For higher Re, Liu, C. H. et al. (2002) gave a range of critical spacing ratio because they observed a "hysteresis" phenomenon, in which different critical spacing ratios exist when the spacing is varying in two different ways, i.e., from large to small, or from small to large. They also claimed that the hysteresis regime experiences a sharp decrease when Re increases from 2.0×10^3 to 5.3×10^3, then it remains nearly unchanged until 1.6×10^4.

Conclusively, the drag force coefficient c_d can be approximately determined based on the discussions above. To make it clear, the usage of c_d is transferred to coefficients r_1 and r_2. For a given block pair, Re and the spacing ratio between them are first calculated. Using the magnitude of Re, the critical spacing ratio $(L/D)_c$ can be determined by referring to Table 4.3. By comparing the actual spacing ratio L/D to the critical spacing ratio $(L/D)_c$, the local flow model is obtained:

$$\begin{aligned} &L/D \leq (L/D)_c, \ \text{mode 1} \\ &L/D > (L/D)_c, \ \text{mode 2} \end{aligned} \tag{4.18}$$

Table 4.3 Relationship between critical spacing ratio and Re

Re	≤150	150,400	400,1200	1200-2000	2000-4000	4000-16000
$(L/D)_c$	3.5	3.5 to 3	$168\mathrm{Re}^{(-2/3)}$	1.5 to 4	4 to 3	3

With the flow mode determined, the coefficient r_1 and r_2 are searched in Table 4.4. For example, let Re = 130 and L/D = 4. From Table 4.3, column 1, because Re <

150 and L/D = 4 > 3.5, the flow is in mode 2. Then refer to Table 4.4, rows Mode 2 and column 1, it is decided that r_1 = 0.75 and r_2 = 0.5.

Table 4.4 Values of r_1 and r_2 for different flow mode and Re

	Re	≤150	150,400	400,1200	1200-2000	2000-16000
r_1	Mode 1	0.75	0.75 to 1	1	1 to 0.75	0.75
	Mode 2	0.75	0.75 to 1		1	
r_2	Mode 1	0	0 to -0.25		-0.25	
	Mode 2	0.5	0.5 to 0.75	0.75	0.75 to 1	1

It is worth noting that when L/D is large enough, i.e. the two blocks are quite far away from each other, the interaction between them should decrease. In Table 4.3 and Table 4.4, this condition is not reflected. Researches suggested when L/D is as great as 10, the interaction is still observed (Chatterjee, D. et al., 2012; Kim, M. K. et al., 2008). Here, a limitation of spacing ratio 15 is defined, and if the spacing ratio between two blocks is greater than that, the interaction between them is no longer considered and they are treated as two individual blocks.

Another problem that needs to address is that the blocks in simulations are of any arbitrary polyhedral shape. Although unified boundary cuboids are employed, they still have different sizes. In order to implement the theory for r_1 and r_2, a weighted average is performed. As illustrated in Figure 4.14, the smaller block, circled by boundary cuboid 1, is the upstream block. To calculate the drag force, the boundary cuboid 1 is first projected to the facet of boundary cuboid 2 along flow velocity direction, and the projection area A_1 is calculated. It is assumed that within the projection area A_1, the drag force should be multiplied by coefficient r_2; the area A_2 - A_1 is not affected by block 1, where A_2 is the facet of boundary cuboid 2. This assumption is based on the fact that many researches in tandem cylinders interaction in flow are of the same size. Because the interaction between blocks of different size is complex and beyond the range of this research, the simple assumption is applicable. With area A_1 affected by block 1 and area A_2 - A_1 is not, an average over facet A_2 is performed to calculate drag force F_d:

$$F_d = \frac{A_1 F_{2,r} + (A_2 - A_1) F_2}{A_2} = \frac{A_2 - (1 - r_2) A_1}{A_2} F_2 \tag{4.19}$$

with

$$F_2 = \rho_f v^2 A_2 \tag{4.20}$$

When $A_2 = A_1$, boundary block 1 shares same size of boundary block 2, equation (4.19) reduces to equation (4.15).

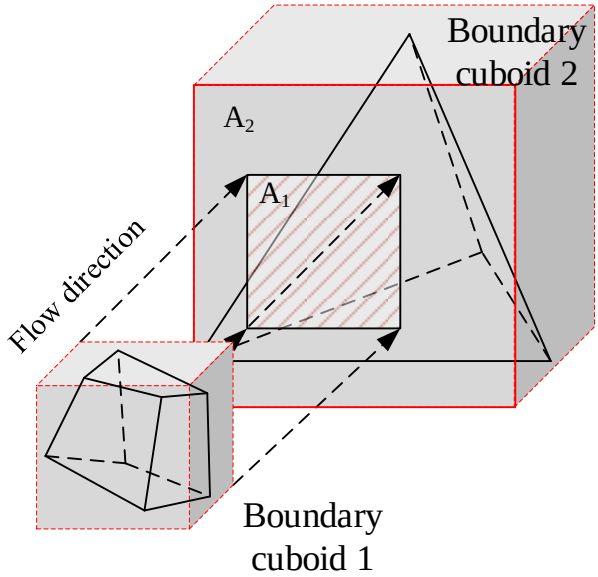

Figure 4.14 drag force calculation for block pair of different size

4.6. AN EQUIVALENT SOLUTION TO ADDRESS BLOCK ACTIONS ON FLOW

The existence of solid blocks may disturb the flow. Such backward action on flow is regarded as a certain elevation of the terrain. As presented in Figure 4.15, a block has a boundary box with the thickness of *H*'. If the block is static, the flow will certainly be blocked or slow down when passing it. It is reflected by an elevation of ΔH of the relevant terrain node, expressed by:

$$\Delta H = \gamma H' \tag{4.21}$$

where γ is a reduction coefficient related to the velocity v_s and v_f:

$$\gamma = \begin{cases} 1, & \vec{v}_s \cdot \vec{v}_f \le 0 \\ 1 - \dfrac{\vec{v}_s \cdot \vec{v}_f}{\left|\vec{v}_f\right|^2}, & \vec{v}_s \cdot \vec{v}_f \in (0, \left|\vec{v}_f\right|^2) \\ 0, & \vec{v}_s \cdot \vec{v}_f \ge \left|\vec{v}_f\right|^2 \end{cases} \tag{4.22}$$

Equation (4.21) and (4.22) imply that the actual elevation of the terrain node is adjusted by velocities. When block moves faster than flow, the block shows no blockage to the flow, thus $\gamma = 0$; the possible speeding up of the flow is neglected. On the other hand, if the block stopped or moves reversely to the flowing direction, $\gamma = 1$. For the projected block velocity within above to extremities, a linear interpolation is employed.

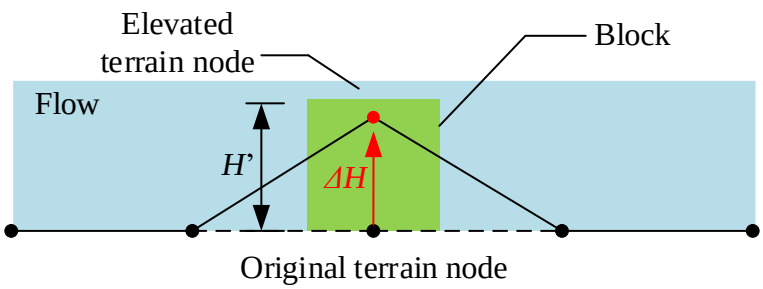

Figure 4.15 Elevation of terrain node to consider the disturbance of block to flow field

4.7. VALIDATION EXAMPLES

Example shown in Figure 4.16 is used to validate the buoyancy calculation. A yellow cubic block, with dimension l = 1 m, is floating in fluid. The density of the flow ρ_f is 1000 kg/m^3, and the velocity is zero. The block density ρ_b serves as a variable. It is obvious that when block density is less than ρ_f, the block will keep floating. With the decrease of block density, the block floats higher, and the height above flow surface d also increases. A series of flow densities are chosen, ranging from 600 to 950 kg/m^3. The corresponding d is calculated by

$$d = l - \frac{\rho}{\rho_f} \tag{4.23}$$

The example is calculated by 3D DDA-DFS program and the calculated *d* is shown in Figure 4.17. It suggests that the simulated *d* matches the theoretical solution well, which further implies that the buoyancy calculation is correct.

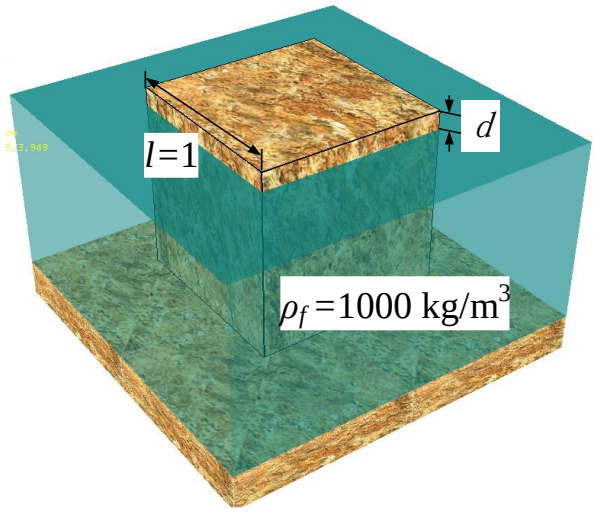

Figure 4.16 A block floating in flow to validate buoyancy calculation

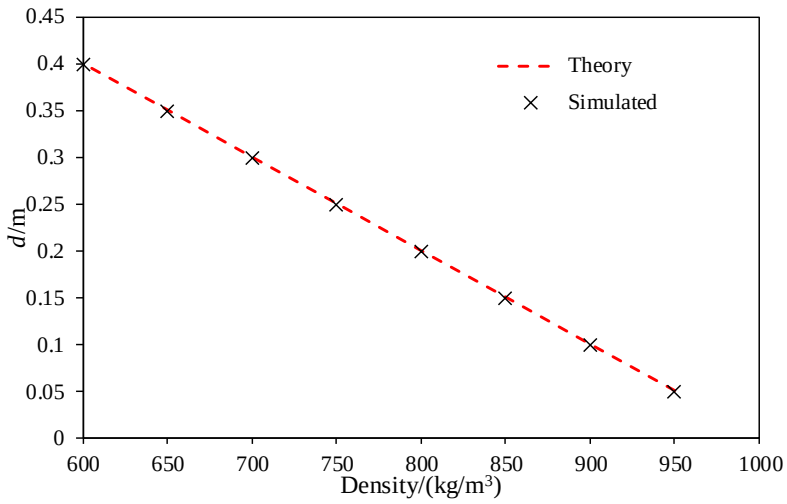

Figure 4.17 Calculated *d* by 3D DDA-DFS and theoretical solution given by equation (4.23)

A block acceleration example is exhibited to illustrate the validity of the impact force calculation. As presented in Figure 4.18, a block (density ρ_s = 900 kg/m^3, elastic modulus 3 GPa) is at the end of a water channel, initially at rest. The flow has a density ρ_f = 1000 kg/m^3 and a velocity v_f = 1m/s. Assuming the flow velocity is always constant everywhere despite the resistance of the block. In this

example, 9/10 of the block is submerged by the flow. Due to the given size and density, the suspending block is vertically balanced. The block will be pushed and accelerated by the flow from the static state, approaching the flow velocity v_f eventually if time is long enough. As a benchmark, an analytical solution is given before simulation.

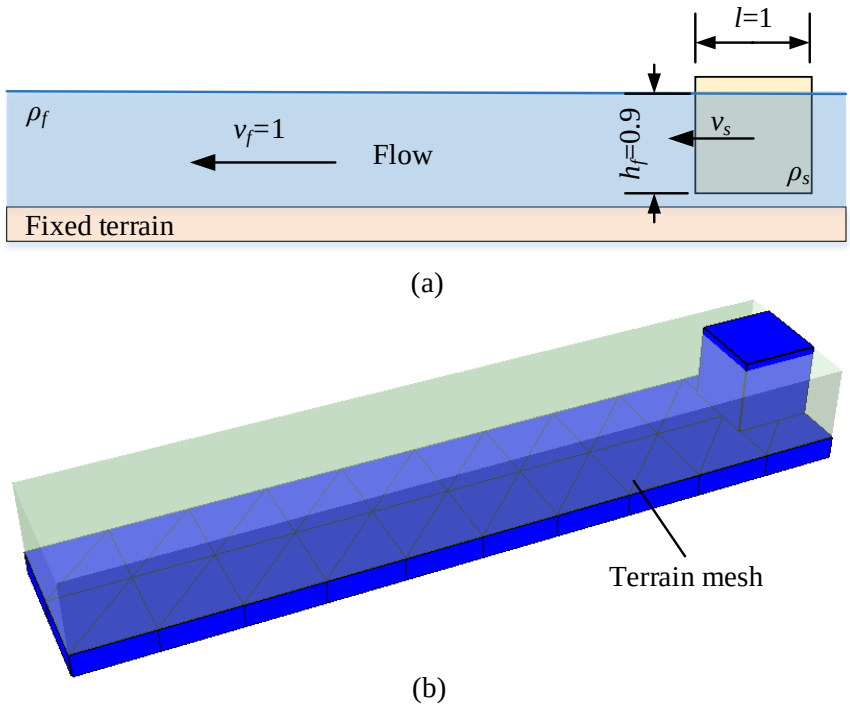

Figure 4.18 (a) A schematic figure and (b) calculation model in the 3D DDA-DFS of the block acceleration example (Unit: m, s)

According to the diagram in Figure 4.18 (a), the block has a velocity v_s while the flow velocity is v_f. For the given scenario, a condition of $v_s < v_f$ is always satisfied. The drag force F_d is obtained by recalling equation (4.12):

$$F_d = \rho_f l h_f (v_f - v_s)^2 \tag{4.24}$$

where l is the edge length of the block, and h_f is the submerged depth. Applying the momentum equation $dv_s/dt = F_d/m$ to the block combining with equation (4.24), a differential equation yields

$$\frac{dv_s}{dt} = \frac{\alpha_h (v_f - v_s)^2}{\alpha_\rho l} \tag{4.25}$$

where t is time, the coefficients $\alpha_\rho = \rho_s/\rho_f$, and $\alpha_h = h_f/l$. In this example, it can be calculated that both coefficients equal to 0.9. Then equation (4.25) is modified for l =1 m, v_f = 1 m/s and rewritten as

$$\frac{dv_s}{(1-v_s)^2} = dt \tag{4.26}$$

Considering the boundary condition of t = 0 s, v_s = 0 m/s, v_s is obtained as

$$v_s = \frac{1}{1+\frac{1}{t}} \tag{4.27}$$

Subsequently, it is calculated by the proposed extended 3D DDA with a step duration of 0.005 s and contact spring stiffness of 3 GPa. The simulated movement process is shown in Figure 4.19. The simulated block velocity is compared against the analytical solution, as shown in Figure 4.20, exhibiting good convergence.

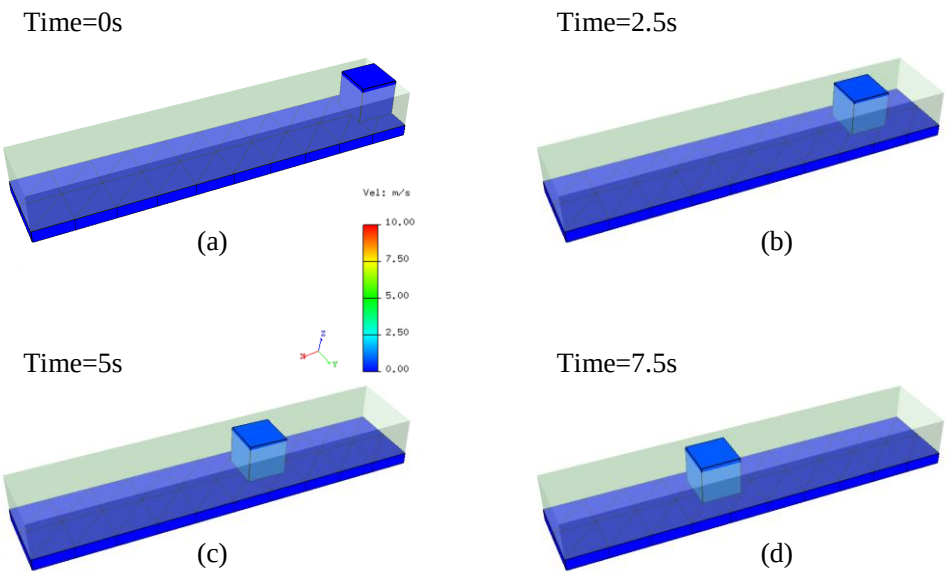

Figure 4.19 Block acceleration model calculated by the extended 3D DDA with fluid dynamics

To further address the drag force computing, another block rotation example is also presented. The block is also floated in the fluid to test the buoyancy during the dynamic process. However, the differences from the last validation example are

the block initial state (rotating with an angular velocity ω_0 = 1 rad/s) and the flow state (being static). As a result, the rotation of the floating block will be gradually decelerated by the fluid. An analytical solution is first deduced.

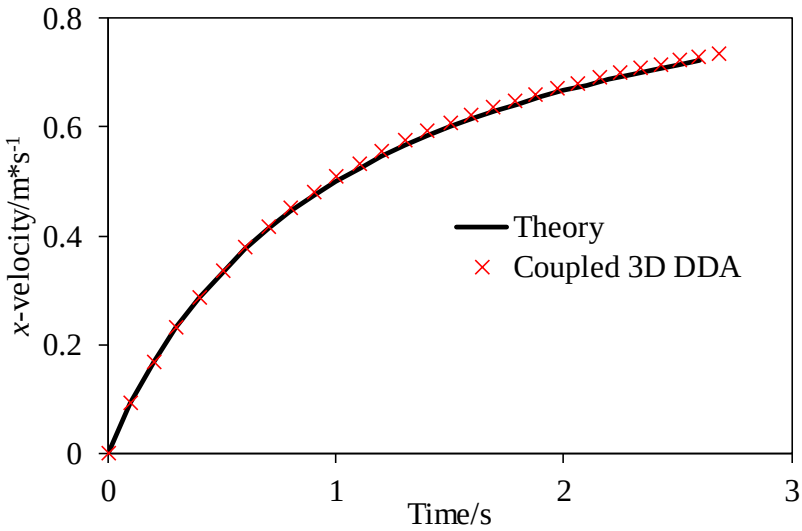

Figure 4.20 Block velocity calculated by the extended 3D DDA and analytical solution

In Figure 4.21 (a), the normal relative velocity distribution between the facets of the rotating block and the surrounding static fluid is in a triangle pattern.

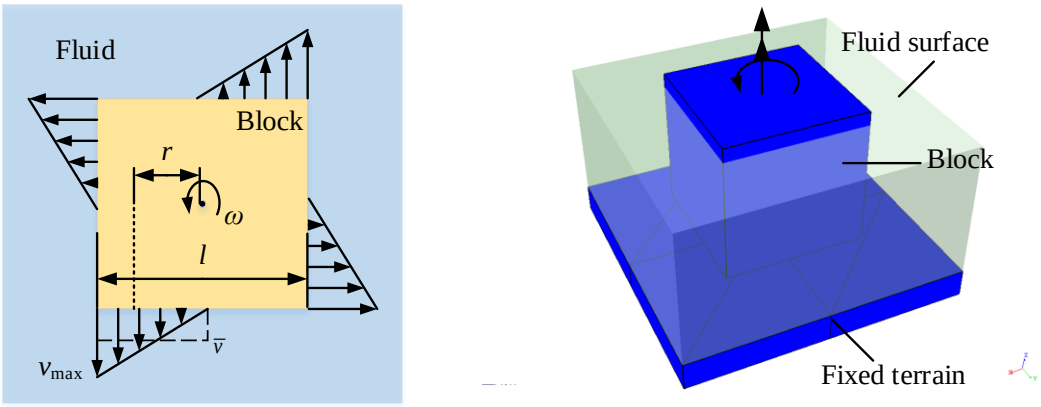

(a) (b)

Figure 4.21 (a) A schematic figure and (b) calculation model in the E-DDA of the block rotation deceleration example (Unit: m, s)

Denote the maximum relative perpendicular velocity as v_{max}. Referring to a simple geometric relation, v_{max} can be written as

$$v_{\max} = \omega \frac{\sqrt{2}}{2} l \cdot \frac{\sqrt{2}}{2} = \frac{\omega l}{2} \tag{4.28}$$

where ω is the instant angular velocity of the rotating block. Let F_r denotes the resistant force on a lateral facet acted by flow. For simplicity, the average relative velocity $\bar{v}$ is used to uniform the triangularly distributed velocity, and $\bar{v} = v_{\max} / 2 = \omega l / 4$. The acting area of $\bar{v}$ is the half facet in Figure 4.21 (a). Then F_r is represented by

$$F_r = \rho_f A \bar{v}^2 = \rho_f (\frac{\omega l}{4})^2 h_f \frac{l}{2} = \frac{\rho_f l^3 h_f}{32} \omega^2 \tag{4.29}$$

It is worth to note that in accordance with the rule $\boldsymbol{v} \cdot \boldsymbol{n} < 0$ mentioned in Section 4.4, only half of the facet area (marked by distributed force) in equation (4.29) is counted for drag force so that the negative drag forces are avoided. In this example, the resultant action is a moment M generated by the drag forces on four facets, which is calculated by

$$M = 4 F_r r \tag{4.30}$$

where r is the distance from the resistant force F to the center of the block. In this case, because the drag force is distributed in a triangular form, therefore $r = l/3$. Then a differential equation is derived:

$$-\frac{d\omega}{dt} = \frac{M}{I} = 4 \frac{\rho_f l^3 h_w}{32} \omega^2 \frac{l}{3} \frac{6}{\rho_s l^5} = \frac{\alpha_h}{4\alpha_\rho} \omega^2 \tag{4.31}$$

where I denotes the moment of inertia. For the given cube, $I = \rho_s l^5/6$. Similarly, α_h and α_ρ both equal to 0.9. Applying the boundary condition $t = 0$, $\omega = \omega_0 = 1$ rad/s, the angular velocity of the floating block can be expressed as

$$\omega = \frac{1}{\frac{t}{4} + 1} \tag{4.32}$$

Subsequently, it is calculated by the 3D DDA-DFS. Computational parameters are the same as those used in the last example. The simulated movement process is

shown in Figure 4.22. The simulated block angular velocity is compared against the analytical solution, as shown in Figure 4.23. A good agreement between them can be observed.

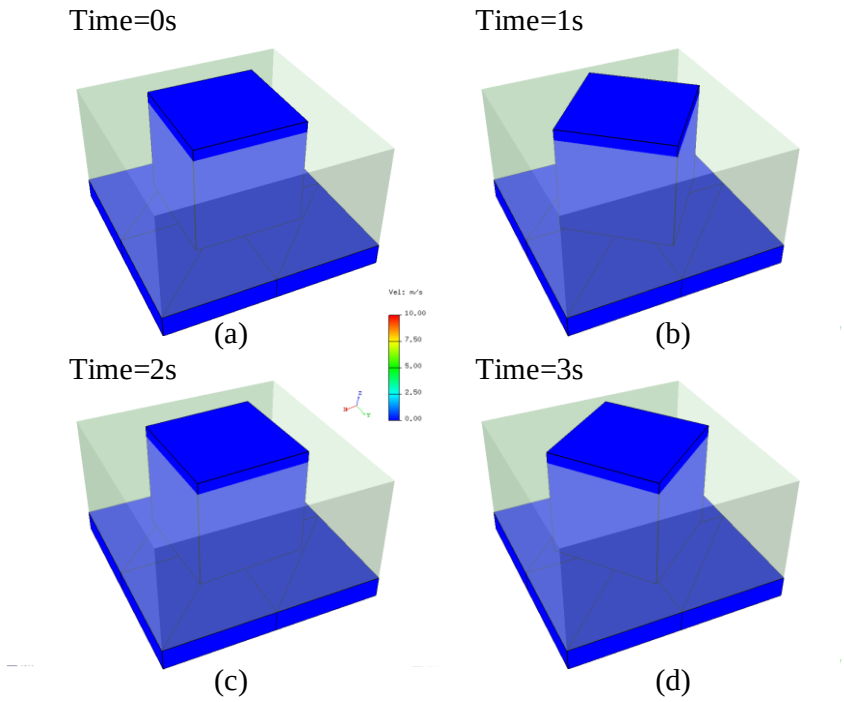

Figure 4.22 Diagram of the floated rotating block decelerated by fluid

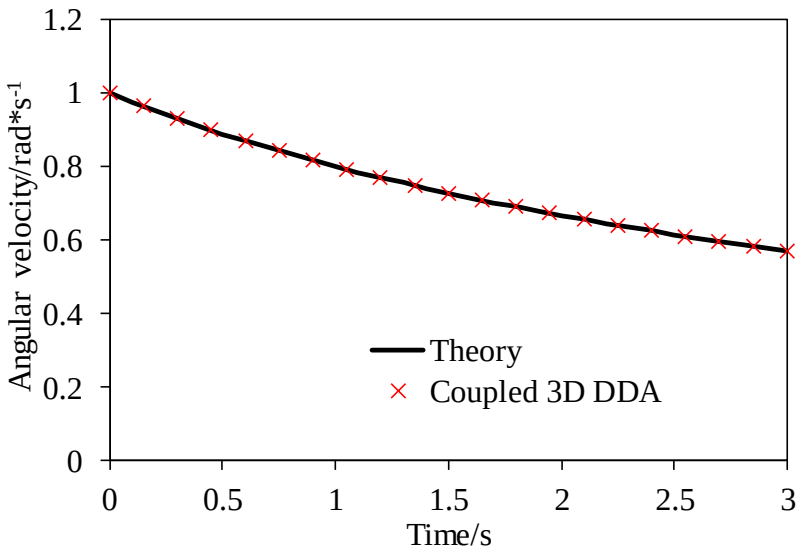

Figure 4.23 Block angular velocity calculated by the extended 3D DDA and analytical solution

The example given in Figure 4.24 is used to illustrate the interactions between blocks when they are both in flow. Two blocks are floating in flow, and they are initially static. The flow has a constant velocity 1 m/s. The model is executed by 3D DDA-DFS and the simulated results are presented in Figure 4.25. It is observed that when block interaction in flow is considered, the movement of the upstream block is faster than the downstream one. In comparison, without the implementation of interaction, the two blocks are accelerated and travelling at the same velocity.

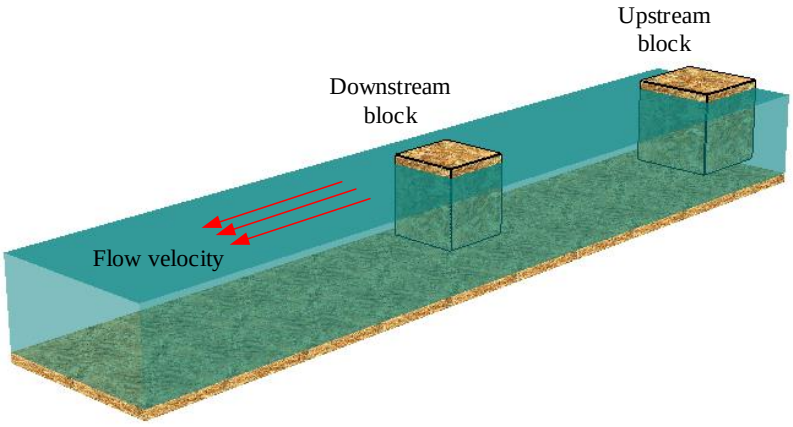

Figure 4.24 Example used to illustrate multi-block interaction

4.8. CONCLUSIONS

An interactive framework of coupled 3D DDA–DFS was proposed to simulate the debris flow with large boulders, and the flow – solid interactions are also presented in detail. The additional interactive module is used to evaluate the interactive forces between flow and solid phase and synchronize the 3D DDA module and DFS module. The following conclusions can be drawn:

(1) The proposed interactive framework is applicable to the coupled 3D DDA-DFS program.

(2) The flow force on solid blocks, including static pressure, buoyancy and drag force, are considered and calculated. Algorithms have been developed to evaluate those flow forces for arbitrarily shaped polyhedral blocks on complex meshed 3D terrain. In addition, the influence of nearby blocks on drag force is addressed so that the calculated drag force is more realistic.

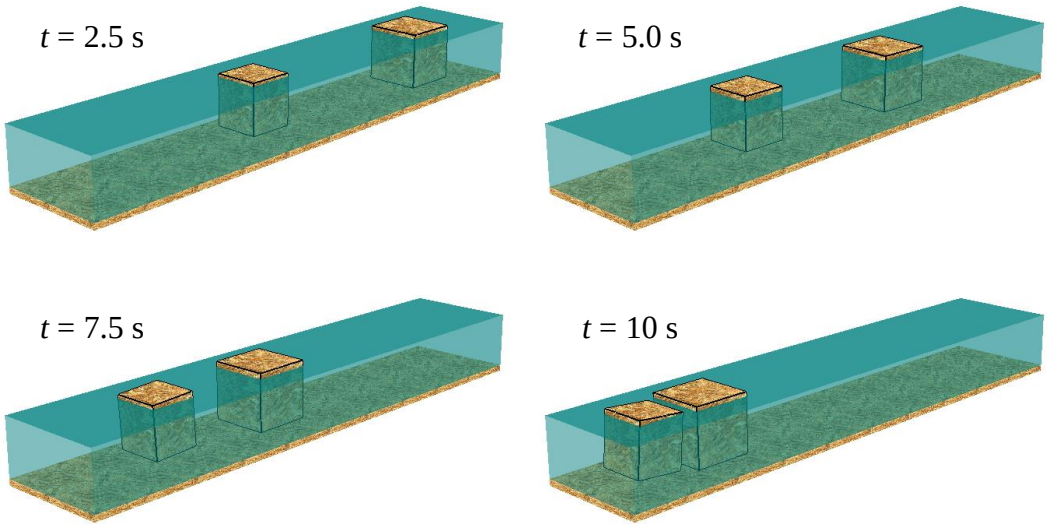

(a)

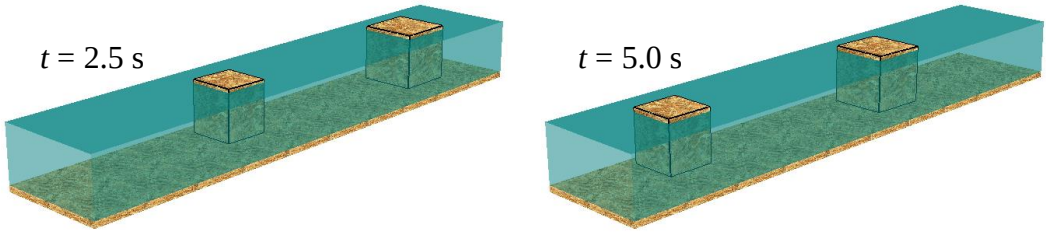

(b)

Figure 4.25 Simulated results for (a) considering blocks interaction in flow and (b) no interaction

(3) The actions of solid blocks to flow are also discussed. The direct implementation of force on flow is difficult because it is a problem involving large deformed boundary condition in the flow governing equation. An equivalent solution is proposed, in which the action of blocks on flow is regarded as time-varying terrain node elevation.

(4) Examples are given to validate the coupling scheme as well as the calculations of the interaction forces. The related interactive forces are calculated in a series of examples, and the validity of the calculations is confirmed.

REFERENCE

Bao, H. R., & Zhao, Z. Y. (2012). The vertex-to-vertex contact analysis in the two-dimensional discontinuous deformation analysis. Advances in Engineering Software, 45(1), 1-10.

Bearman, P. W., & Obasaju, E. D. (1982). An experimental-study of pressure-fluctuations on fixed and oscillating square-section cylinders. Journal of Fluid Mechanics, 119(Jun), 297-321.

Bhattacharyya, S., & Dhinakaran, S. (2008). Vortex shedding in shear flow past tandem square cylinders in the vicinity of a plane wall. Journal of Fluids and Structures, 24(3), 400-417.

Bishop, R. E. D., & Hassan, A. Y. (1964). The lift and drag forces on a circular cylinder in a flowing fluid. Proceedings of the Royal Society of London. Series A. Mathematical and Physical Sciences, 277(1368), 32-50.

Chatterjee, D., & Mondal, B. (2012). Forced convection heat transfer from tandem square cylinders for various spacing ratios. Numerical Heat Transfer, Part A: Applications, 61(5), 381-400.

Chen, G. Q., Zheng, L., Zhang, Y. B., & Wu, J. (2013). Numerical simulation in rockfall analysis: a close comparison of 2-D and 3-D DDA. Rock Mechanics and Rock Engineering, 46(3), 527-541.

Doolin, D. M. (2005). Unified displacement boundary constraint formulation for discontinuous deformation analysis (DDA). International Journal for Numerical and Analytical Methods in Geomechanics, 29(12), 1199-1207.

Fu, X. D., Sheng, Q., Zhang, Y. H., & Chen, J. (2015). Application of the discontinuous deformation analysis method to stress wave propagation through a one-dimensional rock mass. International Journal of Rock Mechanics and Mining Sciences, 80, 155-170.

Gao, L., Zhang, L. M., & Chen, H. X. (2017). Two-dimensional simulation of debris flow impact pressures on buildings. Engineering Geology, 226, 236-244.

Guo, L., Li, T., Chen, G., Yu, P., Peng, X., & Yang, D. (2019). A method for microscopic unsaturated soil-water interaction analysis based on DDA. Computers and Geotechnics, 108, 143-151.

Han, Z., Chen, G., Li, Y., Tang, C., Xu, L., He, Y., Huang, X., & Wang, W. (2015). Numerical simulation of debris-flow behavior incorporating a dynamic method for estimating the entrainment. Engineering Geology, 190, 52-64.

Han, Z., Chen, G., Li, Y., Zhang, H., & He, Y. (2014). Elementary analysis on the bed-sediment entrainment by debris flow and its application using the TopFlowDF model. Geomatics, Natural Hazards and Risk, 7(2), 764-785.

Hoerner, S. F. (1965). Fluid-dynamic drag: practical information on aerodynamic drag and hydrodynamic resistance (2ed ed.): Hoerner Fluid Dynamics.

Hopkins, M. A. (2014). Polyhedra faster than spheres? Engineering Computations, 31(3), 567-583.

Hunger, O., & Morgan, G. C. (1984). Quantitative analysis of debris torrent hazards for design of remedial measures. Canadian Geotechnical Journal, 21(4), 663-677.

Jiao, Y.-Y., Zhao, Q., Wang, L., Huang, G.-H., & Tan, F. (2019). A hybrid MPI/OpenMP parallel computing model for spherical discontinuous deformation analysis. Computers and Geotechnics, 106, 217-227.

Jsce. (1971). Hydraulic formula. Japan: Japan Society of Civil Engineers.

Kaidi, S., Rouainia, M., & Ouahsine, A. (2012). Stability of breakwaters under hydrodynamic loading using a coupled DDA/FEM approach. Ocean Engineering, 55, 62-70.

Kim, M. K., Kim, D. K., Yoon, S. H., & Lee, D. H. (2008). Measurements of the flow fields around two square cylinders in a tandem arrangement. Journal of Mechanical Science and Technology, 22(2), 397-407.

Li, Z. J., Liu, S. G., Zhang, H., Chen, G. Q., Wu, W., Zhu, H. H., Zhuang, X. Y., & Wang, W. (2018). Simulating the damage extent of unreinforced brick masonry buildings under boulder impact using three-dimensional discontinuous deformation analysis (3-D DDA). Engineering Failure Analysis, 93, 122-143.

Liu, C. H., & Chen, J. M. (2002). Observations of hysteresis in flow around two square cylinders in a tandem arrangement. Journal of Wind Engineering and Industrial Aerodynamics, 90(9), 1019-1050.

Lo, S.-C., Hoffmann, K. A., & Dietiker, J.-F. (2005). Numerical investigation of high Reynolds Number flows over square and circular cylinders. Journal of Thermophysics and Heat Transfer, 19(1), 72-80.

Ma, G. C., Kaneko, F., & Hori, S. (2010). Application of DDA to evaluate the dynamic behaviour of submarine landslides which generated tsunamis in the Marmara Sea. Analysis of Discontinuous Deformation: New Developments and Applications, 185-192.

Ma, G. C., Yashima, A., Nishiyama, S., Ohnishi, Y., Monma, K., & Matsuyama, H. (2008). Application of DDA to evaluate the mechanism of rock slope instability/rock fall. 3rd International Symposium on Modern Mining & Safety Technology Proceedings, 67-78.

Ma, S. Q., Zhao, Z. Y., Nie, W., Nemcik, J., Zhang, Z. Y., & Zhu, X. (2017). Implementation of displacement-dependent Barton-Bandis rock joint model into discontinuous deformation analysis. Computers and Geotechnics, 86, 1-8.

Mikola, R., & Sitar, N. (2013). Next generation discontinuous rock mass models: 3-D and rock-fluid interaction. Frontiers of Discontinuous Numerical Methods Practical Simulations in Engineering Disaster Prevention, 81-90.

Peng, X., Chen, G., Yu, P., Zhang, Y., Guo, L., Wang, C., Cheng, X., & Niu, H. (2019a). Parallel computing of three-dimensional discontinuous deformation analysis based on OpenMP. Computers and Geotechnics, 106, 304-313.

Peng, X., Chen, G., Yu, P., Zhang, Y., & Wang, J. (2019b). Improvement of joint definition and determination in three-dimensional discontinuous deformation analysis. Computers and Geotechnics, 110, 148-160.

Peng, X., Yu, P., Zhang, Y., & Chen, G. (2018). Applying modified discontinuous deformation analysis to assess the dynamic response of sites containing discontinuities. Engineering Geology, 246, 349-360.

Rajani, B. N., Kandasamy, A., & Majumdar, S. (2009). Numerical simulation of laminar flow past a circular cylinder. Applied Mathematical Modelling, 33(3), 1228-1247.

Sakamoto, H., Hainu, H., & Obata, Y. (1987). Fluctuating forces acting on two square prisms in a tandem arrangement. Journal of Wind Engineering and Industrial Aerodynamics, 26(1), 85-103.

Shen, W., Li, T., Li, P., & Guo, J. (2018). A modified finite difference model for the modeling of flowslides. Landslides, 15(8), 1577-1593.

Shi, G. (1989). Discontinuous deformation analysis a new numerical model for the static and dynamics of block systems. (Ph.D.). UC Berkeley, USA.

Singha, S., & Sinhamahapatra, K. P. (2010). High-resolution numerical simulation of low Reynolds Number incompressible flow about two cylinders in tandem. Journal of Fluids Engineering-Transactions of the Asme, 132(1).

Sohankar, A. (2012). A numerical investigation of the flow over a pair of identical square cylinders in a tandem arrangement. International Journal for Numerical Methods in Fluids, 70(10), 1244-1257.

Sutherland, I. E., & Hodgman, G. W. (1974). Reentrant polygon clipping. Communications of the ACM, 17(1), 32-42.

Tatsutani, K., Devarakonda, R., & Humphrey, J. a. C. (1993). Unsteady-flow and heat-transfer for cylinder pairs in a channel. International Journal of Heat and Mass Transfer, 36(13), 3311-3328.

Troesch, A. W., & Kim, S. K. (1991). Hydrodynamic-forces acting on cylinders oscillating at small amplitudes. Journal of Fluids and Structures, 5(1), 113-126.

Wang, L.-Z., Jiang, H.-Y., Yang, Z.-X., Xu, Y.-C., & Zhu, X.-B. (2013). Development of discontinuous deformation analysis with displacement-dependent interface shear strength. Computers and Geotechnics, 47, 91-101.

Wang, W., Chen, G. Q., Zhang, H., Zhou, S. H., Liu, S. G., Wu, Y. Q., & Fan, F. S. (2016). Analysis of landslide-generated impulsive waves using a coupled DDA-SPH method. Engineering Analysis with Boundary Elements, 64, 267-277.

Wang, W., Chen, G. Q., Zhang, Y. B., Zheng, L., & Zhang, H. (2017). Dynamic simulation of landslide dam behavior considering kinematic characteristics using a coupled DDA-SPH method. Engineering Analysis with Boundary Elements, 80, 172-183.

Wang, X., Wu, W., Zhu, H., Lin, J.-S., & Zhang, H. (2019). Contact detection between polygonal blocks based on a novel multi-cover system for discontinuous deformation analysis. Computers and Geotechnics, 111, 56-65.

Weiler, K., & Atherton, P. (1977). Hidden surface removal using polygon area sorting. Paper presented at the ACM SIGGRAPH computer graphics.

Wu, J.-H., Ohnishi, Y., Shi, G.-H., & Nishiyama, S. J. I. J. O. G. (2005). Theory of three-dimensional discontinuous deformation analysis and its application to a slope toppling at Amatoribashi, Japan. 5(3), 179-195.

Wu, J. H., & Chen, C. H. (2011). Application of DDA to simulate characteristics of the Tsaoling landslide. Computers and Geotechnics, 38(5), 741-750.

Wu, J. H., Ohnishi, Y., & Nishiyama, S. (2004). Simulation of the mechanical behavior of inclined jointed rock masses during tunnel construction using Discontinuous Deformation Analysis (DDA). International Journal of Rock Mechanics and Mining Sciences, 41(5), 731-743.

Yen, S. C., San, K. C., & Chuang, T. H. (2008). Interactions of tandem square cylinders at low Reynolds numbers. Experimental Thermal and Fluid Science, 32(4), 927-938.

Yu, P., Zhang, Y., Peng, X., Wang, J., Chen, G., & Zhao, J. X. (2019). Evaluation of impact force of rock landslides acting on structures using discontinuous deformation analysis. Computers and Geotechnics, 114.

Zevenbergen, L., Arneson, L., Hunt, J., & Miller, A. C. (2012). Hydraulic design of safe bridges. Federal Highway Administration.

Zhang, H., Liu, S.-G., Chen, G.-Q., Zheng, L., Zhang, Y.-B., Wu, Y.-Q., Jing, P.-D., Wang, W., Han, Z., Zhong, G.-H., & Lou, S. (2016). Extension of three-dimensional discontinuous deformation analysis to frictional-cohesive materials. International Journal of Rock Mechanics and Mining Sciences, 86, 65-79.

Zhang, Y., Chen, G., Zheng, L., Li, Y., & Wu, J. (2013). Effects of near-fault seismic loadings on run-out of large-scale landslide: A case study. Engineering Geology, 166, 216-236.

Zhang, Y., Xu, Q., Chen, G., Zhao, J., & Zheng, L. (2014). Extension of discontinuous deformation analysis and application in cohesive-frictional slope analysis. International Journal of Rock Mechanics and Mining Sciences, 70, 533-545.

Zhang, Y., Zhang, J., Chen, G., Zheng, L., & Li, Y. (2015). Effects of vertical seismic force on initiation of the Daguangbao landslide induced by the 2008 Wenchuan earthquake. Soil Dynamics and Earthquake Engineering, 73, 91-102.

Zhang, Y. B., Wang, J. M., Xu, Q., Chen, G. Q., Zhao, J. X., Zheng, L., Han, Z., & Yu, P. C. (2015). DDA validation of the mobility of earthquake-induced landslides. Engineering Geology, 194, 38-51.

Zhao, X., Cheng, D., Zhang, D., & Hu, Z. (2016). Numerical study of low-Reynolds-number flow past two tandem square cylinders with varying incident angles of the downstream one using a CIP-based model. Ocean Engineering, 121, 414-421.

Zheng, L., Chen, G., Zen, K., & Kasama, K. (2011). The method of slope modelling for rockfall analysis using 3D DDA. Paper presented at the 10th International Conference on Advances in Discontinuous Numerical Methods and Applications in Geomechanics and Geoengineering, Honolulu, Hawaii.

CHAPTER 5

CLARIFICATION OF THE BEHAVIORS OF LARGE BOULDERS AND DRIFTWOODS IN DEBRIS FLOW[2]

5.1. INTRODUCTION

Conventional debris flow simulation with a depth-integrated model based on Navier-Stokes equations has been widely used because it can be easily applied to simulate evolutions of debris flow with bed-sediment erosion as well as estimate kinematic behaviors such as flowing velocity, depth and volume of debris flow and inundated area with high efficiency. However, large boulders and driftwoods are often involved in debris flows according to a large number of past events. It is obvious that the behaviors and impact force of boulder debris flow cannot be correctly estimated by DFS with a two-phase fluid model.

Those involved large objects may be able to cause serious damage to the structures in its path. It is important to investigate the impact forces and deformations that the dam suffers from are analyzed under different kinds of debris flows. In this section, the impact force and deformation that the dam suffers from

---

[2] Chapter 5 is partially based on the following journal paper:

Yu P, Zhang Y, Peng X, Wang J, Chen G, Zhao JX (2019) Evaluation of impact force of rock landslides acting on structures using discontinuous deformation analysis Computers and Geotechnics 114 doi:10.1016/j.compgeo.2019.103137

are studied under the varying factors of existence of the boulders, the size, the distribution and the shape of the boulders.

5.2. MODEL SETTINGS, PARAMETERS AND CONSTRUCTION

A conceptual model is built to clarify the influence of large boulders on the flow evolving and dam safety. The general setting of the adopted model is giving in Figure 5.1. A slope with an inclination of 20° is placed on a horizontal plane. At the middle of the slope, there is a wedged channel. The upper surfaces of the slope, channel and the horizontal plane together form the terrain of the model. The terrain has been meshed in 2.5×2.5 m cells. To reflect the ground coarseness in reality, random height variations are assigned to the terrain nodes. The terrain has a total dimension of 200×300×53 m. A dam with a rectangular section profile 5×3 m is settled at the bottom of the channel, which is comprised of hundreds of sub-blocks. Given to the channel shape, the maximum dam length is 47 m. Above the dam along the slope there are some boulders, and above the boulders is the initial position of the debris flow mass. When the simulation begins, the mass starts to move downslope due to gravity, which further triggers the motions of boulders when flow passes by. The mixture of flow mass and boulders then collapses with the dam. If the dam is strong enough, the mixture will be stopped at the dam; otherwise, the dam will be damaged or even destroyed, the fragments of the dam will travel together with the mixture and finally be stopped when the kinetic energy is dissipated. The influence of boulder, flow property to the debris flow runout and dam safety will be tested in the following sections.

The dam used in the examples is meshed by joints in prior. There are two types of joints in 3D DDA: real joints and virtual joints. The real joints are generated due to the existence of fractures in a single material or the boundary between two objects. Whereas the virtual joints represent the block boundary of the continuous area, which are created to enable the detailed cracking failure process (Zhu, W. et al., 2014). The strength of virtual joint is determined by the strength of the continuous material, and it is generally much larger than that of a real joint. When the stress exceeds the strength of the virtual joint, it will be developed to be a real joint. The

idea of virtual joints has been widely used in the application of DDA method. For example, Jiao, Y. et al. (2012) proposed a DDARF method with the use of virtual joints to realize crack propagation when modelling jointed rock failure process; Choo, L. Q. et al. (2016) studied hydraulic fracturing problems using DDA incorporating with virtual joints. Here, the idea of virtual joints will be adopted to realize the progressive fracturing of the dam.

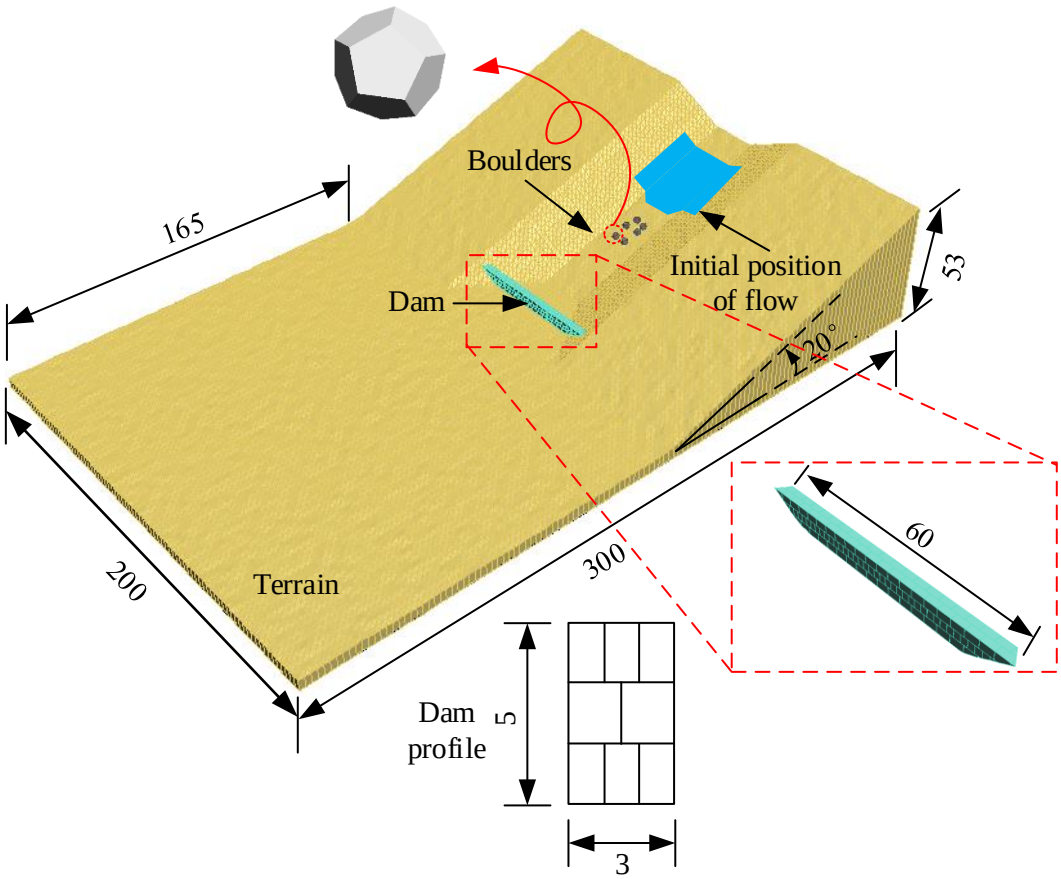

Figure 5.1 Description of the adopted model (unit: m)

The model base is a large 3D DDA block which is fixed, and the upper surfaces of which is served as terrain mesh. The relative physical parameters for the base block are: Young's Modulus 10 GPa, Poisson's ratio 0.1, density 2000 kg/m^3. The surface joint parameters are: friction angle 40°, cohesion and tensile strength 0. The physical parameters for the dam are: Young's Modulus 30 GPa, Poisson's ratio 0.2, density 2500 kg/m^3. The joint parameters are: friction angle 54.9°, cohesion 3.18 MPa, tensile strength 0. The joint parameters are selected according to the

properties of C30 concrete. The friction angle is greater than 45° because the dam is intact, and the joint friction angle should be internal. The physical parameters of the boulders are: Young's Modulus 10 GPa, Poisson's ratio 0.1, density 2500 kg/m^3. The joint parameters are: friction angle 40°, cohesion and tensile strength 0.

The control parameters for calculation are: maximum time step size 0.0001 s, maximum allowed displacement ratio 0.02, contact spring stiffness 100 GPa. To address the energy dissipation in collisions, the contact damping coefficient is employed. As presented in Section 3.2 and Section 3.4, a two-block dynamic system is built to evaluate a proper contact damping ratio. Rewrite equation (3.36) here:

$$c = 2(\xi - \xi_n)\sqrt{\frac{m_1 m_2}{m_1 + m_2}k} = 2\left(-\frac{\ln e_i}{\sqrt{\ln^2 e_i + \pi^2}} - \frac{\ln(1+\Omega^2/2)}{2\Omega}\right)\sqrt{\frac{m_1 m_2}{m_1 + m_2}k} \tag{4.33}$$

The blocks are in different sizes. However, according to volumes of blocks, the mass range can be determined. A typical dam block has a volume of about 7.5 m^3, and for a boulder block, it is about 9.5 m^3. Using densities of the dam and boulder, the masses of individual dam and boulder block are calculated as m_1 = 7.5 × 2500 = 18750 kg, m_2 = 9.5 × 2500 = 23750 kg. The value of COR is empirically selected based on researches from rockfall researches (Asteriou, P. et al., 2012; Asteriou, P. et al., 2015; Li, L.-P. et al., 2015), in which the CORs of rock can vary within a wide range. The collisions between the dam and boulders are focused. It is assumed that the dam and boulders in this study are relatively stiff, therefore, a COR around 0.8 is acceptable. According to the discussions above, the input parameter, i.e., damping ratio for damped contact, is selected as 30000 N/(m/s), which leads to a COR of about 0.81.

The properties of debris flow are: density 1650 kg/m^3, dynamic viscosity 0.11 Pa·s, step time duration 0.001 s, flow mass internal 28° and moment correction ratio 1.25. For simplicity, the entrainment and deposition of debris flow are not considered. The initial flow is defined as shown in Figure 5.2. The initial volume of debris flow mass is controlled by the height of the mass.

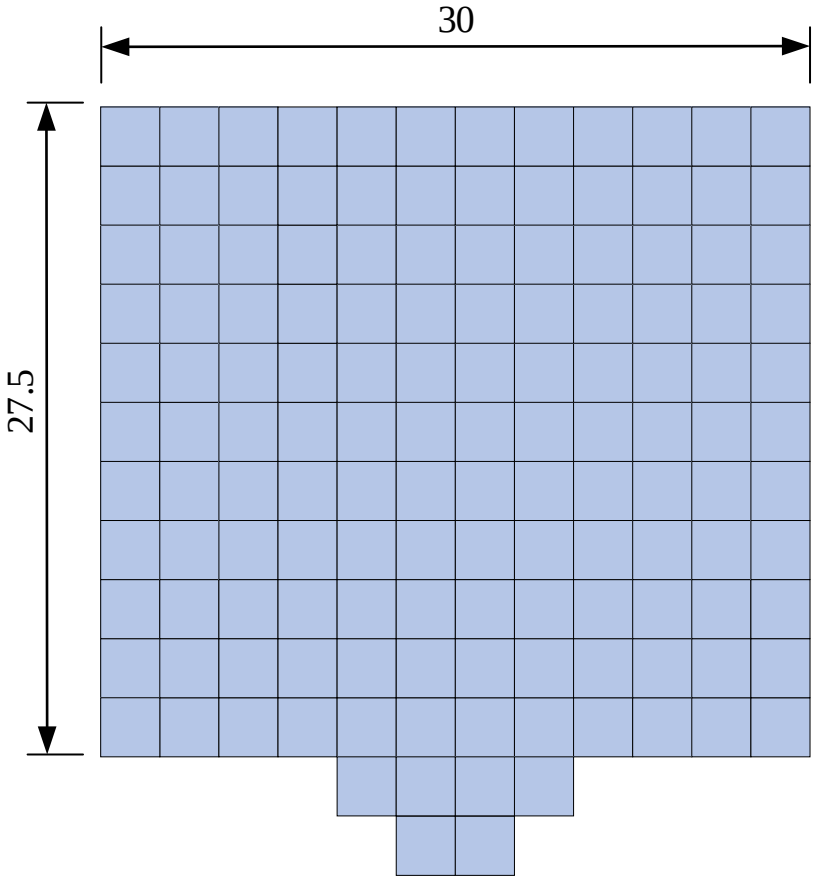

Figure 5.2 The dimension of the initial debris flow mass area (unit: m)

The models involved are generated by a “free-fall” method, because the terrain is uneven, and the location of boulders is hard to assign. To properly address the boulder positions, a “boulder zone” is first defined on the slope, about 50 m away horizontally from the dam. The boulders are modelled in this area, however not in touch with the channel surface. This model is then simulated using 3D DDA-DFS, in which only gravity exists as an external force so that the suspended boulders will fall on to the terrain surface. After dissipating all the kinetic energy, the boulders eventually stop. Record and output the ultimate block geometry, and the models with boulders in proper positions are constructed. To accelerate the stabilizing of the boulders, extra damping is implemented by the kinetic ratio in 3D DDA 0.98. Debris flow is not involved at this stage. Examples of 6 boulders and 20 boulders are given to show the model construction procedures. Figure 5.3 and Figure 5.4 are the stabilizing of 6 boulders example. In Figure 5.3, the velocities after 15 s

decrease to negligibly small values, and the maximum displacement is about 0.7 m, as shown in Figure 5.4, which suggested that the model becomes stable without experiencing evident altering. Therefore, the geometries evolved after 15 s is suitable for an initial simulation state.

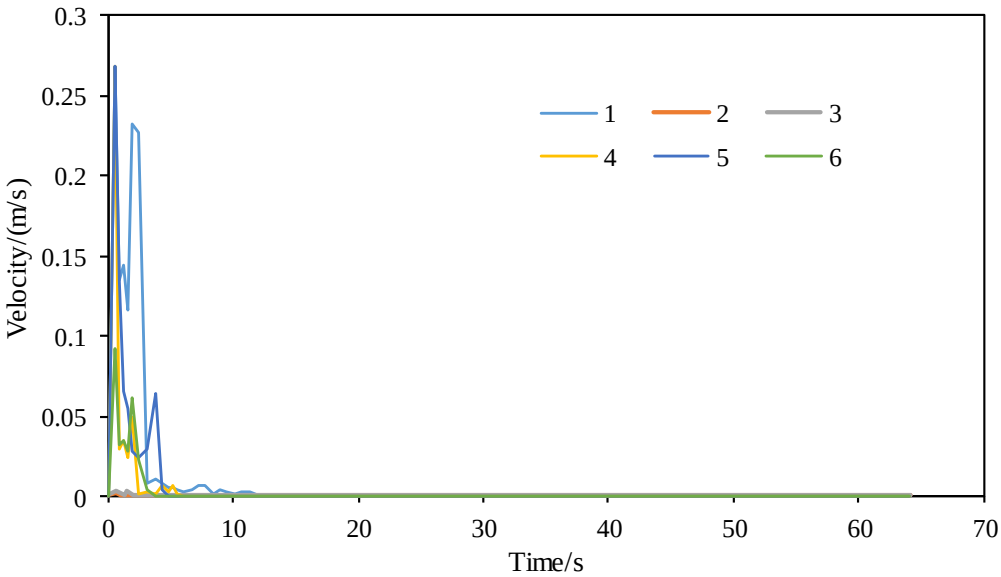

Figure 5.3 Block velocities in model generation

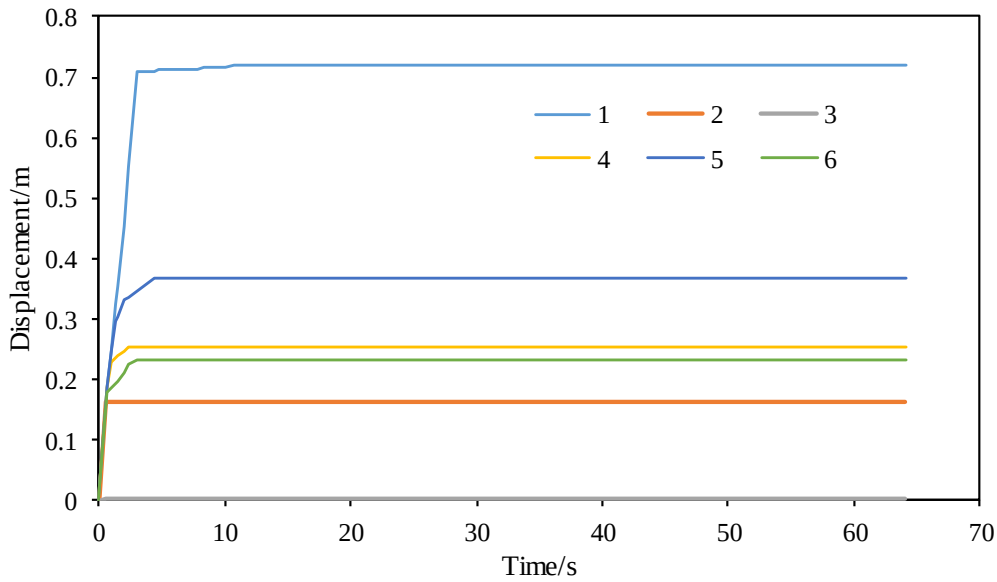

Figure 5.4 Block displacements in model generation

5.3. CONFIGURATION CASES: DAM STABILITY UNDER VARYING FLOW VOLUME

To configure the dynamic behaviors of the model under selected parameters, three cases without boulders are first tested. The models used are shown in Figure 5.1, and the changing flow mass volume is selected as variables. The changing volume is performed by modifying the initial depth of the flow mass in its defined area, which is given in Figure 5.2. The area of the flow initial position is 862.5 m^2. Therefore, the initial depths of 1 m, 2 m and 3 m corresponds to initial volume 862.5 m^3, 1725 m^3 and 2587.5 m^3. By setting the initial depth of the flow mass to 1 m, 2 m and 3 m, three cases (case 1, case 2 and case 3) of different flow mass volumes are established. Subsequently, these models are simulated by 3D DDA-DFS program. The screenshots of the simulations are given in Figure 5.5 – Figure 5.7. For the cases whose initial height equals to 1 m and 2 m, as shown in Figure 5.5 and Figure 5.6, respectively, the mass begins to flow down as driven by gravity. When t = 15 s, the very front of the flow in case 1 begins to arrive at the dam, however the flow mass has already been accumulated at the same time in case 2. It suggests that with the growth of debris flow volume, the flow travels faster. Although in different flow conditions, the debris flow in case 1 and case 2 still travel in a similar pattern: flow down, impact with dam and accumulate in front of it. The dams in those two cases remain stable, and the flow is also stopped by the dam. However, the situation changed in case 3 (Figure 5.7). Due to the increase of debris flow volume, although not much, some flow mass overflows the dam. In addition, the dam is no longer stable under growing impact force and pressure. After t = 20 s, an observable deformation occurs in the middle of the dam. It is further proven by the displacement time-history figures presented in Figure 5.8. The displacement in case 3 climbs to more than 0.4 m at t = 20 s, meanwhile the displacements of case 1 and 2 are only a few centimeters. Figure 5.9 exhibits the impact forces on dam, and the average magnitudes are growing with the increase of mass volume. Because the flow reaches the dam earlier when flow mass is larger, the impact force emerges in case 3 at 11 s, then case 2 about 13 s and case 1 about 15 s. Comparing to the displacements in Figure 5.8, the impact force generates earlier than

displacements, which is logical because displacements depend on the accumulation of momentum.

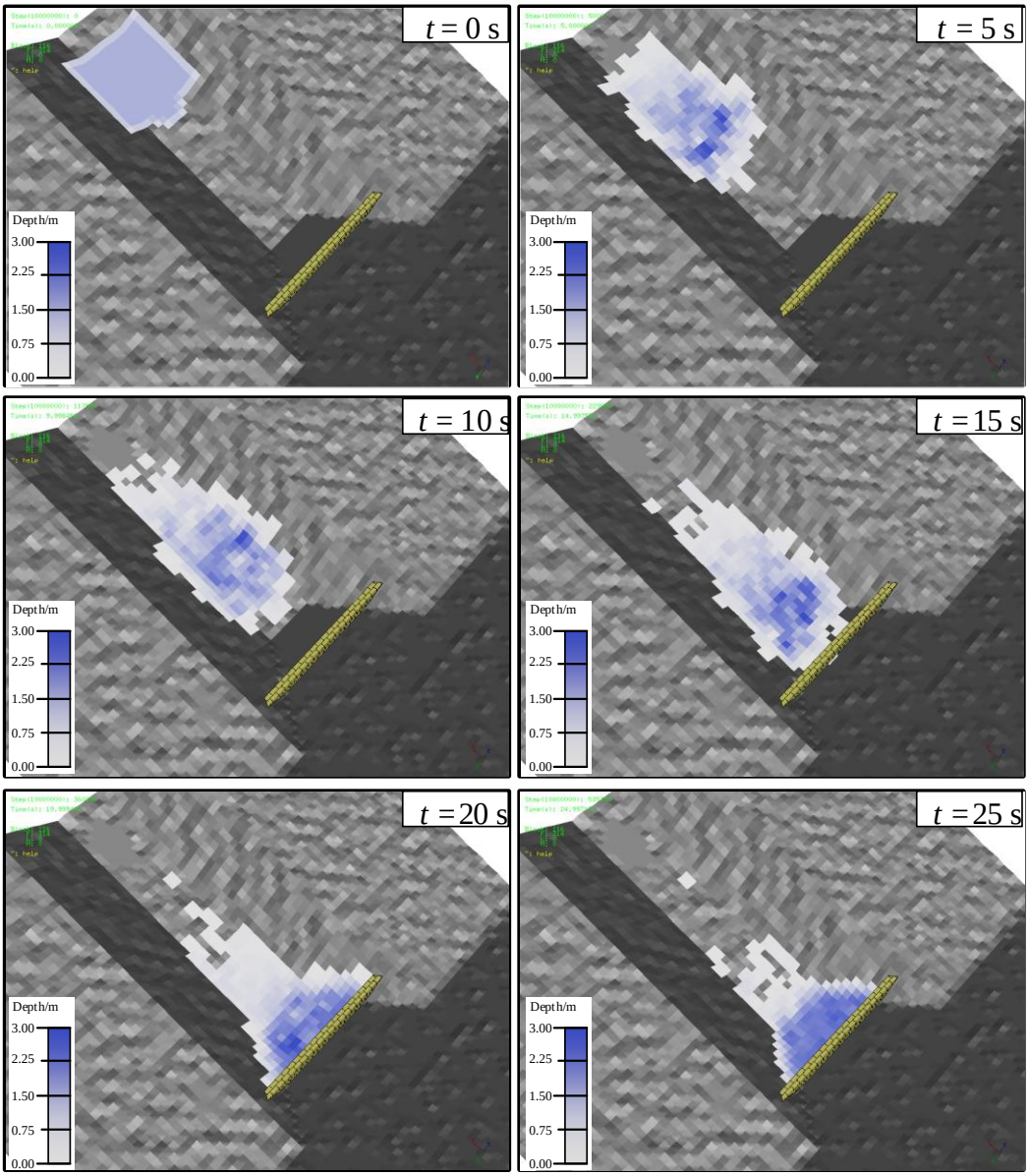

Figure 5.5 Flow depth of the simulation result with initial flow mass height 1 m

The results illustrated above are partially validated by a semi-analytical solution as follows. Referring to Figure 5.10, a rectangular dam with thickness b is subject to flow pressure. For a specific horizontal section at depth h, the resultant force of flow F_r is

$$F_r = (\rho_f g h^2) / 2 \tag{4.34}$$

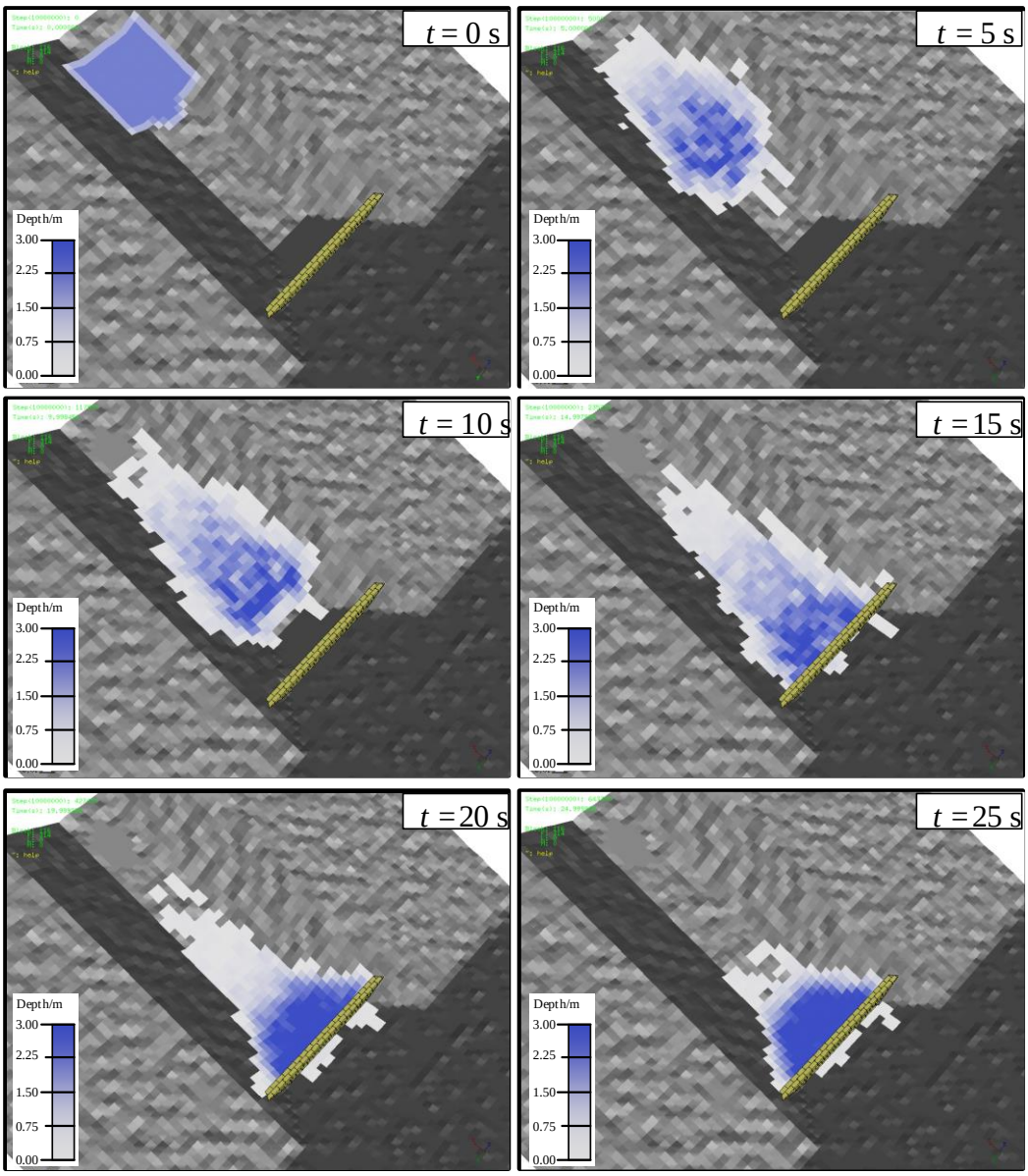

Figure 5.6 Flow depth of the simulation result with initial flow mass height 2 m

Meanwhile, the resistant frictional force is calculated by Mohr-Coulomb law:

$$f = b\rho_s g(h + \Delta h)\tan\phi \tag{4.35}$$

where ρ_s and ϕ is the density and internal friction angle of the dam. The critical h (noted as h_c) can be calculated by letting (4.34) equals to (4.35):

$$(\rho_f g h_c^2)/2 = b\rho_s g(h_c + \Delta h)\tan\phi \tag{4.36}$$

The solution is

$$h_c = b\lambda \tan\phi \pm \sqrt{b^2\lambda^2 \tan^2\phi + 2\lambda\beta\Delta h \tan\phi} \tag{4.37}$$

where ratio λ equals to ρ_s/ρ_f. In case 3, the flow accumulated in front of the dam is about 5 m in depth, which is the same height of the dam. Therefore, Δh equals to 0, and equation (4.37) is simplified as

$$h_c = 2b\lambda \tan\phi \tag{4.38}$$

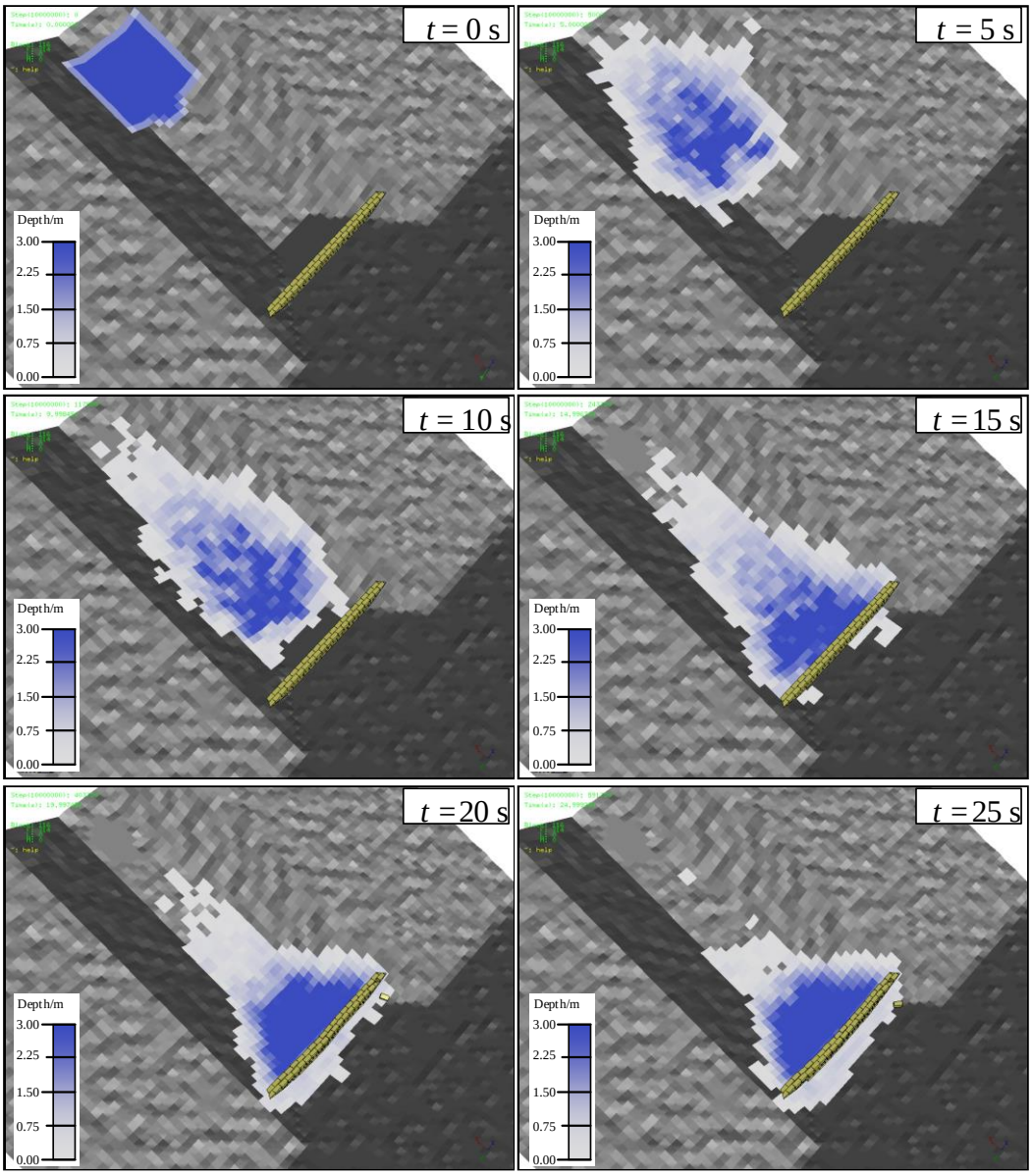

Figure 5.7 Flow depth of the simulation result with initial flow mass height 3 m

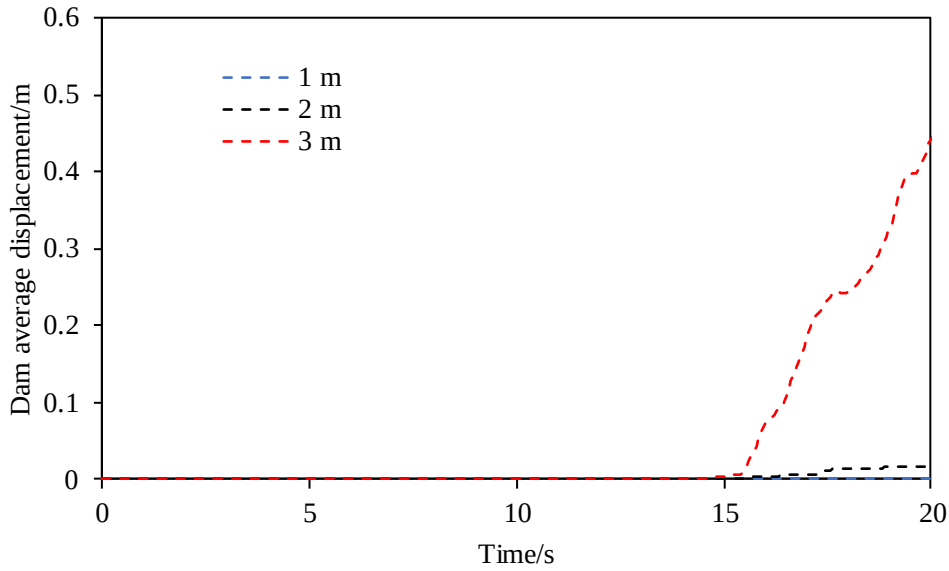

Figure 5.8 Average displacement of the dam in case 1 to 3

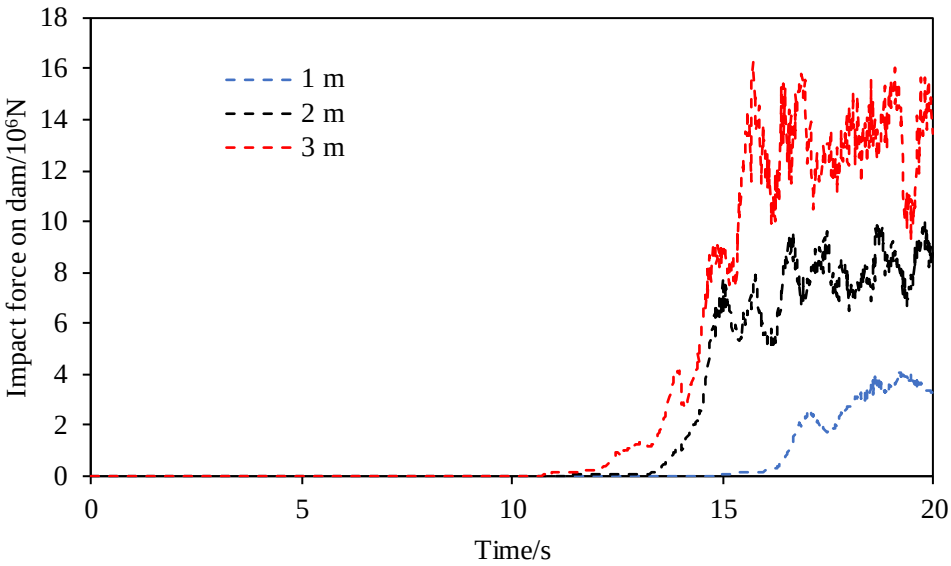

Figure 5.9 Total impact force on the dam in case 1 to 3

Taking values in case 3, $h_c \approx 7.63$ m. Because the bottom of the dam is selected to be the section, the frictional angle 40° is used. Since 7.63 m > 5 m, the dam should be stable under static water pressure. Nevertheless, the flow action in case 3 is not just static pressure. The force shown in Figure 5.9 also includes dynamic flow actions. The width of the dam is about 50 m, and the maximum friction is

$$f_{\max} = bhl\rho_s g \tan\phi \approx 1.5\times10^7 \text{ N} \tag{4.39}$$

The maximum flow action in case 3 is about 1.6×10^7 N, which is greater than f_{max}. But the action is just a little bit greater than friction, therefore the dam is just gradually deformed (from 20 s to 35 s), not be suddenly destroyed, as demonstrated in Figure 5.7.

According to the discussions above, the results yielded by simulations of 3D DDA-DFS is reasonable, which makes further studies involving boulders possible.

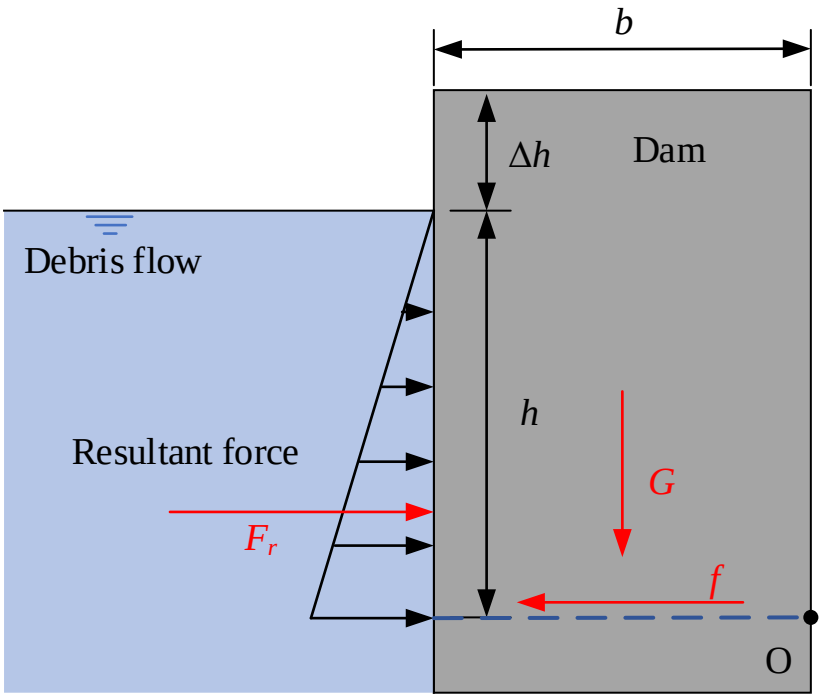

Figure 5.10 Force analysis diagram of dam stability

5.4. THE EFFECT OF BOULDERS ON THE CHECK DAM

Since the dam remains stable in case 1 and 2 in which the initial mass height is 1 m and 2 m, and unstable in case 3, the conditions in case 1 and 2 are used in this section to demonstrate the effects of boulders when exist. These two cases are named as case 6 and case 7, with case 4 (same with case 1) and 5 (same with case 2) the contract case without any boulders under the same condition. The screenshots for case 4-7 at t = 20 s are shown in Figure 5.12, and from which one may notice that the exitance of boulders causes much larger damages to the dam than the contrast cases 4 and 5 without boulders. Figure 5.12 (a) and (b) are the results under initial mass height 1 m. The flow along shows no damage on the dam, however the

impact of boulders makes observable deformation. Although the flow does not go through the dam, the large dam deformation implies that the dam is no longer safe. Figure 5.12 (c) and (d) are the results under initial mass height 2 m. Given the increase of flow mass volume, a small amount of flow overflows the dam, but the dam is still stable. When boulders exist, the dam is severely damaged. In Figure 5.12 (d), several dam blocks are knocked off due to the huge impacts of the boulders, which clearly gains more kinetic energy than case 6.

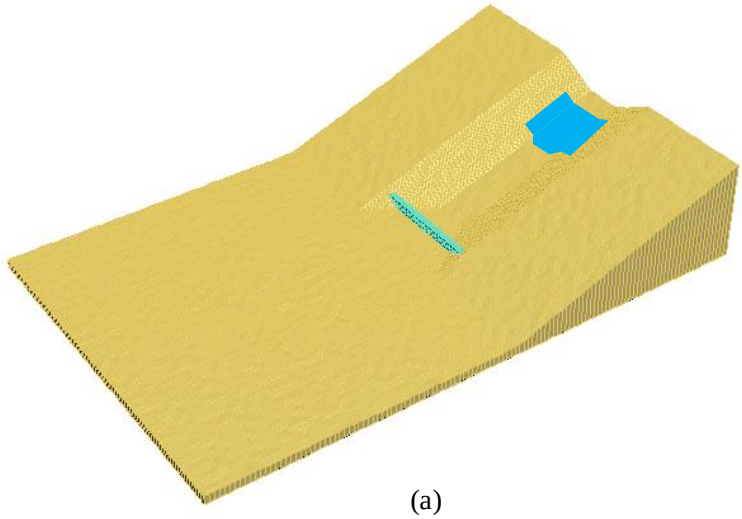

(a)

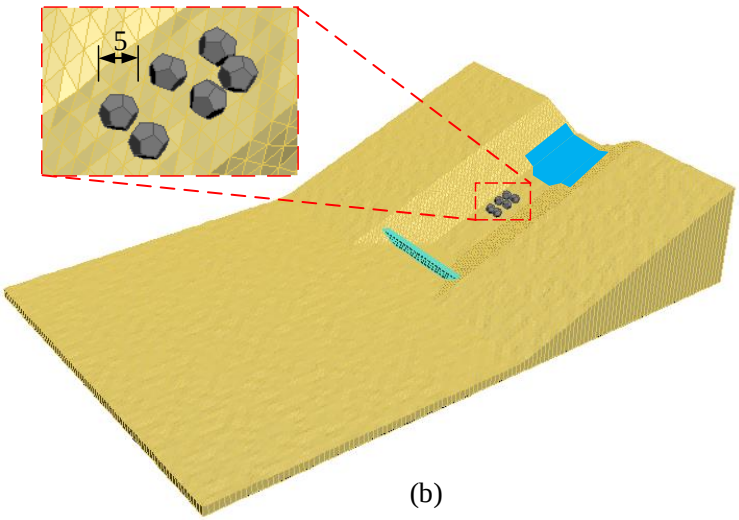

(b)

Figure 5.11 The cases used to illustrate the effect when boulders exist (a) the contrast cases without boulders, the initial flow mass height is 1 m (case 4) and 2 m (case 5) (b) the tested cases with boulders and initial flow mass height 1 m (case 6) and 2 m (case 7) (unit: m)

The flow goes through the breaches of the dam. The damage of the dam can be measured by the average deformation, shown in Figure 5.13. The average dam displacement $\bar{d}_{dam}$ is defined by

$$\bar{d}_{dam} = \frac{\sum m^i_{dam} d^i_{dam}}{\sum m^i_{dam}} \tag{4.40}$$

where d^i_{dam} and m^i_{dam} are the mass and deformation of dam block i. Figure 5.13 demonstrates that when there is no boulder, the deformation of the dam in case 4 is negligible, while very small in case 5. In contrast, the existence of boulders enlarges the deformation by dozens of times. In case 7 with an initial mass height 2 m, the average dam deformation climbs to nearly 0.9 m.

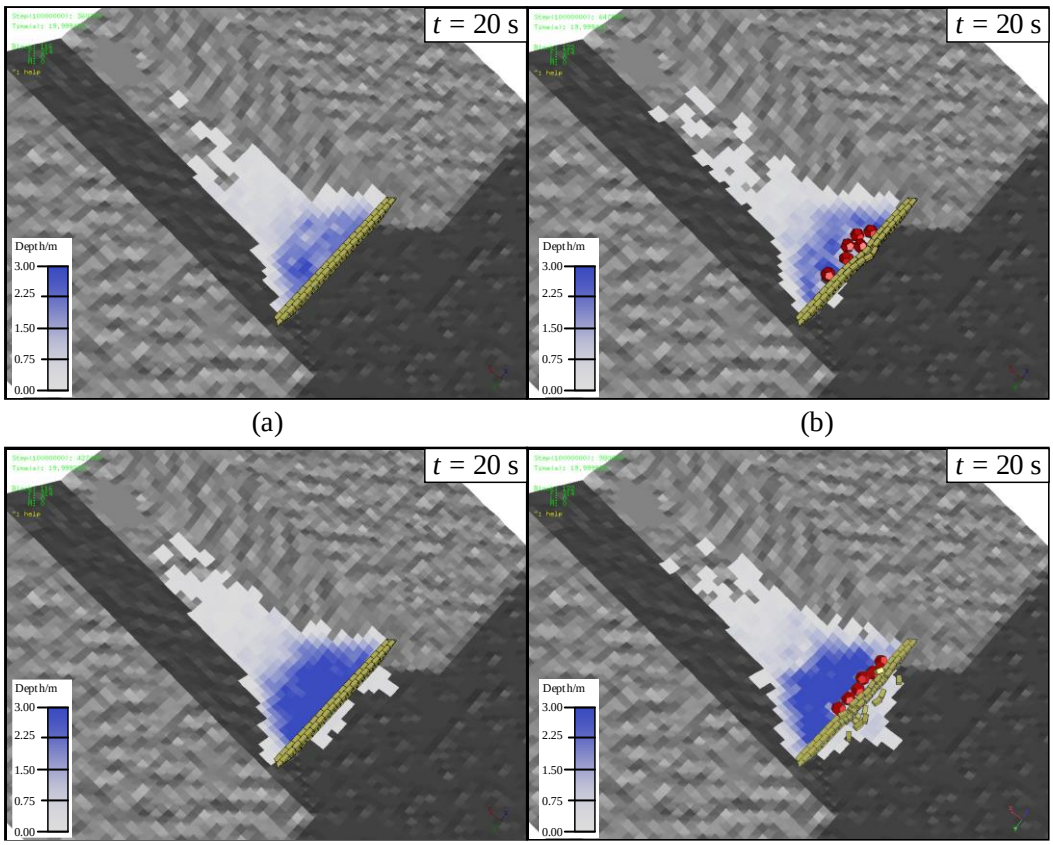

Figure 5.12 Flow depth and dam safety at t = 20 s for (a) initial height 1 m and no boulder (b) initial height 1 m with boulders (c) initial height 2 m and no boulder (b) initial height 2 m with boulders

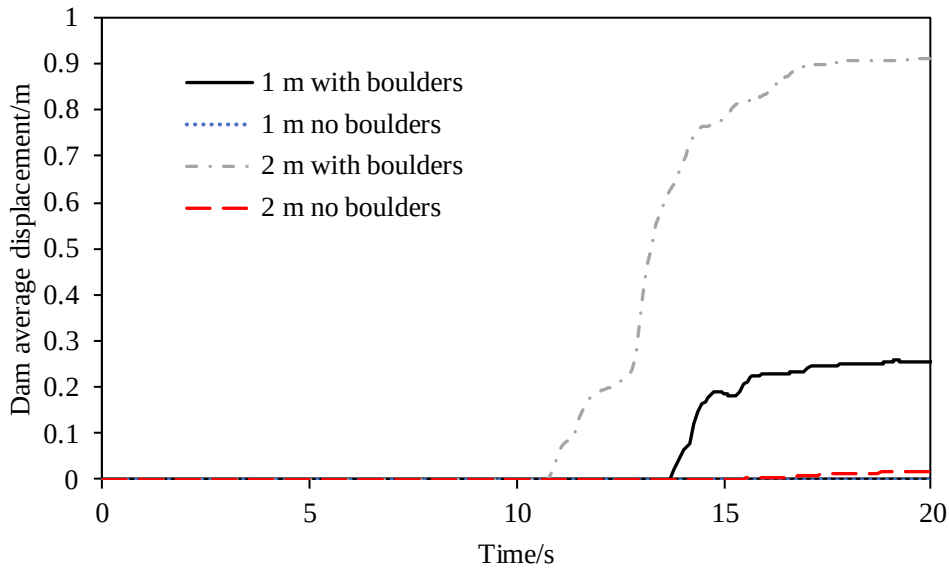

Figure 5.13 Average displacement of the dam in case 4 to 7

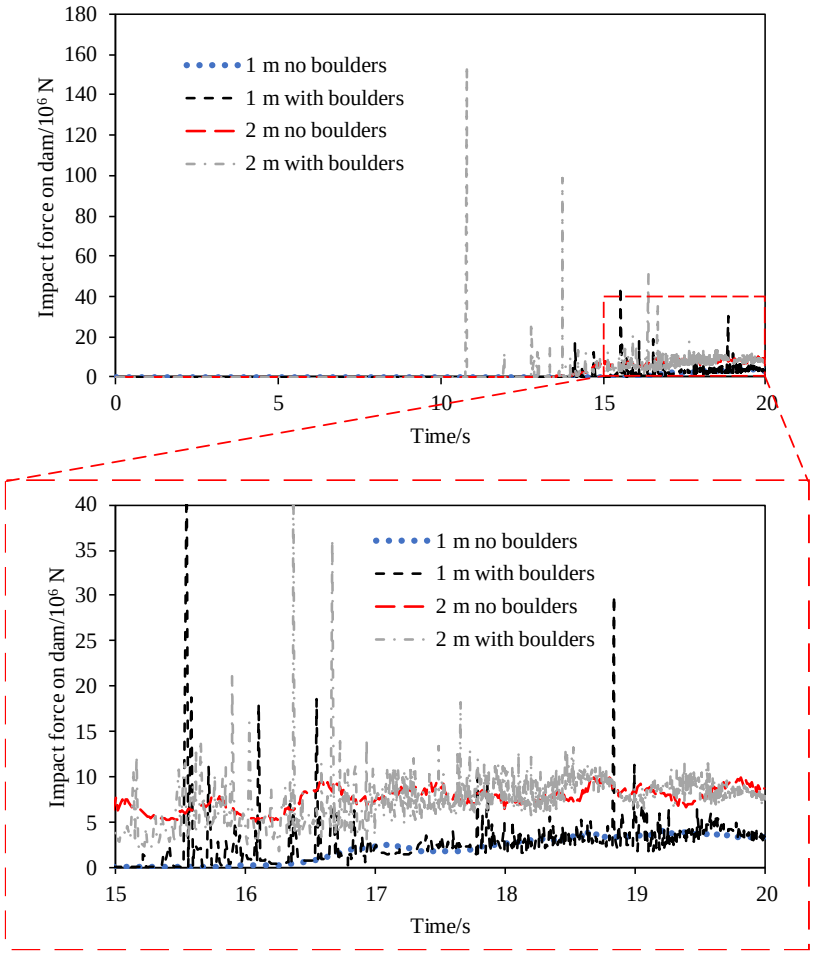

Figure 5.14 Total impact force on the dam in case 4 to 7

Figure 5.14 shows the total forces acted on the dam in case 4 to 7. The total dam force includes the flow action and boulder impacts. The impact force of large boulders is calculated by referring to the research of Yu, P. et al. (2019). The forces include the flow actions and boulders collisions. In general, the impact forces of the boulders are transient, however much larger than the relatively continuous flow actions. The highest impact force of case 7 is nearly 1.6×10^8 N, meanwhile it is about 4.5×10^7 N in case 6. The occurrence of impacts is also earlier in case 7. However, the existence of boulders does not change the trend of force. For example, the force curves of case 4 and case 6 are quite close, and the amplified figure shows that both curves converge to about 7.3×10^6 N, which is the double of case 5 and case 7. The transient large impact forces of case 7 are generally greater than those of case 5, which suggest that the impact force increase with the growth of flow mass volume. From the discussions above it is clear that the existence of large boulders is capable of creating great damage. Sometimes the dam is stable under the condition of flow action, it still can be dangerous when boulders are considered. Moreover, the impact forces also grow as the flow mass volume increases. Because of the higher speed, the impacts are also earlier in cases with more flow mass. Therefore, the proper address of the large boulders in debris flow is both necessary and important. The following sections will focus on the factors that influence the flow mobility and dam safety.

In addition, the collisions are also presented in detail in Figure 5.15-Figure 5.17. Given the size of the boulders, the major impact position is the middle and upper levels of the dam blocks. The close view of the dam further proves that the dam is destroyed by the boulders. Since the impact position does not show many patterns, those figures are not included in the following discussions.

5.5. THE EFFECT OF BOULDER SIZE

The influence of the size of the boulders is discussed in this section. Before that, two cases with boulder diameter 1 m and 2 m are simulated in advance to determine the boulder size that has a significant impact on dam safety. The calculation results are given in Figure 5.18 and Figure 5.19, which suggest that the

boulders with diameters 1 m and 2 m can hardly damage or destroy the dam. Similar results are also obtained from Shima, J. et al. (2015) and Ishikawa, N. et al. (2016). In their researches, the dam is still safe with boulder impacts whose diameter is less than 3 meters (although local failure took place at the impact spot), but the boulder with diameter of 6.7 meters is capable of destroying the dam.

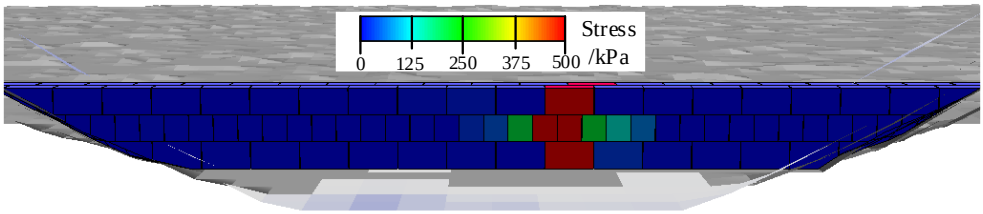

(a)

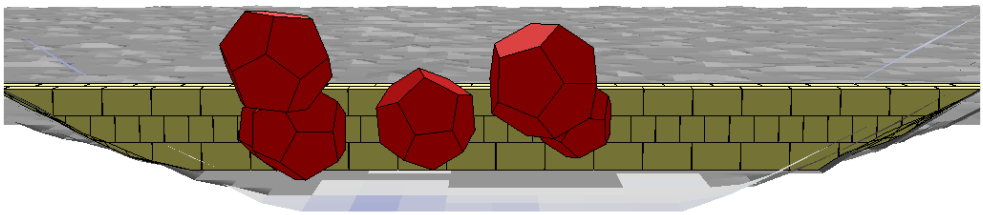

(b)

Figure 5.15 (a) impact stress and (b) boulders distribution at first major impact (about 10.8 s)

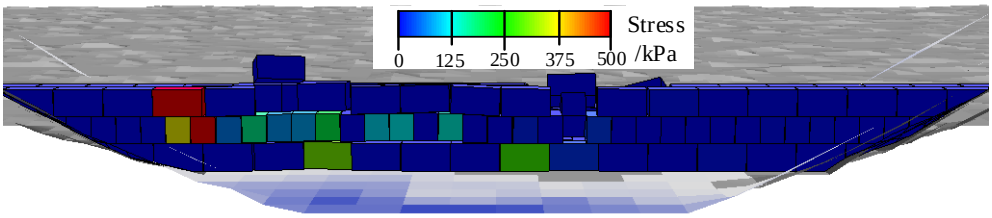

(a)

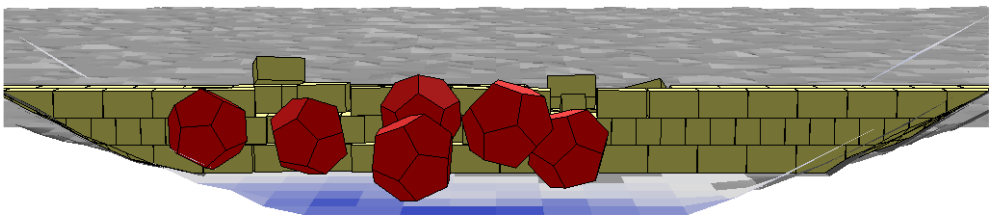

(b)

Figure 5.16 (a) impact stress and (b) boulders distribution at second major impact (about 13.1 s)

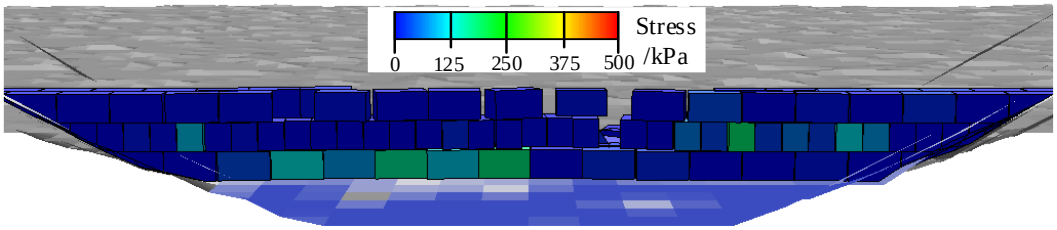

(a)

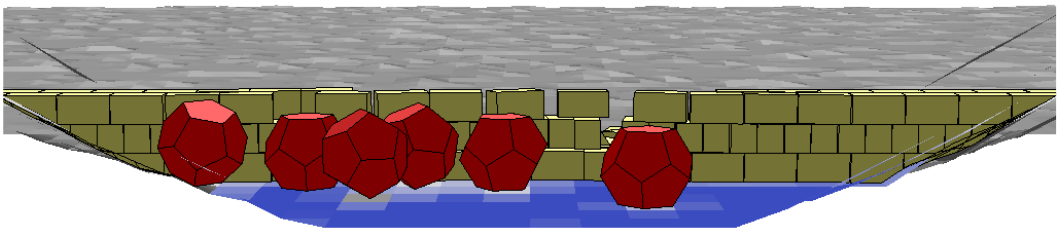

(b)

Figure 5.17 (a) impact stress and (b) boulders distribution at the end of the simulation (20 s)

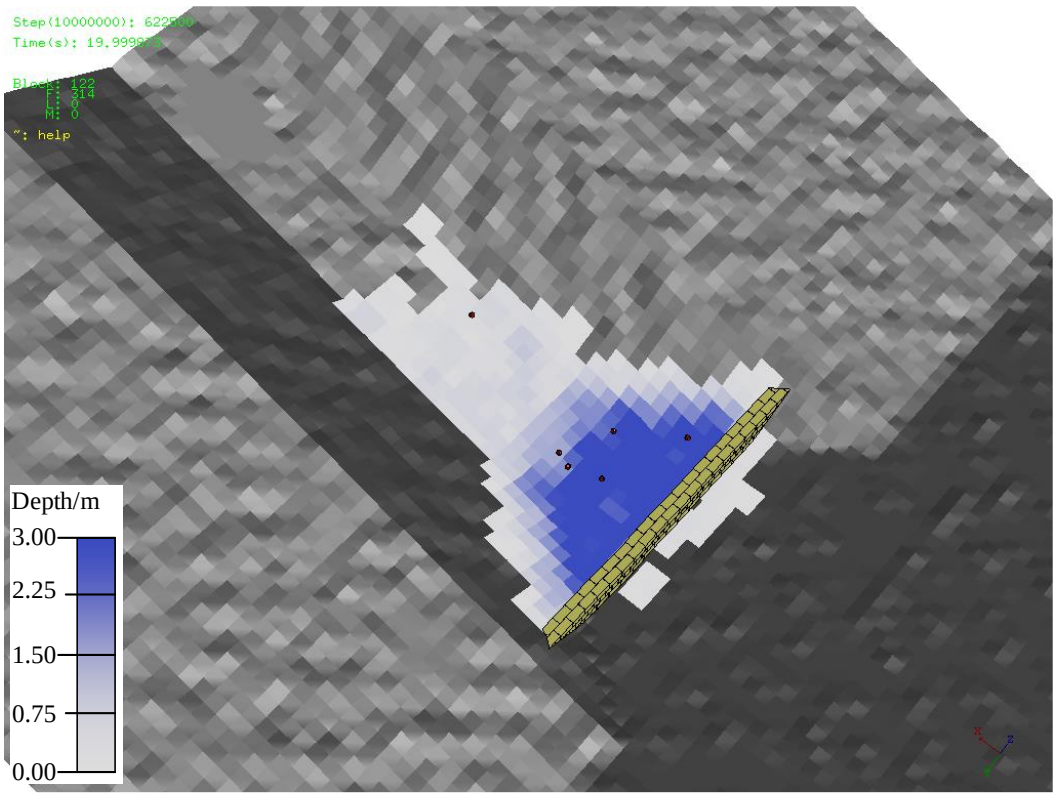

Figure 5.18 Flow depth and dam safety at t = 20 s with boulders of 1 m diameter

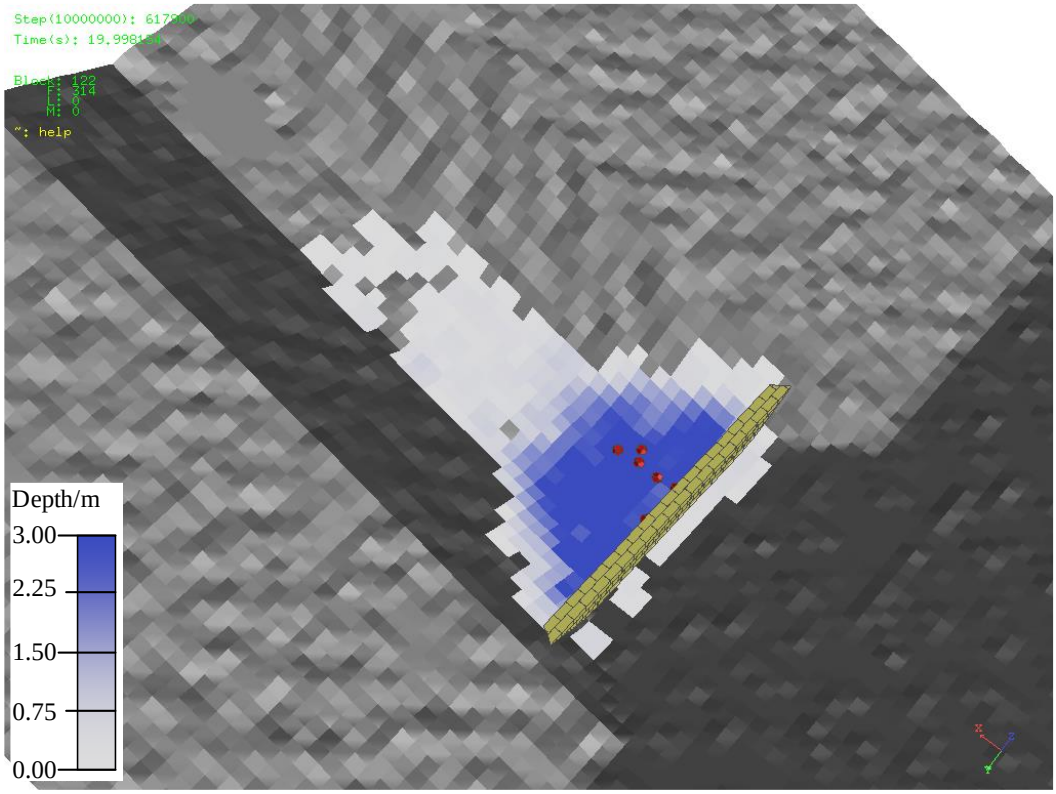

Figure 5.19 Flow depth and dam safety at t = 20 s with boulders of 2 m diameter

Based on the trial examples of diameter 1 m and 2 m and the previous researches (Ishikawa, N. et al., 2016; Shima, J. et al., 2015) about boulder impacts on the dam, the following three cases (8, 9 and 10) are designed, as shown in Figure 5.20. All three cases contain six boulders at similar locations. However, the boulders have varying size: the boulders in case 8 have diameters 3 m and volumes 9.4 m^3, while 4 m and 22.3 m^3 for the boulders in case 9 and 5 m and 43 m^3 in case 10. The debris flow properties remain unchanged. The screenshots of cases 8, 9 and 10 are presented in Figure 5.21 - Figure 5.23.

The screenshots of cases 8 – 10 suggest that the movement of the boulders is not necessarily connected to the boulder size, however the large boulder is, the large impact force and damage it causes. From those screenshots, it seems that the medium boulders (in Figure 5.22) move fastest among all three cases, meanwhile, the mobility of debris flow does not change much. This speed trend is also reflected by Figure 5.24, in which the medium-sized boulders travel faster than the large boulders before 10 s. The average boulder velocity $\bar{v}_{boulder}$ is defined by

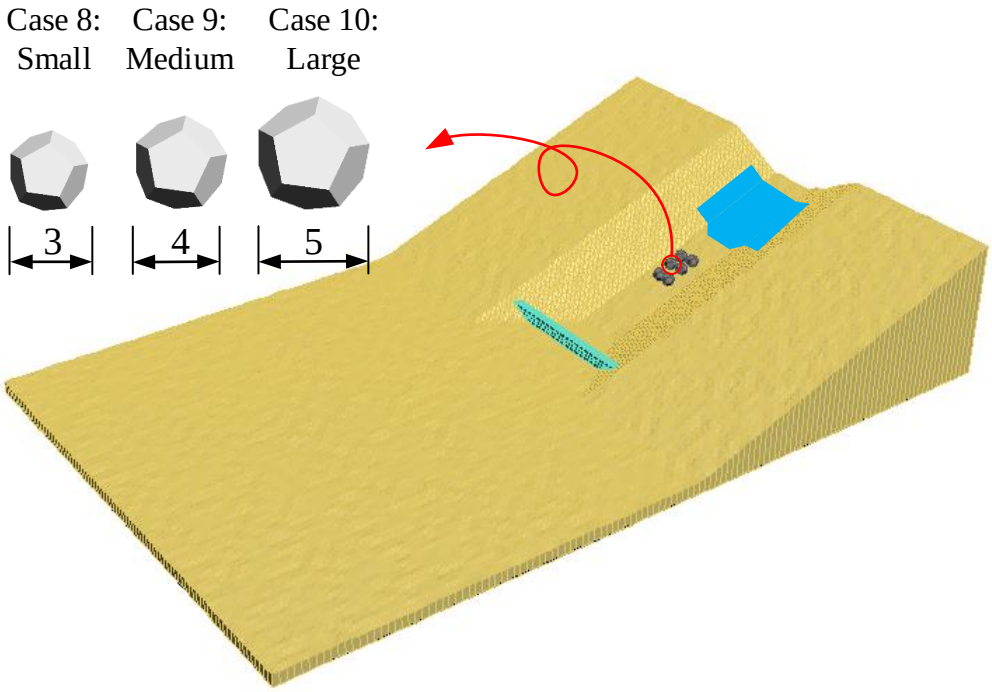

Figure 5.20 Schematic diagram for case 8, 9 and 10 with boulders of different sizes

$$\bar{v}_{boulder} = \frac{\sum m^i_{boulder} v^i_{boulder}}{\sum m^i_{boulder}} \tag{4.41}$$

where $v^i_{boulder}$ and $m^i_{boulder}$ are the mass and deformation of dam block i. The absolute velocities are used. The reason for this phenomenon is that the flow forces on the large boulders are not relatively large enough comparing to their own mass. The flow actions are related to the surface area. When the boulder size grows, the surface area grows quadratically, however the volume, or the mass, increases cubically. The mass grows faster than the surface area, so is flow force. This is reflected by the late initiation of the large boulders. Nevertheless, one may also notice that in case 1, boulders still travel slower than case 2, even case 3. It seems to violate the theory above. In fact, the slow velocities of the 3 m boulders should attribute to the small absolute flow force, although the force is “relatively” large to the 5 m boulders. Small flow forces on boulders make the resistant force, i.e. the friction, significant. The resistant force consumes energy and slows down the boulders. After 10 s, the velocities of the 4 m boulders drop and the 5 m boulders

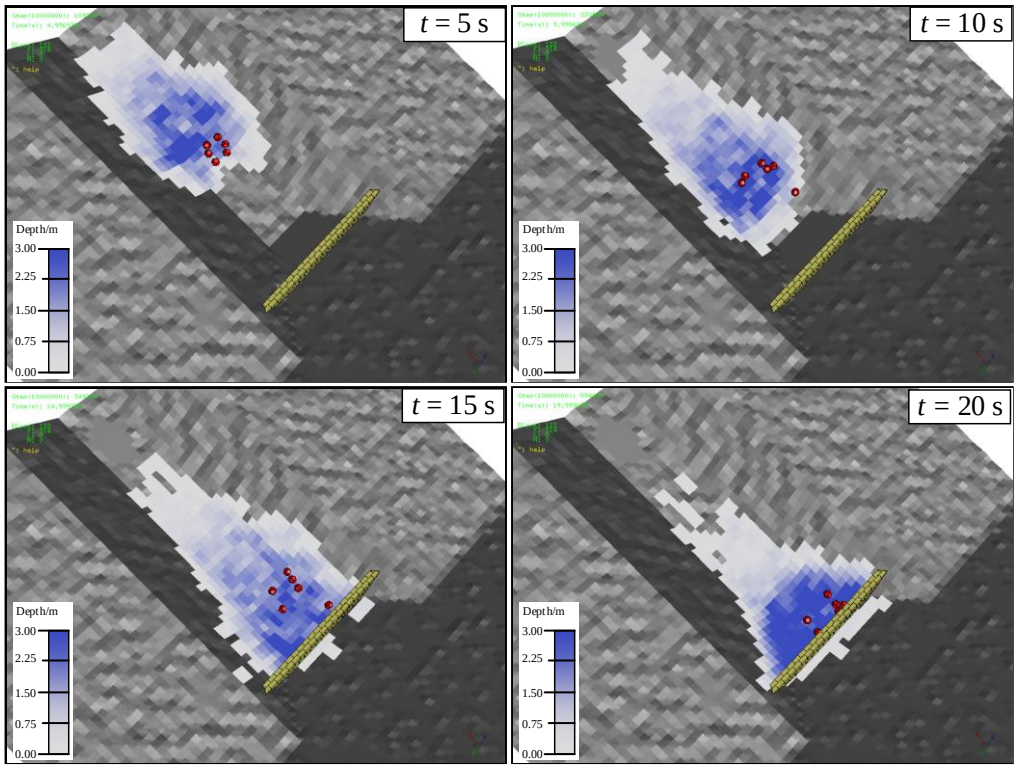

Figure 5.21 Simulated flow depth and dam safety in case 8

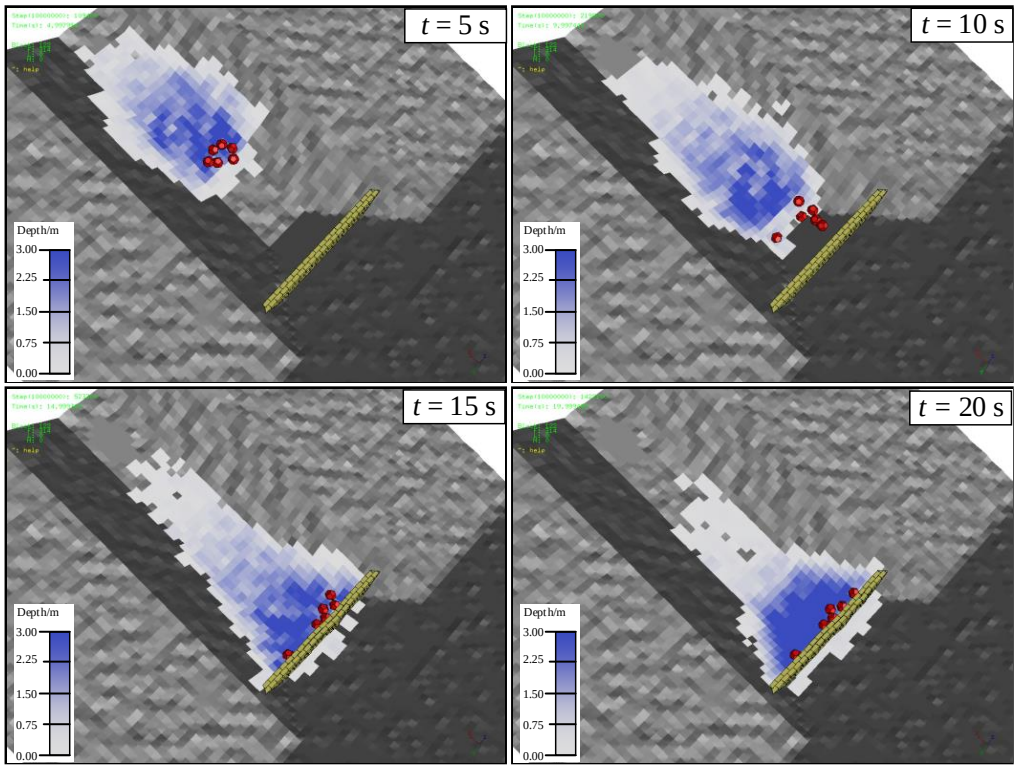

Figure 5.22 Simulated flow depth and dam safety in case 9

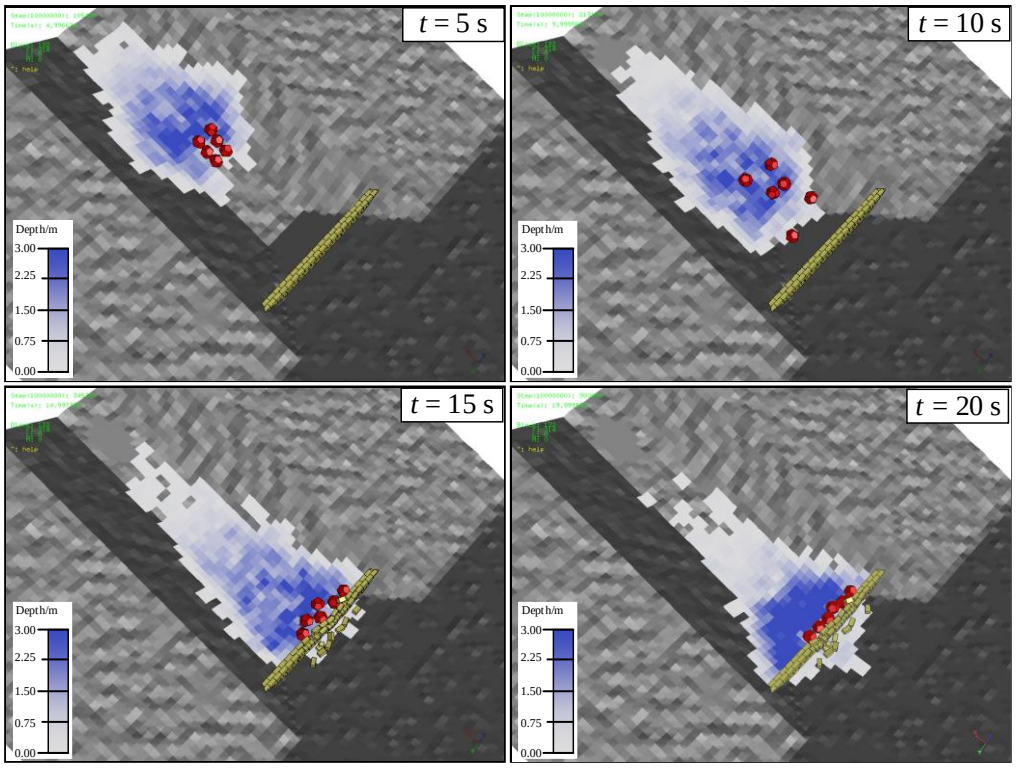

Figure 5.23 Simulated flow depth and dam safety in case 10

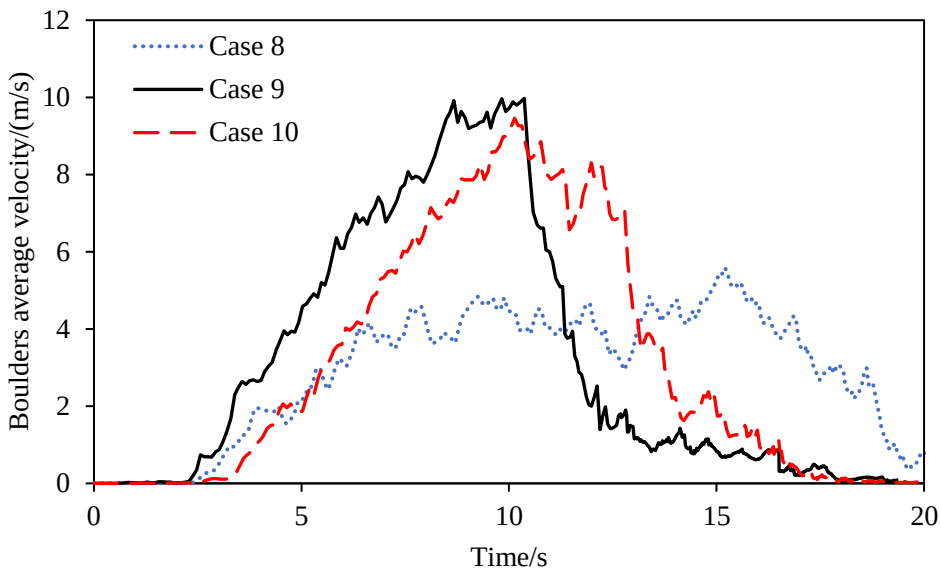

Figure 5.24 Average velocities of the boulders in case 8 to 10

become the fastest. This is because the boulders are travelling on the flat terrain in front of the dam. The flow cannot provide enough energy to the boulders on flat terrain, and the 5 m boulders experience lower energy loss during the slowing down

process. After 15 s, the velocities of the 4 m and 5 m boulders drop sharply since the kinetic energy has been passed to the dam blocks. The 3 m boulders are able to maintain their velocities around 15 s because they travel slower than the larger boulders and the main collisions have not occurred before that.

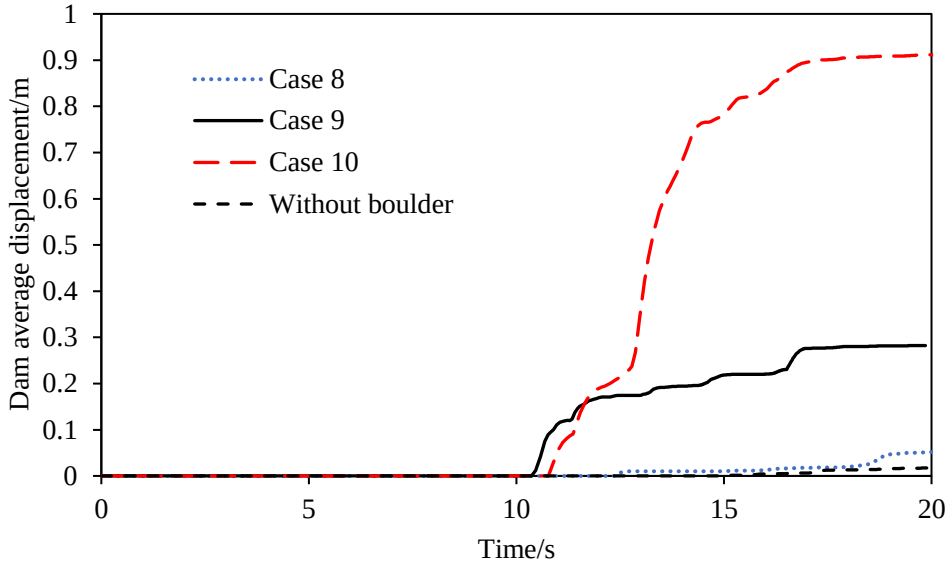

Figure 5.25 Average displacement of the dam in case 8 to 10

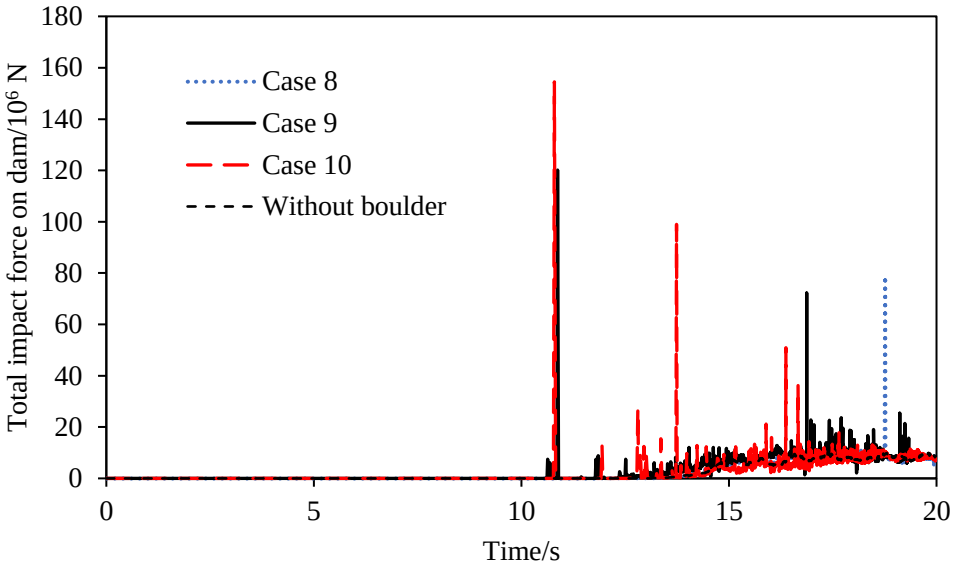

Figure 5.26 Total impact force on the dam in case 8 to 10

Figure 5.25 shows the average displacements of the dams in case 8 – 10, together with the dam deformation in no-boulder case 2 as a contrast. In general,

the results of cases with boulders show larger dam displacements than the contrast case. In 3 m boulder case, the average dam displacement at 20 s is 0.05 m, more than double of the 0.02 m in the contrast case. The displacement develops to 0.28 m in case 9, and 0.9 m in case 10. It grows much faster than the increase of the size, which are 3 m, 4 m and 5 m in diameter, and 9.4 m^3, 22.3 m^3 and 43 m^3 in volume for case 8, 9 and 10, respectively. It suggests that the increase of boulder size may greatly amplifies the damage in a non-linear way. The impact forces presented in Figure 5.26 also support this idea. Although the trend is similar, the peak impact force in case 10 is the highest, nearly 1.6×10^8 N.

5.6. THE EFFECT OF BOULDER DISTRIBUTION

The influence of the position of the boulders is discussed in this section. As shown in Figure 5.27, four cases (11, 12, 13 and 14) are designed. All the cases contain six identical boulders arranged in a similar pattern but in a different location, case 11 highest and case 14 lowest on the slope. The boulder diameter is 4 m and the volume is about 22 m^3. The debris flow properties remain unchanged.

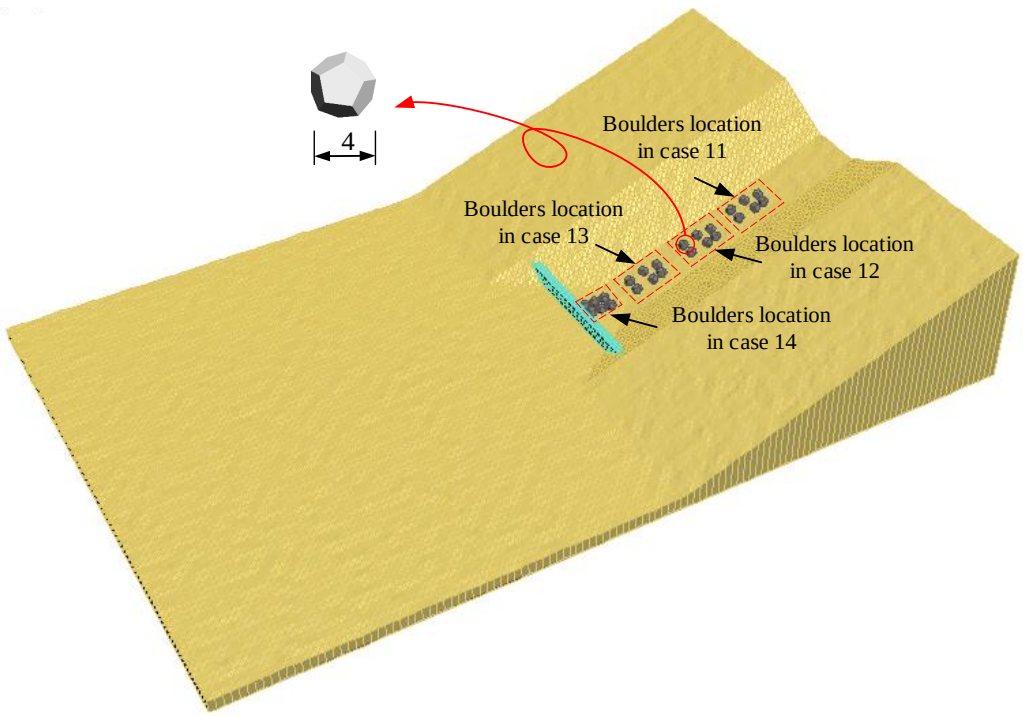

Figure 5.27 Schematic diagram for case 11 – 14 with boulders of different positions (unit: m)

The four cases are simulated by 3D DDA-DFS, and the screenshots at 5 s, 10 s, 15 s and 20 s are presented in Figure 5.28 – Figure 5.31. From those screenshots, one may notice that the higher boulders initiate earlier. In addition, referring to the system condition at 20 s, some dam blocks in case 11 are knocked off during the impact with boulders, while the dam in case 12 shows observable deformation. The rest two dams in case 13 and 14 do not exhibit any damages, which means the boulders that are close to the dam may not create significant damage because there is no enough space to accelerate. It suggests that the higher initial position of the boulders may cause heavier damage.

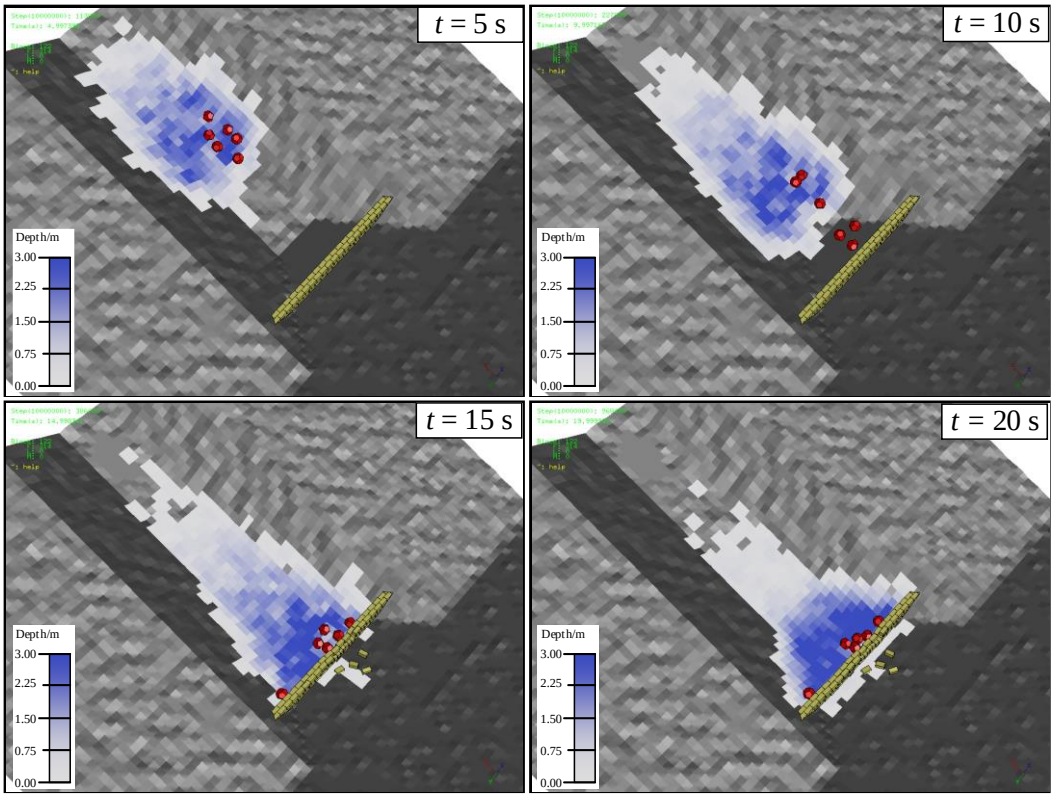

Figure 5.28 Simulated flow depth and dam safety in case 11

Figure 5.32 shows the average boulder velocity of the case 11 – 14. Because the position of the boulder in case 11 is the highest, they begin to be accelerated when simulation starts, then the boulders in case 12, 13 and 14. The early moving and high position offer a chance of accumulating greater kinetic energy to the boulders in case 11, but they show similar peak velocities to the boulders in case 12, whose initial position is lower. This could attribute to the limitation of flow actions, which

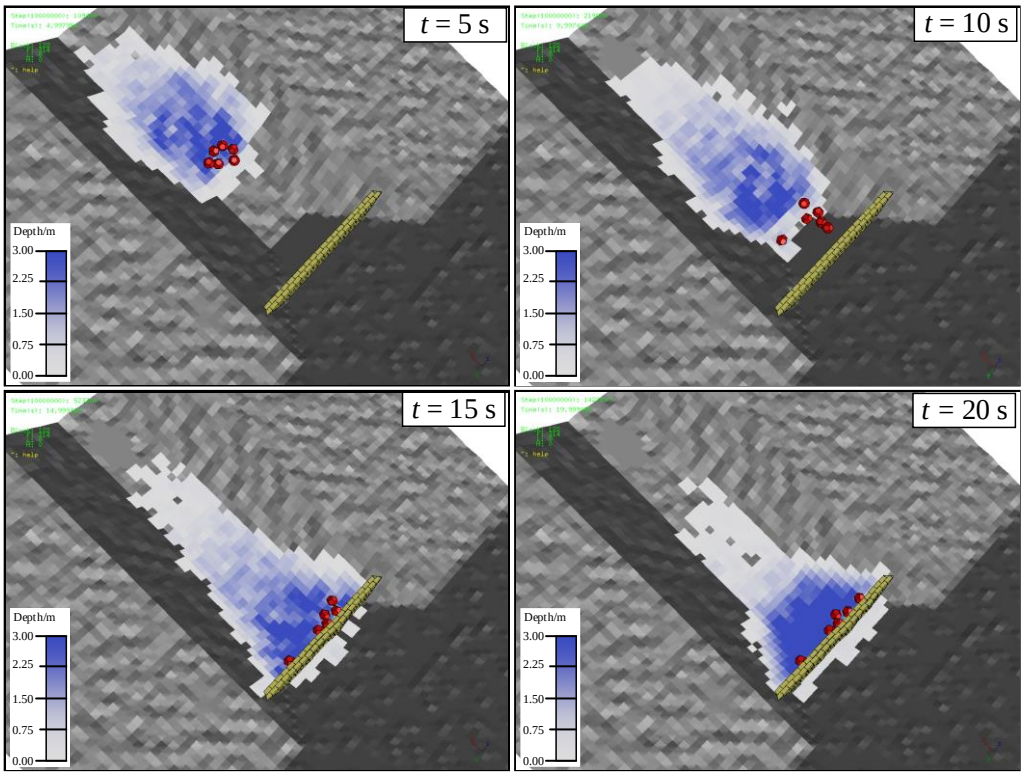

Figure 5.29 Simulated flow depth and dam safety in case 12

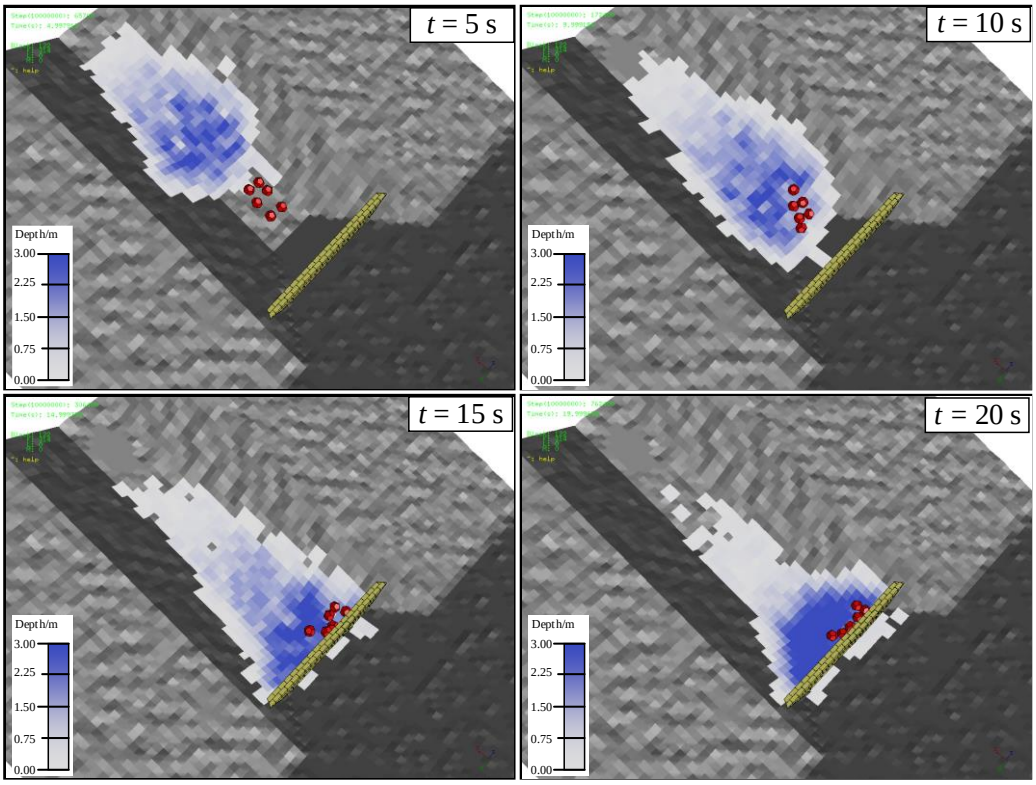

Figure 5.30 Simulated flow depth and dam safety in case 13

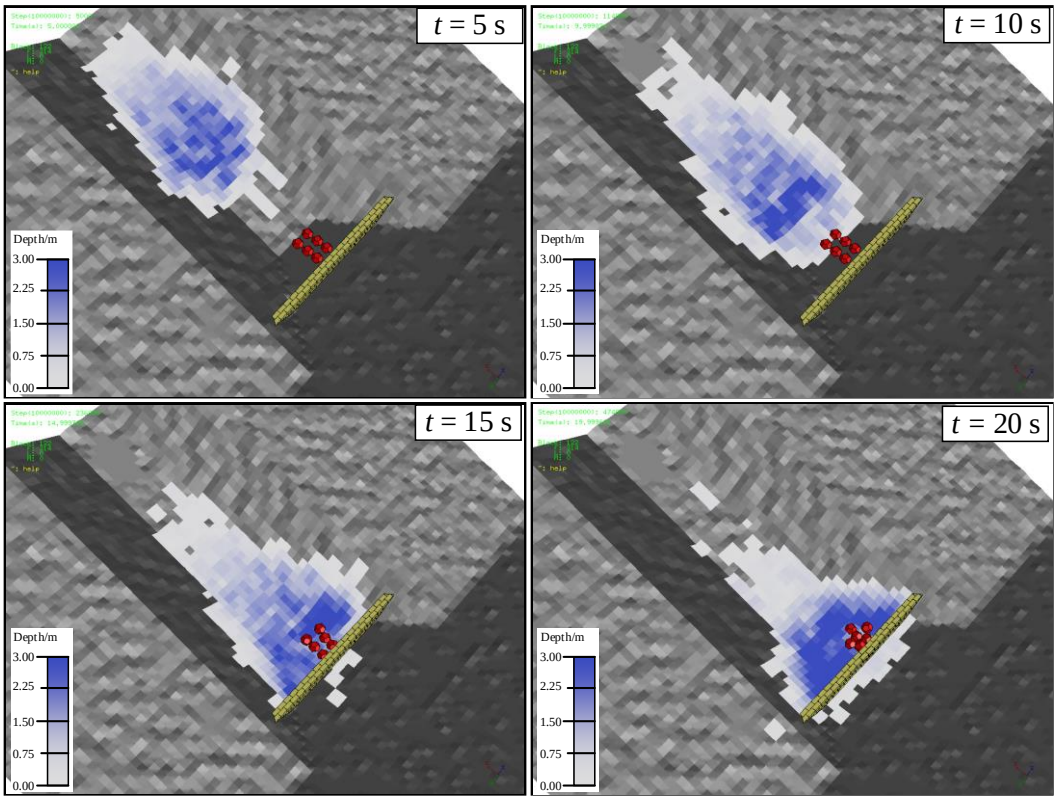

Figure 5.31 Simulated flow depth and dam safety in case 14

can only drive the boulders in a maximum velocity, about 10 m/s here. Because the sizes of the boulders are the same in those four cases, before collisions with the dam, the boulders should experience resemble deceleration process, as the boulder velocities at 10 s – 15 s in case 11 and 13. The shape drop in velocity of case 12 is because the boulders already collide with the dam before 15 s. Figure 5.33 presents the average dam deformation in case 11 – 14, together with the contrast case without any boulder. No matter where the boulders locate initially, the dams in the cases with boulders show larger deformation: at t = 20 s, the average dam average is 0.02 m without boulders, while ranges from 0.1 m to 0.56 m with boulder impacts, depending on their initial position. The higher initial position of the boulders creates a larger dam deformation. This is due to the increasing impact forces, which are drawn in Figure 5.34. The maximum impact force is recorded in case 11 at about 10.7 s, which is nearly 1.8×10^8 N. The dam safety is highly influenced by the impact forces.

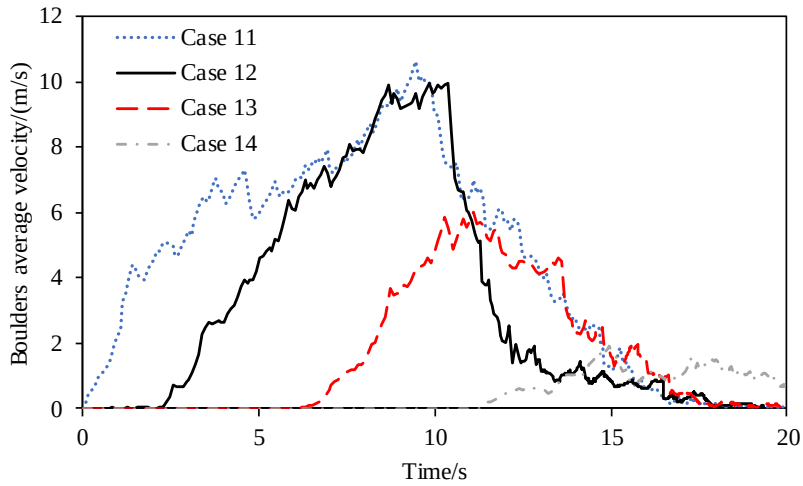

Figure 5.32 Average velocities of the boulders in case 11 to 14

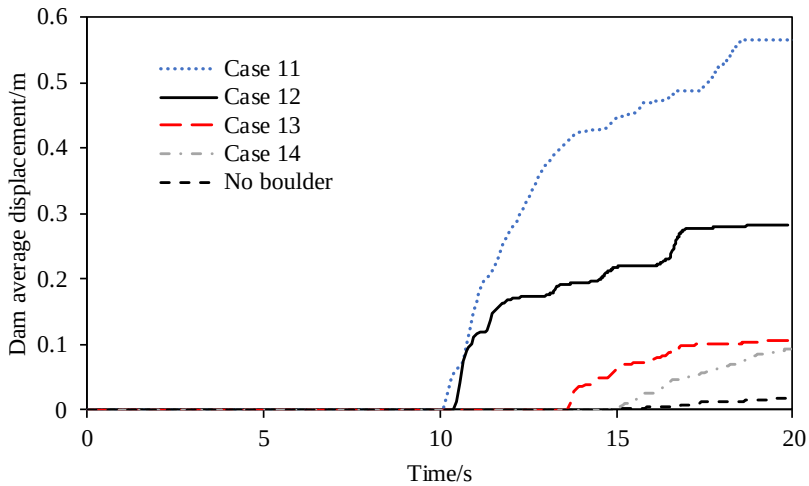

Figure 5.33 Average displacement of dam in case 11 to 14

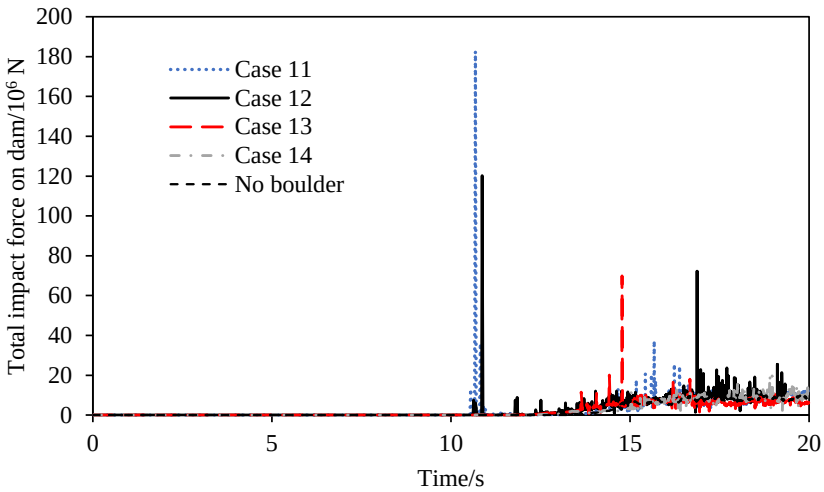

Figure 5.34 Total impact force on dam in case 11 to 14

5.7. THE EFFECT OF BOULDER SHAPE

The influence of the shape of the boulders is discussed in this section. As shown in Figure 5.35, three cases (15, 16 and 17) are designed. All three cases contain six boulders at similar positions. However, the boulders have varying shapes: the boulders in case 15 are dodecahedral with diameters 4 m, the boulders in case 16 are cubic with diameters 5.3 m, the boulders in case 17 are tetrahedral with diameters 7 m. The boulder volumes are controlled as about 22 m^3. In conclusion, only the boulder shape is the variable. The debris flow properties in these cases remain unchanged. The three cases are simulated by 3D DDA-DFS, and the screenshots at 20 s are presented in Figure 5.36 – Figure 5.38. The screenshots suggest that the dodecahedral boulders in case 15 have much higher mobility than the cubic and tetrahedral boulders in case 16 and 17. Take the screenshots at 20 s as an example, all the dodecahedral boulders in Figure 5.36 have collided with the dam and been stopped in front of it. In contrast, most of the cubic boulders in Figure 5.37 fail to collide with the dam, and even no tetrahedral boulders managed to reach the dam in Figure 5.38. If the boulders do not in contact with the dam, then the effect of boulder impacts disappears. This result roughly suggests that the shape of the boulders can greatly affect mobility, which further influences the actual damage to the dam.

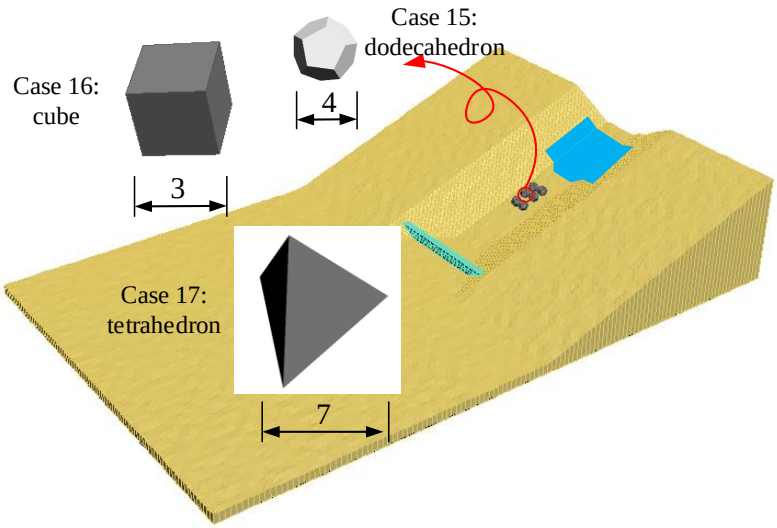

Figure 5.35 Schematic diagram for (a) case 15, dodecahedral boulders (b) case 16, cubic boulders and (c) case 17, tetrahedral boulders (unit: m)

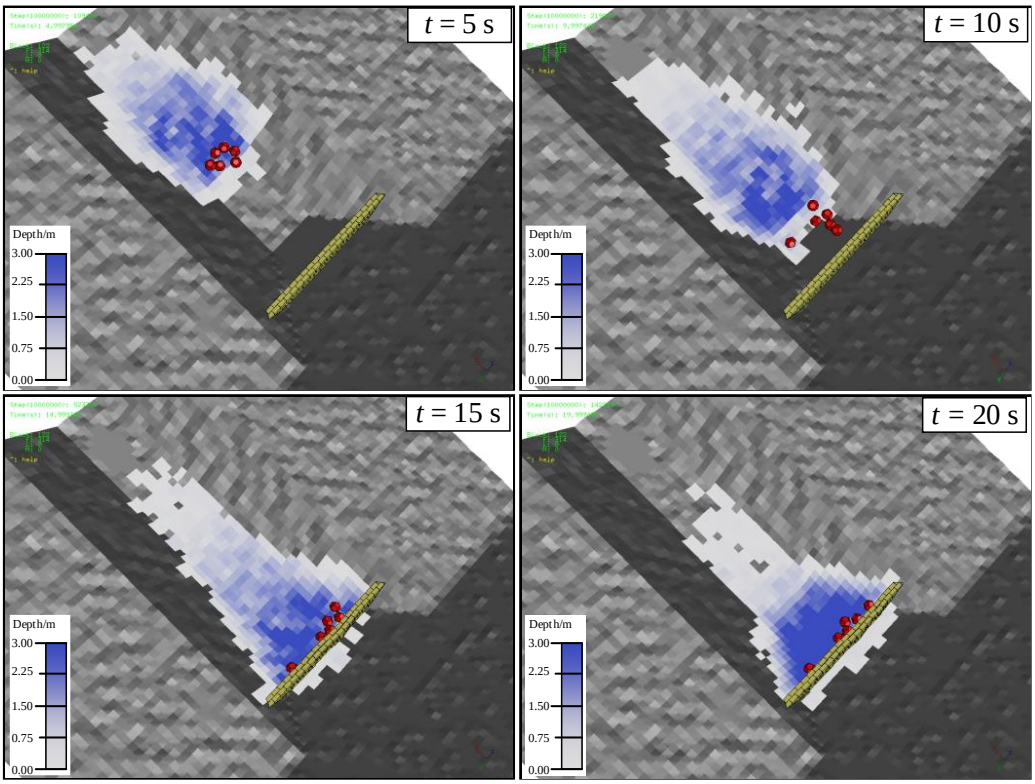

Figure 5.36 Simulated flow depth and dam safety of case 15

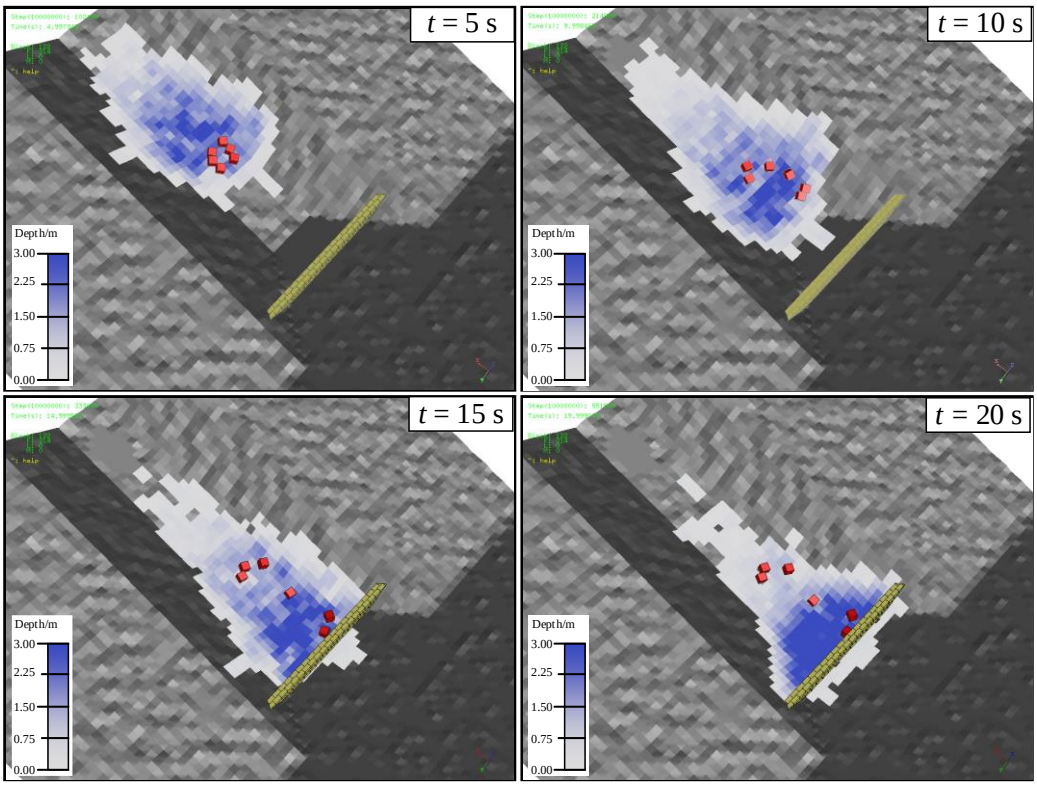

Figure 5.37 Simulated flow depth and dam safety of case 16

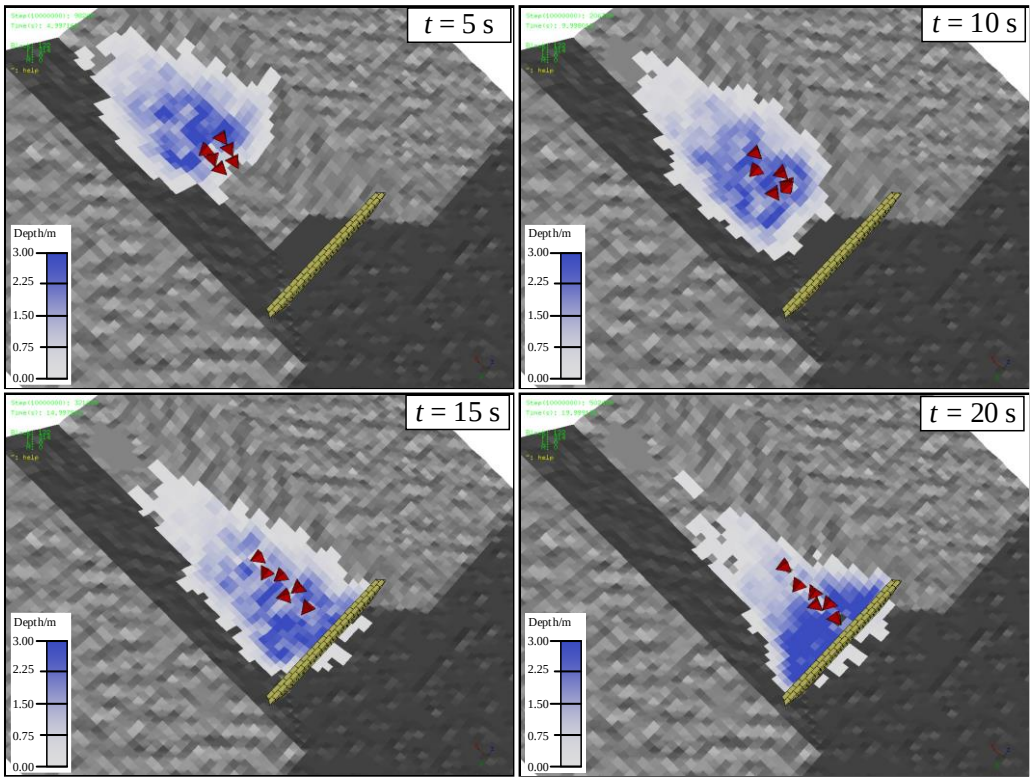

Figure 5.38 Simulated flow depth and dam safety of case 17

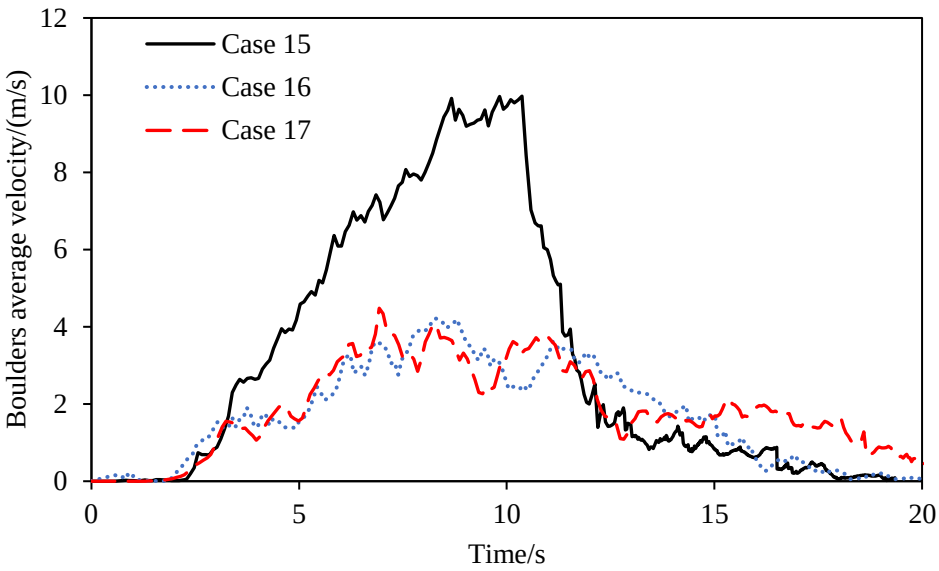

Figure 5.39 Average velocities of the boulders in case 15 to 17

Figure 5.39 shows the boulders' average velocities in simulation. It clearly displays that the dodecahedron-shaped boulders have significantly larger velocities than the boulders in the other two cases. Although under the same condition, the

dodecahedral boulders travel faster because dodecahedra are closer to spheres. The subrounded shapes are more flexible to roll compared to the angular shapes, thus increasing the travelling velocities. With higher velocities, the boulders in case 15 are more capable of generating large impact force and dam deformation, as presented in Figure 5.40 and Figure 5.41. Since no significant impacts are observed in case 16 and 17, the slight altering of the deformation in Figure 5.40 is caused by the changing of flow field due to the existence of boulders of various shapes.

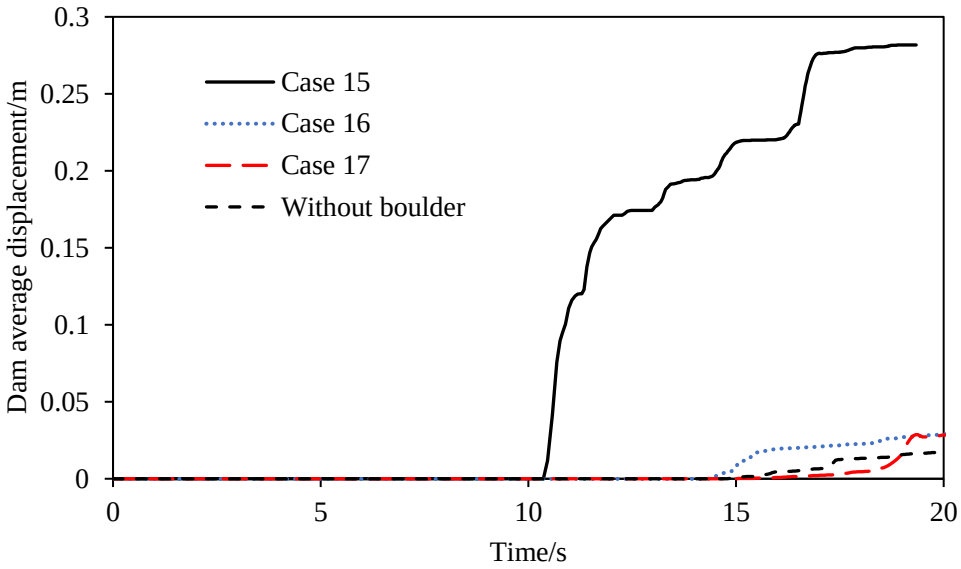

Figure 5.40 Average displacement of the dam in case 15 to 17

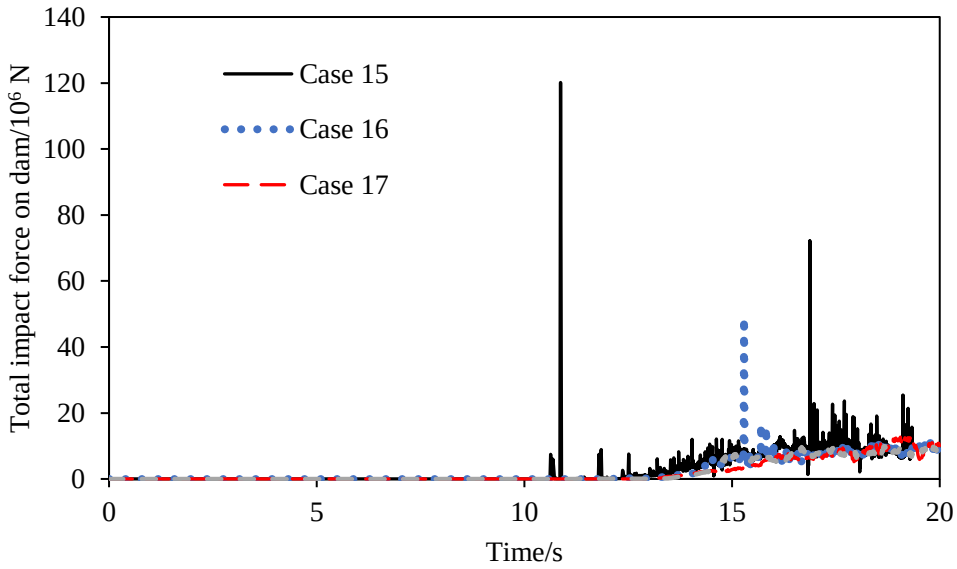

Figure 5.41 Total impact force on the dam in case 15 to 17

5.8. SIMULATION OF DRIFTWOODS IN DEBRIS FLOW

Driftwoods are commonly observed in debris flow events. The developed 3D DDA-DFS can also be used to analyzing the behavior of driftwoods during interaction with the check dam. As shown in Figure 5.42, 20 driftwoods are distributed in the channel. According to the studies about driftwood (Comiti, F. et al., 2006; Paquier, A. et al., 2018; Shrestha, B. B. et al., 2011), the density of the driftwoods is selected as 700 kg/m^3, 800 kg/m^3 and 900 kg/m^3 (case 18 - 20). The total volume of the woods is approximately equal to the volume of boulders of case 9. The debris flow has an initial depth of 2 m. The simulation results are presented in Figure 5.43 - Figure 5.45. It is observed that the driftwoods are accumulated in front of the dam. In case 19, some woods pass over the dam. With the varying density, the behaviors of the driftwood show no obvious pattern. The maximum total impact force on the dam in those three cases are presented in Figure 5.46. It shows that when the maximum impact force can be greater than pure debris flow if driftwoods are considered, but the force is still smaller than that generated by boulders with the same volume.

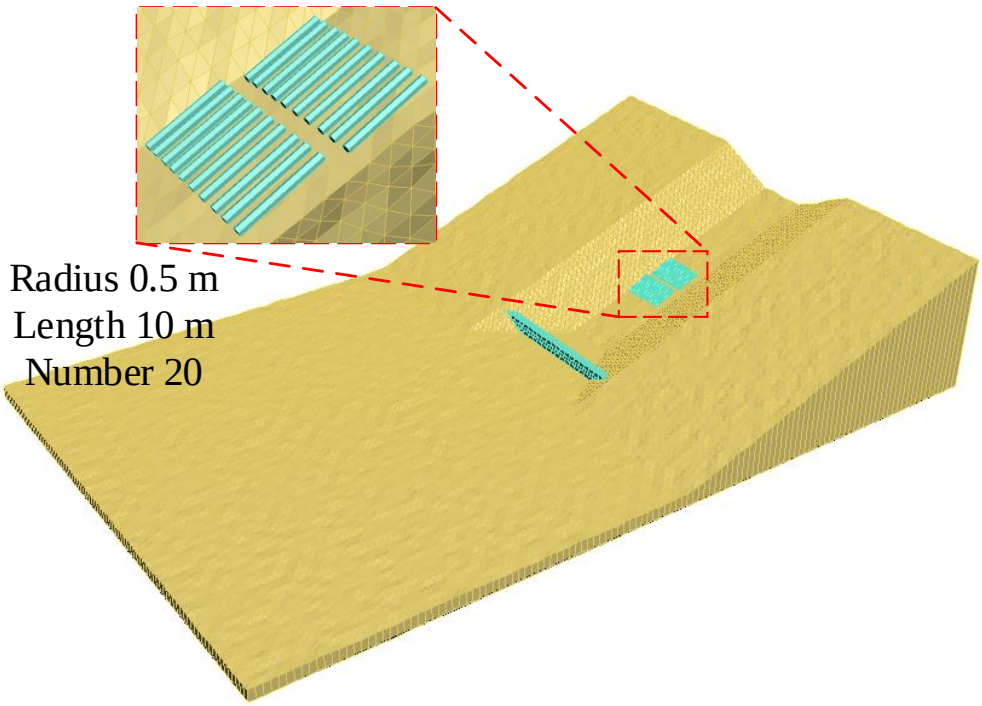

Figure 5.42 Schematic diagram for driftwoods simulation

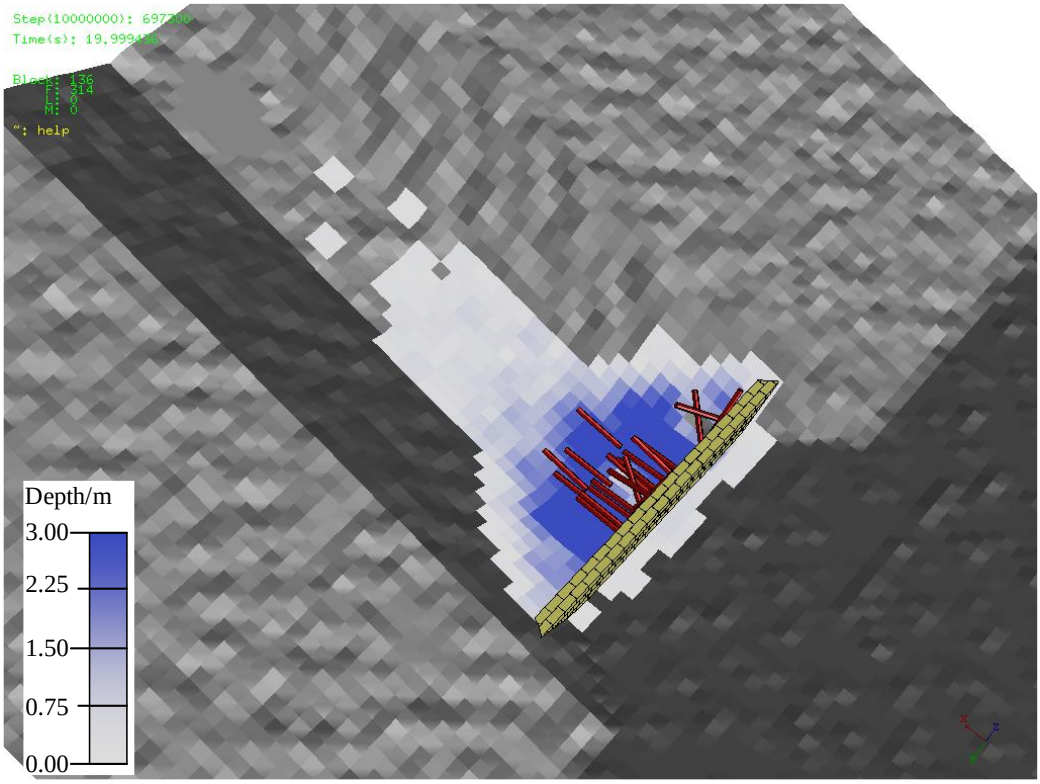

Figure 5.43 Simulated flow depth and dam safety of case 18

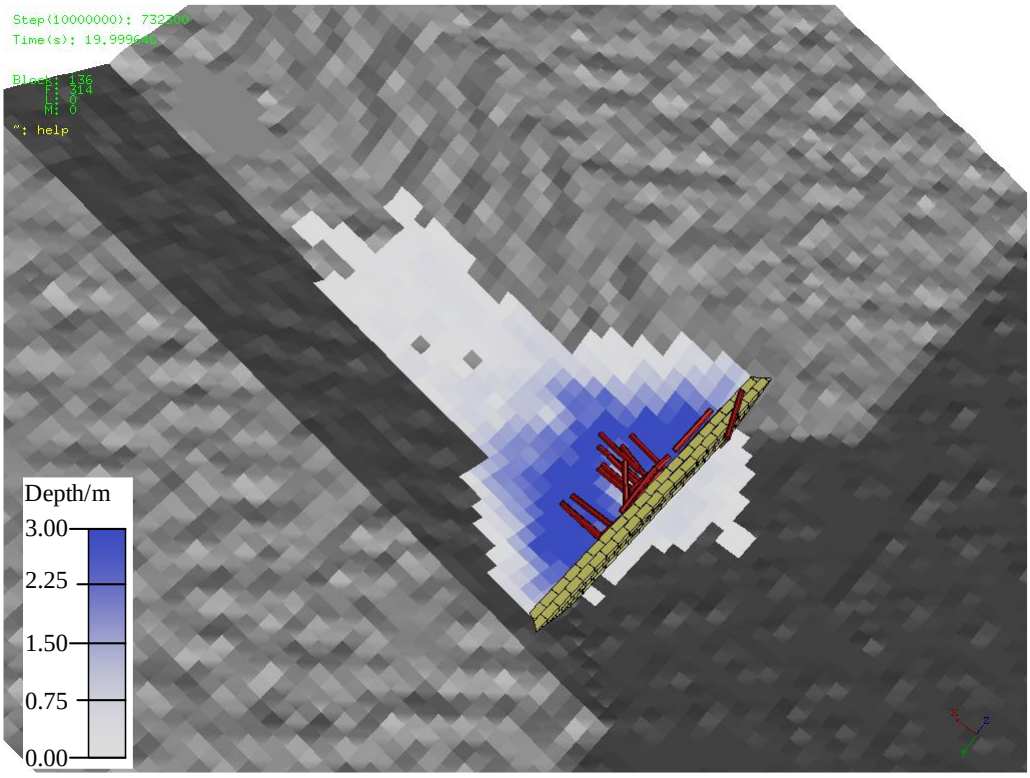

Figure 5.44 Simulated flow depth and dam safety of case 19

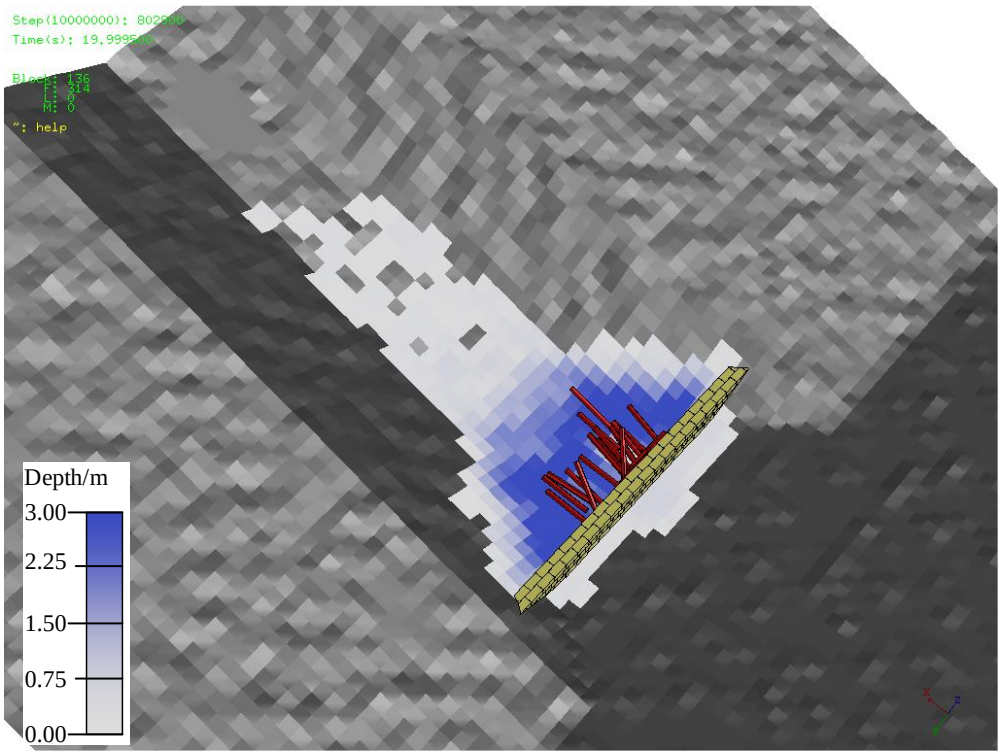

Figure 5.45 Simulated flow depth and dam safety of case 20

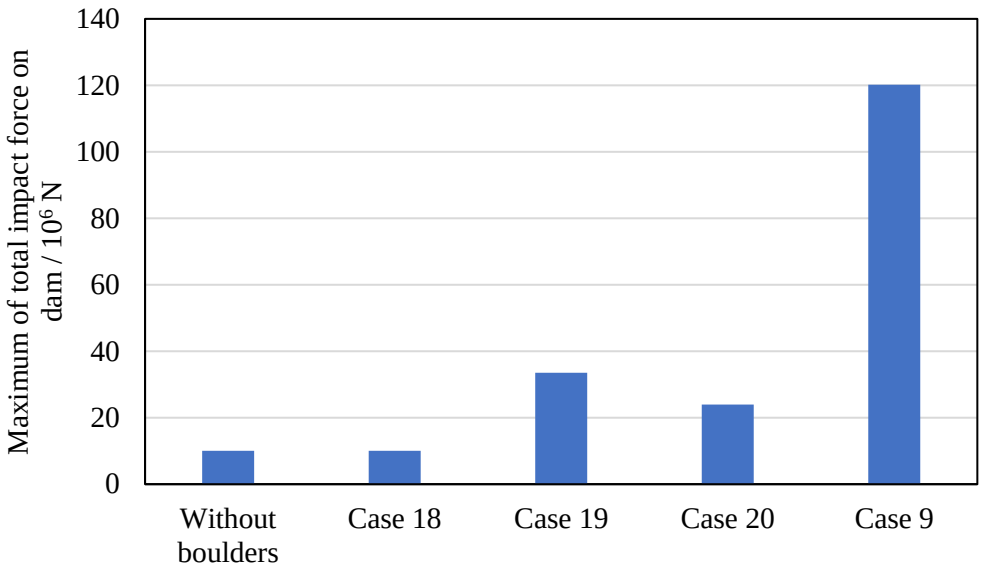

Figure 5.46 The maximum total impact force on dam

5.9. CONCLUSIONS

The influences of large boulders in debris flow on downstream check dams were clarified by a series of examples in chapter 5. It is important because the

understanding of the influence factors may help the prevention and mitigation of the damages caused by large boulders in debris flow.

The clarifications are based on on a channel model, and at the bottom of which there is a check dam. A mixture of debris flow and boulders are flushed downslope and hit the dam. The position, size, shape and material of the boulders are chosen as variables, and the mobility of the boulders, deformation of the dam and imposed impact force on the dam are investigated. The following conclusions can be drawn:

(1) boulder debris flow can destroy the check dam that cannot be destroyed by the corresponding pure debris flow, and the impact force of the boulder debris flow is about 15 times larger than that of the pure debris flow.

(2) A boulder can run in front of fluid when its size is large enough in a boulder debris flow.

(3) Boulders with larger sizes are capable of causing more damages to the dam within a certain range.

(4) Higher initial position of the boulders is capable of causing more damages to the dam within a certain range.

(5) The subcircular shaped boulders create large damages to the dam than subangular shaped boulders.

(6) The driftwood in debris flow is also studied by modifying the shape and density of the 3D DDA blocks. The result suggests that the driftwoods tend to accumulate in front of the dam, some of them also pass the dam if the flow is deep enough in front of the dam. The impact force is larger than that of pure debris flow but smaller than that of the boulder with the same volume.

REFERENCE

Asteriou, P., Saroglou, H., & Tsiambaos, G. (2012). Geotechnical and kinematic parameters affecting the coefficients of restitution for rock fall analysis. International Journal of Rock Mechanics and Mining Sciences, 54, 103-113.

Asteriou, P., & Tsiambaos, G. (2015). Empirical model for predicting rockfall trajectory direction. Rock Mechanics and Rock Engineering, 49(3), 927-941.

Choo, L. Q., Zhao, Z. Y., Chen, H. M., & Tian, Q. (2016). Hydraulic fracturing modeling using the discontinuous deformation analysis (DDA) method. Computers and Geotechnics, 76, 12-22.

Comiti, F., Andreoli, A., Lenzi, M. A., & Mao, L. (2006). Spatial density and characteristics of woody debris in five mountain rivers of the Dolomites (Italian Alps). Geomorphology, 78(1-2), 44-63.

Ishikawa, N., Shima, J., Matsuzawa, R., Beppu, M., & Mizuyama, T. (2016). Damage of steel open sabo dams by rock impact. Paper presented at the 4th International Conference on Protective Structures, Beijing, China.

Jiao, Y., & Zhang, X. (2012). DDARF-A simple solution for simulating rock fragmentation. Advances in discontinuous numerical methods and applications in geomechanics and geoengineering, 85-98.

Li, L.-P., Sun, S.-Q., Li, S.-C., Zhang, Q.-Q., Hu, C., & Shi, S.-S. (2015). Coefficient of restitution and kinetic energy loss of rockfall impacts. KSCE Journal of Civil Engineering, 20(6), 2297-2307.

Paquier, A., Kimura, I., Kitazono, K., & Rivière, N. (2018). Studies on Driftwood Motions around Obstacles by Laboratory and Nnumerical Experiments. E3S Web of Conferences, 40.

Shima, J., Takeda, I., Matsuzawa, R., Beppu, M., Ishikawa, N., & Mizuyama, T. (2015). Failure mechanism of concrete sabo dam by rock impact. Paper presented at the 11th International Conference on Shock & Impact Loads on Structures, Ottawa, Canada.

Shrestha, B. B., Nakagawa, H., Kawaike, K., Baba, Y., & Zhang, H. (2011). Driftwood deposition from debris flows at slit-check dams and fans. Natural Hazards, 61(2), 577-602.

Yu, P., Zhang, Y., Peng, X., Wang, J., Chen, G., & Zhao, J. X. (2019). Evaluation of impact force of rock landslides acting on structures using discontinuous deformation analysis. Computers and Geotechnics, 114.

Zhu, W., Chen, Y., Li, S., Yin, F., Yu, S., & Li, Y. (2014). Rock failure and its jointed surrounding rocks: A multi-scale grid meshing method for DDARF. Tunnelling and Underground Space Technology, 43, 370-376.

CHAPTER 6

CASE STUDY: USING THE 3D DDA-DFS METHOD BASED ON A REAL TERRAIN TERRITORY MODEL LOCATED IN AMAMI OSHIMA, JAPAN TO ESTIMATE CHECK DAM SAFETY

6.1. INTRODUCTION

In this section, the effects of traveling large boulders driven by debris flow are considered to analyze debris flow runout and the safety of check dam based on a real catchment –Yohutagawa, Amami Oshima, where a debris flow occurred in 2010. The previous studies of the authors' research team have already studied the event regarding the parameter selection, simulation method, entrainment and deposition (Han, Z. et al., 2015a; Han, Z. et al., 2015b; Wu, J. et al., 2013a), which provide sound research foundation in this thesis. Since this research is focused on the effects of the boulders in debris flow, those researches are followed.

The Yohutagawa debris flow located in Kagoshima Prefecture, Amami-Oshima Island, which was one of the hazards that were triggered by the intense rainfall on Oct. 20, 2010. According to the statistical data from Saboka, department of civil engineering, Kagoshima prefecture, there were 58 disasters triggered in total. The rain was so heavy that it reached 600 mm in total from 8 pm, Oct. 19 to 7 pm, Oct. 20. Before the occurrence of Yohutagawa debris flow at 6 pm, a maximum rainfall strength per hour of 73 mm was recorded from 3 pm to 4 pm. From the investigation performed by Kokusai Kogyo Co., LTD (KKC), the initial flow mass

volume was 5843 m^3. It was sooner increased to 8697 m^3 due to the sediment entrainment. When passing the check dam, flow mass of 5621 m^3 was intercepted, and the rest kept moving and finally deposited at the alluvial fan. Two buildings were destroyed during the event. Referring to Figure 6.1, an in-situ investigation conducted by KCC suggested that the debris flow is triggered in the higher part of the slope, which is greater than 26°. Then the slope decreases to 18.16° on average and erosion is observed. The alluvial fan area is relatively flat, less than 12°, is the place where flow mass deposited.

Figure 6.1 Air photo of the morphology of 2010 Yohutagawa debris flow (based on the investigation of KKC, image © Google Maps, 2020 Maxar Technologies)

6.2. MODEL SETTINGS AND PARAMETERS

The studied model is constructed based on the topology of Yohutagawa debris flow based on a DEM model with a resolution of 2.5 × 2.5 m, as shown in Figure 6.2. The dimensions of the topology are 1135 × 1422.5 m. The terrain surface attitude ranges from 1.5 m to 310 m. A dam is added to the valley according to the real dam location. The shape and size of the check dam are given in Figure 6.3. The

dam has been meshed into small blocks due to the reason given in Chapter 5. To discuss the effects of the large boulders, ten boulders are added to the valley. The boulders are regular dodecahedra with a radius 3 m.

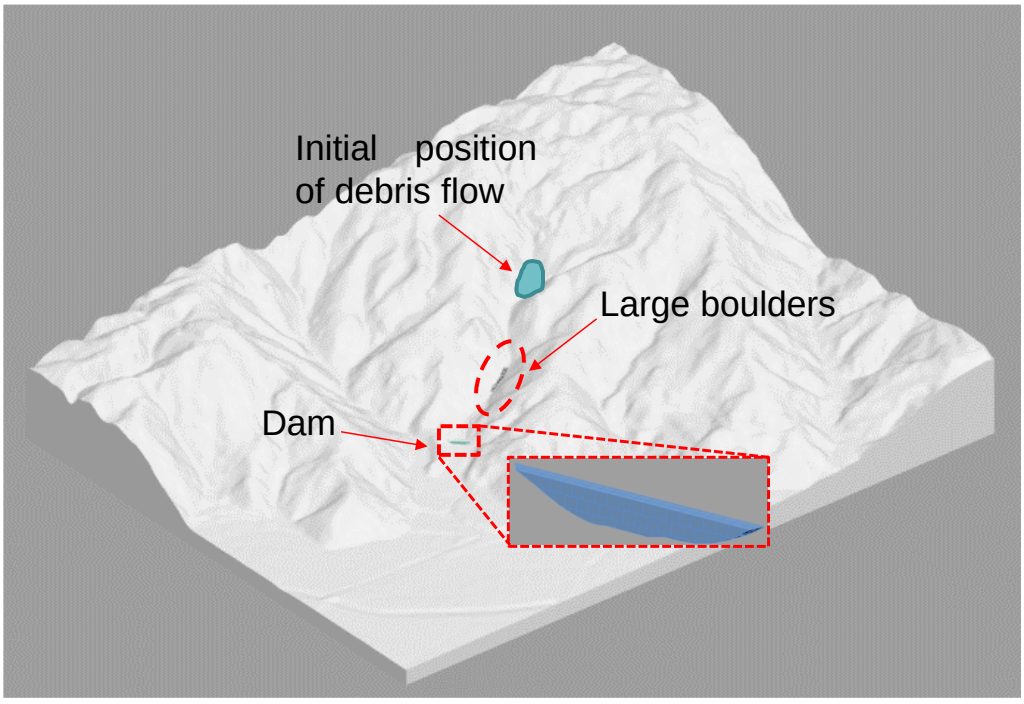

Figure 6.2 Studied model based on topology and debris flow of Yohutagawa, 2010

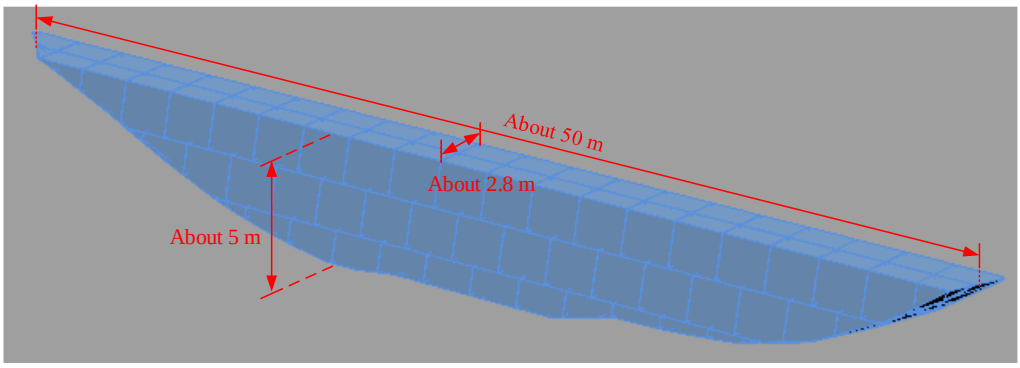

Figure 6.3 The check dam and the dimensions

The parameters regarding debris flow are listed in Table 6.1. The parameters are selected according to previous literatures (Han, Z. et al., 2015a; Han, Z. et al., 2015b; Wu, J. et al., 2013a; Wu, J. et al., 2013b). The parameters regarding solid blocks are listed in Table 6.2. The control parameters for simulations are given in Table 6.3. The step time duration in DFS and 3D DDA modules are different. The damping coefficient introduced in Table 6.3 leads to a COR about 0.8-0.9. As

presented in chapter 5, the boulders are distributed in the valley using a freefall method prior to simulation.

Table 6.1 Debris flow parameters used in analyses

Parameters	Value
Debris flow density: ρ_f (kg/m^3)	1650
Bulk basal friction $\tan\varphi_{bulk}$	0.2
Dynamic viscosity: μ (Pa·s)	5.4
Pore pressure ratio λ_2	0.7
Fatting parameter s_1	0.5
Bed friction angle: $\tan\varphi_{bed}$	0.53
Time interval: Δt (s)	0.001
Mesh size: $\Delta x = \Delta y$ (m)	2.5

Table 6.2 Solid phase parameters used in analyses

Parameters	Terrain	Boulders	dam
Density (kg/m^3)	2000	2500	2500
Poisson's ratio	0.1	0.1	0.2
Young's modulus (GPa)	10	10	30
Friction angle (°)	25	25	10
Tensile strength (Pa)	0	0	0
Cohesion (Pa)	0	0	0
Gravity acceleration (m/s^2)	-	9.8	9.8

Table 6.3 Model control parameters used in analyses

Parameters	Value
Contact spring stiffness (GPa)	100
Time interval: Δt (s)	0.00005
Displacement ratio	0.02
Damping coefficient (N·s/m)	30000

6.3. DAM STABILITY UNDER PURE DEBRIS FLOW AND BOULDER DEBRIS FLOW

As a comparing example, the pure flow condition without large boulders is first modelled. The initial system condition is given in Figure 6.4. The simulation result at physical time t = 120 s is given in Figure 6.5. After the evolution of 120 s, the flow mass accumulated in front of the dam. The maximum depth of the debris flow is about 5 m. Although a small amount of debris flow passes the check dam through the corner, the majority of the flow mass has been stopped by the check dam. The dam remains safe under such conditions. The result suggests that even though for a weak joint (frictional angle 10°, Tensile strength and cohesion 0, seeing Table 6.2), the check dam is still strong enough to hold the debris flow.

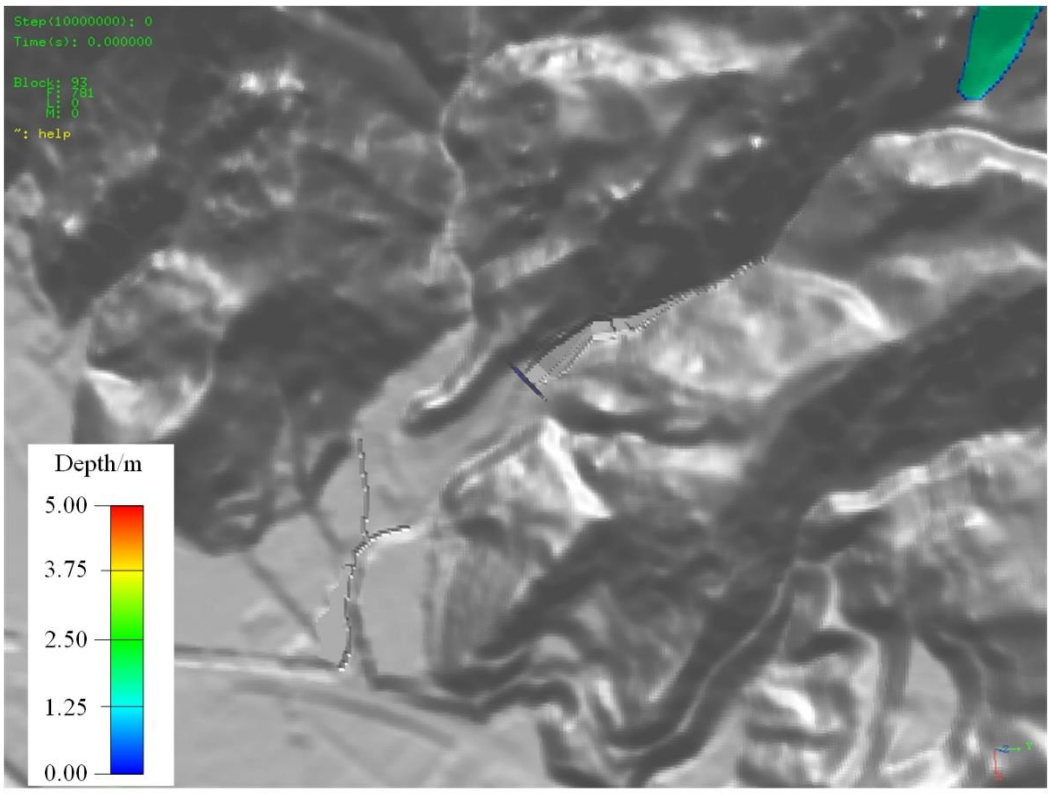

Figure 6.4 Flow depth and dam in the initial state of the model with pure debris flow

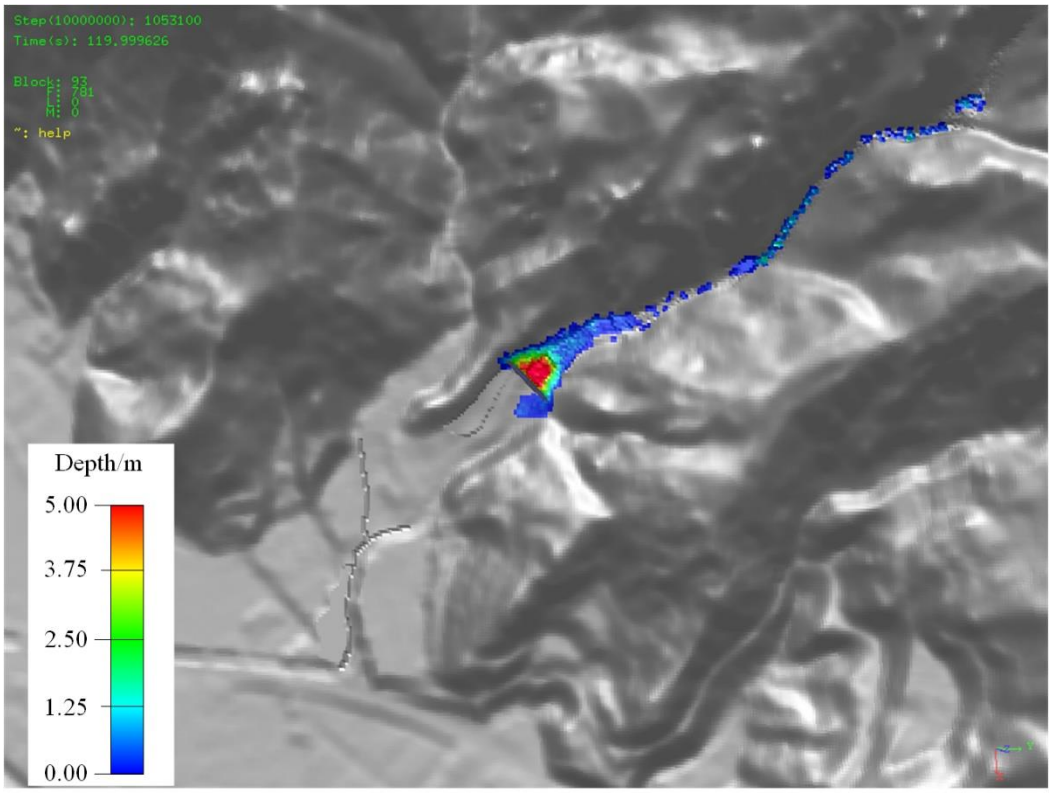

Figure 6.5 Flow depth and dam at t = 120 s of simulation with pure debris flow

The model including boulder debris flow is then simulated. All the parameters are the same as the previous simulation of pure flow. The initial condition is given in Figure 6.6. The first collision between boulders and check dam occurred at about t = 82 s, referring to Figure 6.7, and the huge impact force leads to the breakage of the check dam immediately. In addition, not all the boulders travel with debris flow. It is observed that four boulders stopped in the middle of the valley and do not reach the dam. The final system state at t = 120 s is shown in Figure 6.8. Due to the failure of the dam, debris flow will deposit beyond the check dam, and the deposition extension is significantly enlarged. It is concluded that the same check dam that cannot be destroyed by the corresponding pure debris flow, can be destroyed by a boulder debris flow.

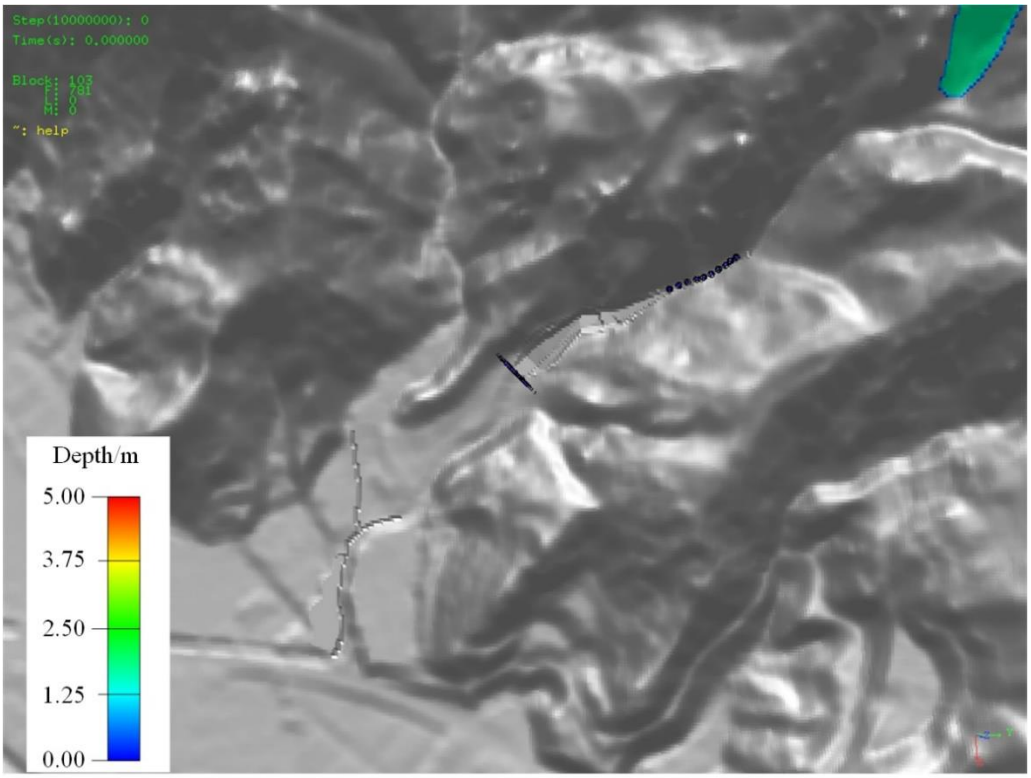

Figure 6.6 Initial flow depth and dam of the model with boulder debris flow

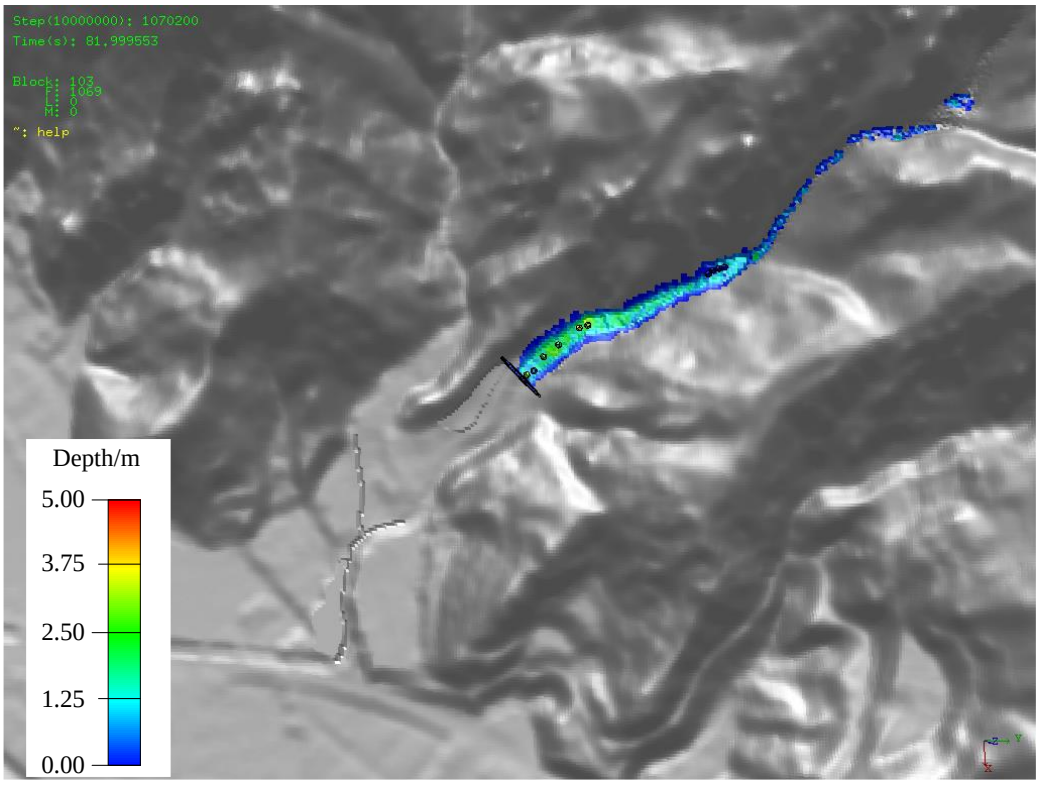

Figure 6.7 Flow depth and dam at t = 82 s of simulation with boulder debris flow

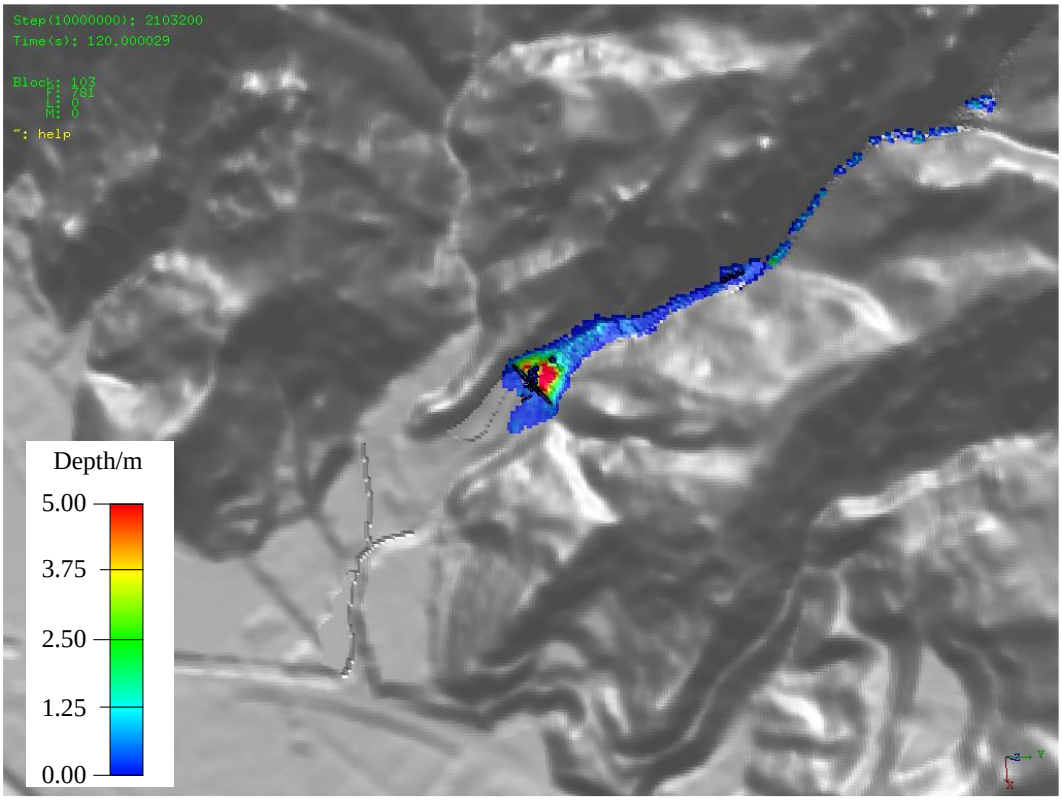

Figure 6.8 Flow depth and dam at t = 120 s of simulation with boulder debris flow

6.4. ESTIMATION OF SAFE DAM PARAMETERS UNDER BOULDER DEBRIS FLOW

The check dam in section 6.3 is stable under pure debris flow, however, it is destroyed by boulder debris flow. The developed 3D DDA-DFS can be applied to determine a set of proper virtual joint parameters to keep the dam safe under boulder debris flow. The virtual joint, as mentioned in chapter 5, is a commonly used method to estimate the breakage of continuous medium as well as the post failure movement. In order to do so, a number of dams with different virtual joint parameters are designed, as shown in Table 6.4. The discussed property is cohesion. The tensile strength in those cases is set to a fixed value 1 MPa. The friction angles in cases 1, 2 and 3 are 45°, 50° and 55°, respectively. The original cohesions in those three cases are 50 MPa, then reduced by 10 MPa every trial until an unsafe cohesion is found. When the friction angle is great, it indicates that the dam is intact, and the joints between dam blocks are virtual; on the other hand, a small friction angle indicates that the joints are real.

Table 6.4 Virtual joint parameters of the dam in case 1-3

Case	1	2	3
Friction angle (°)	45	50	55
Tensile strength (MPa)	1	1	1
Cohesion (MPa)		Reduce from 50	

Cases 1-3 are simulated by 3D DDA-DFS method using a set of cohesion, and the results of case 1 with different parameters are given in Figure 6.9-Figure 6.11. When cohesion is lower than 40 MPa, some blocks begin to fall off due to the impact of boulders.

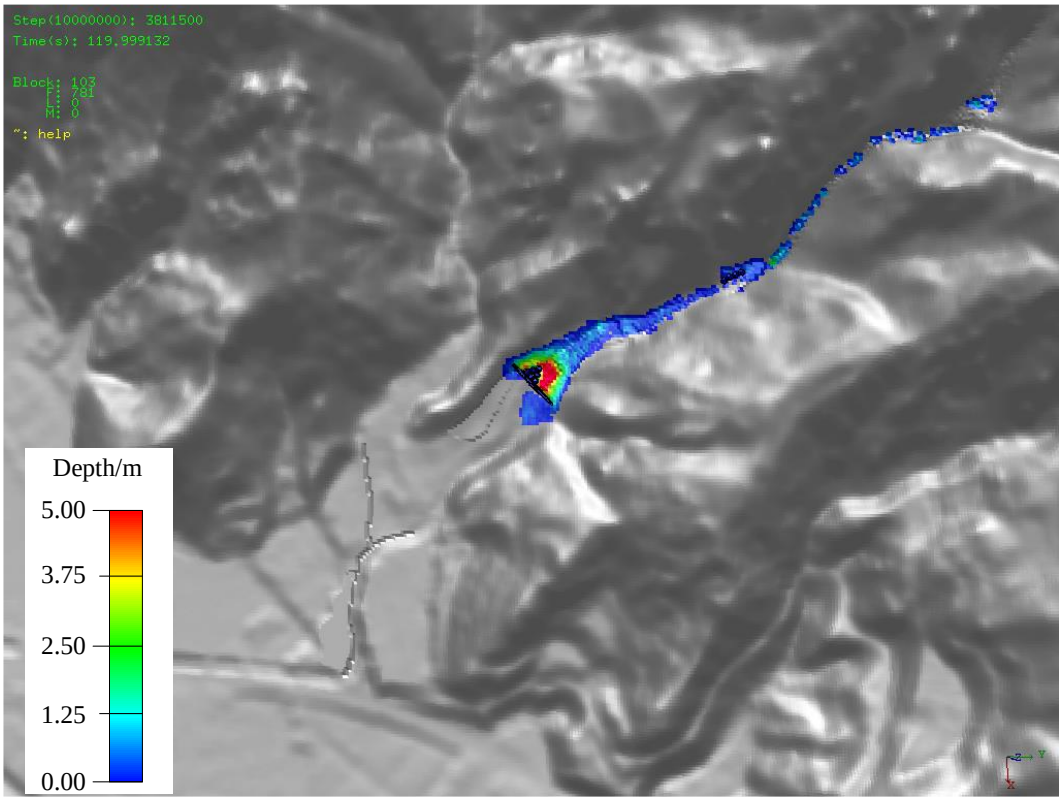

Figure 6.9 Flow depth and dam at t = 120 s of case 1 with cohesion 50 MPa (dam is safe)

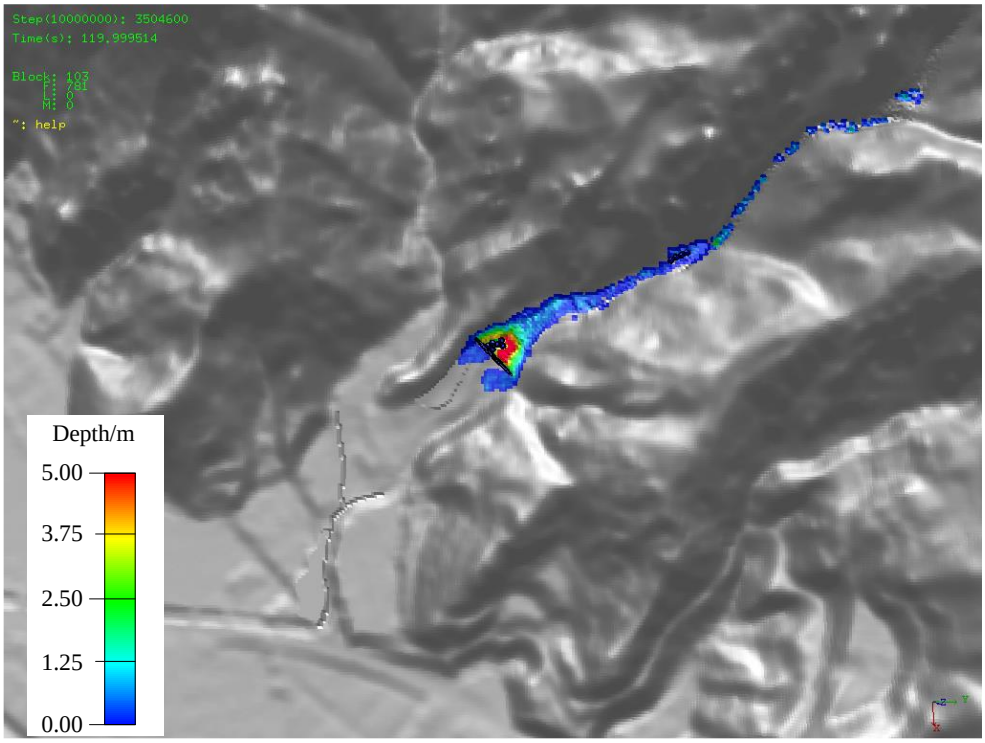

Figure 6.10 Flow depth and dam at t = 120 s of case 1 with cohesion 40 MPa (dam is safe)

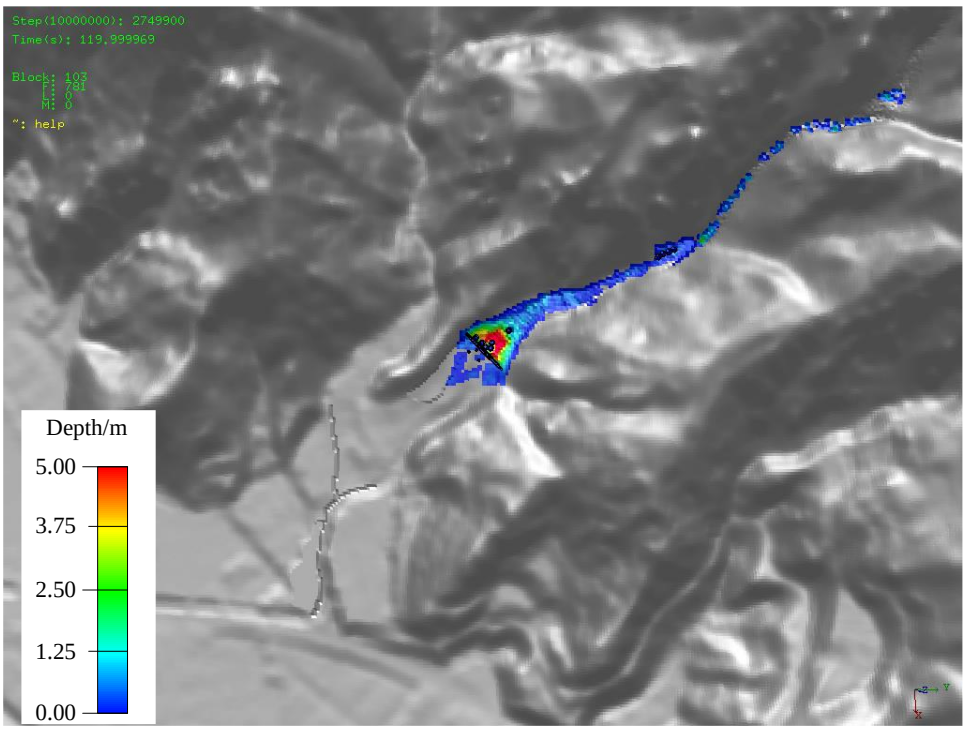

Figure 6.11 Flow depth and dam at t = 120 s of case 1 with cohesion 30 MPa (dam is unsafe)

Similarly, the results of case 2 with different parameters are given in Figure 6.12 and Figure 6.13. Although reduced from 50 MPa, only the simulations with critical parameters are given since the internal friction angle of virtual joints in case 2 is greater than in case 1, In Figure 6.12, the cohesion of 30 MPa is strong enough for the dam, meanwhile, it has to be 40 MPa to maintain safety in case 1.

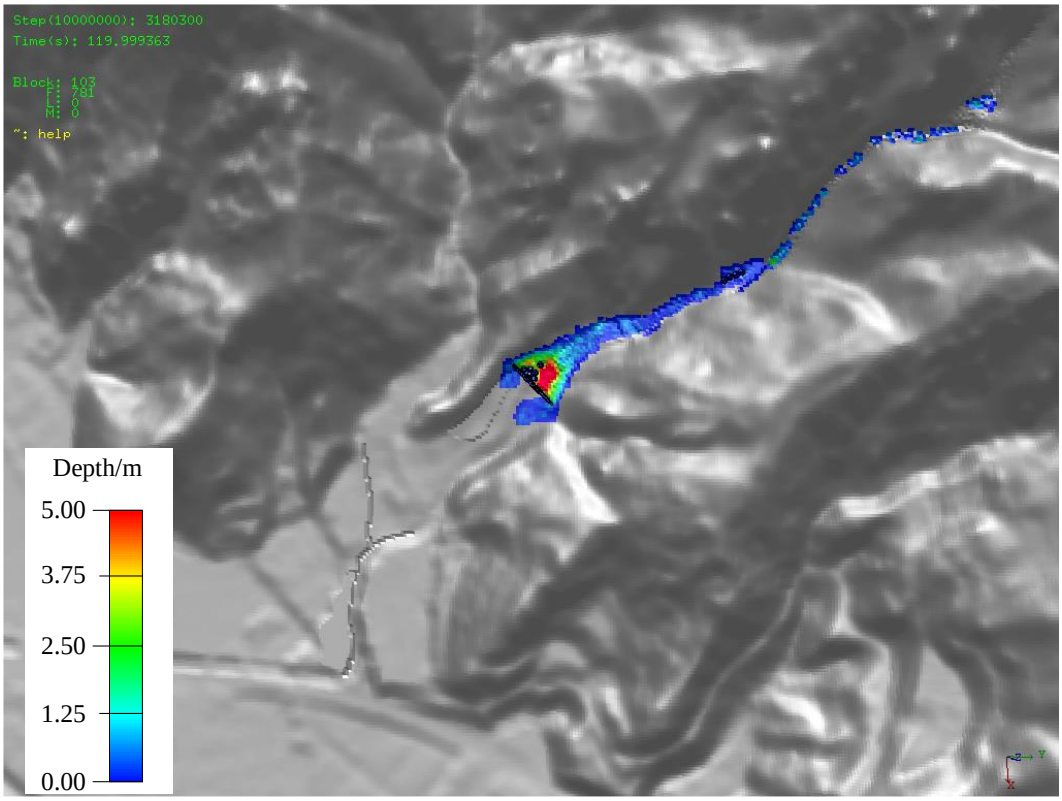

Figure 6.12 Flow depth and dam at t = 120 s of case 2 with cohesion 30 MPa (dam is safe)

Then the results of case 3 with different parameters are given in Figure 6.14 and Figure 6.15. It suggests that 1 MPa of cohesion is still enough when the friction angle is 55°. The reason to chose 1 MPa instead of 0 MPa following the patterns is that the actual cohesion should be greater than 0 MPa if the structure still has some integrity. Therefore, when the internal friction angle equals to 55°, the required cohesion is 1 MPa.

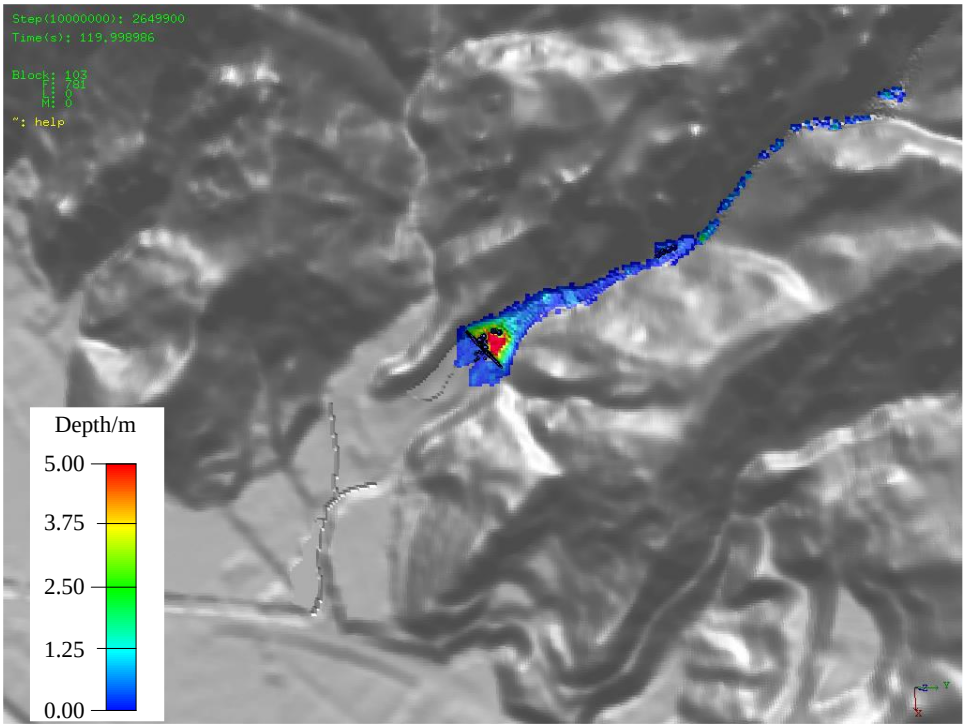

Figure 6.13 Flow depth and dam at t = 120 s of case 2 with cohesion 20 MPa (dam is unsafe)

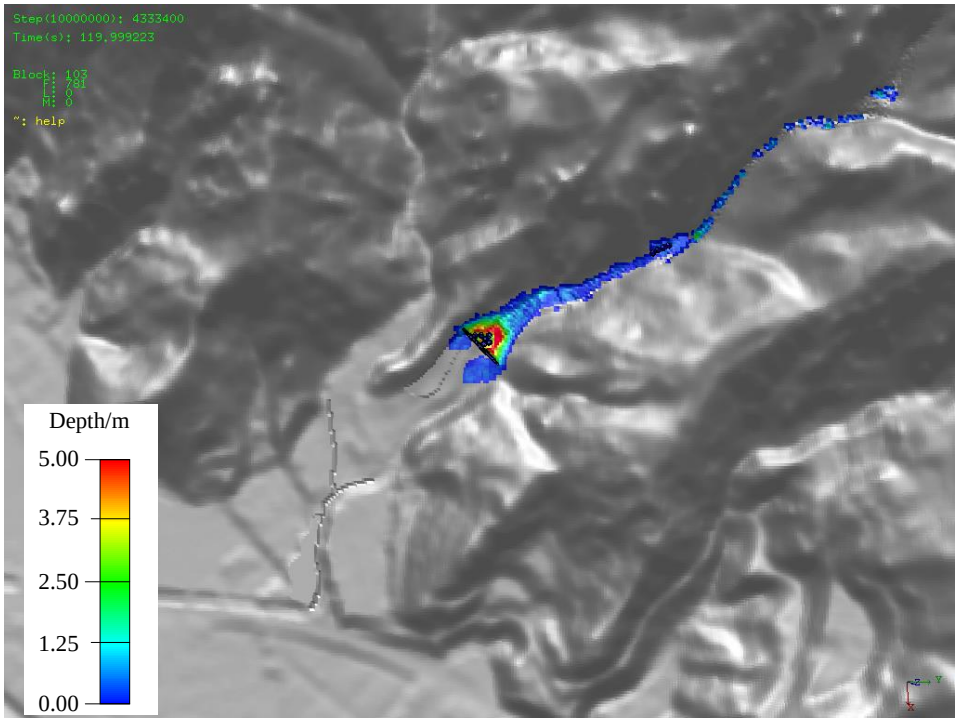

Figure 6.14 Flow depth and dam at t = 120 s of case 3 with cohesion 10 MPa (dam is safe)

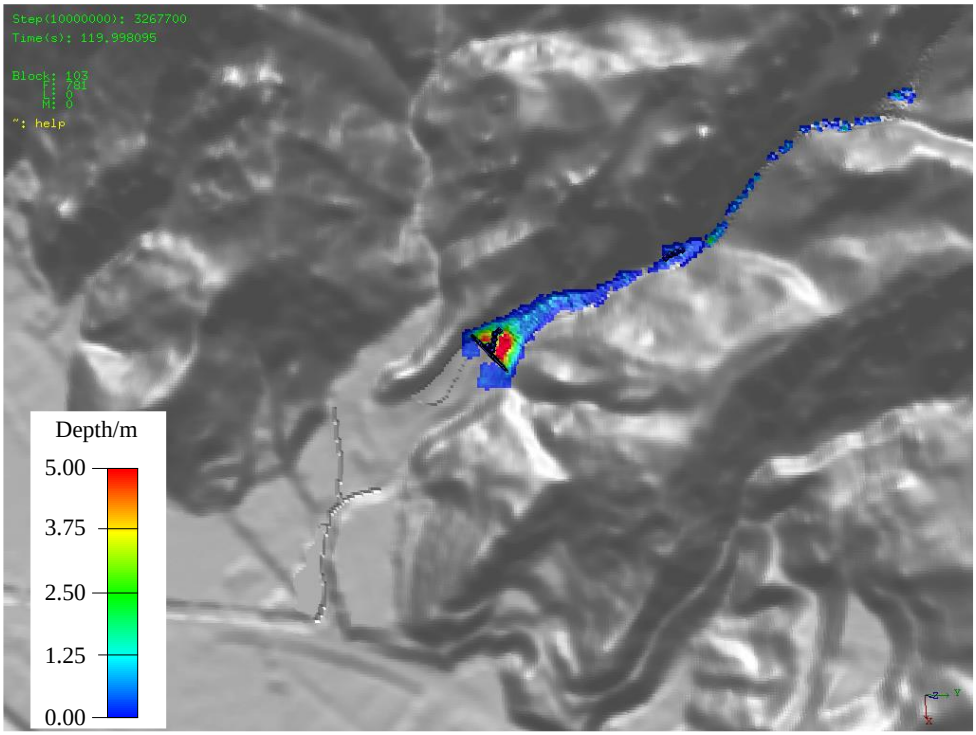

Figure 6.15 Flow depth and dam at t = 120 s of case 3 with cohesion 1 MPa (dam is safe)

The simulation results are summarised in Table 6.5. It suggests that the safe joint parameters for dam under boulder debris flow reduced as the increase of internal friction angle, which is reasonable.

Table 6.5 Safety of the dam in case 1-3

Case	1	2	3
Internal friction angle (°)	45	50	55
Required cohesion (MPa)	40	30	1

6.5. CONCLUSIONS

In this section, a case study is performed by using the 3D DDA-DFS method based on a real terrain territory model with a real check dam located in Amami Oshima, Japan, where the 2010 Yohutagawa debris-flow event occurred. The same source area of the debris flow is used, and a number of boulders are distributed in the valley path. When debris flow passes by, the boulders are driven and move along

with debris flow. The dam safety is analyzed by a number of dam properties. The following conclusions can be drawn:

(1) The transported boulders can break the dam, and more area will be affected by the alluvial fan although the dam was not destroyed under the real debris flows up to now due to no large boulders involved. In the studied cases, when the internal friction angle equals 10°, the dam is safe under the condition of pure debris flow, however it will be destroyed under boulder debris flow.

(2) The 3D DDA-DFS method is applicable to the simulation of debris flow with large boulders. The strength of the dam should be much higher if boulders are involved in a potential debris flow rather than a pure debris flow. For example, in the studied cases, when the friction angle is 45°, the safe cohesion is 40 MPa; when the friction angle is 55°, the 1 MPa of cohesion is enough.

(3) Given to the simulation results, the effect of the transported large boulders in a debris flow should be thoroughly considered for the design of protective structures.

REFERENCE

Han, Z., Chen, G., Li, Y., & He, Y. (2015a). Assessing entrainment of bed material in a debris-flow event: a theoretical approach incorporating Monte Carlo method. Earth Surface Processes and Landforms, 40(14), 1877-1890.

Han, Z., Chen, G., Li, Y., Tang, C., Xu, L., He, Y., Huang, X., & Wang, W. (2015b). Numerical simulation of debris-flow behavior incorporating a dynamic method for estimating the entrainment. Engineering Geology, 190, 52-64.

Wu, J., Chen, G.-Q., Zheng, L., & Zhang, Y.-B. (2013a). GIS-based numerical modelling of debris flow motion across three-dimensional terrain. Journal of Mountain Science, 10(4), 522-531.

Wu, J., Chen, G., Zheng, L., & Zhang, Y. (2013b). GIS-based numerical simulation of Amamioshima debris flow in Japan. Frontiers of Structural and Civil Engineering, 7(2), 206-214.

CHAPTER 7

CONCLUSIONS AND FUTURE STUDIES

7.1. HIGHLIGHTS AND MAJOR CONCLUSIONS

Debris flow is a geo-hazard frequently occurred in mountainous regions. Due to the sudden occurrence, high-speed motion, and the large volume of sediment, debris flow can cause serious disaster and is one of the major threats to residents and structures in susceptible areas. For example, the 1999 Venezuela debris flow killed about 15,000 lives and destroyed or damaged more than 88,000 buildings. Various kinds of countermeasures, such as check dams and concrete canals, have been developed for disaster mitigation. In order to design proper countermeasure structures, it is important and necessary to estimate the kinematic and mechanic behaviors of a potential debris flow as well as impact forces on structures at risk.

In recent decades, many studies on debris flows have been conducted by using numerical methods, analytical methods, empirical approaches based on in-situ investigations and laboratory experiments. With the advancement of computer techniques, numerical methods become more and more attractive in researchers in this field. Among them, DFS with a depth-integrated model based on Navier-Stokes equations has been widely used because it can be easily applied to simulate evolutions of debris flow with bed-sediment erosion as well as estimate kinematic behaviors such as flowing velocity, depth and volume of debris flow and inundated area with high efficiency. However, since DFS is based on a two-phase fluid of

water and solid, called pure debris flow here, using the so-called volume concentration for different ratios of solid to water, there are seldom debris flows of two-phase fluid in nature. In fact, large boulders and driftwoods are often involved in debris flows, called boulder debris flow here, according to a large number of past events. It is obvious that the behaviors and impact force of boulder debris flow cannot be correctly estimated by DFS with a two-phase fluid model. How to simulate boulder debris flows remains an unsolved problem.

(1) Development of a new numeric technique for simulating boulder debris flows by coupling 3D DDA with conventional DFS:

Firstly, 3D DDA is improved by incorporating a damped contact model for inelastic collisions. In order to make DDA applicable to real collisions, a damped contact model based on linear spring-dashpot assumption is incorporated into 3D DDA. How to determine the control parameter of dashpots and viscous damping coefficient is discussed and clarified using a predefined coefficient of restitution (COR). The results show that the damping effect is significant and should be properly addressed.

Secondly, a framework for flow-solid interaction is proposed. An interactive module is incorporated for evaluating the interactive forces between DFS flow and DDA solid blocks through the synchronization of the 3D DDA module and DFS module. The flow force on solid blocks, including static pressure, buoyancy and drag force, are incorporated for arbitrarily shaped polyhedral blocks on complex 3D terrain. In addition, the drag effect between adjacent blocks is addressed so that the calculated drag force is more realistic. An equivalent solution is proposed by taking the action of blocks on flow as a time-varying elevation of terrain node. The coupling scheme as well as the calculations of the interaction forces are validated by a number of examples.

(2) Clarification of the behaviors of large boulders and driftwoods in debris flow:

A series of simulations are carried out on debris flows with boulders in a channel model with a downstream check dam. The impact forces and deformations that the dam suffers from are analyzed under different kinds of debris flows.

The results show that: a boulder can run in front of fluid when its size is large enough in a boulder debris flow; A boulder debris flow can destroy the check dam that cannot be destroyed by the corresponding pure debris flow, and the impact force of the boulder debris flow is about 15 times larger in one case than that of the pure debris flow; The impact forces and deformations are related to the size, distribution and shape of the boulders very much. The dam can be deformed slightly or largely and even destroyed totally under different boulders. Larger size, higher initial attitude, subcircular shape of the boulders are capable of causing more damages to the dam.

The behaviors of driftwoods in debris flow are also investigated. The movement looks reasonable, and the impact force is larger than that of pure debris flow but smaller than that of the boulder with the same volume. The driftwoods can either be stopped by the dam or pass over the dam when overflowing occurs

(3) Performing of a case study by using the 3D DDA-DFS method based on a real terrain territory model with a real check dam located in Amami Oshima, Japan, where the 2010 Yohutagawa debris-flow event occurred:

The same source area of the debris flow is used and a number of boulders are distributed in the valley path. When debris flow passes by, the boulders are driven and move along with debris flow.

The simulation results show that the transported boulders can break the dam, and more area will be affected by the alluvial fan although the dam was not destroyed under the real debris flows up to now due to no large boulders involved. The dam safety is analyzed by a number of dam properties and the results suggest that the strength of the dam should be much higher if boulders are involved in a potential debris flow rather than a pure debris flow.

Therefore, the effect of the transported large boulders in a debris flow should be thoroughly considered for the design of protective structures. It has also been shown that the 3D DDA-DFS method is applicable to simulations of debris flow with large boulders.

7.2. FUTURE STUDIES

This study aims at developing a new numeric technique for simulating boulder debris flows by coupling DDA with conventional DFS. The impact forces of large boulders on check dams are investigated and discussed through conceptual examples. A case study is carried out using the developed 3D DDA-DFS method to discuss the kinematic and mechanic behaviors of a boulder debris flow based on a practical model. However, there is still space for further improvements.

(1) The developed 3D DDA-DFS has been proven to be applicable to boulder debris flow simulation. However, a real application is still desired. The boulders used in this study are conceptual with regular shapes. In future work, the method will be used to a real district that is vulnerable to debris flow. The potential large boulders in the flow path should be investigated in prior. The real shapes and distribution of the boulders are first measured and then input to the model. In this way, the developed method can be used to predict the boulder debris flow disaster.

(2) The implementation of force from DDA blocks on DFS flow is solved by an equivalent solution of taking the action of blocks on flow as a time-varying elevation of terrain node. It has sufficient accuracy in debris flow research, but the equivalent method is not delicate enough if a high precision simulation is desired. Future work should be performed about more accurate estimations of actions of blocks on flow.

(3) The terrain used in this study can be complex. But it is fixed. Earthquakes can also trigger debris flow. Apparently, a fixed terrain cannot represent the dynamic behavior of terrain under earthquake. Further research is desired to introduce flexible terrain so that the effect of an earthquake can be addressed.

(4) The safety of the check dam is focused on in this research. In reality, many structures are threatened by boulder debris flow. The different kinds of structures show different safety characteristics. In addition, sometimes the interaction among structures during a boulder debris flow event is also significant. In future studies, more structures should be involved and discussed under the condition of boulder debris flow.